SILK-BASED TISSUE ENGINEERED INTERVERTEBRAL DISC USING ADIPOSE-DERIVED STEM CELLS

NEO PUAY YONG

NATIONAL UNIVERSITY OF SINGAPORE

2014

SILK-BASED TISSUE ENGINEERED INTERVERTEBRAL DISC USING ADIPOSE-DERIVED STEM CELLS

NEO PUAY YONG

(B.Eng. (Hons.), NUS)

A THESIS SUBMITTED FOR THE DEGREE OF DOCTOR OF PHILOSOPHY

DEPARTMENT OF BIOMEDICAL ENGINEERING
NATIONAL UNIVERSITY OF SINGAPORE

2014

DECLARATION

I hereby declare that this thesis is my original work and it has been written by me in its entirety. I have duly acknowledged all the sources of information which have been used in the thesis.

This thesis has also not been submitted for any degree in any university previously.

Neo Puay Yong

23rd July 2014

Acknowledgements

The author would like to take this opportunity to express her deepest gratitude to the following people who have made the completion of this thesis possible.

To A/P Toh Siew Lok and Prof James Goh, I would like to express my heartfelt gratitude for your invaluable guidance rendered throughout the course of my PhD. You have been more than just my PhD supervisors, but also inspiring mentors I always look up to.

To Dr Eugene See, Dr Thomas Teh and Dr Shi Pujiang, a big thank you for all your selfless mentoring and sharing of knowledge during the various stages of my PhD. Special thanks goes to Serene, Yee Wei and Si Ning for the various support you have given in order to bring this project to fruition.

To my friends and colleagues from the NUS Tissue Engineering Programme and Tissue Repair Lab, thank you for the encouragement and support all these years. The camaraderie we have forged will be one of my most precious memories.

To the staff and ex-staff at the Department of Biomedical Engineering (Aneel, Jacqueline, Melinda, Annie, Millie, Hock Wei and Matthew), a huge thank you for going out of your way to help me on numerous occasions.

Credit is also due to the 9 FYP and attachment students (Andrew, Piers, Mabel, Jenghis, Liting, Fanzhe, Jinglong, Zhulin and Daryl) who have contributed one way or another to the project.

Last but not the least, to my family and bunch of best friends (Wei, Yu, Teng and Qi), thank you for all your understanding and being my unwavering pillar of strength all these years.

Table of Contents

Summary

Tissue engineering (TE) a functional intervertebral disc (IVD) replacement offers a promising treatment modality over current options. Majority of IVD TE studies today focus on either the nucleus pulposus (NP) or the annulus fibrosus (AF). However, the NP and AF work intimately to enable the functionality of the IVD, and hence it is difficult to repair one without affecting the other. For example, without a proper strategy to regenerate a functional AF, NP replacement strategies would have limited clinical success.

The overarching objective of this dissertation is to develop a de novo disc assembly for potential whole disc replacement application. Using a combination of TE strategies, adipose-tissue derived mesenchymal stem cells (ASCs) are used in conjunction with silk-based biomaterials to recapitulate the NP and AF of the IVD. The translation of swelling pressure from the NP to radial compression and circumferential tension in the AF is recreated in the de novo disc assembly, and studied in depth using a real-time load monitoring bioreactor designed to be used in conjunction with it. There are four phases in this dissertation:

In phase one, the suitability of ASCs and ASC cell-sheets (CSs) for IVD TE is explored. The availability and ease of harvesting adipose tissues makes it an attractive and readily available cell source. Results show that ASC CSs retain their multipotentiality; while ASCs are suitable for use in the inner AF, ASC CSs are suitable for the less chondrogenic-like but Col I rich outer AF.

Function and form are intimately related, and hence materials that can mimic the anatomical form of the native tissue are often desirable. In phase two, electrospun-knitted hybrid laminates that resemble the native architecture of the AF are

successfully fabricated. The thin morphology of the TE laminates enable the recapitulation of the circumferentially aligned multi-ply architecture of the native AF when assembled in phase four.

The NP component of the de novo disc assembly consists of a silk/polyvinyl alcohol (PVA) cryogel and is developed in phase three. The addition of silk to PVA improves the cellular compliance and swelling abilities of the cryogels. Analogous to the highly negative proteoglycan content of the native NP, the highly negatively charged PVA allows for water to be imbibed into the silk/PVA croyogels to form a swollen network. The swelling of the NP is a lynchpin to the overarching strategy of this dissertation –creating circumferential tension and radial compression forces on the surrounding AF in the de novo disc assembled in phase four.

In the final phase, a bioreactor that can conduct real-time load monitoring, while allowing for a simultaneous dynamic compression culture of the de novo disc assembly is developed. Results show that culturing the de novo disc under compression influences the development of its AF ECM into a circumferential multi-ply like manner (similar to the native disc). Load monitoring results also demonstrated the mechanical strength of the de novo disc to be comparable to reported values for human discs, thereby attesting to its promising potential as a whole disc replacement treatment option.

List of Tables

List of Figures

List of Abbreviations and Symbols

2D	Two Dimensional
3D	Three Dimensional
ν	Poisson's ratio
ε	Strain
σ	Stress
M_o	Original cryogel weight
M_{fd}	Freeze dried cryogel weight
M_x	Weight of freeze-dried cryogel after x days in PBS
Mn_x	Weight of non freeze-dried cryogel after x days in PBS
AF	Annulus Fibrosus
Agg	Aggrecans
ANOVA	Analysis of Variance
aP2	Adipocyte-binding Protein
ASCs	Adipose-Tissue Derived Mesenchymal Stem Cells
BMSCs	Bone Marrow Derived Mesenchymal Stem Cells
BSA	Bovine Serum Albumin
cDNA	Complementary DNA
CI	Conventional Induced
CNI	Conventional Not Induced
CO_2	Carbon Dioxide
CS	Cell-Sheets
Col I	Collagen Type I
Col II	Collagen Type II
CSI	Cell-Sheet Induced
CSNI	Cell-Sheet Not Induced
DAPI	4',6-Diamidino-2-Phenylindole
DAQ	Data Acquisition

DDD	Degenerative Disc Diseases
DMEM	Dulbecco's Modified Eagle Medium
DNA	Deoxyribonucleic Acid
E	Young's Modulus
ECM	Extracellular Matrix
FBS	Fetal Bovine Serum
FFT	Fast Fourier Transform
GAGs	Glycoaminosglycans
GAPDH	Glyceraldehydes 3-phosphate Dehydrogenase
HFIP	1,1,1,3,3,3-Hexafluoro-2-propanol
H&E	Hematoxylin and Eosin
IAF	Inner Annulus Fibrosus
IL-1	Interleukin-1
IVD	Intervertebral Disc
LBP	Low Back Pain
LG-DMEM	Low Glucose Dulbecco's Modified Eagle Medium
MSCs	Mesenchymal Stem Cells
Mw	Molecular Weight
Na_2CO_3	Sodium Carbonate
NAFL	Native AF like
NP	Nucleus Pulposus
O_2	Oxygen
OAF	Outer Annulus Fibrosus
ON	Osteonectin
OPN	Osteopontin
PBS	Phosphate Buffered Solution
PE	Polyethylene
PPARγ2	Peroxisome Proliferator-Activator Receptor
PS	Penicillin/Streptomycin

PVA	Polyvinyl Alcohol
RNA	Ribonucleic Acid
RT-PCR	Reverse Transcription Polymerase Chain Reaction
Runx2	Runt-related transcription factor 2
SB	Sudan Black
SEM	Scanning Electron Microscopy
SD	Standard Deviation
SF	Silk Fibroin
SOX9	Sex-determining-region-Y-type high-mobility group box 9
TE	Tissue Engineering
TGF β	Transforming Growth Factor β
TNF-α	Tumar Necrosis Factor- alpha
Vit C	L-Ascorbic Acid

Chapter 1. Introduction

1.1 Background and Significance

The Unmet Clinical Need

Low back pain (LBP) is a major socioeconomic burden on the healthcare system worldwide. With an aging population in developed nations, and an increasing life expectancy, studies have estimated the spine market to grow at an annual compound rate of >20% (1,2). The intervertebral disc (IVD) consists of i) the nucleus pulposus (NP), a gelatinous core in the middle, ii) the annulus fibrosus (AF), the fibrous layer surrounding the core, and iii) the vertebral endplates interfacing the IVD with the adjacent vertebral bodies (3). Disc herniation and degenerative disc diseases (DDD) are one of the most common reasons leading to LBP. Due to injury, degeneration or aging, the extracellular matrix (ECM) network of proteoglycans and collagens in the disc may be disturbed, affecting disc hydration, diminishing disc height, and hence increasing strain on the surrounding AF fibres. This causes the AF to tear, and fissures to form at the AF - thereby leading to the protrusion of the NP, causing back pain (4). Current treatment options for DDD, however, address its clinical symptoms as opposed to the pathophysiology of the problem. While early stages of DDD can be treated symptomatically with therapy and administration of medications such as non-steroidal anti-inflammatory drugs, spinal fusion is the more commonly used approach for DDD at the late stages, whereby the entire degenerated disc is debrided and bone fusion is carried out to fuse the vertebral bodies. Both former and latter approaches neither reverse nor repair the damages at the degenerated disc, and patients do not regain the normal functions of the vertebral column (5-8). In particular, spinal fusion initiates and further heightens the risks of IVD degeneration happening to the neighbouring levels of the vertebral column. Hence, there remains a need for a better treatment solution that aims to either cure the disease or restore spinal function.

Bridging the Gap with Tissue Engineering

Tissue engineering (TE) a functional disc replacement offers a promising treatment alternative (6). With a TE approach, the biology and structural architecture of the IVD can be taken into consideration and perhaps mimicked to produce a TE IVD that is robust enough for eventual replacement of the degenerated IVD. Success in IVD TE hinges on the advancement of strategies for both the NP and AF. Most research focus on either the NP or the AF, which is more applicable for treatment in early stages DDD, whereby the overall integrity of the AF is intact, and treatment by hydrogel injection to the NP compartment together with a tissue glue or patch for the AF is sufficient. For late stage DDD cases, a complete disectomy of the degenerated disc would be necessary, and a whole disc replacement or bone fusion would be required. Few TE studies have targeted the replacement of the entire disc, in part due to the challenges faced by such composite TE discs. These include issues pertaining to integration of the TE disc with the adjacent vertebrae, and complexity dealing with multiple cell types and materials with dissimilar properties in a single construct (9).

Successful TE of a functional replacement of the IVD is heavily contingent upon rebuilding its structure, composition, and mechanical properties. Few studies have replicated the IVD as an entire disc, and even for those that do, lack the use of a dynamic culture to accurately reflect the physiological conditions native IVD tissue undergoes. This thesis intends to address such knowledge gaps in current research.

1.2 Objectives and Hypotheses

Using a combination of TE strategies, the overarching objective of this dissertation is to develop a de novo IVD for potential whole disc replacement application to address late stage DDD cases. Adipose-tissue derived mesenchymal stem cells (ASCs) are used in conjunction with silk-based biomaterials to recreate the NP and AF of the IVD. Bio-mimetic culture was then conducted with a custom-designed bioreactor on the assembled de novo IVD. There are four phases in this dissertation, and the respective objectives for each phase are as follows:

Phase 1: Assessment of Adipose-Derived Stem Cells and Cell-Sheet Technology for IVD Tissue Engineering

To assess the suitability of ASCs and ASCs cell-sheets for IVD TE. The specific aims to be achieved under this phase are: i) Characterizing the influence of hyperconfluent culture conditions on the temporal growth of ASCs cell-sheets; ii) Studying the effects of a hyperconfluent environment by temporal profiling the differentiation efficiency and capability of ASCs within cell-sheets (over the adipogenic, osteogenic and chondrogenic lineages) in comparison with ASCs that were directly differentiated with no prior cell-sheet formation, and iii) Determining whether ASCs or ASCs cell-sheets should be used in the subsequent phases.

Hypothesis 1: Hyperconfluent culture of ASCs allows the formation of a rich ECM layer; whilst the effects of which influences ASCs to behave differently.

Phase 2: Development of Hierarchical Hybrid Silk-based Laminates for Annulus Fibrosus Tissue Engineering

To fabricate electrospun-knitted hybrid laminates that resemble the native architecture of the AF – with the electrospun silk mats being aligned to confer

topographical cues, while the thinly knitted silk mesh reinforces the hybrid lamella and enables ease of handling. In addition, the objective under this phase was to also determine the viability and performance of the ASCs and ASCs cell-sheets on the fabricated aligned hybrid silk laminates for application as TE AF to be used in the subsequent phases.

Hypothesis 2: The responses of ASCs and ASCs cell-sheets are different on the hybrid silk laminates, which can be leveraged on to recreate the stratified architecture of the native AF.

Phase 3: Fabrication and Characterization of Silk/PVA Cryogels for Nucleus Pulposus Replacement

To characterize silk/PVA cryogels fabricated by a physical (freeze-thaw) crosslinking regime to determine an optimal condition for cellular compliance. Specifically, the effect of silk in the silk/PVA cryogels on some properties relating to cellular attachment and proliferation are investigated (Eg. hydrophobicity/hydrophilicity and porosity). Proliferation of ASCs in these silk/PVA cryogels is subsequently assessed and mechanical assessments pertaining specifically for NP replacement purposes are investigated (Eg. hoop stress and compressive modulus).

Hypothesis 3: Doping PVA with silk will improve cell attachment and proliferation abilities of PVA, and hence allow the resultant composite (silk/PVA) cryogel to be a better tissue engineered NP replacement candidate

Phase 4: Assembly and Evaluation of Multimodal De Novo IVD Construct with Real-time Monitoring Compression Loading Bioreactor

To assemble a de novo IVD construct using the tissue engineered AF and NP components from Phase 2 and 3 respectively. The de novo disc will be held together

by a knitted silk cuff (Figure 1-**1**), and evaluated for its suitability as an IVD replacement. In addition, the objective under this phase was also to develop a bioreactor that can conduct real time load monitoring of the de novo IVD constructs while undergoing dynamic compression culture mimicking physiological loading conditions. And finally to evaluate the de novo IVD constructs as potential whole disc replacements (using the bioreactor and comparison with constructs under the influence of chemical cues).

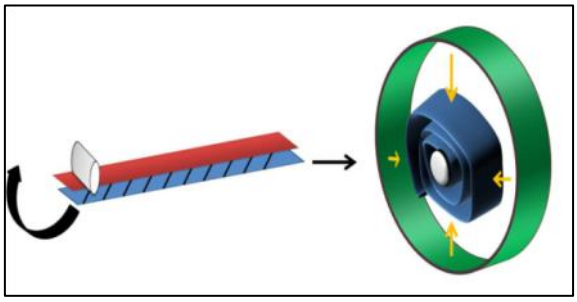

Figure 1-1. Illustration of assembly concept of the de novo IVD construct. Red indicates presence of ASCs or ASCs cell-sheets evaluated in Phase 1. Blue indicates hybrid silk-based AF laminates developed from Phase 2. Grey indicates silk/PVA NP replacement developed from Phase 3. Green represents knitted silk cuff.

Hypothesis 4: Fibers within the extracellular matrix (ECM) of the ASCs are able to detect mechanical stimulus and adapt accordingly, just like in the native IVD where the AF cells undergo a circumferential tensile and radial compression stress due to the radial bulging of the NP. And by culturing the de novo IVD construct under stimulating forces similar to those experienced in the native condition, the ECM of the construct would be enhanced to be closer to that of a native disc.

1.3 Outline of Dissertation

Research work pertaining to this dissertation was carried out in four phases and this thesis comprises of seven main chapters. They are structured as such:

Chapter 1 provides an introduction to the background and clinical significance of this dissertation. The objectives and hypotheses underpinning the work done are also covered in detail.

Chapter 2 is a literature review on the anatomy and function of the IVD, followed by information on the pathophysiology and current treatment options for IVD degeneration. Insights into the area of TE are also mentioned. These include some of the TE approaches undertaken for IVD related work, and the use of ASCs, silk and physical cues (topographical and mechanical) in TE. The chapter ends off with a critical evaluation of the IVD related TE strategies discussed.

Chapter 3 consists of phase one, whereby ASCs and cell-sheet technology are evaluated for its suitability in IVD tissue engineering. ASCs and ASCs cell-sheets are first characterized and assessed for their multi-potentialities, before being evaluated for their suitability for use in IVD TE.

Chapter 4 covers phase two, on the development of hierarchical hybrid silk-based laminates for TE AF fabrication. Comprising of electrospun silk nano-mats incorporated with thinly knitted silk meshes, the hybrid laminates are first characterized for their physical properties, before being assessed for their cell-hosting abilities.

Chapter 5 focuses on phase three, involving the fabrication and characterization of silk/PVA cryogels that will be used as NP replacements. Blending silk with polyvinyl alcohol (PVA), various formulations of silk/PVA are explored for its physical and cell-compliant characteristics. An ideal candidate was then selected for use in the assembly of the de novo IVD construct in phase four of the study.

Chapter 6 is on phase four, where a multimodal de novo IVD construct comprising both the NP and AF components developed in the earlier phases is assembled and evaluated. Chapter 6 is also on the development and use of a real-time load monitoring bioreactor for biomimetic assessment of the assembled de novo IVD construct. Results from the dynamic culture loading condition will be compared to those from the static culture condition and those under the influence of chemical cues.

Chapter 7 concludes the key points derived from this dissertation, and provides recommendation for future works.

Chapter 2. Literature Review

2.1 Anatomy and Function of the Intervertebral Disc

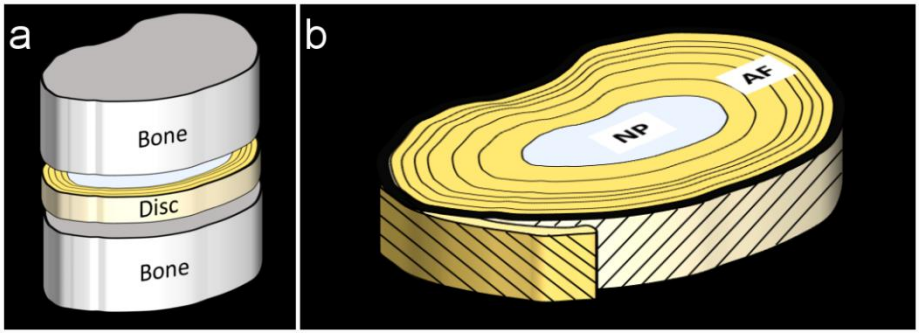

Figure 2-1. Schematic drawings of (a) an IVD between two vertebrae bodies and (b) a sagittal section of the IVD showing the NP and surrounding AF.

The IVD can be found between two vertebrae bodies and consists of 3 distinct components, namely i) the gelatinous NP in the central region, ii) the fibrous AF surrounding the NP, and iii) the endplates interfacing the disc with the adjoining vertebral columns in the cephalic and caudal directions (3,10) (**Figure 2-1**). The major functional role of the IVD is to withstand loads whilst enabling some degree of flexibility along the vertebral column, allowing movements like bending (flexion) and turning (torsion). During loading conditions, the IVD absorbs and disperses loads - an ability that is intimately related to its capability to absorb and release water (3) (Figure 2-**2**). This capability is in turn related to the constituents of the NP.

Water is the main component of the NP (>80%), together with proteoglycans, collagen and elastin (3,11). While the interconnected network of collagen and elastin provide the elasticity and general morphology of the NP, the proteoglycans maintain the osmotic pressure, and in turn confer compressive strength, stiffness and viscoelasticity properties to the IVD as a whole (3,11) (Figure 2-**2**). During loading, lateral expansion of the NP is confined by the surrounding AF through i) tension of the AF in the circumferential direction, and ii) compression of the AF in the radial direction (12). The AF is a highly oriented structure with concentric layers of collagen fibres that are aligned in a parallel fashion within the same lamella, but lie in

opposite directions between successive layers of lamellae (Figure 2-**1**). These collagen fibres lie at an approximately 60^{o} angle to the spinal axis (13-15). In terms of constituents, water contributes to 65%-75% of tissue weight in the inner AF, and 55%–65% in the outer AF (16). The bulk of the extracellular matrix on the other hand consists of mainly collagen fibres, constituting 40–60% of the outer AF and 25–40% of the inner AF (16,17). Type I collagen is most prevalent in the outer AF and decreases radially inwards; while Type II collagen is dominant in the inner AF and decreases radially outwards, thereby creating an opposing gradient between these two collagen types (18,19). Other major constituents of the AF includes proteoglycans, in particular aggrecans, which constitute (by dry weight) 5–8% of the outer AF and 11–20% of the inner AF (11,16), thereby creating an increasing proteoglycan gradient from the outer AF to the inner AF (11,16,17). Collagen fibres in the outer AF insert into the vertebral bodies, while those of the inner AF insert into the endplates (11,20,21). The cartilaginous endplates on the other hand serve an important role in terms of nutrients and wastes exchange between the NP/AF and the vascular systems in the neighboring vertebral bodies (11).

Such unique structural properties and constituents confer the AF with the ability to carry out two important physiological functions. The first function is to contain the radial bulging of the NP during physiological loadings of the spinal column to enable a uniform distribution and transfer of compressive loads between the vertebral bodies. The second function is to allow distension and rotation to facilitate joint mobility (3,12,19).

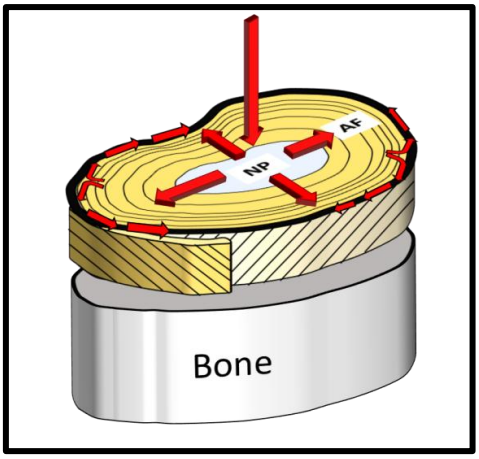

Figure 2-2. Illustration of the vertebral column during physiological loading. The NP bulges during loading, allowing dissipation of forces to the AF.

2.2 Pathophysiology of Intervertebral Disc Degeneration

Low back pain (LBP) has been estimated to affect about 80% of the population at some point in their lifetime (1,2). Despite its ubiquitous nature, the exact causes of LBP remain debatable, with numerous theories present in literature (22,23). Rather than being a condition itself (with a precise pathogenesis), LBP should be considered as a symptom that is brought about by multiple conditions (22,23). One of the conditions that LBP is most strongly correlated with is degenerative disc disease (DDD) (24-26), which will be the focus of this thesis.

DDD can be morphologically characterized by several features (27). In the NP, they include a change in the type of collagen synthesized (more Col I than Col II), and a decrease in the amount of proteoglycans, in particular aggrecans (28,29). The former resulting in the disappearance of the delineation zone between the NP and AF, and the latter resulting in the NP being dehydrated. The NP becomes more fibrous (Eg. stiffer), with lesser water content, resulting in a narrowing of disc height and disrupting the normal mechanics of load dissipation in the spinal unit. In the AF, some of the changes include fibre orientation in the collagen rich lamellae becoming disorganized, and fissures appearing on the AF with structural disruption to the lamellae (15). All these coupled to result in an instability in the spinal unit and

further exacerbates the degeneration by rendering it even more difficult for the disc to repair itself while making it easier for further injuries to be inflicted (23). In late stages DDD, the NP and AF may eventually be replaced by scar tissues (30). Neovascularization may also take place, extending into the central NP region, causing innervations of the disc (31). Some of the underlying factors responsible for such morphological changes include genetic influences (32), injuries, age, and lifestyle choices (Eg. nutrition, smoking). Research into the molecular mechanisms of DDD have shown that central to the pathogenesis of DDD is an increased presence of IL-1 (interleukin-1) amd TNF-α (tumor necrosis factor-alpha). Both IL-1 and TNF-α belong to a family of pro-inflammatory cytokines and inflammatory mediators, and are believed to play important roles in the catabolism of the disc matrix (33,34). For example, a study by Le Maitre and colleagues (35) showed that recombinant IL-1 was able to stimulate human NP cells to produce i) an upregulation of MMPs, ii) a change in relative Col I/Col II expression, and iii) a decrement in aggrecan expression.

Associating DDD back to the clinical problem, there are several possibilities by which DDD can bring about LBP. They include a combination of one or more of the following: i) pain generated by the disc itself (also termed "discogenic pain"), ii) pain generated at the highly innervated facet joint as a consequence of a lowered disc height, iii) pain caused by the inflammatory response and impingement of nerves of a herniated NP, and iv) activation of inflammatory stimuli at the nerve endings and mechanoreceptors on the AF (22).

2.3 Current Treatment Modalities for Intervertebral Disc Degeneration

Lumbar disectomy is one of the most commonly performed surgical procedure for patients who suffer from LBP (36). While discectomy can provide favourable results most of the time, there remain unmet clinical needs in conditions involving large disc protrusion with minimal disc degeneration and adolescent disc protrusion. In these

conditions, damage to the surrounding annulus often results in recurrent herniations and hence requiring further surgical interventions (37,38). In addition, to prevent patients from "post-disectomy syndrome", whereby recurrent herniation happens, surgeons will remove a greater portion of disc tissues during the original herniation surgery. Furthermore, a study by DePalma and workers in 2012 (39) suggests that the main cause for the painful symptoms experienced by patients after surgical disectomy may be due to the fissures and tears on the AF. These further substantiate the importance repair and/or regeneration of the AF to go in tandem with the NP.

Several approaches have also been undertaken to attempt to close an AF defect after discectomy (40). One of which is the use of sutures to directly repair the defect site. However, this is very technically demanding due to the constraints in space and potential injury to the close-by neurological structures. Sealants such as fibrin glue (41) are often used in conjunction with the sutures to provide sufficient reinforcement. For large AF defects, the inner AF would also be damaged more severely and hence recurrent disc herniation would also be more likely. To repair such defects, there are clinical implants available today that can seal and reinforce the AF by suturing to the remaining sides of the AF (InClose) or by anchoring into the adjacent vertebral body (Barricaid) (40,42). However, there is still a dearth in published data today on the long term effectiveness and safety of these devices.

The traditional treatment strategy for DDD would be spinal fusion, a procedure which first involves the removal of the entire degenerated IVD and then subsequently stimulating bone growth in the debrided space through the use of autograft or allograft bone tissues, growth factors and/or synthetic cages. Spinal fusion remains the current gold standard treatment for DDD, especially in late stage DDD cases (43). Despite its prevalent usage, spinal fusion is still not reliable, often failing to alleviate pain, and causing instability at adjacent levels of the intervertebral column (44-46).

Alternative technologies such as artificial disc replacement show promise in recent years because of its ability to restore degree of motion without causing adjacent joint segment rigidity – thereby preventing future adjacent segment related abnormalities and surgeries. One of the most prominent artificial disc prostheses in clinical use today is the SB Charit**é**. Introduced in the 1980s, the SB Charit**é** is a ball-and-socket articulating joint consisting of two cobalt chromium endplates (coated with titanium and hydroxyapatite for better osteointegration with the vertebral bodies), and a polyethylene (PE) core (27,47). While such artificial disc prostheses allow for axial rotational freedom, it is also plagued with drawbacks ranging from a lack of absorbance of compressive forces, extrusion/loosening of the device, infection at the surgical site, and long term wear and tear of the PE components (which may also exhibit material creep and fatigue) (48,49). Indeed, several long term studies of such prostheses have showed that the approach is still marred by such complications and will in fact cause adjacent segment degeneration and require revision surgeries (50,51).

2.4 Biologic Treatment Approach for Degenerative Disc Diseases

Beyond the clinical treatments mentioned in section 2.3, other treatment approaches that are still in the research phases today include the therapeutic injection of biologic compounds. Biologic treatment approaches to address DDD has been reported in literature for more than 20 years (52), with one of the earliest studies using TGF-β to target IVD cells in a canine model being reported in 1991 (53). Homeostasis in the disc is maintained by a balance of anabolic and catabolic activities of the cells residing in the IVD. An imbalance of which affects the ECM constituents, and hence brings about the onset and progress of DDD (52). The aim of biologic treatment is then correction of such imbalances through the use of anabolic agents like growth factors (Eg. BMP-7, TFG-B) or catabolic inhibitors (Eg. IL-1 receptors antagonists).

In vitro studies in this regard were mostly carried out by studying the effects of bioactive molecules like TGF-β, BMP-2 and dexamethasone on isolated IVD cells (54-56). In vivo studies mostly involves introduction of the therapeutic agents by intradiscal injection, and studying the changes in disc height, proteglycan contents and gene expressions among other parameters after a period of time (Eg. 4 weeks) (52,57). However, such biologic treatments are still very much at the research stages, and results generated thus far are based on in vitro and pre-clinical data.

2.5 Intervertebral Disc Tissue Engineering

It is important to note that none of the clinically available treatment modalities mentioned in section 2.3 address the pathophysiology of DDD nor aim to fully restore normal spinal functions (5-7). Hence, there remains a need for a better solution that can achieve at least one if not both of the above mentioned objectives. Apart from the biologic treatment approach covered in section 2.4, an attractive alternative approach would be TE. Involving combinations of one or more of the following: cells, materials, biomolecules and mechanical stimulatory cues (58), TE may be defined as "*the creation (or formation) of new tissue for the therapeutic reconstruction of the human body, by the deliberate and controlled stimulation of selected target cells through a systematic combination of molecular and mechanical signals*" (59). Beyond architectural reconstruction of the IVD tissue, TE offers the potential to recapitulate the normal functionality of the IVD by means of a repair, replacement and/or regeneration of damaged disc tissues.

Application of TE strategies can be carried out concomitantly with discectomy (27), thereby reducing patient morbidity. Biocompatible biomaterials meeting the requirements of the intended IVD tissue of interest can be implanted (with or without the combination of cells and chemical cues) to the debrided space after the full or partial removal of a degenerated disc. For earlier cases of DDD where removal of an

entire disc is not necessary, NP tissue can be replaced by injection of hydrogels, in conjunction with tissue sealants, or AF fissures can be potentially patched with engineered AF patches. Essential to the concept of TE is the role of biochemical and/or biophysical stimulatory cues. On this note, developments mentioned in the preceding paragraphs on biologic treatment approaches overlap with the former, while more on the latter will be discussed in the following sections.

2.5.1 Tissue Engineering Approaches for Annulus Fibrosus Repair and Regeneration

As mentioned in the earlier sections, the AF experiences complex loading conditions, and is exposed to residual stresses even when the spinal column is unloaded (60). The objectives of AF TE are mainly to mend the damaged AF to prevent disc herniation and further AF degeneration (61). Form is intimately related to function, and this is especially true for the AF. Hence, AF-related TE strategies reported in literature over the years have focused on recapitulating the complex architecture of the native AF, in a bid to restore functionality. These include the use of natural or synthetic lamellar-like scaffolds, with or without fibre orientations to mimic the ECM constituents and architecture of the native AF (61).

One of the earliest studies that reported a TE AF involved the use of Type I atelocollagen scaffolds made by freeze-drying and seeded with AF cells (62). A range of biomaterials have also been reported in literature for use in AF TE, they include silk (63,64), poly-L-lactide (65), and polycaprolactone (8,66,67). Other AF-related TE studies reported in literature include those published by Shao et al (68) and Bowles et al (69), involving the use of alginate/chitosan scaffolds and collagen gels contraction respectively. In particular, the system described by Bowles and co-workers involved the contraction of collagen gels around a cylinder to allow for cellular alignment in a lamellar fashion in their collagen-based AF constructs (69).

Extending the discussion on alignment, several published studies by the McKay Orthopaedic Research Laboratory at the University of Pennsylvania demonstrated the importance of mimicking the hierarchical structure of the native AF in AF tissue engineering (8,67,70). In one study, it was shown that planar sheets of scaffolds, consisting of aligned polycaprolactone (PCL) nanofibres, directed the seeded MSCs to deposit a organized and collagen rich ECM. Furthermore, by assembling the MSCs loaded planar sheets into a rolled up construct with concentric lamellae, shearing interactions between lamellae was shown to play a part in reinforcing the tensile response of the construct. In another study (67), aligned nanofibrous scaffolds were tested under uni-axial tension at multiple fibre angle orientations. It was shown that there is a nonlinear dependence of modulas on fibre angle. This resembles the anisotrophic nature of the native AF, and that at fiber angles of 28^{o}–44^{o}, the engineered scaffold material behaved most like native AF tissue.

2.5.2 Tissue Engineering Approaches for Nucleus Pulposus Repair, Regeneration and Replacements

Hydrogels emulating the NP have been a popular approach undertaken in IVD regeneration over the last decade or so (71). The high water content and highly tunable physical/chemical properties of hydrogels make them attractive candidates for NP regeneration. Various materials have been widely researched to make hydrogels for NP regeneration purposes. These include chitosan (72), alginate (73,74), Type I collagen (75,76), hyaluronic acid (77,78) and gellan gum (79) - with majority of these strategies involve administering the hydrogels as injectables. Such an approach has its inherent disadvantages, as it inflicts micro-damages to the surrounding AF tissue and disrupts its cellular and mechanical integrity. A compromised AF further poses the risk of future herniation of the injected hydrogel material (9). Hence, research into injectable hydrogel technologies is required to go in tandem with developments in AF

closure solutions involving devices (Eg. plug) and adhesives (80-82). For example, Wiltsey and co-workers described in a recent study, a novel injectable hydrogel made of poly(N-isopropylacrylamide) and chondroitin sulfate that had adhesive capabilities to form an interface with the surrounding disc tissue (83).

An alternative to the hydrogel approach would be the use of strong and elastic gels as NP replacement prostheses (Eg. NuCore, NeuDisc) (84,85). In this regard, poly (vinyl) alcohol (PVA) cryogels have been reported as a suitable material for NP replacement (86). Wang and Campbell, through a series of mechanical assessments on various PVA cryogel formulations, conclude that PVA cryogels can be tuned during the manufacturing process to resemble some of the properties of the human IVD (86). Joshi and co-workers combine poly (vinyl) pyrrolidone (PVP) with PVA and conclude the hybrid material to be a mechanically feasible candidate for use as an NP replacement (87). However, these studies are acellular approaches and hence such implanted NP replacements do not possess any regeneration capabilities and will probably not be able to have good implant integration at the end-plates interface. Poor integration of the NP replacements will bring about device migration issues and poor clinical success rates as has been demonstrated by the PDN device (88) in the late 1990s (89).

2.5.3 Tissue Engineering Approaches for Whole Disc Replacements

The intimate relationship between the NP and AF also imply the underlying challenges involved in repairing the damaged IVD - it is very difficult to repair/replace either the NP or the AF without considering the effect or compatibility of one with the other. Moreover, TE the NP or AP alone can only replicate the endemic properties of the respective tissues, and do not necessarily translate to a functional replication at the disc level. As such, TE an entire IVD replacement appear to be an emerging trend, whereby an entire engineered disc is inserted between the

joint space after the degenerated disc is debrided. Such a whole disc approach is in turn hampered by several challenges including: i) complexity working with multiple materials with disparate properties, ii) eventual integration issues at the pre-clinical stages of the TE disc with the adjacent vertebral bodies, and iii) overcoming diffusion limits to ensure survival of cells within the TE disc (9) (90).

Biphasic composite engineered discs containing components analogous to the NP and AF have been reported in literature in this regard. Mizuno and co-workers were one of the pioneers in this aspect, reporting on the fabrication of an IVD composite disc comprising of a PGA/PLA mesh as the AF, and an alginate gel as the NP (7,91). Nerurkar and colleagues brought the AF-related TE work that was described in section 2.5.2 further by incorporating the PCL lamellas with an agarose core to form a composite disc in 2010 (70,92), while the AF lamella work covered earlier in section 2.5.2 by Bowles and colleagues were part of a composite disc consisting of alginate as the NP (69,93).

Other research groups that have reported TE composite discs include those by Wilke et al (75) and Nesti et al (94), involving the use of Col I and PLLA (in combination with hyauronic acid as the NP) as biomaterials respectively. Some of the more recent studies in this area are those by Park et al (95,96), Bhattacharjee et al (97,98) and Lazebnik et al (99), with the former two studies using silk to form the AF (Park et al used a fibrin-hyauronan hydrogel as the NP core, while Bhattacharjee et al utilized a silk fibroin hydrogel as the NP instead). Lazebnik and co-workers electropsun PCL as the AF, and incorporated agarose as the NP. In a bid to address the issue of integration of engineered discs with the vertebral bodies, Chik and colleagues (100) described in a recent study the fabrication of the first tri-phasic engineered IVD consisting of two osteochondral subunits, a NP core, and coupled with a multi-lamellar AF-like component. Different forms of collagen were used for all three

components, with the aim of leveraging on the osteochondral subunits for better integration with the neighboring vertebral bodies. Other examples of such assembled discs include those described by Tsai and co-workers (101) (consisting of electrospun PLLA /PCL as the AF and PuraMatrix as the NP) and See and co-workers (102) (consisting of silk sponge lamellae and cell-sheets as the AF with silicone as the NP surrogate).

2.6 Adipose-Derived Stem Cells and Cell-Sheet Tissue Engineering

2.6.1 Background on ASCs

The therapeutic applications of MSCs for various clinical conditions have been widely researched on. These include (but is not limited to) the use of MSCs for skeletal tissue repair (103), kidney injuries (104), bone tissue engineering (105), soft tissue augmentation (106), cardiac tissue engineering (107) and ocular diseases (108). BMSCs are typically used in tissue engineering approaches, but have limited availability and accessibility. Adipose tissue on the other hand is expendable and can be abundantly found in humans and most animal models. ASCs which are isolated from fat tissues, possess self-renewing capacity and display multipotentiality (109,110). It has been shown that under controlled conventional differentiation conditions, ASCs can differentiate into osteogenic, chondrogenic, adipogenic, endothelial and neurogenic lineages (111-116).

2.6.2 Cell-Sheet Engineering: Concept and Advantages

Cell-sheet engineering typically involves the culturing of cells using a thermoresponsive polymer as the substrate (117). Cells are cultured to confluence or hyperconfluence, thereby forming a two-dimensional sheet which can be lifted off the substrate by changing the hydrophobicity / hydrophilicity of the substrate through temperature changes (59). Other alternative approaches in cell-sheet fabrication/harvest include the use of magnetite cationic liposomes (MCLs),

polyelectrolytes and enzymatic digestion of culture substrate. MCLs can either be transfected into cells or adsorbed by cell membranes. Magnetic forces are subsequently utilized to form and harvest the multilayered cell-sheets (118,119). Polyelectrolyte coatings serve as sacrificial substrates on which cell-sheets are cultured, and cell-sheets are released upon disruption of the polyelectrolyte multilayers by various approaches (120,121). Cell-sheets can also be harvested by culturing cells on enzymatically digestable substrates, as reported by Nagai and co-workers (122). Human periodontal ligament cells were cultured on a salmon atelocollagen fibrillar gel which was later digested by collagenase for cell-sheet harvest (122).

The emergence of cell-sheet engineering in recent years addresses some of the shortcomings in traditional TE approaches which involve the use of biodegradable scaffolds as a short-term substitute for the extracellular matrix (ECM), in the hope that seeded cells would generate their native tissue architecture and replace the role of the scaffold (58). With a cell-sheet approach, cell-to-cell connections are not disrupted and cells are harvested as a contiguous cell-sheet - thus enabling cell-to-cell junction proteins, and natively secreted ECM (by the cells) to remain undamaged within the cell-sheets (123,124). In fact, some researchers had found that cell adhesion proteins maintained underneath the cell-sheets would play a desirable role as an adhesive agent in transferring cell-sheets onto other culture materials, other cell-sheets and possibly scaffold materials (125).

Furthermore, there have been new evidence of the ECM improving propagation of stem cells in culture and playing a role in stem cell differentiation. It was shown in two different studies involving 1) a mineralized ECM which was created in vitro and subsequently decellularised (126) and 2) a bone specific ECM derived from an osteogenic cell line (127), that the ECM directs osteogenic differentiation of hMSCs

and murine ESCs respectively. Chen and co-workers (128) described the role of a decellularised adipocyte matrix directing the adipocyte differentiation of hMSCs without the need of additional induction supplements; while See and co-workers (129) described a higher expression of lineage-specific genes by bone marrow derived stem cells (BMSCs) cell-sheets over conventionally differentiated BMSCs.

2.7 Silk as a Biomaterial

Silk has long been established as an excellent compatible biomaterial for use in various tissue regeneration strategies (130,131). Silk fibroin from the bombyx mori (B Mori) silkworm consists of a light (~26kDa) and a heavy (~390kDa) chain, and has high contents of glycine (~46%) and alanine (~30%) amino acids, in addition to tyrosine (Tyr; ~5%), and sparing amounts of tryptophan (Trp; 0.25%) (131,132).

Due to its ease and versatility in processing, silk can be tailored into various forms for different applications (133). For example, silk fibroin extracted and purified from silkworms have been used to make microparticles, electrospun nano mats and films for use as drug delivery vehicles (134,135), scaffolds (136) and electronics biointerfaces (137) respectively. Silk has also been shown to possess the appropriate properties for AF regeneration in several studies (63,64,95-98), which demonstrated silk-derived scaffolds to be good substrates for TE of the AF.

2.7.1 Autofluorescence of Silk

Silk fibroin contains Tyr and Trp which are aromatic amino acids with well established excitation and emission spectral properties, and have been widely used as intrinsic fluorescent probes in fluorescence spectroscopy to study conformations of proteins (138). In this regard, studies have reported the use of endogenous fluorescence signals from silk (also termed autofluorescence) to relate to its structural conformational changes (132,139). Georgakoudi and co-workers reported the

endogenous fluorescence spectral prints of three different forms of silk (Eg. in solution, gel and sponge-like scaffold forms), and correlated the differences in the spectral profiles of the three forms to the degree of silk fibroin structural conformational changes (139).

Such autofluorescence behaviour, though exploited to be a tool for research analysis as described in the preceding paragraph, is also concurrently a hindrance for TE applications. This is because silk exhibits strong autofluorescence signals across a broad spectrum of wavelengths which interferes with fluorescence imaging analysis of fluorescently tagged cells and proteins on silk-derived biomaterials. Fluorescence microscopy is an instrumental analysis technique for TE applications, as it is a convenient approach that allows for multiple signals from different antibodies (and hence different proteins and targets of interest) to be simultaneously viewed and analysed in a singular image (140). This allows for co-localization studies to take place, and a better assessment and analysis to be made on the performance of the biomaterial in relation to its intended function.

2.8 Stimulatory Cues in IVD Tissue Engineering

2.8.1 The Use of Nanotopography

To reproduce the intricate architecture of the AF, a couple of research groups have attempted to use electrospinning to fabricate scaffolds with nanotopographical cues (8,65,70). Electrospinning is a fabrication technique that utilizes electrostatic charging of a polymer solution through the use of a high voltage generator. The highly charged polymer solution is in turn drawn through a narrow conduit. When electrostatic repulsion overcomes the surface tension experienced by the polymer solution at the exit tip of the conduit, formation of a Taylor's cone enables a polymer jet to be drawn out through a high-voltage gradient. Such drawing stretches the

polymer solution. Coupled with a highly volatile solvent, this causes fine polymeric fibres to be collected at the collecting end of the voltage gradient (141,142).

Beyond collecting the fibres as a random mesh of fibres with sub-micron diameters, modifications can be made to the collecting end of a typical electrospinning setup to enable alignment of electrospun fibres. Various approaches have been reported in literature that can be used to create intricate fibre assemblies of aligned fibres, patterned fibres, and complex 3D fibres structures (143). One of the easiest and most straightforward way of achieving aligned and anisotropic fibre meshes would be the use of a fast rotating collector, that can come in the form of a frame or drum (70,136,143). As a highly manipulable scaffold fabrication technique, electrospinning is commonly used to fabricate nanofibrous scaffolds for tissue engineering (144-146), and can be used to manufacture 2D sheet scaffolds to mimic topographic features like the ECM, for example of in vivo collagen fibers (147). Since fiber alignment can also be easily controlled during electrospinning, it has also been routinely used to produce TE scaffolds that can mimic oriented tissue architecture, such as those reported for ligament applications (136,148,149) and AF applications (8,65,70).

The advantages of having a nanofibrous scaffold are multifold. In addition to bio-mimicry (having the scaffold topography similar to the native tissue's architecture), some of the benefits of a nanofibrous scaffold include: 1) promotion of cell adhesion and proliferation, ii) enhancement of differentiation of MSCs (150), and iii) serving as a template for the deposition of an oriented ECM (8). To elucidate point (1), it has been widely shown in literature that mammalian cells respond to the nanotopographical cues of synthetic substrates in terms of adhesion, proliferation and migration (151). For example, having a nano-scale substrate increases the surface area by which adhesion proteins can adhere to, thereby exposing more potential cell membrane receptor binding sites which cells can get attached to the substrate (152).

2.8.2 The Use of Bioreactors

Bioreactors have been widely used for TE applications (153,154). In TE, a bioreactor is commonly used to carry out one or more of the following functions (153,154):

i) ensuring uniform distribution of cells on cell-seeded constructs,

ii) maintenance of gases, wastes and nutrients gradients in culture medium,

iii) as a means for better mass transport into TE constructs,

iv) stimulating TE constructs (Eg. Mechanical loading, electromagnetic field), and

v) as a monitoring system of the construct cultured within

To elucidate point (iv), cells are known to respond to biophysical stimulatory cues (Eg. Tension, compression, electromagnetic field stimulation). Such responses can take the form of a change in ECM production, an increased tendency to be guided down a certain differentiation pathway, or even influencing the speed of tissue maturation (155). Bioreactors have been designed, studied and even being sold commercially today that serve such purposes. Some of the commercially available bioreactors include the EBERS TC-3 Bioreactor and Instron LigaGen and CartiGen Bioreactor Systems.

In the area of IVD TE, the use of a bioreactor to serve functions (iii) and (v) is widely reported for organ culture studies that aim to understand the influence of loading on native disc matrix homeostasis (156). Studies have shown that dynamic loading the disc itself or disc cells at certain physiological parameters (Eg. magnitude, frequency, duration) would positively affect disc matrix metabolism, and may even enhance differentiation (157,158). Conversely, matrix catabolism or disc degeneration takes place under static loading, or when dynamic loading conditions become too low or too high with respect to physiological parameters (157-159). The effect of loading on IVD cell metabolism is two-fold: i) from the direct mechanical stimulation cues on

the IVD cell or matrix and ii) from the changes in the surrounding physical environment (Eg. fluid flow, osmolarity changes, concentration of wastes, nutrients and bioactive factors (156). There are extensive coverage of both areas in literature today on the effect of various parameters, such as hydrostatic pressure, osmotic pressure, tensile loading, static and dynamic compression on the IVD both at the tissue matrix level and cellular level (156,160). Studies on the former two parameters typically use hydrostatic and hydrodynamic pressure bioreactors. Although such approaches do not accurately represent the physiological loading conditions experienced in vivo, they serve as indirect stimulus based studies on osmolarity effects on the IVD (161-163). Direct stimulus studies are equally numerous in literature including, for example, those on loading frequencies, compression magnitudes, and tensile loadings by Ching et al (164), MacLean et al (165), and Rannou et al (166) respectively.

The studies mentioned in the preceding paragraph not only serves to develop a better understanding of loading effects on the IVD so that TE strategies can be better designed, but also enabled the long-term culture of disc explants so that TE-based strategies can be tested on. Recent work in this regard include one by Walter et al (167), whereby a loading bioreactor system was designed to go in tandem with the development of an organ culture technique that includes the vertebral endplates of the IVD. The entire system was showed to closely mimic physiological parameters and is a promising TE tool that can be used for future therapeutic IVD repair studies. On this note, the use of organ culture models as a platform to screen for biomaterials has been previously explored. For example, Peroglio and co-workers reported the use of a bovine organ culture disc model to test for the effectiveness of a thermosensitive hydrogel made using hyaluronan and p-NIPAM in NP repair and regeneration (168). Such a screening approach using organ cultures advances the field of TE as it serves as a stepping stone between in vitro studies and in vivo implantations.

Taking into consideration the context of this dissertation, with regards to the use of bioreactors on engineered discs, there are two studies that need to be highlighted. In a published study by See et al (169), an axial compression bioreactor system was described that could simulate the main physiological loading within the IVD. The bioreactor was designed to dynamically culture a simulated IVD-like assembly that is capable of transmitting the compressive axial load experienced in the silicone NP surrogate into radial compressive and tensive forces to the AF using BMSC cell-sheets on silk sponges to mimic the AF lamellae. In a more recent published study by Chik et al (100) a cyclic torsional/compression bioreactor was used to study the effects of dynamic loading on an engineered disc consisting of a NP core, AF lamellae and osteochondral components all derived from collagen. It was showed in the study that cyclic compression is important for organization of the fiber matrix, while dynamic torsional loading stimulates cell alignment in the AF-like lamellae.

2.9 Critical Evaluation of Current IVD Tissue Engineering Approaches

Majority of tissue engineering studies on the IVD today focused on either the NP or the AF. However, both components have an intimate functional relationship which confers the disc's abilities to carry out its daily functions. For example, without a proper strategy to regenerate or repair the AF to withstand the intradiscal pressure coming from the NP, NP replacement or regeneration strategies would have limited clinical success in restoring the shock absorber function of the IVD (40). Similarly, repairing the AF without targeting the pathogenesis originating from the NP would bring about similar limited clinical success. On this note, tissue engineering an entire disc comprising of both components would perhaps be a better option. Work in this regard are very much in its infancy, in part due to: i) the challenges pertaining to the integration of the TE disc with the adjacent vertebrae, ii) complexity dealing with multiple cell types, and iii) materials with dissimilar properties in a single construct

(9). More importantly, fundamental to the success of this concept (a whole disc replacement approach) is the mechanical strength of the engineered disc. Even under non-loading conditions, studies have shown that residual stresses are present in the IVD (60). Hence, it is essential that an engineered disc must have at least the ability to withstand such residual loads to ensure clinical success when implanted. Surprisingly, few or none of the TE whole disc studies mentioned earlier in section 2.5.3 went on to report their mechanical strength and only two of the studies (100,169), as mentioned in the preceding section, carried out a dynamic loading culture assessment on the assembled disc with the aid of a compression loading bioreactor that can mimic the physiological forces in the native spinal column. It is hence the aim of this dissertation to develop a de novo IVD for potential whole disc replacement application using a combination of TE strategies, and taking into consideration some of the challenges mentioned above.

Chapter 3. Phase One: Assessment of Adipose-Derived Stem Cells and Cell-Sheet Technology for IVD Tissue Engineering

3.1 Introduction

Literature evidences suggest that ASCs cell-sheets (CS), combining the advantages of both ASCs and CS engineering, would be an ideal candidate for TE applications, if the ASCs within the CS retain the potential to differentiate into multi-lineages. However, ASCs CSs have not been studied in detail today, and there are no conclusive evidence on the effect of a hyperconfluent environment on the differentiability of ASCs. Only a handful of published articles exist that are regarding ASC CSs; of which, a previous study (170) showed that undifferentiated ASC CSs implanted under in vivo conditions onto myocardial tissue went on to show presence of cardiomyocytes post implantation. Another study showed that by configuring the culture media constituents, ASC CSs can be inducted into a hepatocyte-like lineage (171). A recently published book chapter article described a protocol to form adipocytes cell-sheets from ASCs (172). These studies have demonstrated the potential of ASC CSs to be multi-potent. However, to the best of our knowledge, a comprehensive study on the ability of ASC CSs to be differentiated into two or more lineages have never been reported in literature. Moreover, the mediation of ASC CSs into the chondrogenic and osteogenic lineages have never been reported, while the growth profile and characterization of ASC CSs is non-existent in literature today.

ASCs were cultured under prolonged hyperconfluent culture conditions to form CSs, and the multipotentiality of ASC CSs was assessed. A comparison was done between differentiation in the CS form and conventionally differentiated ASCs to assess the effect of hyperconfluent culture conditions on the differentiation capacity of ASCs and to assess if CSs should be used for the subsequent aims involving the regeneration of the AF. A temporal profiling of ASCs differentiation in both the

conventional form and CS form was conducted to obtain a deeper insight into the differentiation process so that future culture conditions for the later phases of the dissertation can be better chosen.

3.2 Materials and Methods

3.2.1 Isolation of ASCs

ASCs were isolated from the interscapular fat pads of New Zealand white rabbits by collagenase I digestion (**Figure 3-1**).

Figure 3-1. Photo showing the interscapular fat pads of a New Zealand white rabbit.

Briefly, fur at the rabbits' backs were first shaved and sterilized after euthanasia. Using a scalpel blade, a 10 to 20-cm longitudinal incision over the area of tissue collection was made and lipectomy of the fats posterior to the spine (cervical and thoracic region) was carried out. The adipose tissue harvested was then processed using a modified published protocol (109,173-175). The tissues were first washed with phosphate buffered saline solution (PBS), cut and minced. The minced tissues were then digested with 0.1% (w/v) Type I Collagenase (Invitrogen, Carlsbad, CA) at 37^{o}C for 1 hour. ASCs released from the digested tissues were then pelleted by centrifugation of the stromal vascular fraction and then plated on culture flasks. ASCs were then cultured in low glucose DMEM (LG-DMEM; Invitrogen) supplemented with 10% fetal bovine serum (FBS) and 1% Penicillin/Streptomycin (P/S). After the cells have attached, media was removed and the cells were washed with PBS before fresh growth media was replaced every three days till near confluence (**Figure 3-2**).

Upon this, the ASCs were detached using enzyme digestion by TrypLE (Invitrogen). ASCs of the 2nd to 3rd passages were then used for the subsequent experiments.

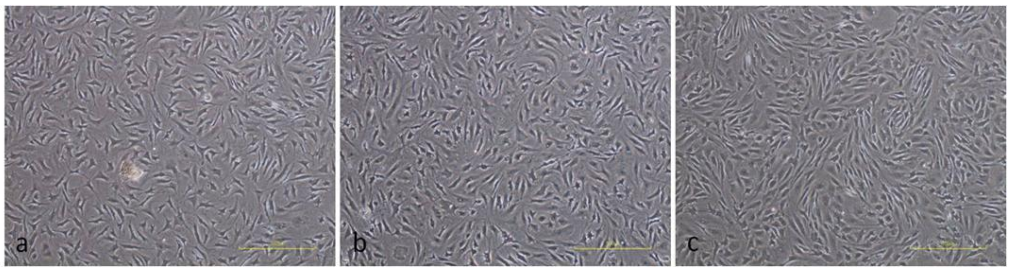

Figure 3-2. Brightfield microscope images of freshly harvested ASCs 1 day (a), 2 days (b) and 3 days (c) after plating.

3.2.2 Growth Characterization of ASCs Cell-Sheets

To form CSs, ASCs were then seeded at a density of $3x10^4$ cells/cm^2 in 6-well culture plates and cultured in a 5% CO_2 incubator at 37^oC till 100% confluence (Week 0). Confluent cells were then cultured in expansion medium (LG-DMEM, 10% FBS, 1% P/S) supplemented with 50µg/ml of ascorbic acid (Wako, Osaka, Japan) for three weeks to profile the growth of the ASC CSs. Ascorbic acid was added to improve ECM deposition (176). Characterization of the CSs was carried out using the following means: (a) Alamar blue assay (Invitrogen) to assess metabolic activity of the ASCs within the cell-sheets; (b) Confocal laser scanning microscopy (Olympus FluoViewConfocal Laser Scanning Microscopes, FV500, Tokyo, Japan) to determine the thickness of the CS; (c) Sircol assay (Biocolor Ltd., Carrickfergus, UK) to quantify collagen content in the ECM and (d) real time RT-PCR to analyze expression of early differentiation gene markers for adipogenesis, osteogenesis and chondrogenesis. (a) and (b) were carried out without detaching the CSs, while (c) and (d) required the CSs to be detached and disrupted.

a. Metabolic Activity Levels of ASCs within Cell-Sheets

Alamar blue colorimetric assay (Invitrogen) was used to determine the metabolic activity of the ASCs within the hyperconfluent CSs. Briefly, expansion culture medium supplemented with 10% (v/v) alamar blue reagent was added to the ASCs CSs and placed in a 5% CO_2 incubator at 37^{o}C for 1 hr. Alamar blue supplemented medium was also added to empty culture wells and placed in a 5% CO_2 incubator at 37^{o}C for 1 hr as negative controls. After incubation, alamar blue supplemented medium from each sample was pipetted to a 96-well plate and absorbance was spectrophotometrically measured at the 570nm and 600nm wavelengths using a microplate reader (Turner Bio- systems, Sunnyvale, CA). Cells which are alive and viable will reduce Resazurin (blue in color), the active ingredient in alamar blue, to Resorufin (pink in color). The amount of colorimetric difference is proportional to the amount of metabolic activity, and can be calculated according to the formula provided (Invitrogen).

b. Cell-Sheet Thickness Measurement

ASCs CSs were first immunostained for collagen Type I (Col I) before being viewed with a confocal microscope (Olympus FluoViewConfocal Laser Scanning Microscopes, FV500). Briefly, at weekly timepoints, ASCs CSs were first fixed with -20^{o}C methanol for 10mins, then blocked with 3% BSA (w/v) in PBS under room temperature for 30mins. Primary antibody for Col I (Sigma Aldrich, St Louis, MO) was then incubated at room temperature for 90mins, before incubation of the secondary antibody (Alexa Fluor 594; Invitrogen) and DAPI (Invitrogen) for 30mins. Immunostained ASCs CSs were then viewed with a confocal microscope (Olympus FluoViewConfocal Laser Scanning Microscopes, FV500) using the z-stack mode and thickness of CSs were determined by taking the difference in z-axis readings between the top and bottom layers (**Figure 3-3**).

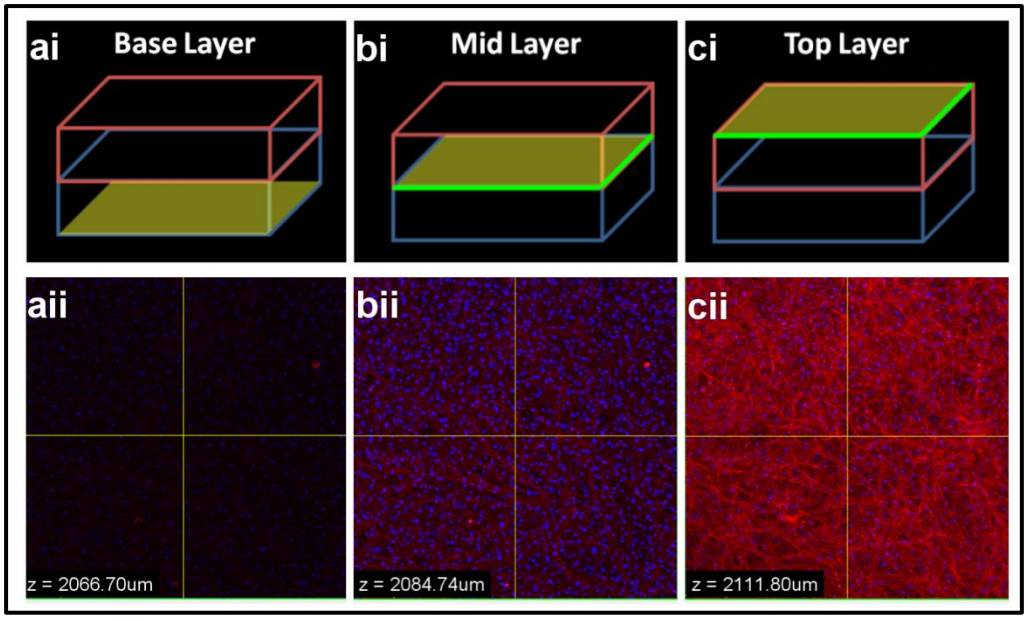

Figure 3-3. ASCs within CSs were stained with DAPI and appear blue . Extracellular matrix of CSs were stained for Col I deposition and appear red. Using confocal microscopy, thickness of CSs were determined by taking the difference in z-axis readings between the top (a) and bottom (c) layers.

c. Collagen Deposition Normalized to DNA Content

Insoluble collagen in the ASCs CSs were first digested using pepsin. Briefly, gastric mucosa pepsin (Roche Diagnostics Asia Pacific, Singapore) was reconstituted in 0.25M HCL to a concentration of 0.25mg/ml and incubated with the CSs for 2 hrs with gentle shaking. Sonication was then introduced at mid-point of pepsin incubation to aid in the digestion of the CSs (177). Sircol Assay (Biocolor) was carried out on the lysates according to the manufacturer's instructions, and dye-complexes released were spectrophotometrically measured at 555nm using a microplate reader (Turner Biosystems). Collagen content of each sample was then normalized to its respective sample's DNA content, which was measured using the Hoechst 33258 dye method (178) using a fluorescence plate reader (FLUOstar Optima; BMG Lab technologies, Offenburg, Germany) at an excitation wavelength of 365nm and emission wavelength of 460nm. A standard curve using known concentrations of calf thymus DNA was used to quantify the DNA content of the CSs samples.

d. RNA Extraction and cDNA Synthesis

TRIzol reagent (Ambion, Life Technologies, Carlsbad, CA) was used to isolate the RNA content from samples. Briefly, after removing culture medium from samples, TRIzol reagent was added to lyse the cells for 5mins. Chloroform (Sigma Aldrich) was then added and samples were centrifuged to isolate the aqueous RNA-containing layer. The RNA-containing layer was then subsequently purified using the RNeasy Kit (Qiagen, USA). Using a NanoDrop spectrophotometer (NanoDrop Technologies, Wilmington, DE), RNA concentration was measured and 100ng of total RNA was used for complementary DNA (cDNA) synthesis for each sample. SuperScript II Reverse Transcriptase (Invitrogen, Carlsbad, CA), a DNA polymerase that can synthesize cDNA from single-stranded RNA, and Oligo(dT)20 primer (Invitrogen) consisting of a string of 20 deoxythymidylic acid residues, were used according to the manufacturer's instructions to synthesize cDNA from each RNA sample.

e. Real-time RT-PCR analysis of Early Differentiation Gene Markers

Real-time polymerase chain reaction (RT-PCR) was then performed using QuantiTect SYBR Green PCR kit (Qiagen). Briefly, 2 µl of cDNA, 10 µl of SYBR Green Master Mix from the QuantiTect SYBR Green PCR kit (Qiagen), and the optimized concentration of primers was topped up with nuclease-free water to give a final volume of 20 µl per reaction. All reactions were then performed using a PCR cycler (Mx3000P; Stratagene, La Jolla, CA). The thermal cycling program for all polymerase chain reactions was as reported previously (129). The early differentiation gene markers analyzed were: Sox9 for chondrogenesis, peroxisome proliferator activated receptor (PPARγ2) for adipogenesis, and Runt-related transcription factor 2 (Runx2) for osteogenesis. Expression levels of all the target genes were first normalized to the respective sample's housekeeping gene: glyceraldehyde 3-phosphate dehydrogenase (GAPDH) and then calculated using the comparative CT ($2^{-\Delta\Delta CT}$) method (179,180) against the reference condition (Week 0

cell sheets). Primer sequences for all target genes and GAPDH were as previously reported (129,181). Details of the primer sequences can be referred to in the Appendix section.

3.2.3 Differentiation of ASCs cell-sheets and ASCs

ASCs were first cultured under a hyperconfluent condition to form one-week old CSs (as described under 3.1.2) prior to either the commencement of differentiation (cell-sheet induced, hereafter termed "CSI") or continued to be cultured as controls using expansion medium (cell-sheet not induced, hereafter termed "CSNI"). Non-confluent ASCs that were differentiated directly with no prior CS formation culture form the conventional induced group (hereafter termed "CI") (**Figure 3-4**).

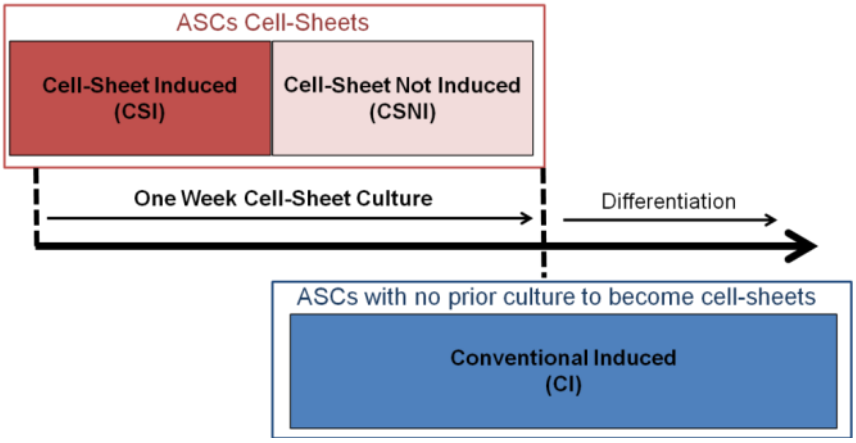

Figure 3-4. Illustration of experimental setup investigating the effect of hyperconfluent conditions on ASCs differentiation capabilities.

a. Adipogenic Differentiation

Using a modified protocol from Yu G et al (182), ASCs from the CI groups were seeded at a density of $5x10^4$ cells/well in 6-well culture plates. Adipogenic induction medium consists of LG-DMEM supplemented with 3% FBS, 0.25mM IBMX (Sigma), 66µM biotin (Sigma), 34µM d-pantothenate (Sigma), 5µM troglitazone (Sigma), 1µM dexamethasone (Sigma) and 200nM human insulin (Sigma). CI and CSI groups were cultured using adipogenic induction medium for 3 days and subsequently adipogenic maintenance medium (identical to induction medium but

with IBMX and troglitazone absent) for up to 14 days prior to sacrificial for assessments after 1 week and 2 weeks in maintenance medium.

b. Osteogenic Differentiation

Using a modified protocol from Arrigoni et al (175) and Kroeze et al (183), ASCs from the CI groups were seeded at a density of $5x10^4$ cells/well in 6-well culture plates. Osteogenic induction medium consists of LG-DMEM supplemented with 10% FBS, 1% penicillin/streptomycin, 10nM dexamethasone (Sigma), 0.01uM vitamin D3 (Sigma), 10mM glycerol-phosphate (Sigma) and 50ug/ml ascorbic acid (Wako). CI and CSI groups were cultured using osteogenic induction medium for up to 5 weeks prior to sacrifice for assessment at weeks 2, 3, 4 and 5.

c. Chondrogenic Differentiation

For chondrogenic differentiation, ASCs from the CI group were cultured as micromass pellets at a density of $2.5x10^5$ cells/pellet. One-week old cell-sheets from the CSI and CSNI groups were mechanically agitated to roll-up to form pellets. Adapting from a previously published protocol (109), chondrogenic induction medium consisted of HG-DMEM (Invitrogen) supplemented with 10% FBS, 1% Penicillin/Streptomycin, 1% ITS+ (BD Biosciences, San Josa, CA), 100nM dexamethasone (Sigma), 50ug/ml ascorbic acid (Wako), 10ng/ml TGF-ß3 (RayBiotech Inc, Norcross, GA) and 10ng/ml BMP-6 (R&D Systems, MN, USA). CI and CSI pellets were cultured in induction medium for up to 5 weeks prior to sacrifice for assessment at weeks 2, 3, 4 and 5.

d. Histological and Immunohistochemical Assessment

Without detaching the CSs, assessment of adipogenic differentiation was carried out by Oil Red O staining for oil containing adipocytes as previously described (129). Briefly, 6ml of stock solution consisting 0.5% (w/v) Oil Red O powder (Sigma) in

Isopropyl Alcohol (Sigma) was mixed with 4ml of ddH_2O to form the working solution. Samples were fixed with 70% ethanol for 20sec, before adding the working solution of Oil Red O for 15mins. Excess dye was rinsed with 70% ethanol followed by ddH_2O wash. Cells were then counterstained with hematoxylin for 30sec, washed and imaged using a bright field microscope.

Assessment of osteogenic differentiation was carried out by Alizarin Red staining for calcium deposits without detaching the cell-sheets. Briefly, samples were fixed in ice cold 70% ethanol for 1 hour before being incubated with 40mM Alizarin Red solution (pH 4.1) for 10mins. Excess dye was washed off thoroughly with ddH_2O and PBS. Samples were then imaged using a bright field microscope.

Assessment of chondrogenic differentiation was carried out by Safranin-O and immunofluorescence staining of Collagen II (Col II). Firstly, pellets were fixed in 10% neutral buffered formalin overnight and then embedded in paraffin through serial dehydration in ethanol and xylene washes. Using a microtome, 5um thick sections were cut and collected on silane-coated glass slides for subsequent Safranin-O and immunofluorescence analysis. For Safranin-O staining, after deparaffinization and rehydration of the slides, samples were first counter stained with Weigert's Iron Hematoxylin for 5mins, then incubated with 0.02% Fast Green and 1% Safranin-O solutions for 1min and 10mins respectively. Slides were then viewed using a brightfield microscope. For immunofluorescence staining, after deparaffinization and rehydration of the slides, samples were first digested in pepsin (Roche Diagnostics) at 37^oC for 30mins for antigen retrieval purposes, blocked with 3% BSA for 1 hr, before incubation with Col II primary antibody (Merck Millipore, MA) for 2 hrs. Secondary antibody conjugated with Alexa Fluor 594nm (Invitrogen) was then added with DAPI (Invitrogen) for 30mins at room temperature. Slides were then imaged using a fluorescence microscope (Olympus).

e. RT-PCR Analysis of Differentiation Genes

RNA from all samples were isolated and used to synthesize cDNA following the procedures as described earlier. RT-PCR analysis for adipogenic genes was conducted for Peroxisome Proliferator-Activator Receptor (PPARγ2), adipocyte-binding protein (aP2) and leptin. RT-PCR analysis for osteogenic genes was conducted for expression of Osteonectin (On), Osteopontin (Opn), Runt related transcription factor 2 (Runx2) and Collagen I (Col I). RT-PCR analysis of chondrogenic genes was conducted for expression of Aggrecan (Agg), Col II and Sox9. The level of expression of all the target genes were all normalized to the respective sample's housekeeping gene (GAPDH) and calculated using the comparative CT ($2^{-\Delta\Delta CT}$) method (179,180) with reference to the CSNI samples. Primer sequences used were as per previously reported (129).

3.2.4 Assessing the Suitability of ASCs and ASCs Cell-Sheets for AF Regeneration

To assess the suitability of ASCs and ASC CSs for inner and outer AF regeneration, chondrogenic differentiation of ASCs and one-week old ASC CSs was carried out as previously described in section 3.2.3c. Histochemical assessment of the pellets was then carried out as per described in section 3.2.3d to obtain 5µm-thick sections on silane-coated glass slides for immunohistochemical staining. After deparaffinization and rehydration, hydrogen peroxide was applied to the sections to block the endogenous peroxidase in them (15mins) before conducting antigen retrieval by pepsin treatment for 20 min at 37^{o}C in a humidified chamber. Collagen Type I monoclonal antibody (Sigma-Aldrich) and Collagen Type II monoclonal antibody (Chemicon Inc., Temecuela, CA) were then added to the sections for 2 hours at room temperature and in a humidified chamber. The sections were then washed with 1xPBS, and incubated with a biotinylated goat anti-mouse secondary antibody (Lab

Vision Corporation, Fremont, CA) for 30 min. After washing the sections with 1xPBS, streptavidin peroxidase was then added for 45 min and 3,30-diaminobenzidine was used as a chromogenic agent to turn positive staining areas to a brown tinge colour. Counterstaining was done with Harris hematoxylin, differentiated in 1% acid alcohol and subsequently dipped in 0.2% ammonia water. The slides were then dehydrated in a series of ethanol and xylene washes before being mounted in DEPEX mounting medium (Sigma) and covered with a coverslip.

3.2.5 Statistical Analysis

Statistical significance between groups were determined using unpaired Student's t-test, with $p<0.05$. All statistical analysis were performed using Excel Analysis ToolPak (Microsoft Inc).

3.3 Results

3.3.1 Cell-Sheet Growth Characterization

Weekly time point results from alamar blue assay showed that ASCs within the CSs remain metabolically active for up to 3 weeks of hyperconfluent culture duration (**Figure 3-5**). Amount of dye reduction was 42.6 ± 0.4 % for week 0, 52.0 ± 1.3 % for week 1, 55.3 ± 0.8 % for week 2 and 60.3 ± 2.3 % for week 3. Significant improvement to metabolic activity occurred between each consecutive weeks, with the most significant increment in dye reduction occurring between week 0 and week 1. The ASCs within the CSs progressively secrete ECM, and this is shown in the CS thickness and collagen content results. CS thickness increased from 32.6 ± 5.0 µm in Week 0 to 52.2 ± 6.8 µm in Week 3 (**Figure 3-5).** Significant increment occurred between week 0 and week 1 (40.6 ± 3.6 µm) and between week 2 and week 3 (52.2 ± 6.8 µm).

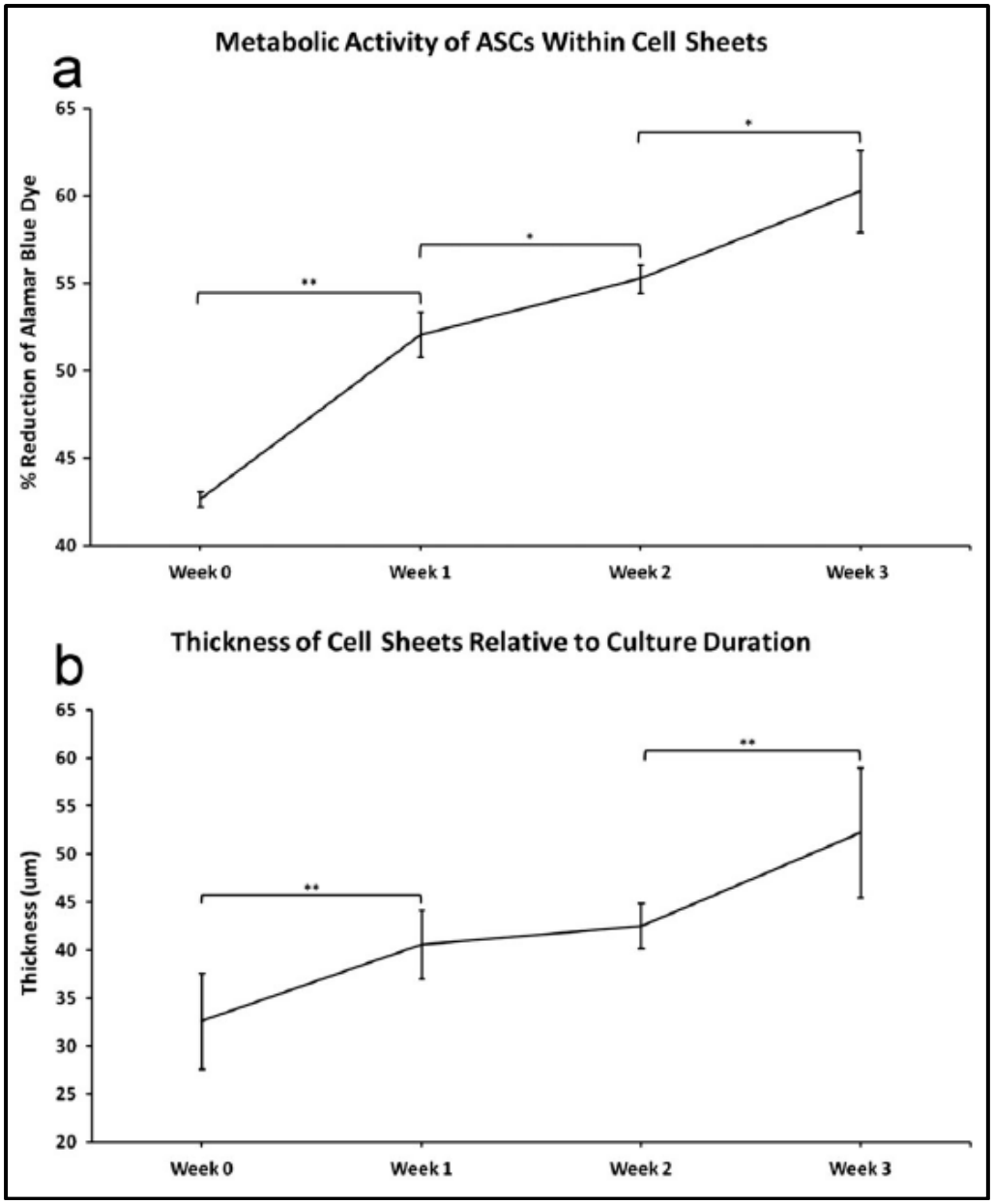

Figure 3-5. (a) Metabolic activity of ASCs within cell sheets, determined by Alamar blue dye reduction. A higher amount of dye reduction corresponds to either a higher cell count and/or better cell viability. (b) Thickness of cell sheets, determined by confocal microscopy and relative to culture duration: **$p<0.01$; *$p<0.05$

Collagen content of the ASC CSs also increased with culture duration, with significant increment occurring between each consecutive weeks (**Figure 3-6**). The increment in collagen content also qualitatively reflected in a ECM that is more densely packed (**Figure 3-6**).

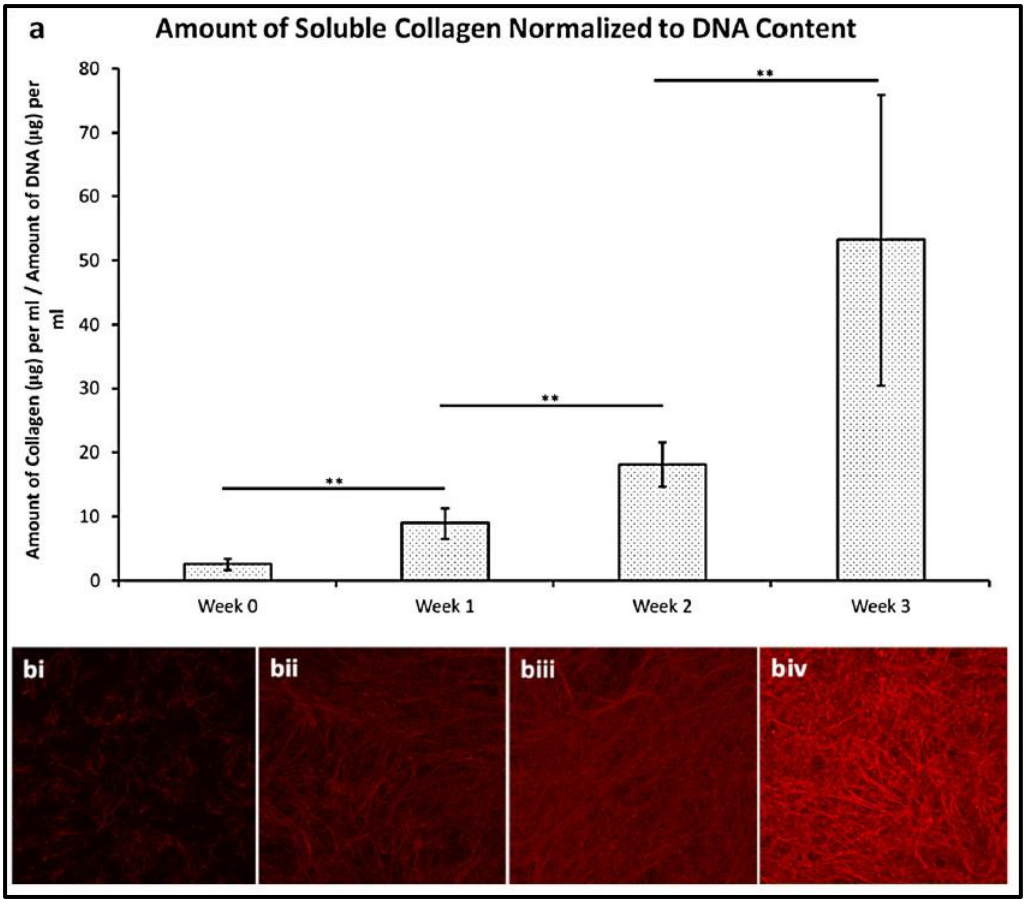

Figure 3-6. Amount of soluble collagen, determined by Sircol assay and normalized to the respective DNA content, as determined by the Hoechst dye method. (b) Confocal images of cell sheets, showing the extracellular matrix of: (i) week 0; (ii) week 1; (iii) week 2; and (iv) week 3 cell sheets, immunostained for Col I deposition: **$p<0.01$

3.3.2 Effect of Hyperconfluent Conditions on Expression of Early Gene Markers

Prolonged hyperconfluent conditions did not affect the gene expression of PPARγ2, with mRNA levels tapering between 1 to 1.5-fold higher than the non-hyperconfluent culture condition (Week 0). However, under one week of hyperconfluent culture conditions, there was significant upregulation of Runx2 and Sox9 genes, as shown by the 3.0 ± 1.3 fold and 5.1 ± 1.4 fold increment in the mRNA levels respectively (**Figure 3-7**). Extending the duration of hyperconfluent culture beyond one week not only did not bring about any further improvement in Runx2 nor Sox9 gene expressions, the mRNA levels dropped to approximately 1.5-fold and 3-fold over the non-hyperconfluent condition (Week 0) respectively (**Figure 3-7**).

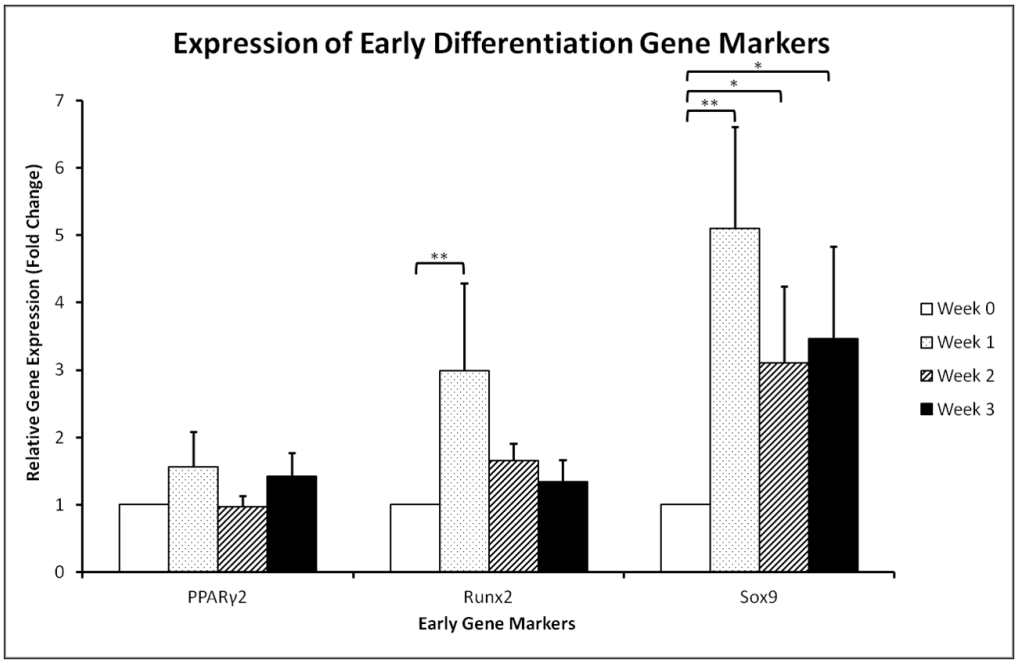

Figure 3-7. Real time RT–PCR of early differentiation gene markers. Relative expression of mRNA levels in week 1–3 cell sheets with respect to week 0 cell sheets: **p<0.01; *p<0.05

3.3.3 Differentiation of ASCs within Cell-Sheets and ASCs Alone

a. Adipogenic Differentiation

Neutral lipid droplets found within the differentiated adipocytes were stained red. Positive staining was obtained for all induced samples at both sacrificial time points (**Figure 3-8**). ASC CSs which were not induced (CSNI) did not display any positive red staining and showed that ASCs within the CSs remain differentiable down the adipogenic lineage given suitable chemical cues. CI and CSI cultures had visible cytoplasmic lipid droplet formations within the cells as early as 10 days into induction.

Looking at the real time RT-PCR results (**Figure 3-9**), CSI samples showed a 26.6 ± 7.8, 1.3 ± 0.6 and 6.4 ± 0.7 fold increase in aP2, Leptin and PPARγ2 mRNA expression levels respectively over the CSNI samples, after being cultured for 3 days in induction medium and 7 days in maintenance medium. Keeping the samples in maintenance medium for an additional 7 days resulted in a change in mRNA

expression levels. After 14 days of maintenance medium, CSI samples showed a higher expression of aP2 with a 37.3 ± 11.0 fold increase over the CSNI samples. mRNA expression of PPARγ2 of the CSI samples did not change much and was at a 6.2 ± 1.8 fold increase over the CSNI samples. Leptin expression however, changed drastically and displayed a down regulation with a 6.0 ± 0.9 fold decrease between the CSI and CSNI samples. Comparing CSI and CI gene expression results (Figure 3-9), apart from the upregulation of the leptin (an adipocyte derived hormone) gene at both time points, PPARγ2 (an important transcription factor in adipogenesis) and aP2 (an adipocyte binding protein) genes were both downregulated in the CSI samples at the 1st time point and was also lesser (though not significant) in the 2nd time point. Looking at the CI versus CSNI results, we observed a consistent upregulation of aP2 and PPARγ2 gene expressions in the CI samples over the CSNI samples (aP2: 71.9 ± 34.0 fold increase for the 1st timepoint and 46.2 ± 6.7 fold increase for the 2nd timepoint; PPARγ2: 14.9 ± 5.5 fold increase for the 1st timepoint and 7.9 ± 1.1 for the 2nd timepoint). The converse was however observed for the Leptin gene expression at both assessment time points.

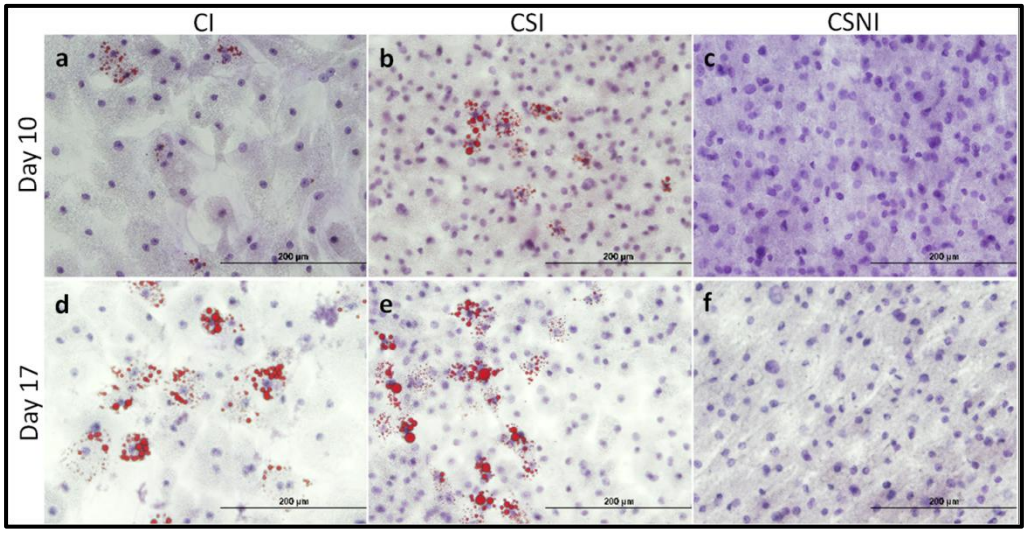

Figure 3-8. Oil red O staining with haematoxylin as counterstain. Oil-containing adipocytes are stained red and confirm adipogenesis. Conventionally induced ASCs (CI) were cultured in induction medium for 3 days, then placed in maintenance medium for 1week (a) and 2weeks (d). ASCs in the CSI groups were cultured in induction medium for 3 days and placed in maintenance medium for 1 week (b) and 2weeks (e). CSNI samples cultured in normal expansion medium (controls) did not display any large cytoplasmic lipid droplets (c, f): scale bars=200µm

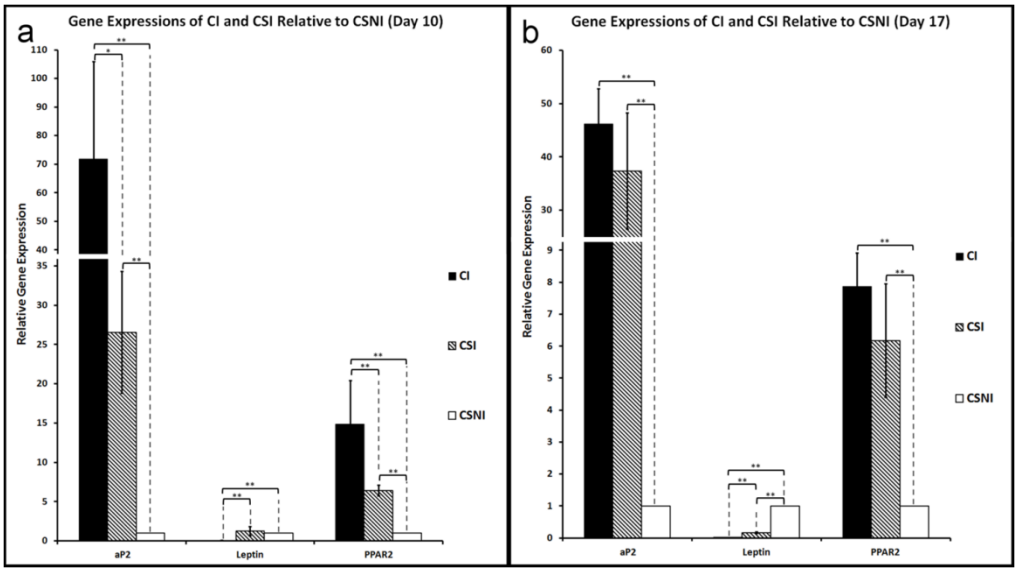

Figure 3-9. RT–PCR analysis of adipogenic genes (ap2, Leptin and PPARγ2) at days 10 (a) and 17 (b). The level of expression of each target gene was normalized to GAPDH and calculated using the $2^{-\Delta\Delta CT}$ formula with reference to the CSNI samples, which were set to 1: *p<0.05; **p<0.01

b. Osteogenic Differentiation

Alizarin Red stains calcium deposits orange-red. Positive staining was obtained for all induced samples (CSI and CI) at all sacrificial time points (**Figure 3-10**). ASCs cell-sheets which were not induced (CSNI) did not display any positive red staining, indicating that suitable chemical cues are required to induce the ASCs within the cell-sheets down the osteogenic lineage. CI and CSI cultures had visible calcium deposition from as early as 2 weeks into induction, although the extent of calcium deposition is observed to be much higher in the CI samples than the CSI samples .

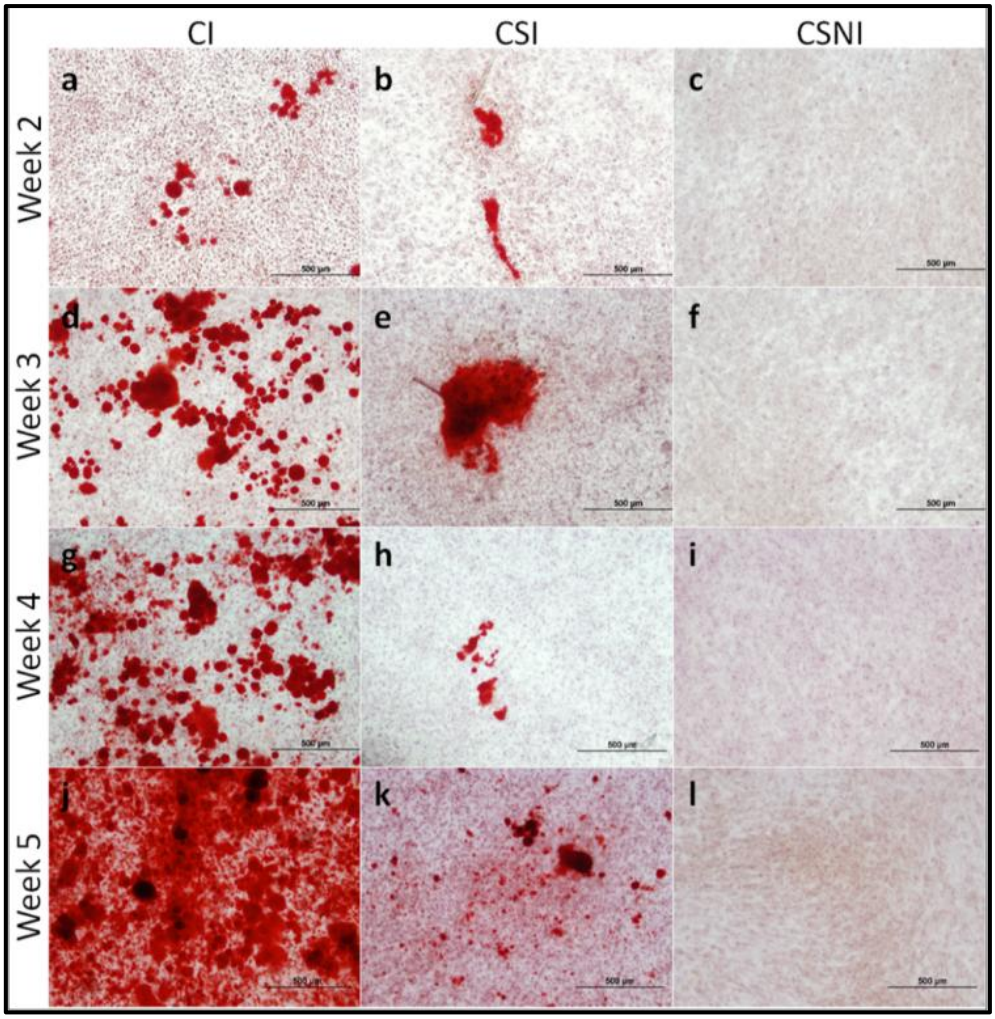

Figure 3-10. Alizarin red stains calcium deposits red and confirm osteogenesis. CI samples (a, d, g, j) displayed positive red staining from as early as week 2. CSI samples (b, e, h, k) displayed positive staining from week 2, but did not have as much calcium deposition as the CI samples. CSNI samples cultured in normal expansion medium (controls) did not display any positive staining (c, f, i, l): scale bars=500µm

Real-time RT-PCR results showed that the CSI groups showed a 5.2 ± 2.7, 12.2 ± 3.2, 8.0 ± 1.9 and 10.5 ± 1.2 fold increase in Runx2 mRNA expression levels over the CSNI samples after 2, 3, 4 and 5 weeks of osteogenic induction respectively (**Figure 3-11**). Between the CSI and CSNI groups, upregulation of osteonectin in the CSI groups took place from week 4 onwards (Week 4: 3.0 ± 1.0 fold; Week 5: 4.4 ± 1.5 fold) and upregulation of osteopontin took place only at the last time point (3.2 ± 1.0 fold at week 5) (**Figure 3-11**). Col I gene in the CSI samples displayed a consistent slight increment (although not significant) throughout 5 weeks of induction over the CSNI samples (**Figure 3-11**), with the highest fold increment displayed in week 3

(2.03 ± 0.79 fold). Comparing the CSI groups with the CI groups, only the osteonectin gene was upregulated at some time points in the CSI group over the CI group. They are at weeks 2, 3 and 5. Runx2 gene expression results between the CSI and CI groups was inconclusive as the expression levels fluctuate throughout the 2 to 5 weeks of induction culture. Only at one sacrificial time point (week 3), did the CSI group displayed a fold increment of all four osteogenic gene markers concurrently over the CI group (although the fold increments in the Col I, osteopontin and Runx2 genes were not significant at that time point). Between the induced CI samples and not-induced CSNI samples, a consistent upregulation of the Runx2 gene was observed across all 4 assessment time points (Week 2: 6.0 ± 0.5 fold; Week 3: 9.3 ± 2.4 fold; Week 4: 15.5 ± 6.6 fold; and Week 5: 7.4 ± 3.0 fold).

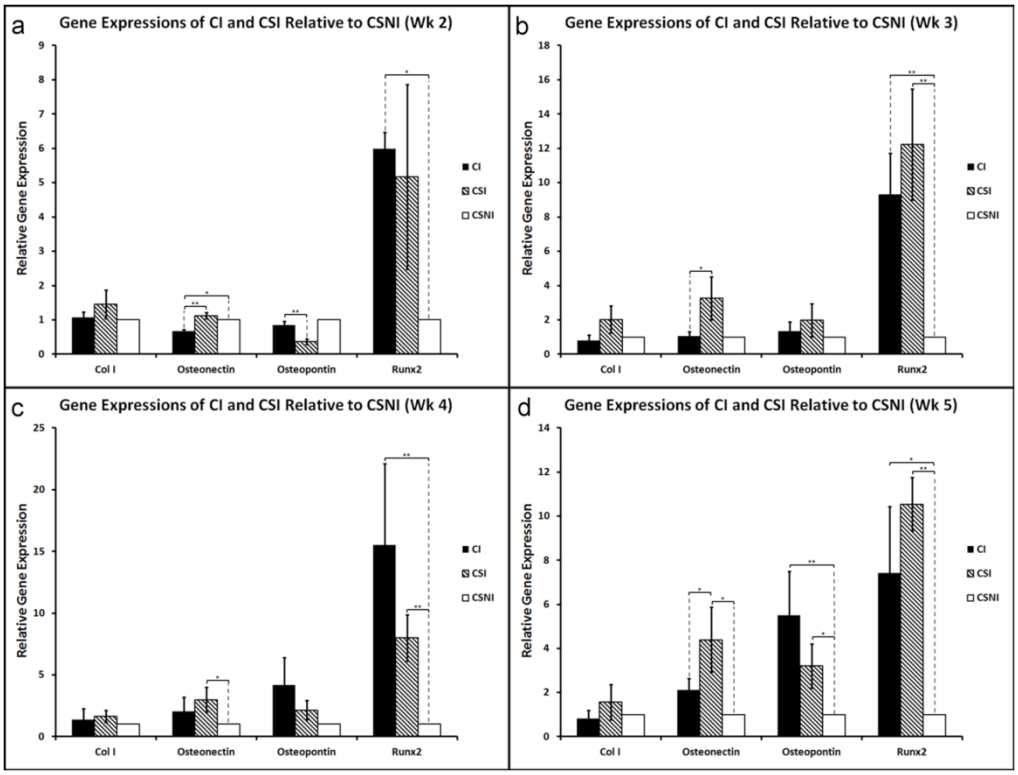

Figure 3-11. RT–PCR analysis of osteogenic genes (Col I, Osteonectin, Osteopontin and Runx2) at week 2 (a), week 3 (b), week 4 (c) and week 5 (d). Target genes expression levels were normalized to GAPDH and calculated using the $2^{-\Delta\Delta CT}$ formula with reference to the CSNI samples, which were set to 1: *p<0.05; **p<0.01

c. Chondrogenic Differentiation

Safranin-O stains for proteoglycans (184) and glycoaminoglycans (185). An orange-red stain is a positive indicator for chondrogenesis.

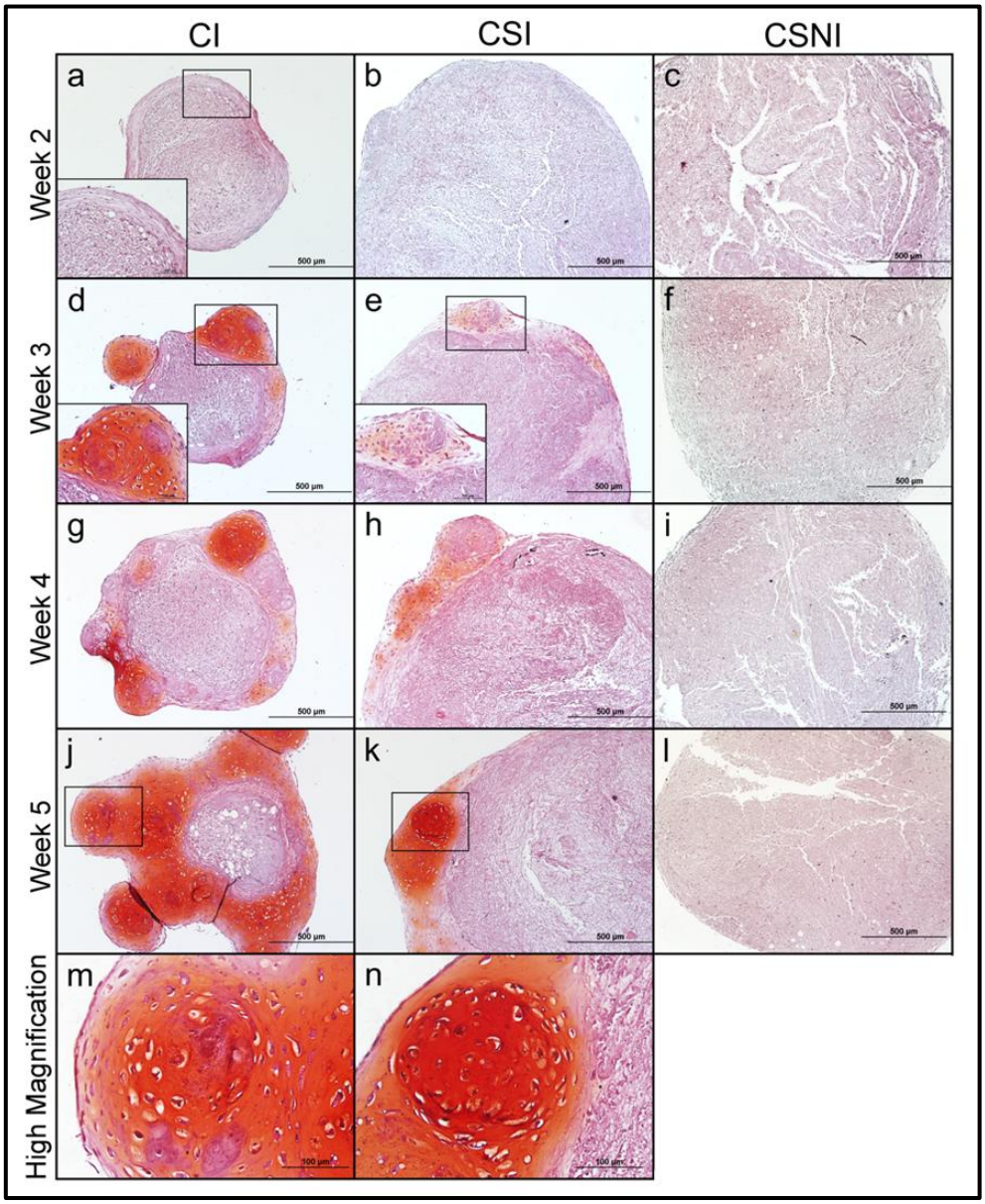

Figure 3-12. Safranin O staining with haematoxylin as counterstain. CI samples (a, d, g, j) displayed positive staining from week 3. CSI samples (b, e, h, k) displayed positive staining from week 4, but did not have as much positive staining as the CI groups. CSNI samples cultured in normal expansion medium (controls) did not display any positive staining (c, f, i, l). Higher magnifications of (j, k) are shown in (m, n), respectively: scale bars=(a–l) 500µm; (m, n) 100µm

Histological staining showed that CI cultures had rich amounts of glycosaminoglycans and proteoglycans by week 5 (**Figure 3-12**), while CSI cultures started displaying distinct positive staining only from week 4 (**Figure 3-12**). The

extent of positive staining observed in the CSI samples after 5 weeks of induction was already observed in the CI samples from as early as 3 weeks into induction. Immunofluorescence staining at week 5 showed that CI samples (**Figure 3-13**) containing a relatively much larger amount of Col II in the ECM as compared to the CSI samples (**Figure 3-13**).

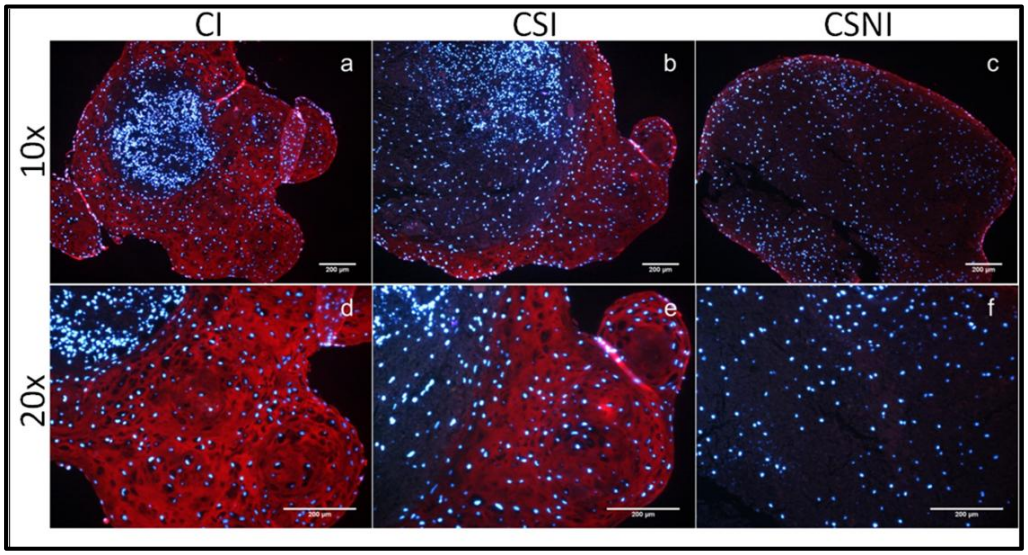

Figure 3-13. Immunofluorescence staining for Col II after 5 weeks of chondrogenic induction. CI samples (a, d) displayed a stronger and larger extent of Col II expression than CSI samples (b, e). CSNI samples (controls) displayed no Col II presence: scale bars=200µm

Real-time RT-PCR results showed that Agg, Col II and Sox9 genes were consistently upregulated in the CSI samples over the non-induced CSNI samples from week 2 to week 5 (**Figure 3-14**). The Sox 9 gene in the CSI group displayed a fold increment of 29.0 ± 7.2 for week 2, 54.6 ± 14.0 for week 3, 27.1 ± 10.6 for week 4 and 31.3 ± 15.2 for week 5, over the not induced CSNI group; while the Agg gene in the CSI group displayed a fold increment of 256.4 ± 79.0 for week 2, 171.1 ± 52.5 for week 3, 111.6 ± 31.7 for week 4 and 87.1 ± 45.4 for week 5 over the not induced CSNI group. mRNA expression levels of the Col II gene for the non-induced CSNI samples were almost nonexistent, hence giving rise to the large amount of relative fold expression increments displayed for both the CSI and CI groups at all assessment time points (**Figure 3-14**).

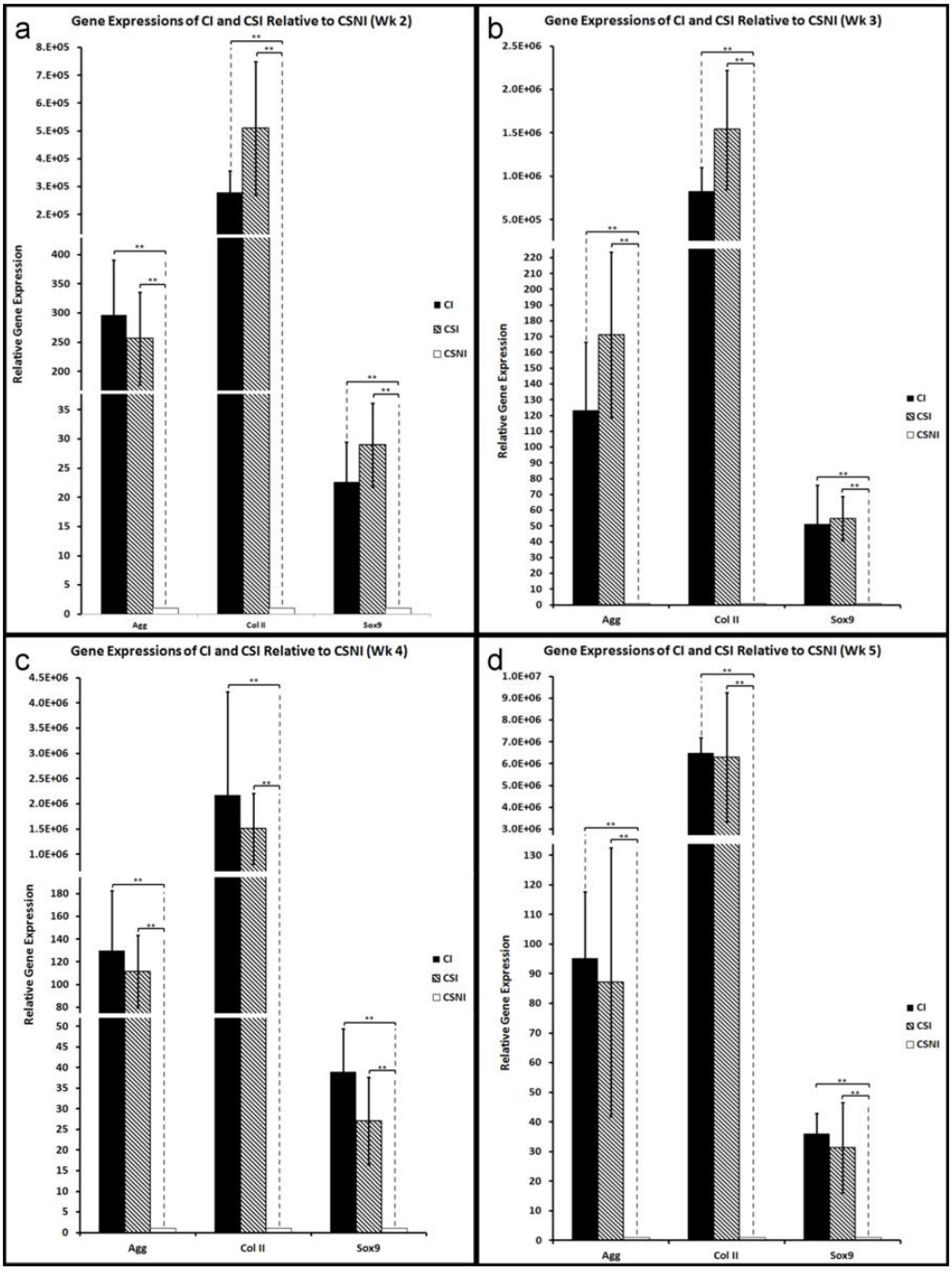

Figure 3-14. RT–PCR analysis of chondrogenic genes (Agg, Col II and Sox9) at week 2 (a), week 3 (b), week 4 (c) and week 5 (d). The level of expression of each target gene was normalized to GAPDH and calculated using the $2^{-\Delta\Delta CT}$ formula with reference to the CSNI samples, which were set to 1; *p<0.05; **p<0.01

Comparing the CI groups with the CSI groups, no significant difference in gene expression levels was obtained for all three genes (Agg, Col II and Sox9) over all 4 timepoints. The relative gene expression levels between the CSI and CI groups all hovered around 1 to 1.5-times of each other (**Figure 3-14**). The CI samples however

showed a consistent upregulation of all three genes over the CSNI samples at all 4 assessment time points (**Figure 3-14**). For the Agg gene, it was a fold increment of 269.2 ± 94.7 for week 2, 123.4 ± 43.1 for week 3, 129.9 ± 52.6 for week 4, and 95.2 ± 22.4 for week 5. For the Sox9 gene, it was a fold increment of 22.6 ± 6.9 for week 2, 51.1 ± 24.8 for week 3, 38.9 ± 10.4 for week 4 and 36.2 ± 6.8 for week 5.

3.3.4 Assessing the suitability of ASCs and ASCs Cell-Sheets for AF Regeneration

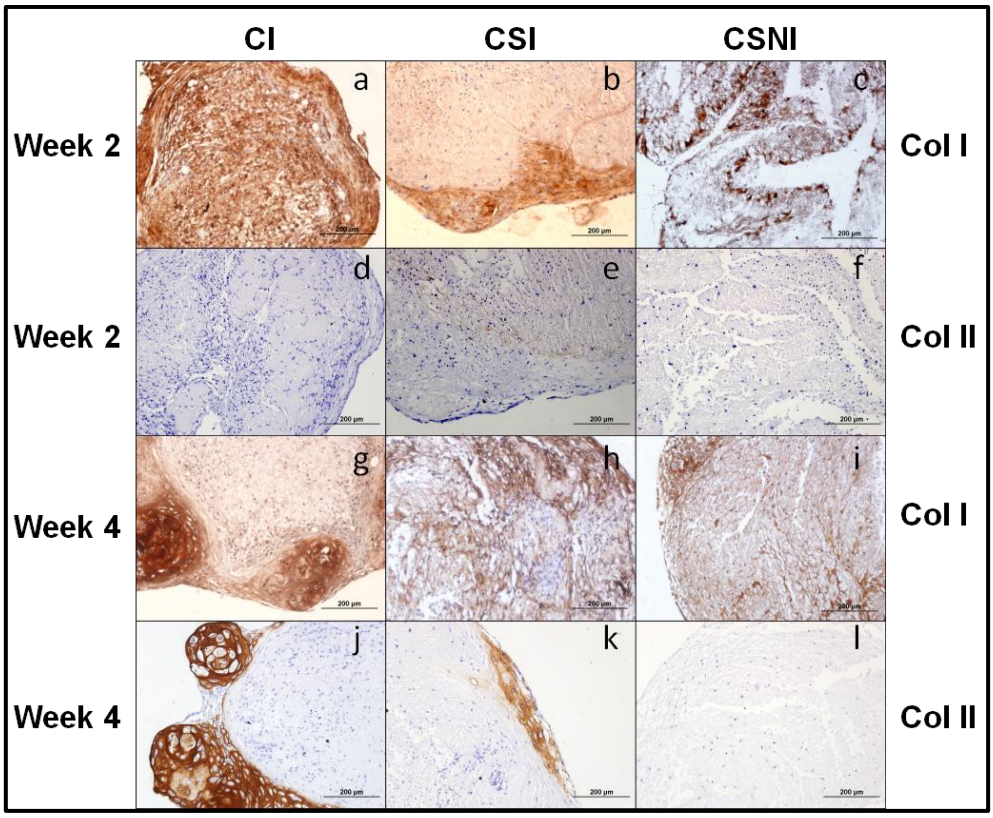

Figure 3-15. Immunohistochemical staining for Col I and Col II after 2 weeks and 4 weeks of chondrogenic induction. CI samples displayed a stronger expression of Col II expression after 4 weeks of differentiation (j), while Col I expression was enhanced in the CSI samples between 2 weeks (b) and 4 weeks (h) of differentiation. Scale bars: 200µm.

Immunohistochemical analysis was conducted using a DAB substrate based staining kit. Positive staining of the intended protein of interest was identified by a brown color stain. There was a stronger expression of Col II in the CI samples compared to CSI samples after 4 weeks of differentiation (**Figure 3-15**). The same was observed

for Aggrecans in the CI samples (**Figure 3-12**). Comparing the CI samples after 2 weeks of differentiation with the CI samples after 4 weeks of differentiation, a remodeling of collagen I and II distribution was observed. The same can be observed for the CSI samples (**Figure 3-15**).

3.4 Discussion

ASCs was chosen as the cell-source of interest. ASCs have been reported to be multipotent (110,186-188) and possess several inherent advantages over the more widely used BMSCs. Given the higher accessibility of adipose tissue, the isolation of ASCs creates less patient morbidity during tissue harvest than that for BMSCs. Adipose tissue is also more expendable and hence the availability of ASCs is higher than BMSCs. The use of ASCs for IVD TE has also been reported in literature. Compared to well-established protocols differentiating ASCs into bone and cartilage, differentiating ASCs into disc-like cells is in general still in the infancy stages. The specific cues to differentiate ASCs into NP cells in vitro are not yet well developed, and hence ASCs are typically injected into a degenerated NP for regeneration purposes (189). Researchers have been using co-culture approaches to study the effects of NP cells or the microenvironment of the NP on ASCs. For example, Yang and co-workers demonstrated a significant increment in proteoglycan and collagen type II production by ASCs (transduced with the Sox-9 gene with a retroviral vector) after co-culturing them with mature NP cells (190). Similarly, Lu et al showed in a micromass co-culture system that soluble factors secreted by NP cells had a positive effect in directing ASCs towards a NP-like phenotype (191); while Choi et al demonstrated the importance of the quality of the NP cells in influencing ASCs micromass co-cultures towards a NP-like lineage (192). There are even fewer studies that have attempted to differentiate ASCs into an AF-like lineage. In a recent preliminary study, Gebraad and co-workers attempted to differentiate human derived ASCs (using a micromass model) towards an AF-like phenotype using serum free

chondrogenic medium without growth factors (193). Initial results based on GAGs contents and gene expressions look promising, but more work will need to be done to confirm the effectiveness of the culture model. An earlier study by Gruber et al showed that using collagen-based Gelfoam sponges and TGF-β, human derived ASCs can be manipulated to display gene expressions favorable towards a disc-like lineage, but did not find concluding results for a specific AF-like lineage (194). These studies display the potential of ASCs for use in IVD TE, although more work will need to be done to establish differentiation protocols and approaches.

Cell-sheet engineering retains the benefits conferred by an intact ECM, allows scaffold-free constructs to be developed, and reduces the amount of cell loss occurring during traditional cell seeding processes (123-125). A previously published study by See et al (129) demonstrated the multipotentiality of BMSC CSs, but there has been no published literature on the multipotentiality of ASC CSs, nor on the behavior of ASCs cultured under prolonged hyperconfluent conditions. Hence one of the motivations for phase 1 is to combine both ASCs and CS TE, each possessing its own inherent strengths, and consequently develop a better understanding of the behavioral characteristics of ASCs within the CSs under prolonged hyperconfluent durations.

Weekly assessment time points for up to 3 weeks of CS culture was chosen for the first stage of the study in order to progressively investigate the behavior and development of the ASCs within the growing CSs. With a better knowledge of the ASC CSs, an optimal time point can then be determined to harvest the CSs for downstream applications. The results showed that with increasing culture duration, the metabolic activity of the ASCs within the CSs can be maintained and the ASCs continue to secrete ECM, thereby creating a thicker and more densely packed layer of ECM above. Alamar blue assay results indicated an improvement in metabolic

activity of the ASCs, which can be attributed to either an increment in cell numbers, and/or improvement in cellular activity. The latter is more probable as we observed a decrement in DNA content from the week 0 to 3 week old CS samples when normalizing the collagen contents of the CS samples to its respective DNA amounts (under the Sircol assay assessment section).

Gene expression results of early differentiation markers (Sox 9 and Runx 2) interestingly demonstrated that a longer CS culture duration to form thicker CSs do not necessarily confer added benefits to the CSs, as indicated by the initial increment in the genes' expression levels in the one-week old CSs and subsequent decline for the two-week and three-week old CSs. Such a phasic behavior in gene expressions of Sox-9 and Runx2 warrants further research into the kinetics and feedback aspects of their gene expressions systems in the future, and should be explored together with the regulation of pluripotency markers in relation to hyperconfluency duration (Eg. Sox-2, Oct-4 and NANOG) as was demonstrated by Yu and co-workers on human derived ASCs (195). A recent study on gene expression kinetics in human derived ASCs showed that CD105 (a cell surface marker) is expressed in undifferentiated ASCs, and would drastically decrease in adipogenically differentiated ASCs (196) – indicating the possibility of tracking cell surface markers kinetics in relation to hyperconfluency as well. It should also be noted that the ASC CSs were able to express stronger levels of early chondrogenic and osteogenic gene markers just purely by the influence of hyperconfluency and under no chemical induction factors. The ideal time point to harvest ASC CSs for subsequent downstream usage should hence be before 2 weeks of CS culture. Giving an allowance of a couple of days for the ECM and cell-to-cell adhesion junctions to form and the CS to stabilize, one-week old CSs were thus chosen for the subsequent differentiation studies. This is in comparison to the two-week old CSs which was used for the previously published BMSC CSs differentiation study [125].

Among the three genes used to assess chondrogenic differentiation (Sox 9, Col II and Agg), Sox 9 (Sex-determining-region-Y type high mobility group box 9) is a transcriptional factor that plays a central role in the development of chondrogenesis. A key transcription factor in chondrogenesis, Sox9 coupled with a number of transcriptional cofactors is a critical regulator in genes such as Col II, a chondrocyte specific gene (197,198). An early gene marker for chondrogenesis, Sox9 was significantly upregulated in the induced CSI groups over the non-induced CSNI groups from week 2 onwards, and the upregulation was maintained till at least week 5 (**Figure 3-14**). Col II in the results above refers to the COL2A1gene that encodes for the alpha-1 chain of type II collagen, a fibrillar collagen found in cartilage. Col II was consistently and significantly upregulated in the CI and CSI groups over the non-induced controls (CSNI) from week 2 to week 5 of culture (**Figure 3-14**) and had evident stronger phenotype expression in the CI than CSI samples (**Figure 3-13**).

Histology and immunofluorescence results from osteogenic and chondrogenic differentiation showed that in both types of differentiation, samples from the CI group displayed the differentiated phenotype much quicker and stronger than the CSI group. For osteogenic differentiation, a larger extent of positive Alizarin Red staining (for calcium deposits) was observed in the CI samples as compared to the CSI samples at the same sacrificial time point (**Figure 3-10**). Qualitatively estimating the amount of positive red staining, it can be observed that the amount of positive staining seen in the CSI group after 5 weeks of induction, was achieved in the CI group from as early as after 3 weeks of induction. It should also be noted that the CSI samples would contain more ASCs numbers than the CI samples, and despite so, we could see that the amount of calcium deposited was still qualitatively larger in the CI samples. For chondrogenic differentiation, a larger extent of positive Safranin-O staining (for proteoglycans and glycosaminoglycans) and Col II formation was also observed in

the CI samples as compared to the CSI samples (**Figure 3-12** and **Figure 3-13**). It should be noted that due to the pre-culture of an ECM layer in the CSI and CSNI samples, the pellets in these groups were much larger than the CI pellets. However, considering the proportion of positive Safranin-O staining relative to the entire pellet's cross-sectional area, it can be visually estimated from Figure 3-**12** that the amount and intensity of positive staining after 5 weeks of induction of the CSI group (**Figure 3-12**) was similar to that of the CI group, induced for only 3 weeks (**Figure 3-12**).

Such results are contrary to those published previously on BMSCs cell-sheets (129), which demonstrated the potential of BMSCs cell-sheets having an enhanced differentiation capability down the osteogenic and chondrogenic lineages than BMSCs alone. This is an illustration of one of the differences between BMSCs and ASCs, despite the many common biological characteristics both types of MSCs share (199). However, the heterogeneity of both BMSCs and ASCs populations in both studies should also be taken into account. Often, there are conflicting results between the differentiation efficiencies of ASCs versus BMSCs (200) and with regards to this, Strioga et al (199) suggested that the heterogeneity of the ASCs and MSCs populations isolated in different studies might have accounted for the predominance of subpopulation of MSCs with a unique differentiation potential down specific lineages (199). That argument can potentially be extended to the differences in stem cell characteristics showed by this study, whereby the ASCs isolated for this study seem to perform better under the CI conditions versus BMSCs isolated previously who preferred a confluent (CSI) environment. A further discussion on the study's experimental design, and genes investigated for adipogenesis and osteogenesis can be found in Appendix A.

The inner AF consists of more aggrecans and Col II than the outer AF, and the converse applies to Col I, which is predominantly in the outer AF. Results from Figure 3-**15** showed that ASCs pellets displayed more aggrecan and Col II than the CSs pellets, which had more Col I. This implies that conducting a pre-conditioning culture in ascorbic acid eliminates the need of two different differentiation cocktails to be used to form the inner and outer AF for the subsequent phases of the dissertation. Hence, in the following section on the integration of cells with the developed silk scaffolds, ASCs was chosen to be directly seeded onto parts of the fabricated lamellae intended for the construction of the inner AF, while ASCs pre-conditioned to form CSs was chosen to be incorporated with parts of the lamellae intended for recapitulation of the outer AF.

3.5 Concluding Remarks

The availability and ease of harvesting adipose tissues, makes it an attractive and readily available source for MSCs. In phase one, the suitability of ASCs and ASC CSs was assessed for IVD TE. ASC CSs were shown to retain their multipotentiality, in particular down the chondrogenic lineage. As hypothesized, hyperconfluent culture of ASCs allowed formation of a robust ECM layer, which was characterized by temporal profiling the growth and gene expressions of the ASC CSs. ASCs also behaved differently, as hypothesized, while under the effects of hyperconfluent culture conditions as shown by the less chondrogenic phenotype displayed by the ASC CSs in comparison with the ASCs. Given such results, it was decided that for the subsequent phases of the project., ASCs would be suitable for use in the inner AF, whilst the use of ASC CSs would be suitable for the less chondrogenic-like but Col I rich outer AF.

Chapter 4. Phase Two: Development of Hierarchical Hybrid Silk-based Laminates for Annulus Fibrosus Tissue Engineering

4.1 Introduction

As covered in the literature review section, the native AF consists of concentric rings of lamellae with aligned and angled collagen fibres. There is also a gradual transition in ECM constituents and structure from the inner AF (mostly Col II and Agg) to the outer AF (mostly Col I). Correspondingly, the variances in ECM constituents reflects the changes in the loading environment from the inner AF (IAF, predominantly compression) to the outer AF (OAF, predominantly tension) (20). Fibres play an essential role to the overall mechanical characteristics of the AF, while the matrix, containing components like proteoglycans, controls the permeability and diffusivity of water and solutes into and out of the disc (20). Fibrous scaffolds that can mimic the native architecture of the AF would be advantageous for use as part of a TE strategy to repair damaged AF tissues. The objective of this phase is to develop hierarchical hybrid silk-based laminates for use in AF TE. Work pertaining to this phase is carried in two stages - firstly the hybrid silk-based laminates were fabricated and characterized, before moving on to the next stage where its cytoxicity and cellular compatibility for AF TE are assessed using ASCs and ASCs cell-sheets. Electrospinning was chosen to provide the necessary nanotopological cues in the form of a thin mat, which will be further reinforced by incorporating it as a layer over knitted silk mats. Electrospinning of silk for TE applications have been reported in literature (201,202), but none for AF regeneration applications. Expanding the work covered in Phase 1 (section 3), two approaches of incorporating the cells are explored. For the outer AF, ASCs were cultured under prolonged hyperconfluent conditions to form cell-sheets prior to integration with the nanofibrous mats, while for the inner AF, direct seeding of the stem cells on the nanofibrous mats was carried out.

4.2 Materials and Methods

4.2.1 Preparation of Silk Fibroin (SF) Solution

B Mori silk was degummed, dissolved and dialysed according to a modified protocol adapted from established protocols (133). Briefly, raw silk fibres were first degummed in boiling solutions of 0.02M Na_2CO_3 (Sigma Aldrich) to remove unwanted sericin before being washed in dH_2O to remove any residual Na_2CO_3 (Sigma Aldrich). Degummed silk fibres were then air-dried before being dissolved in 9.3M lithium bromide (Sigma Aldrich) at 60^oC for 4hours to obtain 20% (w/v) silk fibroin (SF) solutions. SF solutions were then dialyzed against dH2O for 48hrs with at least six changes of dH_2O using SnakeSkinTM dialysis tubing (10,000 MWCO; Thermo Fisher Scientific, Rockford, IL, USA). Dialyzed SF solutions were then centrifuged at 1000g for 10mins to remove impurities, and the supernatant containing the purified SF stock solution was collected and kept at 4^oC for further steps. Small known volumes from the purified SF stock solution were freeze dried in a freeze dryer (Epsilon 1-4; Martin Christ GmbH, Osterode, Germany) and weighed to obtain its concentration after dialysis. 5% (w/v) SF working solutions were then obtained by adding appropriate amounts of dH_2O to the SF stock solution.

4.2.2 Fabrication of Hybrid Electrospun-Knitted Lamellae

a. Electrospinning of SF Polymer

Electrospun mats were obtained using modified protocols in literature (133,136) by first dissolving freeze-dried silk solution sponges in 1,1,1,3,3,3-Hexafluoro-2-propanol (HFIP; Sigma) to form a 10% (w/v) silk polymer solution. The silk polymer solution was then loaded into a 5ml syringe (Nipro, Osaka, Japan) and placed onto a syringe pump (KD-Scientific, Holliston, MA, USA) set at a flow rate of 1ml/hr. The silk polymer solution was subsequently ejected from a 18G hypodermic needle (pre-grinded to have a flat tip) that was subjected to a high voltage of 12kV (Gamma High Voltage Research, Ormond Beach, FL, USA). Using a top-down setup (203), the silk

polymer solution, upon leaving the charged syringe needle, formed a whipping polymer jet which gets evaporated of HFIP, as it gets collected on a grounded (Gamma High Voltage Research) metal platform set 10 to 20cm away.

b. Alignment of Electrospun Fibres

A rotating jig (Figure 4-**1**), consisting of two positively charged parallel steel rods, was designed and custom-built to obtain aligned fibres during the electrospinning process. Apart from the rotational jig, the electrospinning setup also consists of a positively charged concentration brass ring; with the latter helping to limit the deposition area of the polymeric fibres to the jig's rotating frame (~800rpm) to improve efficiency of the fibre collection. Aligned electrospun mats between the parallel rods (5cm apart) of the rotating frame were collected at regular short intervals (5 min) onto custom made collection forks for further processing (Figure 4-**1**).

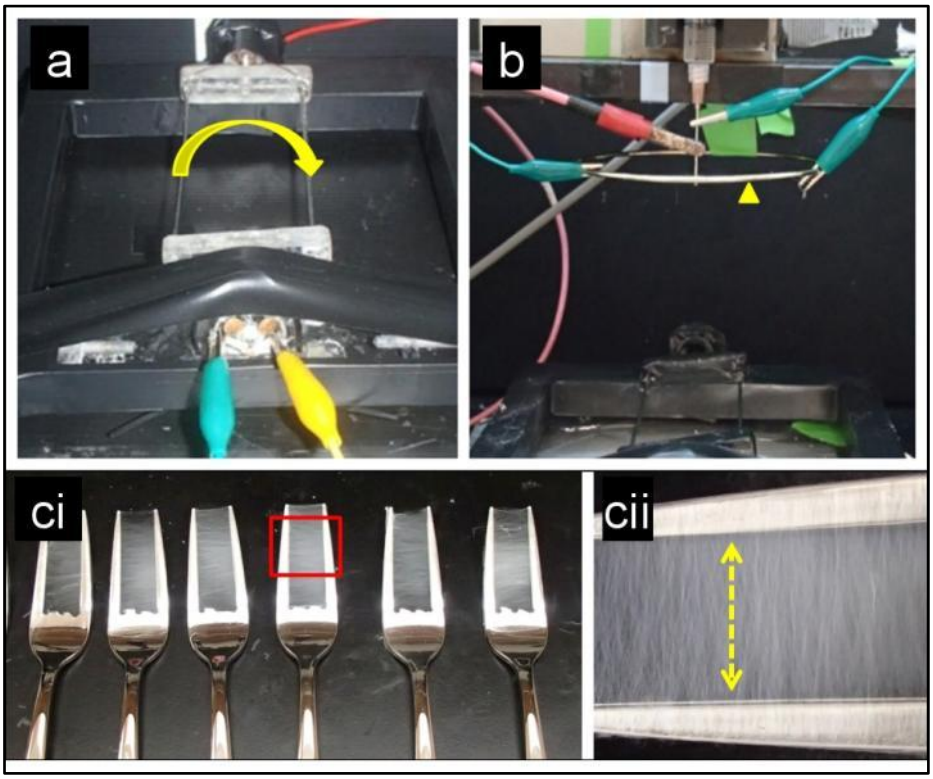

Figure 4-1. Electrospinning setup for collecting aligned fibres. (a): Picture of custom-build rotating jig, (b) Picture of entire setup with concentrating ring (indicated by arrow head), and (c) aligned mats collected on custom made collection forks (i), close-up picture showing alignment of fibres on collection forks (ii).

c. Incorporation of Aligned Electrospun Layer with Knitted Mat

A knitted mat is required to provide reinforcement to the electrospun mat for better mechanical strength, and ease of handling in the subsequent phases. The knitted mat was fabricated using a Silver Reed knitting machine (SK270, Silver Reed, Suzhou, China) with a fine needle pitch of 3.6mm (Figure 4-**2a**). Silk threads obtained from collaborators were strung through the knitting machine without sericin removal. This is to allow sericin to act as a 'binding' and protective agent coating the SF, as the thread gets pulled through the mechanical gears of the knitting machine. Sericin is removed from the knitted mats thereafter using the degumming protocol described earlier in section 4.2.1. The resultant knitted mat is a thin lamella piece of scaffold (Figure 4-**2c**). To integrate the electrospun layer with the knitted mat, the electrospun layer was first placed on knitted mats pre-cut to a 3cm x 2cm dimension (**Figure 4-2b**). Treatment with absolute methanol (Fisher Chemical, Rockford, IL, USA) for β-sheet formation is necessary to render the electrospun mat insoluble in an aqueous environment. Methanol treatment have been reported in literature to shrink silk electrospun mats (136,204), and this phenomenon was leveraged to ensure the electrospun mats (placed onto the knitted mats before introduction of methanol) shrink during methanol treatment to "catch on" to the knitted mat tightly to form a single electrospun-knitted entity (hereafter termed "hybrid laminates") (Figure 4-**2d**).

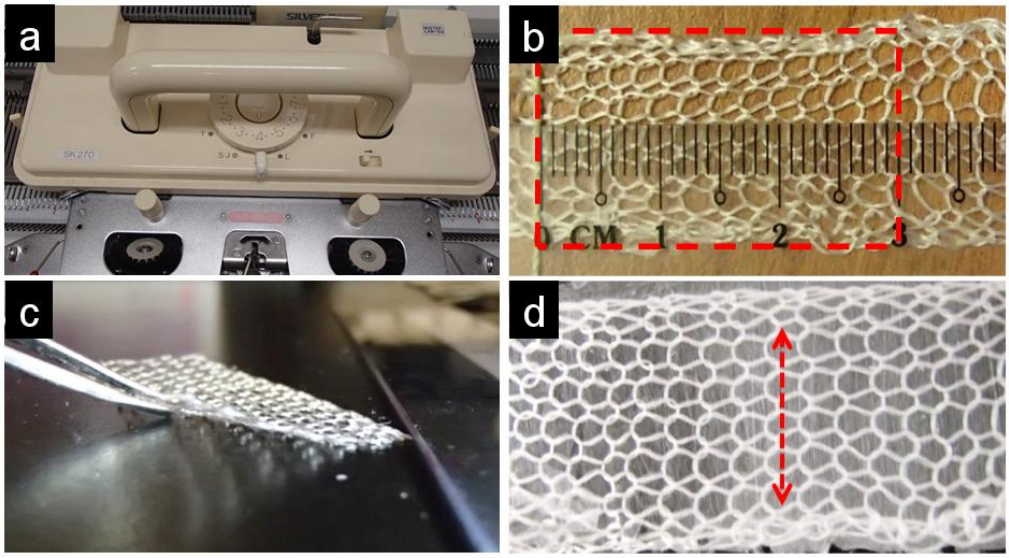

Figure 4-2. Silver Reed knitting machine (a) used to fabricate thin knitted silk mats (b,c), which subsequently had an electrospun layer of aligned nano fibres integrated together (d) after methanol treatment. Red arrow indicates alignment direction.

4.2.3 Physical Characterization of Hybrid Lamella Scaffolds

a. Scanning Electron Microscopy (SEM)

Electrospun mats were evaporated of solvents (methanol, HFIP) before being mounted and placed in a gold coat sputter (JEOL, Tokyo, Japan). Viewing was carried out using a scanning electron microscope from JEOL (JSM-5610/JSM6510; JEOL, Tokyo, Japan). Images were taken from 50x to 5000x magnification.

b. Characterization of Electrospun Mat

Two characterization assessments relevant to the collection of electrospun silk mats from the rotational jig were conducted: i) Shrinkage test, and ii) Fibre diameter quantification. Given that silk electrospun mats shrink after methanol treatment, a shrinkage test was first carried out by subjecting a piece of silk electrospun mat of a known dimension to methanol treatement. The dimension of the mat post treatment was then recorded and the percentage area reduction of the mat was tabulated using open source imaging software FIJI (205). To better understand the effect of the collection approach on the resultant diameters of the electrospun silk mats, electrospun fibres were first collected on different materials (Aluminium foil, Plastic

sheet, Glass slide) and between two metal rods (analogous to the rotational jig setup). SEM imaging of the electrospun mats was then carried out and diameters of the fibres in the SEM images were then tabulated using FIJI (205).

c. Alignment Quantification with Fast Fourier Transform

Alignment of the electrospun silk fibres was quantified using a Fast Fourier Transform (FFT) algorithm modified from published literature (206-208). Briefly, SEM images taken at 1000x magnification were first cropped to square dimensions and converted to 8-bit grayscale images using image processing software FIJI. The images were then subjected to a FFT algorithm in ImageJ to convert the SEM (spatial domain) image to a frequency domain image. The latter maps the rate pixel intensities were changing in the SEM (spatial) domain image. The frequency plot generated by ImageJ places pixels of low frequency at the center of the frequency plot, while high frequency pixels were placed towards the periphery of the frequency plot. Low frequency signals correspond to areas on the spatial domain image that had pixels of similar values (adjacent pixels vary in intensity values to a low extent) (Figure 4-**5a**). A SEM spatial image containing aligned fibres would result in a frequency plot that have pixels concentrated along a certain axis, while a SEM spatial image with random fibres would result in a frequency plot with pixel values scattered homogenously around the origin **(Figure 4-5a**). Thereafter, a OvalProfile plugin was ran on the frequency domain plot to conduct a radial summation of the frequency pixels. Radial summation results in a tabulation plot on the summed intensities taken along a summation line pivoted at the origin of the frequency domain image (**Figure 4-5a**). The characteristic of the peaks in the tabulation plot reflects the degree of fibre alignment in the original SEM spatial domain image. A high and narrow peak indicates that fibres were uniformly oriented at a certain angle, while a broad and flat peak indicates an absence of any distinct orientation (Figure 4-**5a**). Published

literature in this regard would typically describe the peaks or attempt to tabulate the area under the peaks as a way to quantify the alignment (206,208). Such approaches are either semi-quantitative or an estimation, as the degree of alignment is directly associated with the width of the peak rather than the height of or area under the peak. Hence, modifications were made to improve on this existing technique described in order to provide a true quantification over the current approaches. An additional step was carried out by transferring the radial summation plot data from ImageJ to OriginPro to conduct a curve fit. Taking into consideration the random whipping nature of which electrospun fibres are formed from the Taylor's cone to the collection surface, a Gaussian best-fit curve was fitted into each set of data, and the full width half maximum (FWHM) of the fitted curve was read off (Figure 4-**5a**). A smaller FWHM value directly refers to a narrow peak, while a larger FWHM value refers to a broad peak, thereby providing a direct measurement of the degree of alignment of the fibres in the original SEM spatial image.

4.2.4 Cell Culture Conditions

All the scaffolds were sterilized by an Anprolene Ethylene Oxide Gas Sterilizer System (Cole Parmer, Vernon Hills, IL, USA) according to the manufacturer's protocol prior to cell-seeding. rASCs of passages 3 to 5 were used for all the cellular experiments in this phase. Unless otherwise stated, cell cultures were conducted in medium consisting of DMEM (Invitrogen) supplemented with 10% FBS (Hyclone) and 1% P/S (PAN-Biotech GmbH), and maintained in a humidified 5% CO_2 incubator at 37^{o}C. ASCs seeded onto electrospun mats and hybrid laminates were conducted at a density of $3x10^5$ cells/cm^2. ASCs cell-sheets (CS) incorporated with electrospun mats and hybrid laminates were first seeded at a density of $3x10^5$ cells/cm^2 on culture plates, and cultured in medium supplemented with 50 μg/ml ascorbic acid (Vit C, Wako) for one week to form ASCs CS. Chondrogenic medium was needed in some groups, and in those cases, chondrogenic induction medium

consisted of HG-DMEM (Invitrogen) supplemented with 10% FBS, 1% Penicillin/Streptomycin, 1% ITS+ (BD Biosciences, San Josa, CA), 100nM dexamethasone (Sigma), 50ug/ml Vit C (Wako), 10ng/ml TGF-ß3 (RayBiotech Inc) and 10ng/ml BMP-6 (R&D Systems).

4.2.5 Cytotoxicity Assessment of Hybrid Lamella Scaffolds

Alamar blue colorimetric assay (Invitrogen) was used to determine the metabolic activity of the ASCs and ASCs CS on the electrospun mats and hybrid laminates. As mentioned in the previous chapter, ascorbic acid improves ECM deposition (176) - which is important for an AF application. Hence, the influence of Vit C was also investigated, with the use of two culture medium (normal culture medium, and one supplemented with Vit C [50 μg/ml]). The procedure is as described earlier in section 3.2.2.a. Briefly, culture medium supplemented with 10% (v/v) alamar blue reagent was added to the culture wells and placed in a 5% CO_2 incubator at 37^{o}C for 1 hr. Alamar blue supplemented medium was also added to electrospun mats and hybrid laminates with no ASCs nor CSs incorporated as negative controls. After incubation, alamar blue supplemented medium from each sample was pipetted to a 96-well plate and absorbance was spectrophotometrically measured at the 570nm and 600nm wavelengths using a microplate reader (Turner Bio-systems), and metabolic activity levels were calculated according to the formula provided (Invitrogen).

4.2.6 Improving Sample Handling for Fluorescence Assessment

Initial handling of the ASC-CSs with the electrospun mats and hybrid laminates indicated that the ASC CSs required some time for proper integration with the electrospun layer. If left directly as a sheet above the electrospun mats, there was a high rate of premature curling up of the CS, due to the existing tension within the ECM, before adhesion of the CS to the electrospun mat could take place. In the eventual 3D assembling phases (section 6 and 7), this would not be a problem as the

layers of CS and laminates are placed in a multi-ply format on one another, and would hold the CSs in place for proper adhesion to take place. However work in the current phase involved the 2D assessment of the CSs with the electrospun mats and hybrid laminates. Hence, a customized ring frame was designed to "catch on" onto the CS and sterilized stainless steel metal rings fitting the diameter of the culture wells were used to press down the CSs-seeded electrospsun mats (**Figure 4-7a**). The value of the customized frame is contingent on the condition that it would not adversely affect the CSs behavior, and thus alamarblue assessment was carried out to study for adverse effects the frame might have on the CSs. There were two groups: i) a positive control consisting of CSs being cultured and left on the TCPS culture plates, and ii) the experimental group consisting of CSs being lifted off the culture plate by the frame, and placed into a new culture plate with the frame still intact on the CS. Both groups were pre-conditioned with Vit C supplemented medium for one week (50ug/ml) to form CSs, before commencement of the alamarblue assessment.

4.2.7 Fluorescence Imaging Assessment

Fluorescence imaging assessment was conducted on the following molecular constituents: Col I (major component of ECM), F-actin (cytoskeleton of cells), cell nucleus (location of cells), fibronectin (a common cellular adhesion protein). Col I and fibronectin detection was achieved with an antibody approach, F-actin was detected using fluorescently tagged phalloidin, and cell nucleus detection was done with 4',6-diamidino-2-phenylindole (DAPI). Phalloidin is a member of the phallotoxins family of toxins extracted from a poisonous mushroom strain Amanita Phalloides (209). It is a low molecular weight peptide, and has high binding affinity to filamentous actin (F-actin) (209).

Groups involving Col I (with no F-actin) staining were first fixed with -20^{o}C methanol for 10mins, before being washed with 1xPBS. The samples were then

blocked with 1% bovine serum albumin (BSA, Sigma Aldrich) for 1 hr, before overnight incubation with a primary Col I antibody (1/2000; Sigma Aldrich) in a humidified chamber at 4^{o}C. Secondary antibodies (conjugated with Alexa Fluor 488nm (1/400; Invitrogen) and Alexa Fluor 594nm (1/400; Invitrogen) probes) targeting the primary antibody were then added with DAPI (0.5μg/ml; Invitrogen) for counterstaining of the nucleus for 30mins at room temperature.

Groups involving F-actin staining were first fixed in 4% methanol free formaldehyde (Thermo Fisher Scientific) for 10mins, before being washed with 1xPBS 2 times, 5 minutes each. For co-localization studies that also involved Col I, antigen retrieval was required, and was carried out by pepsin digestion (Roche Diagnostics) at 37^{o}C for 20mins. Intracellular F-actin staining required cell membrane permeabilization which was carried out with 0.1% (v/v) Triton-X (Bio-Rad Laboratories Inc, Hercules, CA, USA). The samples were then blocked with 1% BSA for 1 hr, before overnight incubation with the primary antibody of interest (Col I: 1/2000, Sigma; fibronectin 1:100, Sigma) in a humidified chamber at 4^{o}C. Secondary antibodies (conjugated with either Alexa Fluor 594nm of Alexa Fluor 488nm (both 1/400; Invitrogen) probes) targeting the primary antibody were then added with Phalloidin conjugated with Alexa Fluor 488nm fluorescent probes (1/100; Invitrogen) and DAPI (0.5μg/ml; Invitrogen) which was used as a counterstain for nucleus detection, were added for 30mins at room temperature. For groups with only F-actin and DAPI staining, the BSA blocking and antibodies steps were not carried out. Instead, fluorescently tagged Phalloidin and DAPI were incubated for 30mins directly after permeabilization.

All epifluorescence images were viewed with an inverted epifluorescence microscope (IX71, Olympus, Tokyo, Japan), and captured using a DP70 digital colour camera

system (Olympus). Confocal images were viewed and captured using a FluorView FV1000 confocal imaging system.

4.2.8 Assessment of Cell-Seeded Hybrid Laminates

To understand the effects of the hybrid laminates on the behavior of the cells, gene expression assessment was carried out on ASCs seeded hybrid laminates cultured in Vit C supplemented medium and chondrogenic medium (hereafter termed "LmVi ASC" and "LmCh ASC" respectively). Similarly, one-week old CSs were incorporated with the hybrid laminates and cultured in Vit C supplemented medium and chondrogenic medium (hereafter termed "LmVi CS" and "LmCh CS" respectively). The eventual application of the hybrid laminate required multiple layers of it to be stacked on top of one another to recapitulate the multi-lamellar architecture of the native AF. Hence the co-localization effect of having ASC and CS laminates sandwiched with each other is important. As such, one of the groups had two pieces of cell-seeded laminates (one with ASCs and the other with CS) sandwiched together and cultured in Vit C supplemented culture medium and chondrogenic medium (hereafter termed "LmVi Co" and "LmCh Co" respectively). For comparison, gene expression studies also included four experimental groups which were conducted as micromass pellets culture. Two of the groups had $3x10^5$ of ASCs per pellet, one group was cultured in Vit C (50 μg/ml) supplemented medium, while the other group was cultured in chondrogenic medium (termed "PeVi ASC" and "PeCh ASC" respectively). Two of the remaining groups had one-week old ASCs cell-sheets rolled-up and centrifuged to form pellets, one group was cultured in Vit C (50 μg/ml) supplemented medium, while the other was cultured in chondrogenic medium (termed "PeVi CS" and "PeCh CS" respectively). All groups were cultured in their respective medium for 15 days before being sacrificed for RNA extraction. Results were then tabulated with respect to a negative control group consisting of ASCs

directly seeded onto TCPS culture plates ($3x10^4/cm^2$) and cultured in Vit C (50 μg/ml) supplemented culture medium.

a. RNA Extraction, cDNA Synthesis and RT-PCR

RNA extraction and cDNA synthesis were carried out as previously described in section 3.2.2.d. Real-time polymerase chain reaction (RT-PCR) was performed using protocols as described in section 3.2.2.e. The genes analyzed were: Sox9, Col II, Col I, Decorin, Biglycan and Aggrecan (Agg). Sox9 is an early chondrogenesis marker, Col I and Col II are major ECM components in the IVD, while the latter three being proteoglycans commonly found in the IVD. Expression levels of the target genes were normalized to the respective sample's GAPDH gene and then calculated using the comparative CT ($2^{-\Delta\Delta CT}$) method (179,180). Details of the primer sequences for the target genes and GAPDH can be found in Appendix E.

4.2.9 Statistical Analysis

Pairwise comparisons were determined using a two-tailed unpaired Student's t-test and performed using Excel Analysis ToolPak (Microsoft Inc.). Statistical analysis involving multiple comparisons were conducted with a one-way analysis of variance (ANOVA) test and post-hoc Tukey correction using OriginPro9 (OriginLab). $p<0.05$ was taken as significant and all data are expressed as means ± standard deviation.

4.3 Results

4.3.1 Physical Characterization of Electrospun Mats

Electrospinning is a process heavily contingent on the voltage gradient generated between the Taylor's cone and the collection surface. Hence characteristics (Eg. material, form) of the collection surface potentially can affect quality of the elcetrospun fibres obtained. Taking this into consideration, the characteristics of fibres obtained between static parallel rods (analogous to the rotational jig built) were

compared with those obtained on different materials placed flat below the exit needle (traditional collection approach). The diameters of electrospun mats obtained between parallel rods were in the sub-micron range, and were comparable with those obtained on different collection materials placed flat below the exit needle (Figure 4-**3**).

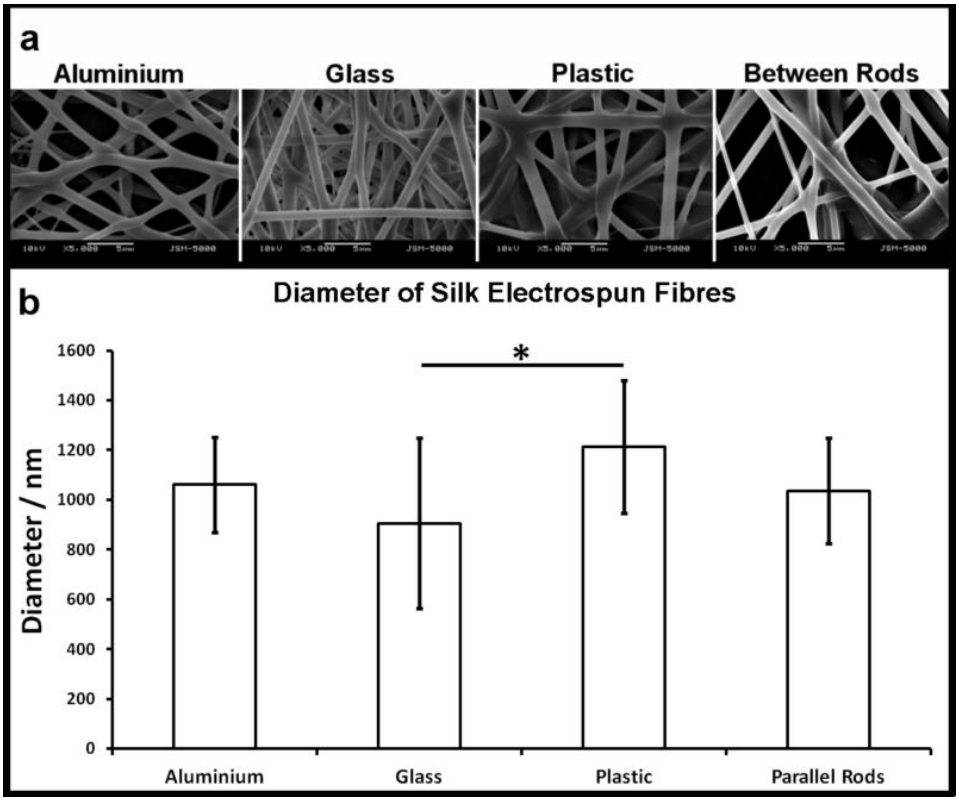

Figure 4-3. Diameter of silk electrospun mats obtained on different collection materials and between rods. *$p<0.05$*

SEM images showed that the morphologies of the fibres obtained between parallel rods and on different materials placed flat below the needle were similar (Figure 4-**4i**). At the fibre level, SEM images also showed that methanol treatment did not have any significant effects (Figure 4-**4i**). However, in line with literature as mentioned earlier in section 4.2.2.c (136,204), methanol treatment did result in a 11.7% shrinkage of the electrospun mat (Figure 4-**4ii**, **Table 1**) on the whole.

Table 1. Tabulation of Electrospun Mat Shrinkage Due to Methanol Treatment

Area Before Methanol Treatment	Area After Methanol Treatment	% Reduction
283.5mm^2	**250.233mm^2**	**11.7%**

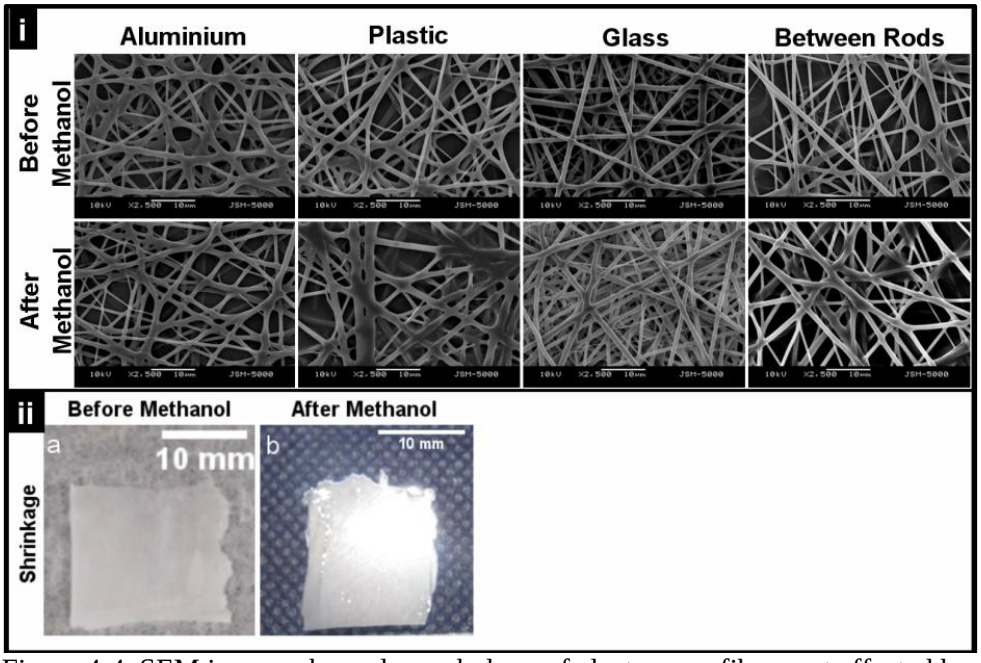

Figure 4-4. SEM images showed morphology of electrospun fibres not affected by methanol treatment (i), but overall mats shrunk nonetheless due to the treatment (ii).

Alignment quantification showed that the use of the custom-build jig was successful in producing electrospun mats with fibres significantly more aligned than not using the jig (Figure 4-**5b**) as indicated by the significantly lower FWHM values of the aligned electrospun mats. A lower FWHM value correspond to a narrower peak, which in turn is associated with a more aligned mat (Figure 4-**5a**).

4.3.2 Cytotoxicity of Electrospun Mats and Hybrid Laminates

Alamar blue assay results (Figure 4-**6**) indicate that the electrospun mats and hybrid laminates were not toxic to the ASCs and ASC CSs for up to 14 days of culture. The presence of Vit C, which will be vital for use in the next phases to improve ECM deposition for recapitulation of the ECM rich AF, did not adversely affect cellular behavior on the electrospun mats and hybrid laminates. Results from (Figure 4-**6ai**) and (Figure 4-**6aii**) indicate that the metabolic activities of ASCs and ASC CSs are similar, and hence only ASCs were used to test the hybrid laminates.

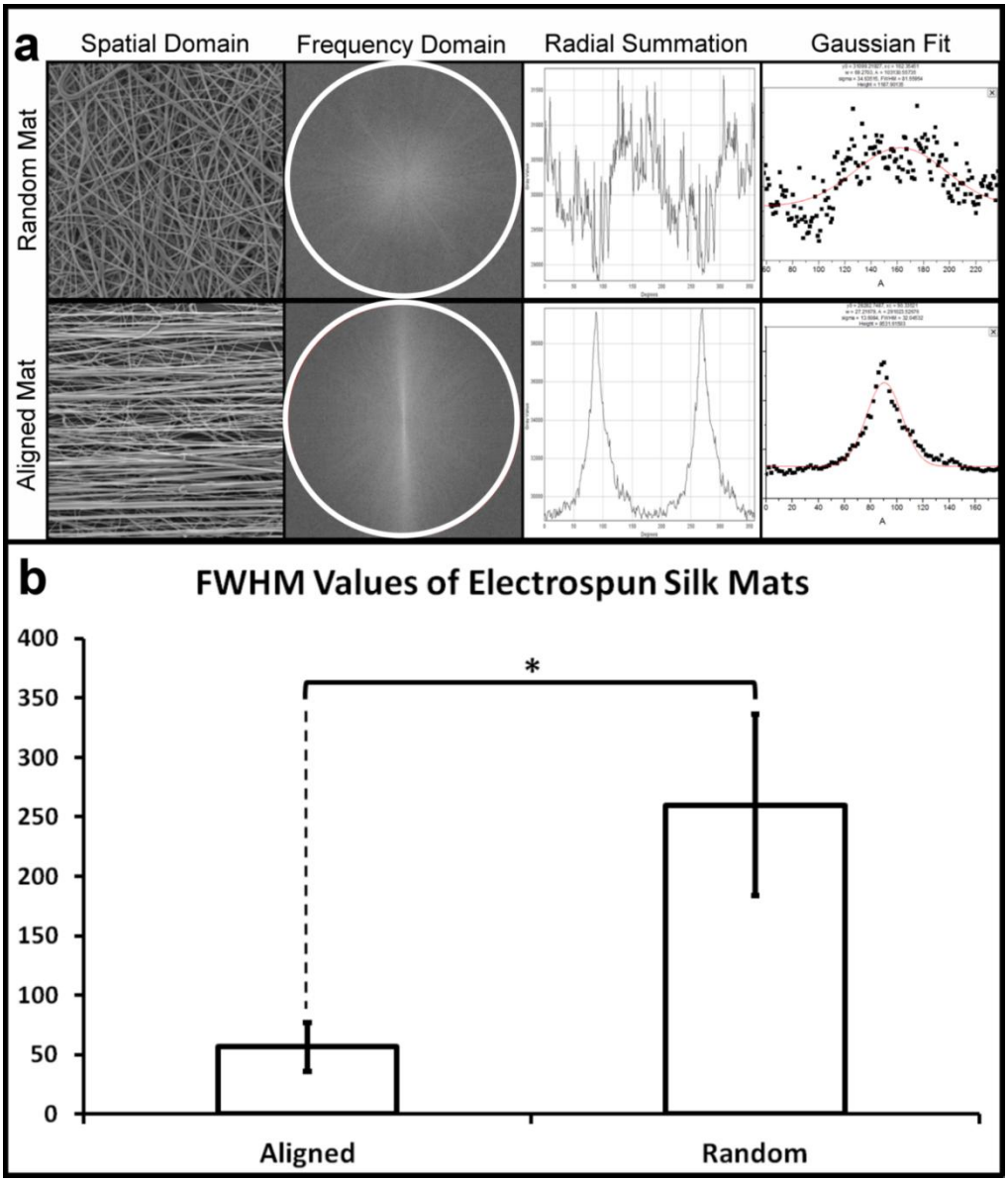

Figure 4-5. (a) Methodology for quantification of fibre alignment on silk electrospun mats using FFT. (b) FWHM values of random electrospun mats versus aligned electrospun mats fabricated using rotational jig. *$p<0.05$*

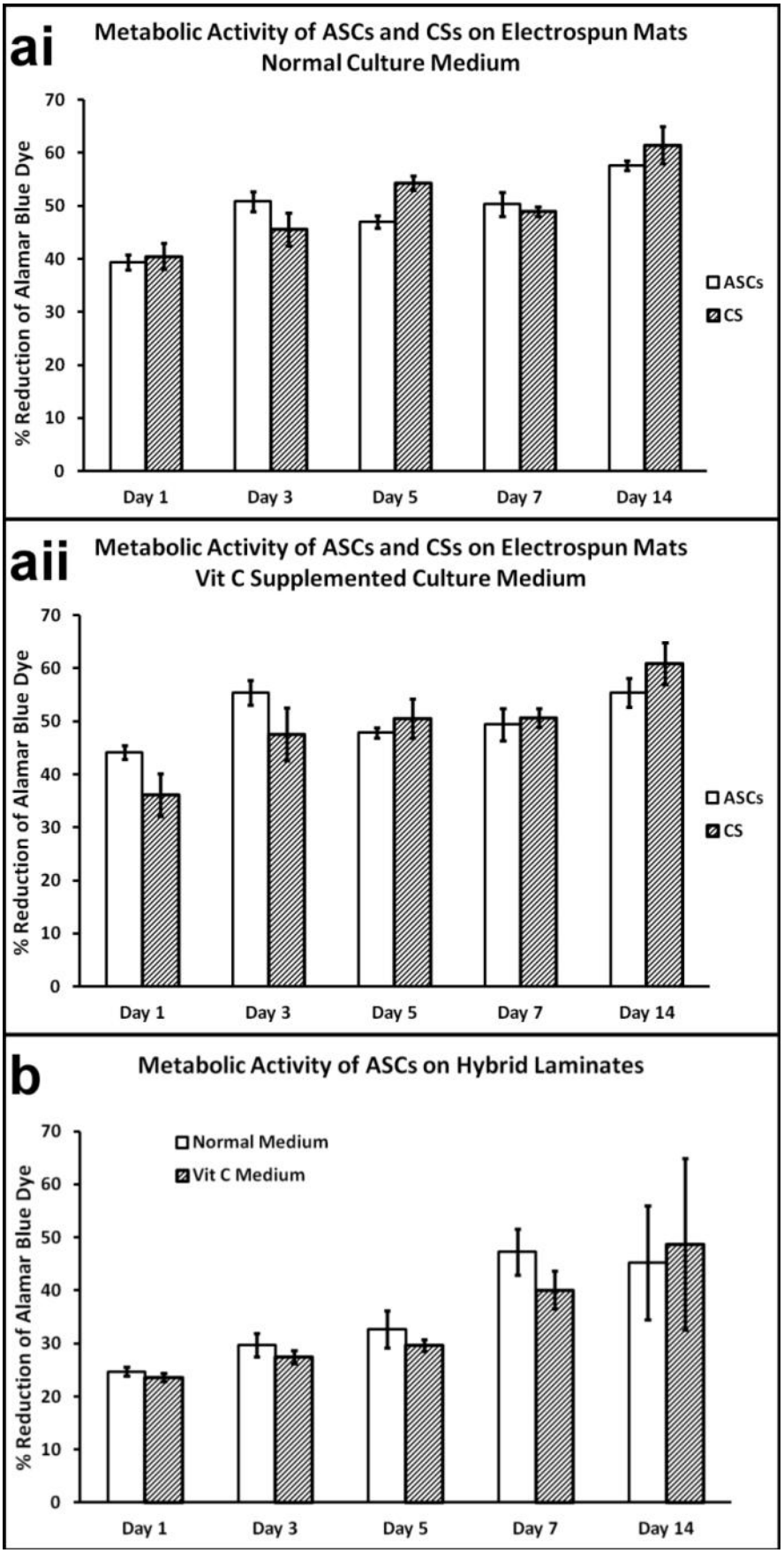

Figure 4-6. Metabolic activities of ASCs and ASC-CS on electrospun mats in normal medium (ai), and Vit C supplemented medium (aii). Metabolic activities of ASCs on hybrid laminates (b).

4.3.3 Improving Sample Handling for Fluorescence Imaging

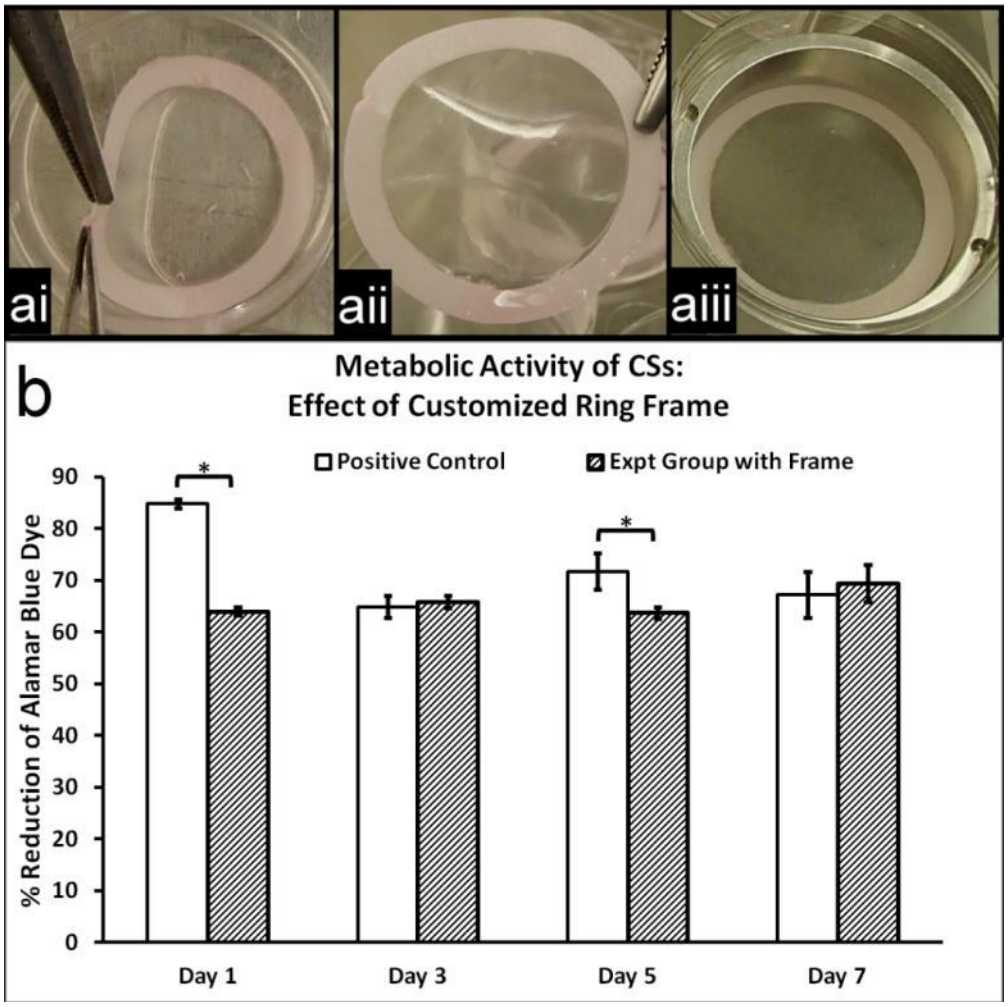

Figure 4-7. Use of a customized ring frame to lift one-week old CS (ai), CS held in tension as a flat 2D sheet by frame (aii), and placed back into culture well with metal ring pressing down (aiii). Metabolic activities of CSs with and without (positive control) frame (b). *$p<0.05$*

Alamar blue assessment results (**Figure 4-7b**) indicate that the initial lifting of CS might have resulted in a slight drop in metabolic activity of the CSs, as indicated by the significant lower dye reduction value on day 1. However, neither the ring-frame nor the lifting had any permanently adverse effects on the CSs as indicated by the similar dye reduction values by day 7 of assessment. This substantiates the use of the ring-frame for the next steps involving imaging assessments.

4.3.4 Fluorescence Imaging Assessment of Cell-Seeded Electrospun Mats and Single Hybrid Laminates

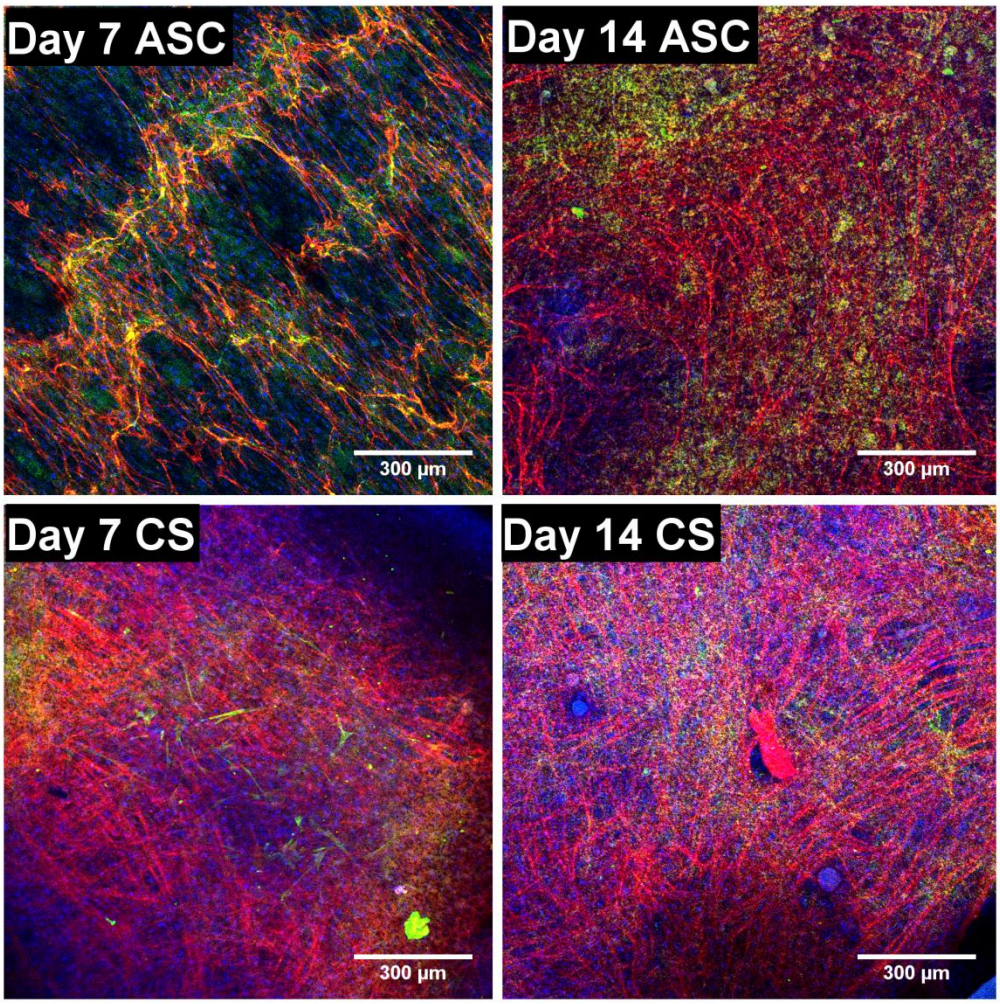

Figure 4-8. Confocal images (z-projected by maximum intensity) of ASCs and CSs on electrospun mats after 7 and 14 days. Samples were immunostained for fibronectin (green) and Col I (red), and counterstained with DAPI for nucleus (blue). Scale bar: 300µm.

From the Day 7 and Day 14 ASCs images in Figure 4-**8**, it can be observed that ASCs deposit fibronectin (green) when first seeded onto the mats, before subsequently depositing Col I. Confocal images of ASCs and CSs on electrospun mats (Figure 4-**8**) also indicate the importance of pre-conditioning ASCs with Vit C to form CS for ECM deposition purposes. Comparing the Col I (red) staining in the Day 7 and Day 14 ASCs images with the corresponding CSs images, a significantly denser Col I

matrix can be observed in the latter images. This is further corroborated with high magnification confocal images in Figure 4-**9** which showed that culturing ASCs on electrospun mats for up to 28 days resulted in lesser Col I deposited than what can be achieved by the CS groups in as fast as 7 days (Figure 4-**9**).

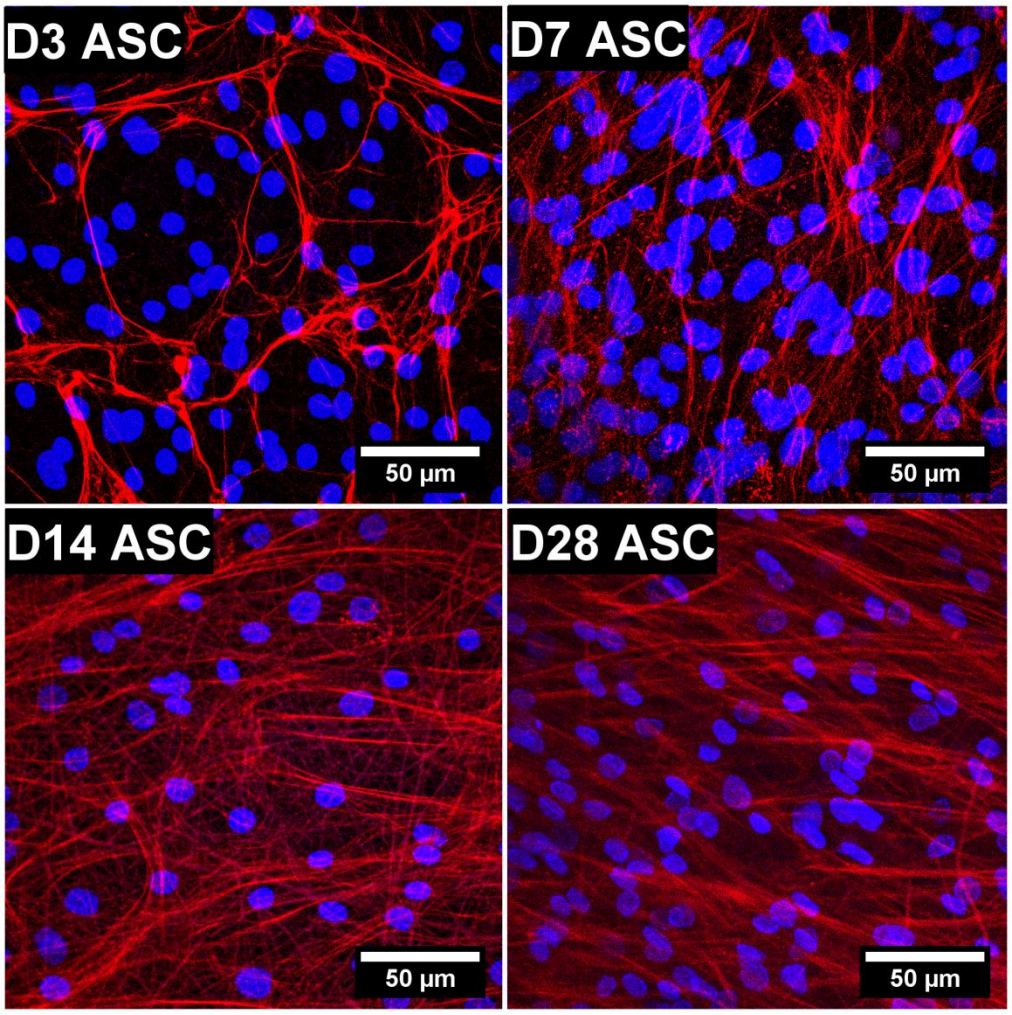

Figure 4-9. High magnification confocal images (z-projected by maximum intensity) of ASCs and CSs on electrospun mats after 3 to 28 days. Samples were immunostained for Col I (red), and counterstained with DAPI (blue). Scale bar: 50µm.

Using random electrospun silk mats, F-actin staining by phalloidin toxin (Figure 4-**10**) indicated that CSs were not influenced by the electrospun mats' topographical cues. F-actin staining of the CS showed that cells retain their orientation (circular fashion) achieved while being conditioned under Vit C to become CSs for up to 14 days culture on the electrospun mats (white dotted lines, Figure 4-**10**). This result

implies that for future phases of the project, electrospun mats are not required in cases where CSs are used. Figure 4-**10** also showed that ASCs when seeded onto the mats adhere well (presence of fibronectin, which increases with culture duration) and proliferated (more compact F-actin staining on Day 14 versus Day 3).

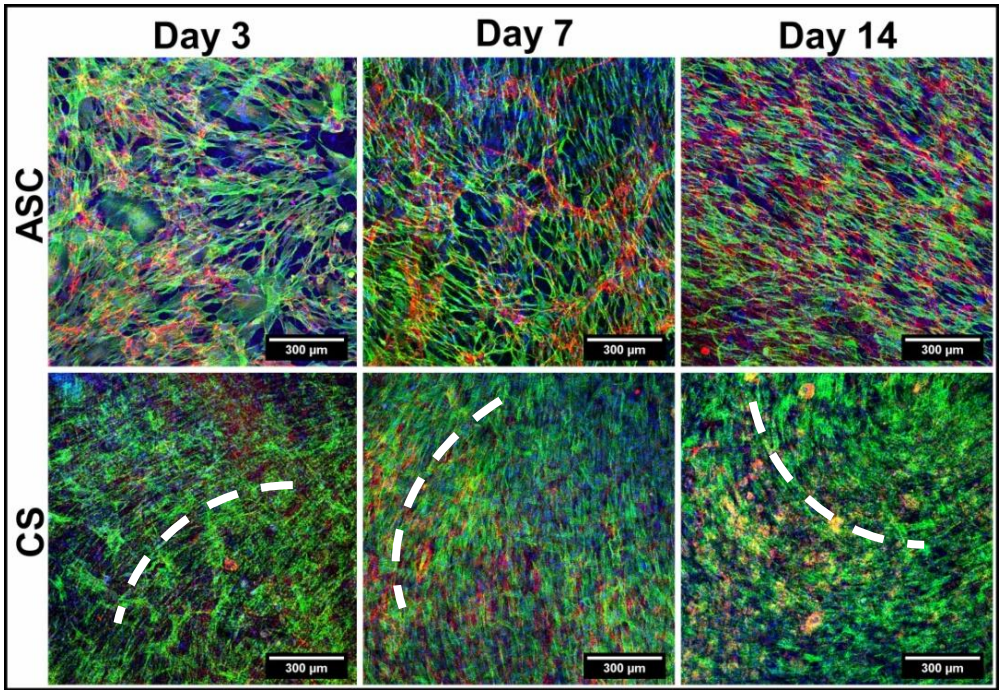

Figure 4-10. Confocal images (z-projected by maximum intensity) of ASCs and CSs on random electrospun mats after 3 to 14 days. Samples were stained for fibronectin (red), F-actin (green), and counterstained with DAPI for nucleus (blue). Circular directional alignment of CSs indicated by white dotted lines. Scale bar: 300µm.

ASCs were subsequently seeded onto the hybrid laminates (containing the aligned electrospun mats) for further assessment (Figure 4-**11**). F-actin staining indicated alignment of the ASCs with the aligned nano silk fibres (Figure 4-**11**), demonstrating the importance of the topographical cues in signaling the aligned assembly of ASCs on the electrospun mats. The absence of the topographical cues, for example in the Day 14 samples (where newly multiplied ASCs were deposited above the layer of older ASCs and ECM covering the mat surface), gives rise to a random arrangement of F-actin above the older aligned F-actin.. This imply that for the next phases of the

project, where ASCs are used, they should be incorporated with the presence of the aligned electrospun mats for topographical signaling purposes.

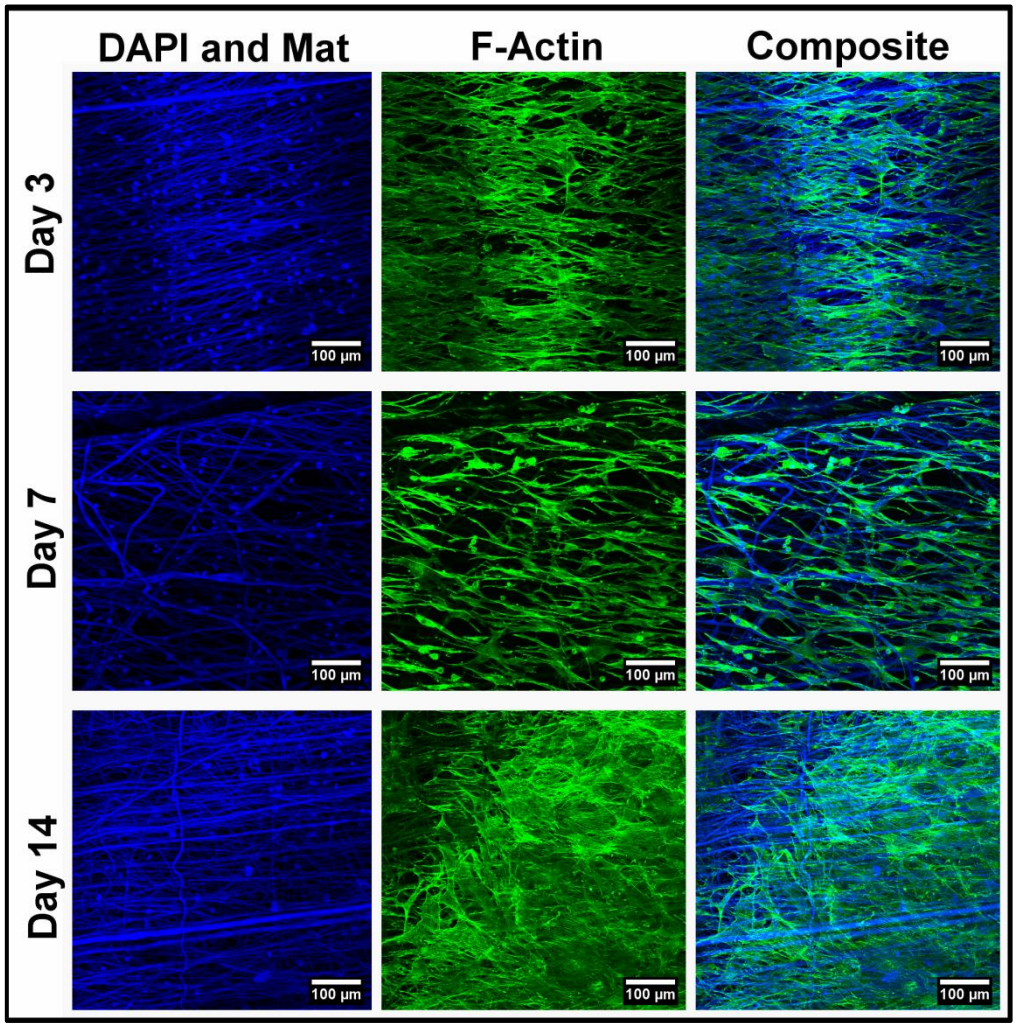

Figure 4-11. Confocal images (z-projected by maximum intensity) of F-actin staining (green) by phalloidin of ASCs on hybrid laminates with aligned electrospun mats after 3 to 14 days of culture. Samples were counterstained with DAPI for nucleus (blue) Scale bar: 100µm

Epifluorescence imaging (Figure 4-**12**) showed the presence of Col I forming across the knitted loops of the knitted mat. Deposition of Col I on the strongly auto-fluorescing knitted silk mat could however not be clearly seen. The modulation of this autofluorescence phenomenon will be discussed in detail in Chapter 6.1.

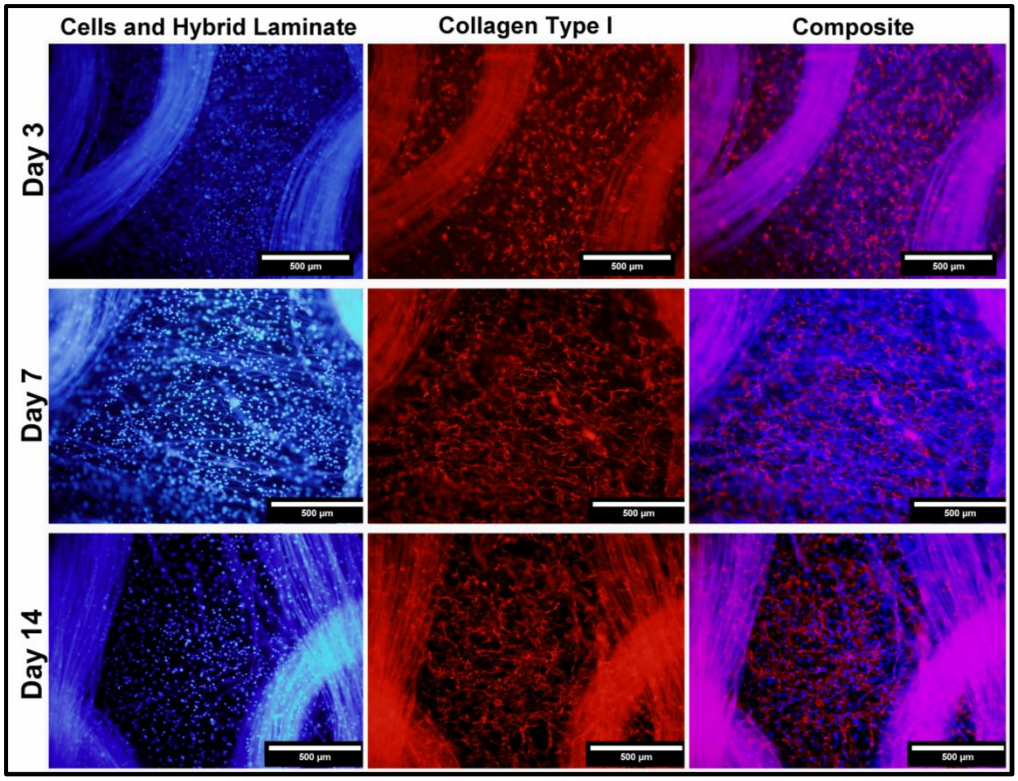

Figure 4-12. Epifluorescence images of ASCs on hybrid laminates. Samples were immunostained for Col I (red), and counterstained with DAPI (Blue) for cell nucleus. Scale bar: 500µm.

4.3.5 Gene Expression Assessment of Cell-Seeded Multi Hybrid Laminates

Gene expression results (**Figure 4-13**) indicate that the highest upregulation of all the genes investigated happened at the positive control groups (PeCh ASC, PeCh CS), validating results from Phase 1, and in line with literature whereby chondrogenic differentiation is typically conducted in a pellet form. ASCs and CSs retain their multi-potentialities when seeded onto the hybrid laminates, even though the chondrogenic samples (LmCh ASCs, LmCh CSs) did not show upregulation values that were on par with those of their pellet counterparts (PeCh ASCs, PeCh CSs). The genes with the most distinct upregulation in the chondrogenically differentiated samples over those in Vit C supplemented medium were those of Aggrecan and Col II. For the Aggrecan gene, LmCh ASC had a fold of 34.4 ± 18.1 as compared to its counterpart LmVi ASC (0.08 ± 0.02). LmCh CS on the other hand had a fold value of 15.6 ± 4.9 as compared to its undifferentiated counterpart LmVi CS (1.3 ± 0.9). A

similar trend was observed for the double-ply groups, where LmCh Co had a fold value of 10.2 ± 3.8 as compared to LmVi Co which only had a fold value of 0.4 ± 0.2.

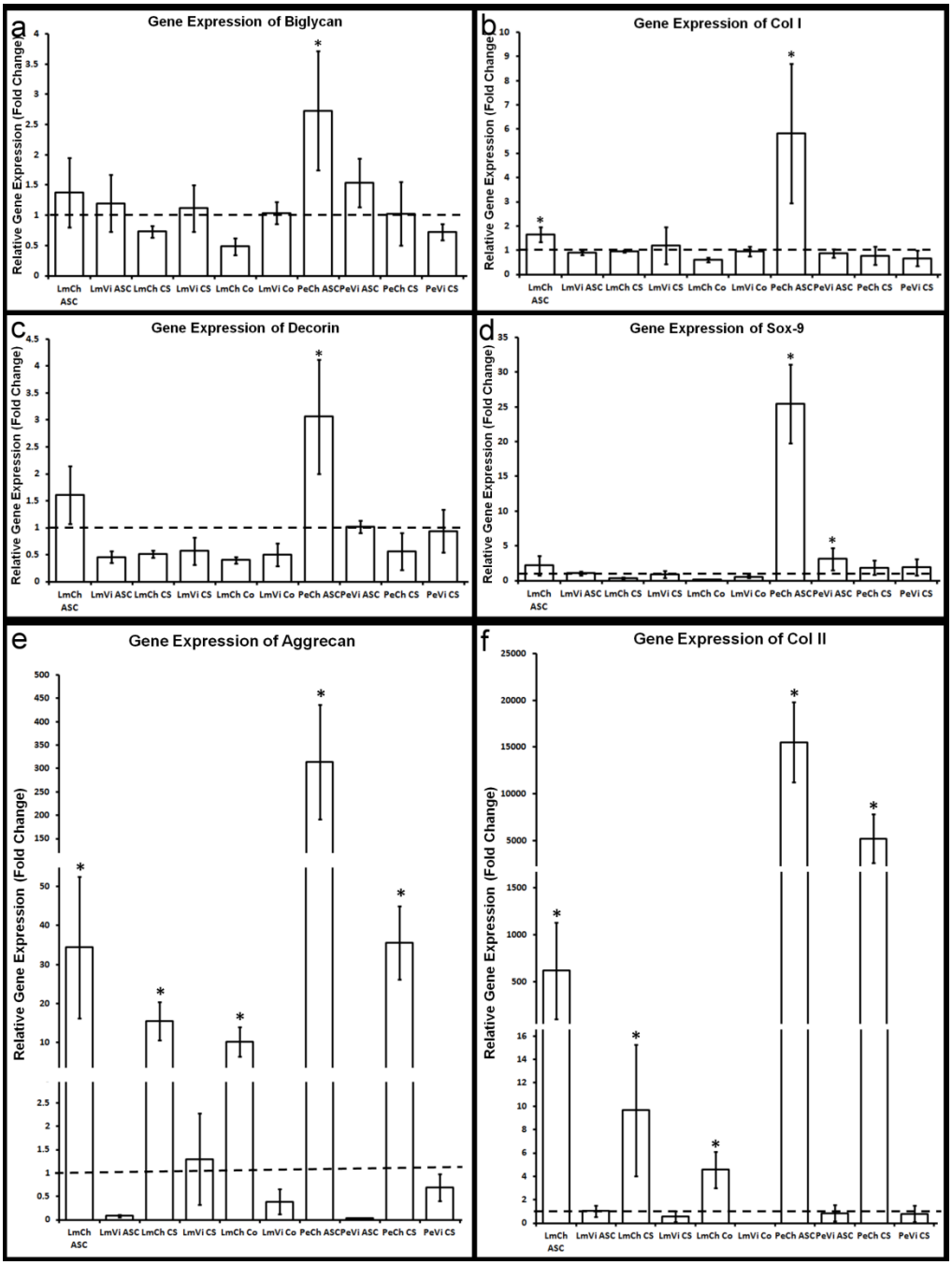

Figure 4-13. Gene expression analysis of ASCs and CSs on hybrid laminates. The level of expression of each target gene was normalized to GAPDH and calculated using the $2^{-\Delta\Delta CT}$ formula with reference to the negative control group, which is set to 1 and as indicated by the dotted lines in the figures. *p<0.05

For the Col II gene, LmCh ASC had a fold of 616.4 ± 516.2 as compared to its counterpart LmVi ASC (1.0 ± 0.5). LmCh CS on the other hand had a fold value of 9.6 ± 5.6 as compared to its undifferentiated counterpart LmVi CS (0.6 ± 0.4).

Similar trend was observed for the double-ply groups, where LmCh Co had a fold value of 4.6 ± 1.5 as compared to LmVi Co which did not exhibit any expression of the Col II gene.

4.4 Discussion

The AF is a difficult tissue to regenerate in part due to its complex architecture. Apart from having angled aligned fibres arranged in a concentric lamellae fashion, there is a gradual transition in ECM constituents and structure from the inner AF (mostly collagen Type II) to the outer AF (mostly collagen Type I). The overarching aim of this thesis is to TE an entire disc for whole disc replacement. Work in this phase is pertaining to the AF component of the TE disc and the aim is to mimic the anatomic form of the AF with the use of laminates that can be assembled to take the concentric form of the multi-lamellar AF in the native IVD. In addition, these laminates contain aligned nano-scale fibres fabricated using electrospinning to provide nanotopographical cues for alignment of ASCs seeded onto them. The roles of the nanofibres also include providing a "net" to prevent loss of ASCs during seeding, and for enhancement of mechanical strength. Concept for the latter has been reported in literature by Nerurkar and workers, who showed the role of shearing between aligned nanomats in opposing directions in reinforcing tensile properties of electrospun laminates (8). The use of chemical cues in addition to the topographical cues was also studied. In conjunction with the development of the rotational jig for collection of aligned electrospun fibres, a better approach in quantifying alignment of these fibres was also developed through the use of a Gaussian curve fitting and measurement of the corresponding fitted curve's FWHM values.

Results have shown that the hybrid laminates are non-toxic to the ASCs used. ASCs is chosen for use in this study due to its multipotentiality and ease of accessibility. The nano cues from the aligned electrospun mats were successful in influencing the

ASCs seeded to align along the topography created as shown in the randomness in F-actin detection on the random electrospun mats in Figure 4-**10** as compared to the aligned manner F-actin was detected on the aligned electrospun mats on the hybrid laminates in **Figure 4-11**. This is in line with literature where the correlation of cellular spreading and nano-fibre mat orientation have been demonstrated (136,148). The CS samples however, do not detect the topographical cues from the electrospun mats as showed by the well aligned but circular manner F-actin was detected in Figure 4-**10** on the random electrospun mats. The alignment is believed to have been caused by the tension formed within the ECM when the CS was cultured under hyperconfluence conditions in the circular shaped culture wells. That alignment remained with the CSs despite the presence of random nano-fibres, and proves that when cultured as CSs, the topographical cues are no longer relevant to the ASCs within the CSs. However, the value of having ASCs pre-cultured to form CSs remains important. Results from Figure 4-**8b** showed the collagen deposition of ASCs over a 28 day culture period, and demonstrated that even with a longer period of culture, the amount of ECM deposition of the ASCs at day 28 is less than what can be achieved by the CSs within 7 days. Given the importance of the ECM in holding the final 3D assembly of the TE disc together, and the tightly packed ECM of the native AF, the use of CS to form bulk of the construct's ECM in the later phases remains paramount, although an aligned fibre mat in those cases would not be needed.

When assessing the use of ASCs for its potential use as a cell-source for IAF and OAF TE in Phase 1, a micromass pellet culture approach was utilized. This do not reflect the manner of which ASCs or ASCs cell-sheets would take in the eventual TE strategy we are developing. Hence a gene expression study was carried out in the last stage of this Phase and results from **Figure 4-13** validates the applicability of ASC and ASC CS for use even when seeded on the hybrid laminates. The upregulation of

the Aggrecan (**Figure 4-13e**) and Col II (**Figure 4-13f**) genes in the LmCh ASCs and LmCh CSs samples over their non chondrogenically differentiated counterparts (LmVi ASCs and LmVi CSs) imply that cues from the hybrid laminates as a substrate is insufficient, and future AF applications of the hybrid laminates would either require the use of chemical cues (like those found in the chondrogenic differentiation medium) or utilizing a substitution of other stimulatory cues for chondrogenesis to take place. There are no known differentiation cocktails available in literature today that can differentiate cells into an AF phenotype, in part due to the complexities of the native AF tissue phenotype as covered earlier in the literature review section. However, the major constituents of the AF (Col I, Col II and Aggrecans) are largely common with those under chondrogenic differentiation. Hence chondrogenic differentiation was utilized in this study, and for some of the studies found in the subsequent phases.

Surprisingly, the LmCh Co samples do not exhibit gene expression values (Figure 4-**13**) that are in between those of only ASCs and CS samples (LmCh CS and LmCh ASC), even though it contains one piece of ASC seeded laminate and one piece of CS seeded laminate. This implies that the interrelationship between ASCs, CSs and those of the hybrid laminates is not as straightforward and much more complex. Factors such as nutrients diffusion, inter-lamellae interaction will need to be taken into account to have a better understanding. Correlating the Col I and Col II gene expression results of the LmCh ASC and LmCh CS samples with the results from the previous chapter (Figure 3-14 and Figure 3-15), an inconsistency between both sets of results can be observed. Such a discrepancy can be attributed to several reasons including: i) the difference between phenotypic and genotypic expressions due to gene expression kinetics, the involvement of epigenetics factors, and a possible feedback system present regulating gene expression, ii) the difference between 2D and 3D culture given that samples in the previous chapter were cultured as pellet

forms versus the 2D formats ASCs and CSs were cultured in this chapter, and iii) the effect of substrate stiffness brought about by the laminates. Hence in the next phases, the laminates will be assembled to take the final 3D form of the TE whole disc before gene expression assessment.

One of the most desirable attributes of silk for TE applications is its versatility to be processed into a wide variety of biomaterials (133). The use of silk in this study allows the fabrication of a scaffold that has several attributes with the use of a single material. These attributes are: i) a thin and flat scaffold that can be assembled to recapitulate the lamellar architecture of the native AF, ii) a superiority in mechanical strength as conferred by the knitted mat, and iii) allowing the introduction of topographical cues by means of electrospinning. Although mechanical testing was not conducted in this phase, the mechanical strength of knitted silk mats, fabricated in a similar manner, has been well reported in literature for ligament TE applications (136,210,211).

Extending the discussion on silk as the material of choice, the use of silk for AF TE has been reported in literature. Chang and colleagues reported seeding isolated AF cells on porous silk sponges (modified with RGD peptides) to study the ability of AF cells to attach to them for tissue formation (63,64). These sponges however, were not made with the intention to mimic the native architecture of the AF. Park and colleagues noted that in their work and reported an improved version of the silk sponges (95). The silk scaffolds Park et al reported were porous silk sponges with lamellar-like pores, with an inter-lamellar spacing of 150–250μm, thereby enabling the silk scaffold to be one step closer to the native AF. However, the native AF architecture was still not accurately recapitulated as the lamellar structures were not circumferentially orientated, as noted by Park and colleagues themselves. Nonetheless the scaffolds were favourable for AF cells adhesion and proliferation,

and was proven to be effective for AF-like tissue formation (95). Further to the discussion on scaffold architecture, the silk scaffolds reported by Bhattacharjee and colleagues were circumferentially oriented (98). However, the lamellar architecture created in the reported scaffolds were not truly laminates in a multi-ply fashion as what is in the native AF or reported by other groups using non-silk materials (8,70). Instead, silk threads (termed "silk fibres" in the paper) were coiled using a winding machine round a silk fibroin gel core to form the oriented AF component (98). Nonetheless, the chondroitin sulphate conjugated silk threads were effective in supporting alignment of the cell/matrix and chondrogenic redifferentiation of isolated chondrocytes, making it a viable candidate for AF TE (98). In this study, the hybrid laminates developed are capable of mimicking the lamellar architecture of the AF when assembled in a multi-ply format. In addition, the hybrid laminates also contain an aligned electrospun mat at the nanometer level that is capable of aligning ASCs seeded on to them.

The choice of cells is also a novel factor in this study. Isolated AF cells are typically used in AF TE studies (8,63,64,95,96). However its applicability for future clinical usage is limited due to several reasons: i) the difficulty in obtaining sufficient amount of AF cells, ii) lack of healthy AF cells in the already degenerated disc, and iii) increased patient morbidity if AF cells are harvested from neighbouring discs. Furthermore, AF cells are a heterogeneous mixture of phenotypes (212), but TE studies often disregard this feature and used them as a homogenous mixture. The use of ASCs and ASCs CSs allows for the choice of a easily accessed and highly abundant cell-source that is also multipotent in nature, and able to be induced to increase secretion of ECM easily with the use of Vit C.

The lynchpin role AF plays in an IVD TE strategy cannot be overemphasized. For example, the success of NP replacement strategies (such as those aiming to restore

the shock absorbing properties of the IVD) is contingent on the presence of a healthy AF to withstand the bulging forces (40). Increasingly, more studies have been focusing on the AF, and in the case of this thesis, the AF component is paramount to the eventual overarching strategy of creating a TE whole disc replacement. The next phase to be covered in the following chapter involves development of the NP component which will be incorporated with the AF hybrid laminates developed in this chapter to form the eventual 3D TE disc.

4.5 Concluding Remarks

In phase two, electrospun-knitted hybrid laminates that resemble the native architecture of the AF were successfully fabricated. The aligned electrospun layer conferred topographical cues, while the knitted silk lamellae serves as a reinforcement. As hypothesized, the responses of ASCs and ASC CSs were different on the hybrid silk laminates, with the ASC CSs being immune to the topographical cues from the electrospun mats. Nonetheless, the laminates were shown to be compliant with the ASCs and ASC CSs. To leverage on the rich ECM deposited by the ASC CSs to recreate the stratified architecture of the native AF, it was decided that ASC CSs would be used for the outer AF but without the electrospun layer, and ASCs would be used in conjunction with the hybrid laminates that have a layer of aligned electrospun fibres. The thin morphology of the knitted mats and hybrid laminates also enabled the recapitulation of the circumferentially aligned multi-ply architecture of the native AF to be achieved in assembly stage in phase four.

Chapter 5. Phase Three: Fabrication and Characterization of Silk/PVA Cryogels for Nucleus Pulposus Replacement

5.1 Introduction

Altering the properties of a well characterized NP replacement material (Eg. PVA (86,87,213)) to make it viable for cells, might bridge the gap between both NP regeneration and NP replacement approaches, and make it a good candidate for use as the NP component of a TE IVD. PVA possesses pendant hydroxyl groups which enable the ease of cross-linking using physical or chemical approaches (214). Various studies have also attempted to functionalize PVA with different materials to improve its cellular attachment abilities. These include fibronectin (215), cell-adhesive peptide RGDS (216) and poly lactic acid (PLA) (217); or by mixing PVA with another polymer which acts also as a chemical cross-linking agent (Eg. polyester polyurethane (PU)) (218).

Only a handful of studies have reported combining silk with PVA. The studies with the closest similarity to this study would the ones by Li and co-workers (219,220), which show that under different freeze-thaw (physical) cross-linking conditions, silk/PVA cryogels with varying pore diameters and mechanical strengths are obtained - indicating the versatility of freeze-thawed silk/PVA as a material with controllable and tunable properties for different purposes. Li and co-workers, however, have not assessed cellular attachment abilities of the silk/PVA cryogels.

To the best of our knowledge, there are no studies in literature today that have reported the cellular attachment abilities of physically cross-linked silk/PVA cryogels and the subsequent consequence in its mechanical properties as a cell-seeded gel. In this study, we aim to characterize silk/PVA cryogels fabricated by a physical (freeze-thaw) crosslinking regime to determine an optimal condition for cellular attachment.

Specifically, the effect of silk in the silk/PVA cryogels on some properties relating to cellular attachment and proliferation are investigated (Eg. hydrophobicity/hydrophilicity and porosity). Proliferation of rabbit adipose-derived mesenchymal stem cells (rASCs) in these silk/PVA cryogels is subsequently assessed and mechanical assessments pertaining specifically for NP replacement purposes are investigated (Eg. hoop stress and compressive modulus). It is hypothesized that the incorporation of silk with PVA will improve cell attachment and proliferation abilities, and hence allows the resultant composite (silk/PVA) cryogel to be a better tissue engineered NP replacement candidate.

5.2 Materials and Methods

There were three major stages in this phase. The first stage consists of cryogel fabrication and characterization based on four physical properties, namely water content (%), swelling capability (%), rehydration capability (%), and mass loss (%). Suitable silk/PVA blend formulations were then selected based on these four properties to be carried on to the second stage, where the hydrophilicity/hydrophobicity and porosity characteristics were investigated using surface contact angle analysis and scanning electron microscopy (SEM) respectively. The most optimal silk/PVA formulation was then selected for the third and last stage of the study where rASCs were seeded into the cryogels and cultured for up to 7 days before being sacrificed for DNA content quantification and mechanical analysis.

5.2.1 Stage One: Cryogel Fabrication and Physical Characterization

5% (wt/vol) PVA (Sigma Aldrich) polymer solutions of two molecular weight (Mw) ranges (Low Mw: 89,000 - 98,000; High Mw: ~130,000) were obtained by dissolving PVA powder in distilled water (dH_2O) according to published protocols (221,222).

Silk fibroin (SF) solution was prepared as described in section 4.22. 5% SF solution (wt/vol) was blended with 5% (wt/vol) PVA solutions (low Mw and high Mw) at the following silk:PVA volume ratios: 0:100, 10:90, 20:80, 30:70, 40:60, 50:50, 60:40 and 70:30 to investigate the effect of silk and PVA Mw on the physical properties of the composite silk/PVA cryogels. 48-well culture plates were used as molds with a total volume of 1ml of the silk/PVA blend added per well. A 72hr freeze-thaw regime adapted from published PVA cryogels fabrication protocols (86,219,220) was carried out to physically cross-link the silk/PVA blends to form cryogels. The regime consists of two rounds of -80^{o}C freezing (12hrs) using an ultra-low temperature freezer and room temperature thawing (12hrs), followed by 6 rounds of -20^{o}C freezing (2hrs) and 20^{o}C thawing (2hrs) using the automated temperature controlling capabilities of a freeze dryer (Epsilon 1-4, Martin Christ).

Freshly fabricated cryogels were removed from their molds and immediately weighed to obtain their original cryogel weight (M_o). A portion of the cryogels were then lyophilized in a freeze dryer (Epsilon 1-4, Martin Christ) and weighed immediately after lyophilization to obtain the freeze dried cryogel weight (M_{fd}). The freeze dried cryogels were then soaked in phosphate buffered solution (PBS) at 37^{o}C for up to 21 days. At days 1, 2, 3, 5, 7, 11, 14 and 21, the cryogels were weighed to obtain the weight of the originally freeze dried cryogel after x days in PBS (M_x). The remaining of the cryogels that were not lyophilized were placed in PBS at 37^{o}C for up to 21 days and at days 1, 2, 3, 5, 7, 11, 14 and 21, the cryogels were weighed to obtain the weight of the non freeze-dried cryogel after x days in PBS (M_{nx}). The percentage water content of the cryogels fabricated were tabulation as per equation (1), while the ability of the cryogels to absorb liquid back into itself is determined by the percentage swelling ratio as tabulated by equation (2). It was observed that although the cryogels reabsorbed liquid after lyophilization, they do not absorb to the extent of returning to its original freshly fabricated weight. As such, the percentage rehydration capability

captures this behavior in equation (3). The cryogels although physically cross-linked, still demonstrated mass loss behavior after being soaked in PBS and as such the percentage mass loss was tabulated as shown in equation (4).

$$\% \text{ Water Content} = \frac{M_o - M_{fd}}{M_o} \times 100 \quad (1)$$

$$\% \text{ Swelling Ratio} = \frac{M_x}{M_{fd}} \times 100 \quad (2)$$

$$\% \text{ Rehydration Capability} = \frac{M_x}{M_o} \times 100 \quad (3)$$

$$\% \text{ Mass Loss} = \frac{M_o - Mn_x}{M_o} \times 100 \quad (4)$$

M_o: Original cryogel weight

M_{fd}: Freeze dried cryogel weight

M_x: Weight of freeze-dried cryogel after x days in PBS

Mn_x: Weight of non freeze-dried cryogel after x days in PBS

5.2.2 Stage Two: Surface Contact Angle and Surface Porosity

Cryogels were lyophilized immediately after fabrication for surface contact angle and SEM imaging purposes. Surface contact angle was conducted using a VCA Optima machine (AST Products Inc, Billerica, MA, USA) on flattened sections of the cryogels. 20µl of dH_2O was dropped onto each sample, and all images were captured 30secs after the droplet of dH_2O made contact with the surface. SEM was conducted using a scanning electron microscope (JSM-561; JEOL) to study the cross-sectional morphologies of the lyophilized silk/PVA cryogels. Cross-sectional surfaces were obtained by quick freezing the cryogels in liquid nitrogen, before fracturing them with a scalpel blade while in the frozen state. Sections of interests were then mounted onto SEM studs and gold sputtered before imaging at 10kV. Surface porosity was then quantified from the SEM images with ImageJ (NIH) and OriginPro9 (OriginLab, Northampton, MA, USA) using a methodology as previously described in published literature (223). SEM images were taken from cryogel triplicates for each silk/PVA formulation of interest for porosity quantification purposes.

5.2.3 Stage Three: Cell Seeding and Mechanical Testing

a. Cell-Seeding

rASCs were isolated from the fat pads New Zealand white rabbits and processed as previously described in section 3.2. Cell cultures were all conducted in complete medium consisting of low-glucose DMEM (Invitrogen) supplemented with 10% FBS and 1% P/S and maintained in a humidified 5% CO_2 incubator at 37^{o}C. Cryogels were freeze-dried, sectioned into halves and sterilized by an Anprolene Ethylene Oxide Gas Sterilizer System (Cole Parmer, Vernon Hills, IL, USA) according to the manufacturer's protocol prior to cell-seeding. $0.5x10^6$ cells were suspended in 100µl of complete medium and seeded into each gel by injection with a hypodermic needle. Cell-seeded cryogels were maintained in complete medium with medium changes every 2 to 3 days till sacrificial time points at days 1, 3 and 7 for DNA quantification and day 7 for mechanical testing.

b. DNA Quantification

At assessment time points days 1,3 and 7, culture medium was aspirated and cell-seeded cryogels were washed once with PBS. Any excess PBS and medium were removed completely, and samples were quickly placed in a -80^{o}C freezer to be frozen overnight. Frozen samples were then transferred to a freeze dryer (Epsilon 1-4, Christ Martin) and lyophilized under manual drying mode. Sterilized surgical scissors were used to cut the lyophilized cryogels into smaller pieces to aid in the subsequent digestion step. Lysis buffer consisting of 0.1mg/ml proteinase K (Sigma Aldrich) in 1x Tris-EDTA buffer (Sigma Aldrich) were added to each sample, vortexed and incubated at 37^{o}C for 4hrs. Cell lysates were then kept frozen at -80^{o}C and thawed for DNA quantification when needed. DNA quantification was carried out with a Quant-iT™ PicoGreen® dsDNA Kit (Molecular Probes, Invitrogen). PicoGreen is a fluorescent nucleic acid stain that binds specifically to double stranded DNA

(dsDNA). Upon binding, samples can be excited at a wavelength of 480 nm and fluorescence intensity measured at an emission of 520nm. The amount of dsDNA present can be correlated with the intensity of fluorescence in a sample as determined by a standard spectrofluorometer. DNA standards provided with the kit were used to plot a standard curve from which the DNA content of the cryogels were quantified. All fluorescence measurements were conducted using a FLUOstar Optima fluorescence plate reader (BMG Lab Technologies).

c. Mechanical Testing

Uniaxial mechanical testing was conducted using an Instron 3345 machine (Instron, Norwood, MA, USA), with a 100N load cell and at a pre-load of 0.1N. A compression rate of 2mm/min was chosen, in line with a previously published study on PVA cryogels intended as IVD substitutes by Wang and Campbell (86), and also similar to typical mechanical compression studies in literature that are related to the spine (224,225). Mechanical testing of cell-seeded and non cell-seeded silk/PVA cryogels was conducted to investigate the consequence of having cells within the silk/PVA cryogels on its mechanical properties. Cell-seeded cryogels were seeded with rASCs as mentioned previously and all cell-seeded and non cell-seeded cyrogels were cultured in complete medium for 7 days at 37^{o}C in a humidified CO_2 incubator. Samples were then removed from the incubator and tested fresh at the Instron machine. The Instron machine was fixed with a flat metal platen, and samples were compressed between two flat impervious glass surfaces under an unconfined condition. Parameters studied include the compressive modulus and swelling pressure (hoop stress) at 15% to 45% amount of axial strain.

Raw data was recorded by the Bluehill (Instron) software, plotted into a stress-strain curve and best fitted using a fourth order polynomial equation using MS Office Excel (Microsoft Inc). The instantaneous compressive modulus at a particular axial strain

was then obtained by substituting the desired strain value into the differential of the fourth order polynomial equation. To obtain the hoop stress (σ_θ) at a particular compressive axial strain, the generalized Hooke's law was used:

$$\varepsilon_\theta = \frac{1}{\mathrm{E}}[\sigma_\theta - \upsilon(\sigma_r + \sigma_a)] \quad (5) \qquad \text{where} \qquad \upsilon = -\frac{\varepsilon_\theta}{\varepsilon_a} \quad (6)$$

E: Young's Modulus ν: Poisson's ratio ε: Strain σ: Stress

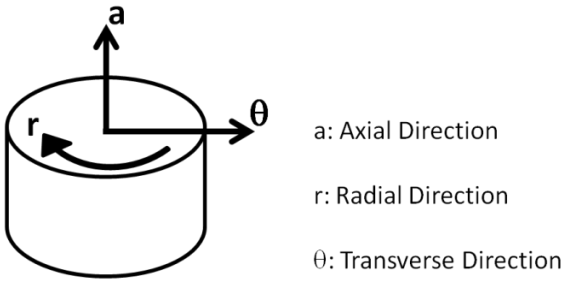

Figure 5-1. Illustration on axial, radial and transverse orientations defined for this study.

We assume σ_r to be 0, σ_a is obtained from the raw data recorded by the Instron machine and E is the instantaneous compressive modulus which was tabulated as per earlier mentioned. Samples were also video-imaged by a high resolution camera (Olympus, Tokyo, Japan) before and while undergoing compression. The width of the silk/PVA disc before and during compression was captured by the camera and measured using open source software FIJI (205). The transverse strain (ε_θ) at a particular axial strain value (ε_a) was tabulated by taking the ratio of the change in width during compression (at the instant of that axial strain value) over the original width of the disc. The Poisson's ratio was then calculated using equation (6).

5.2.4 Statistical Analysis

Pairwise comparisons were determined using a two-tailed unpaired Student's t-test and performed using Excel Analysis ToolPak (Microsoft Inc.). Statistical analysis involving multiple comparisons were conducted with a one-way analysis of variance

(ANOVA) test and post-hoc Tukey correction using OriginPro9 (OriginLab). $p<0.05$ was taken as significant and all data are expressed as means ± standard deviation.

5.3 Results

5.3.1 Stage One: Physical Characterization

a. Water Content

Cryogels have water content of more than 90% across all groups regardless of silk:PVA ratios and PVA Mw. The group with the highest amount of water (93.9 ± 0.4%) had 20% of silk and 80% of low Mw PVA in the blend. There was no significant difference in the water content of high Mw groups regardless of the amount silk added. However, significantly higher water content was observed in the low Mw groups with 0% to 40% silk content over those with more than 50% of silk (**Figure 5-2**). Although the low Mw cryogels generally have a slightly higher water content than its high Mw counterparts, the difference is insignificant given that the maximum difference do not exceed 1%.

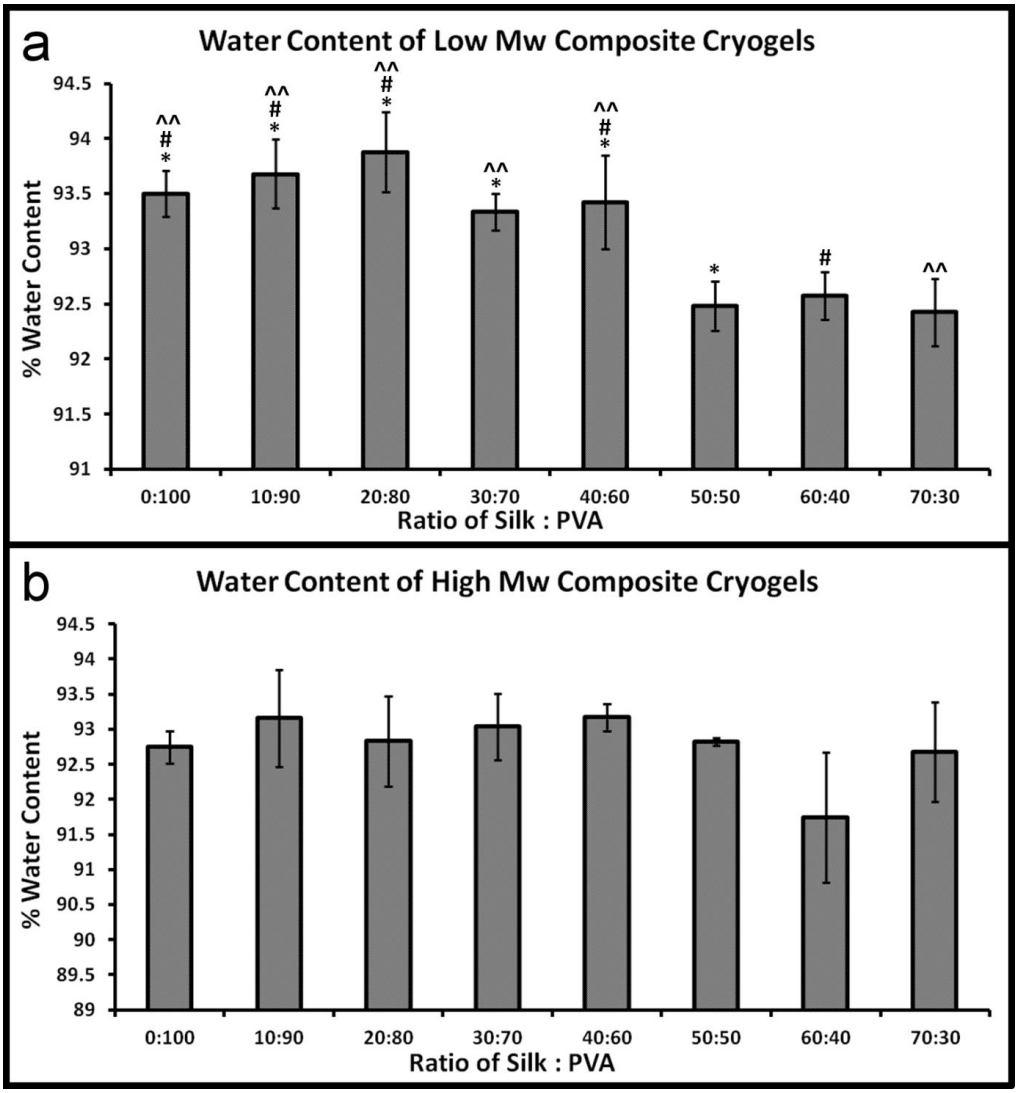

Figure 5-2. Percentage water content of silk:PVA cryogels consisting of (a) Low Mw PVA and (b) High Mw PVA. Significantly higher water content was observed for low Mw PVA cryogels with 0% to 40% silk content over their counterparts with 50% (*$p<0.05$), 60% (#$p<0.05$) and 70% (^^$p<0.05$) of silk.

b. Swelling Ratio and Rehydration Capability

10% to 50% of silk in the low Mw and 10 to 30% of silk in the high Mw silk/PVA blends resulted in composite cryogels that swelled more than 10 times (>1000%) of its original dry weight (**Figure 5-3**) and rehydrated to at least 70% of its original wet weight (**Figure 5-4**) over a 21 day period. In contrast, pure PVA cryogels with no silk added displayed a much lower tendency to swell (low Mw: 784.0 $\pm$ 264.1%; high Mw: 416.1 $\pm$ 19.6%) and a much diminished ability to rehydrate back to its original

freshly fabricated weight (low Mw: 50.6 ± 15.7%; High Mw: 30.2 ± 0.5%) before freeze-drying. All cryogels showed a high initial rate of increment within the first day of soaking, indicating the ability of the cryogels to quickly absorb back water into itself. The low Mw cryogels generally have a better swelling ratio than the high Mw counterparts, indicating a better ability to take in water. This is in line with the water content results showed in **Figure 5-2**.

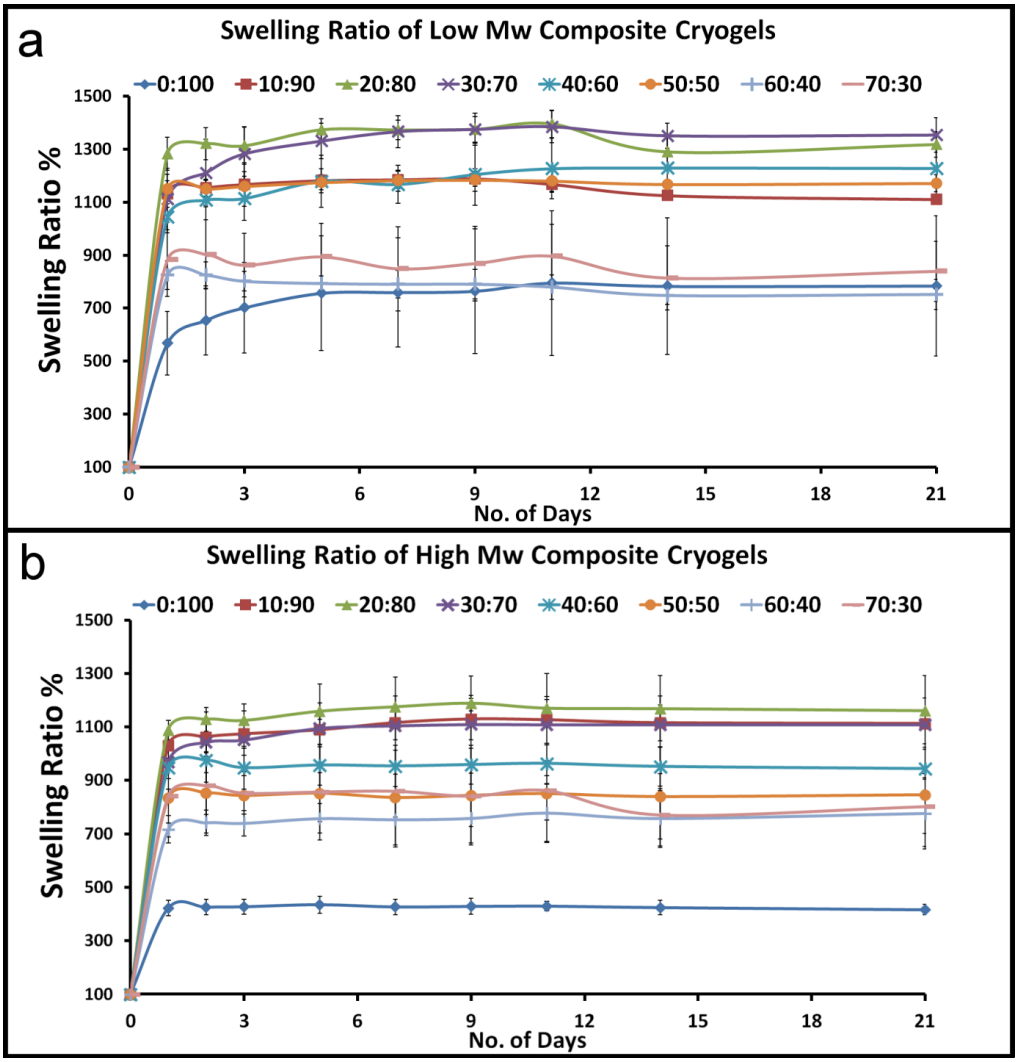

Figure 5-3. Swelling ratios of silk:PVA cryogels consisting of (a) low Mw PVA and (b) high Mw PVA over a period of 21 days. Swelling ratio was determined as a weight percentage ratio of soaked cryogels over its original freeze-dried weight at d0.

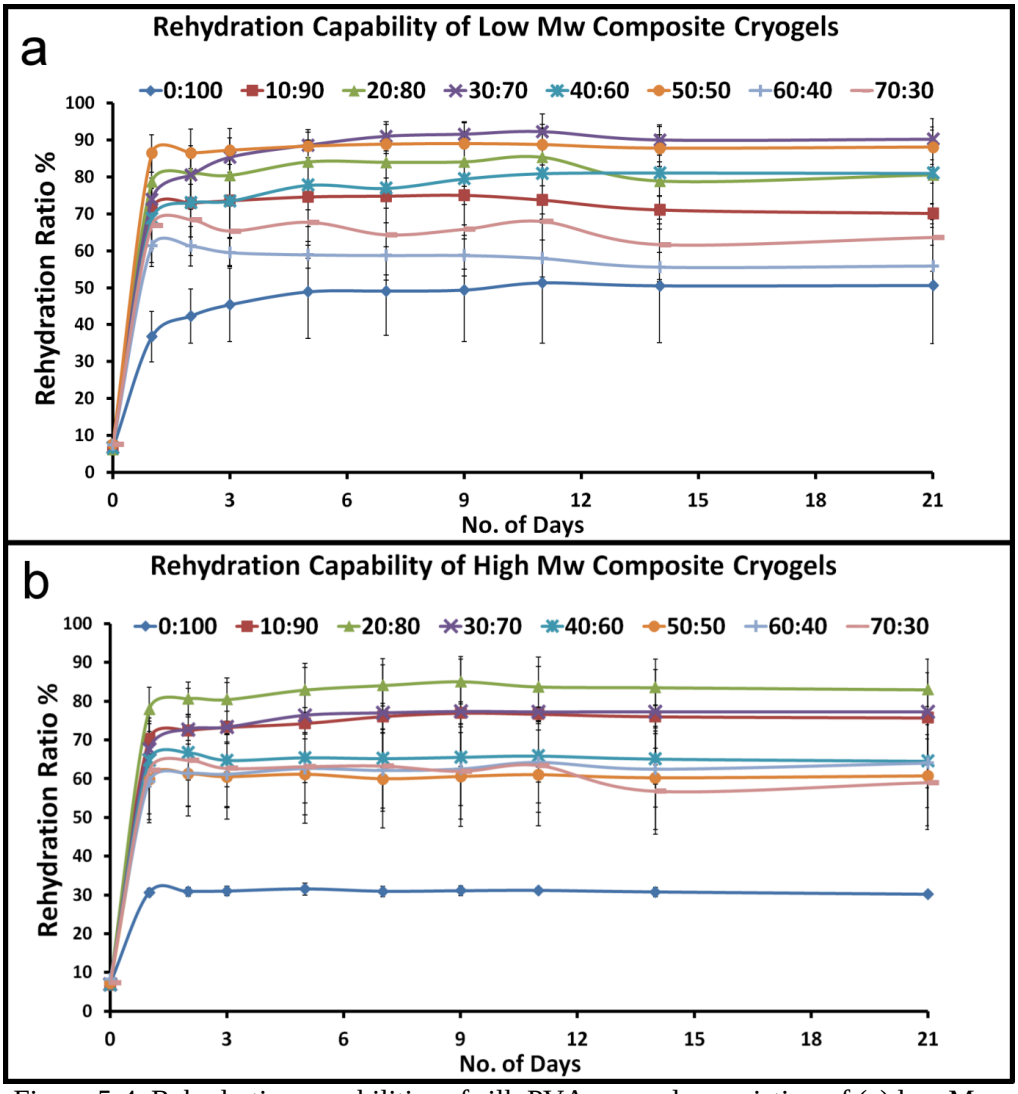

Figure 5-4. Rehydration capabilities of silk:PVA cryogels consisting of (a) low Mw PVA and (b) high Mw PVA over a period of 21 days. Rehydration ratio was determined as a weight percentage ratio of soaked cryogels over its original (freshly fabricated) weight prior to freeze drying.

c. Mass Loss Profile

Mass loss was documented as a reduction in weight of the gels after a certain amount of time in PBS at 37°C. From **Figure 5-5** it was observed that over a 14-day period, controlled mass loss rates (less than 10% weight loss) was displayed in composite cryogels with 20% to 40% of silk in the low Mw group (6.7 ± 9.3%, 7.7 ± 1.4% and 9.1 ± 5.0% for 20:80, 30:70 and 40:60 silk:PVA cryogels respectively) and 20% to 30% of silk in the high Mw group (9.3 ± 4.7% and 10.0 ± 4.0% for 20:80 and 30:70 silk:PVA cryogels respectively). Negative values can be observed in **Figure 5-5a**

for groups with 20%, 50% and 70% silk. This is because cryogels in these groups were not yet saturated with water after the fabrication process, and still had capacity to absorb PBS into itself.

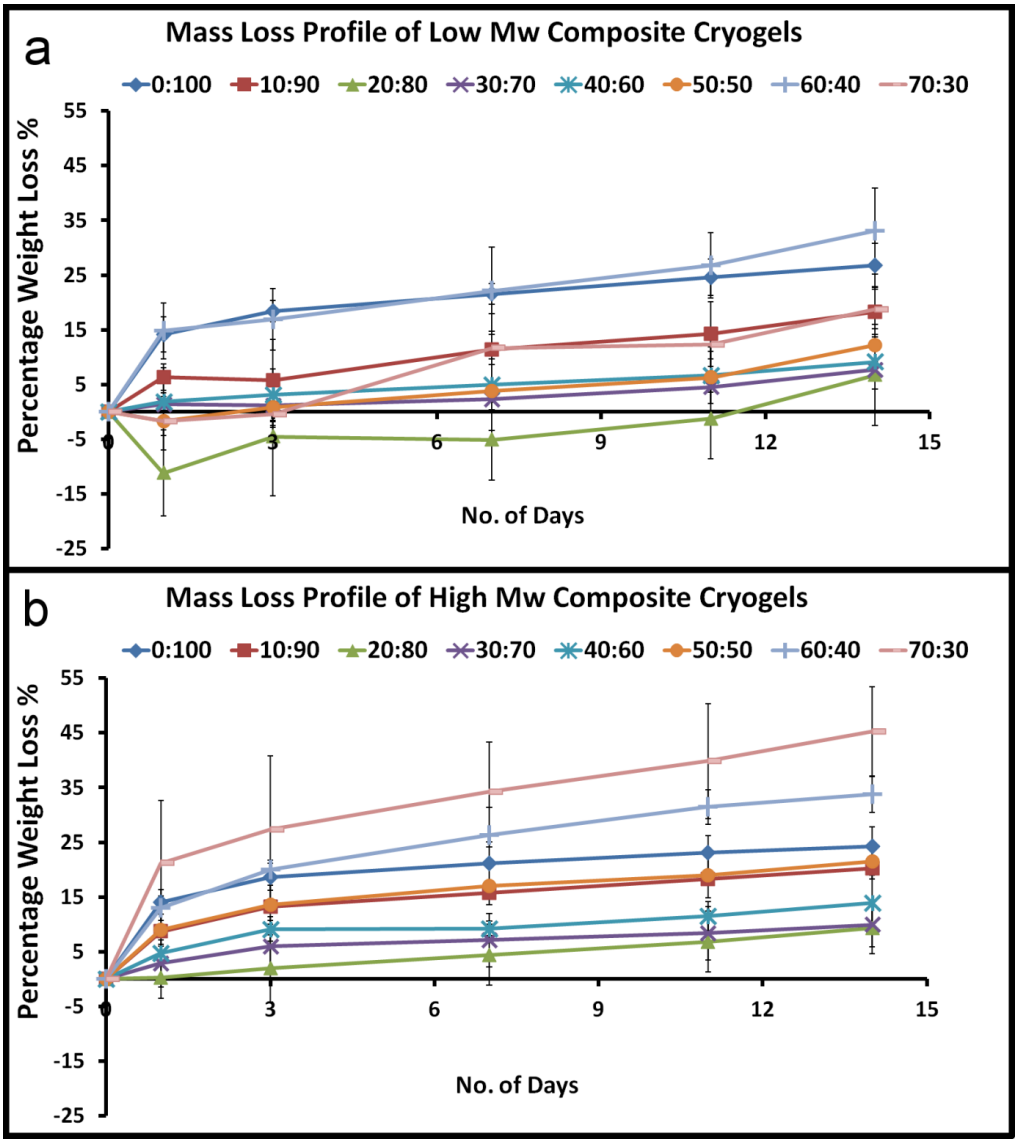

Figure 5-5. Degradation profile of silk:PVA cryogels consisting of (a) low Mw PVA and (b) high Mw PVA over a period of 14 days. Freshly fabricated cryogels were soaked directly in PBS at 37^{o}C, percentage weight loss of the cryogels was tabulated by the difference in weight of the cryogels at the respective time points over its original (freshly fabricated) weight.

Table 2 summarises the physical characterization properties in the first stage of the study. Some of the desired properties of the composite cryogels are i) a high water content to mimic the physiological state of the NP, ii) good swelling and rehydration

ratios to enable the gel to perform the load bearing and cushioning roles of the NP as mentioned in the introduction, and iii) a controlled mass loss profile to allow time for tissue regeneration upon implantation during future clinical application. The latter potentially can either take the form of a cellular penetration from the neighbouring vascular rich subchondral end-plates or a proliferation and extracellular matrix growth from seeded cells within the cryogels (Eg. NP cells, stem cells). Groups were then selected (20 to 40% of silk and 20 to 30% of silk for the low Mw and high Mw groups respectively) based on these criteria for the subsequent stages of the study. Controls were included (0% silk, low and high Mw PVA) for comparison purposes.

Table 2. Summary of Properties Exhibited in First Stage of Study

Low Molecular Weight Groups	Silk:PVA							
Selection Criteria[a]	0:100	10:90	20:80	30:70	40:60	50:50	60:40	70:30
1. Water Content (>90%)	*	*	*	*	*	*	*	*
2. Swelling Ratio (>10x)		*	*	*	*	*		
3. Rehydration Ratio (>70%)		*	*	*	*	*		
4. Mass Loss (<10%)			*	*	*			
High Molecular Weight Groups	Silk:PVA							
Selection Criteria[a]	0:100	10:90	20:80	30:70	40:60	50:50	60:40	70:30
1. Water Content (>90%)	*	*	*	*	*	*	*	*
2. Swelling Ratio (>10x)		*	*	*				
3. Rehydration Ratio (>70%)		*	*	*				
4. Mass Loss (<10%)			*	*				

[a]Based on results from Figures 2 to 5. * indicates group met selection criteria.

5.3.2. Stage Two: Hydrophilicity/Hydrophobicity and Porosity

a. Surface Contact Angle

A larger surface contact angle correlates with a more hydrophobic surface. Adding silk significantly improved the surface hydrophobicity of both the low Mw and high Mw composite cryogels (**Figure 5-6**). An increment in surface hydrophobicity was observed with increasing amount of silk added. In the low Mw groups, 20:80, 30:70 and 40:60 silk:PVA cryogels have surface contact angles of 77.5 ± 8.1^{o}, 85.7 ± 5.2^{o} and 99.8 ± 10.9^{o} respectively as compared with the control PVA cryogel group with no silk added (62.1 ± 8.2^{o}). In the high Mw groups, 20:80 and 30:70 silk:PVA

cryogels have surface contact angles of 94.7 ± 5.6^{o} and 104.3 ± 9.6^{o} respectively as compared with the control PVA cryogel group with no silk added (56.3 ± 6.9^{o}).

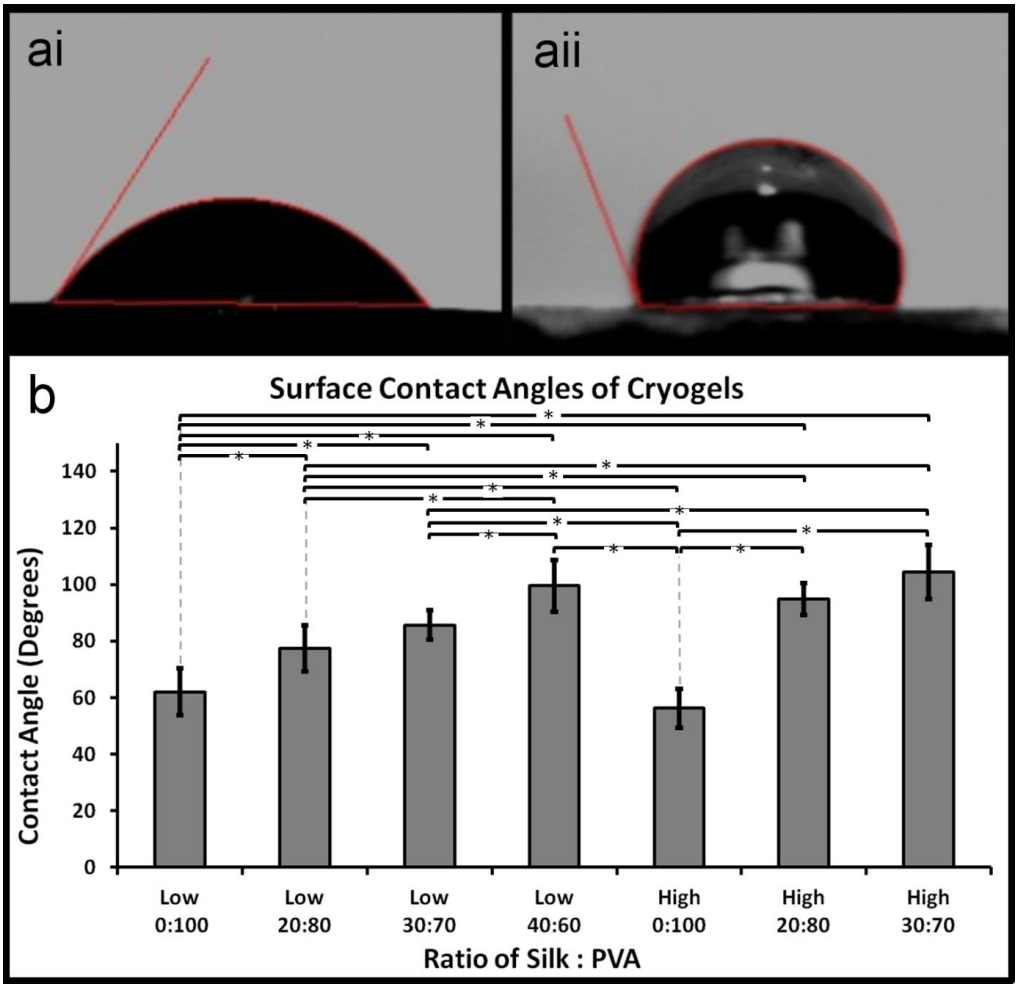

Figure 5-6. Typical contact angle images of cryogels with (ai) hydrophilic surface and (aii) hydrophobic surface. (b) Surface contact angles of silk:PVA cryogels consisting of low Mw ("Low") PVA and high Mw ("High") PVA. Adding silk to both low Mw and high Mw PVA resulted in an improvement to surface hydrophobicity. *p<0.05.

b. Scanning Electron Microscopy (SEM) and Surface Porosity

SEM images of the cross-sectional surface of the cryogels showed the 3D network structure of the cryogels. Uniform porous morphology was observed for all groups investigated, with pores being interconnected as well (**Figure 5-7a**). Pure PVA groups have slightly more regular pore shapes, but the overall size of the pores remain relatively the same, independent of the presence of silk. Quantitative analysis revealed a decrement in surface porosity of the cross-sections with the addition of silk

in the high Mw groups in particular. The highest surface porosity was in the high Mw control group, with no silk added (0:100) at 45.8 ± 5.4%, and adding 30% silk to the blend resulted in a significant drop in surface porosity to 29.3 ± 3.0% (**Figure 5-7b**).

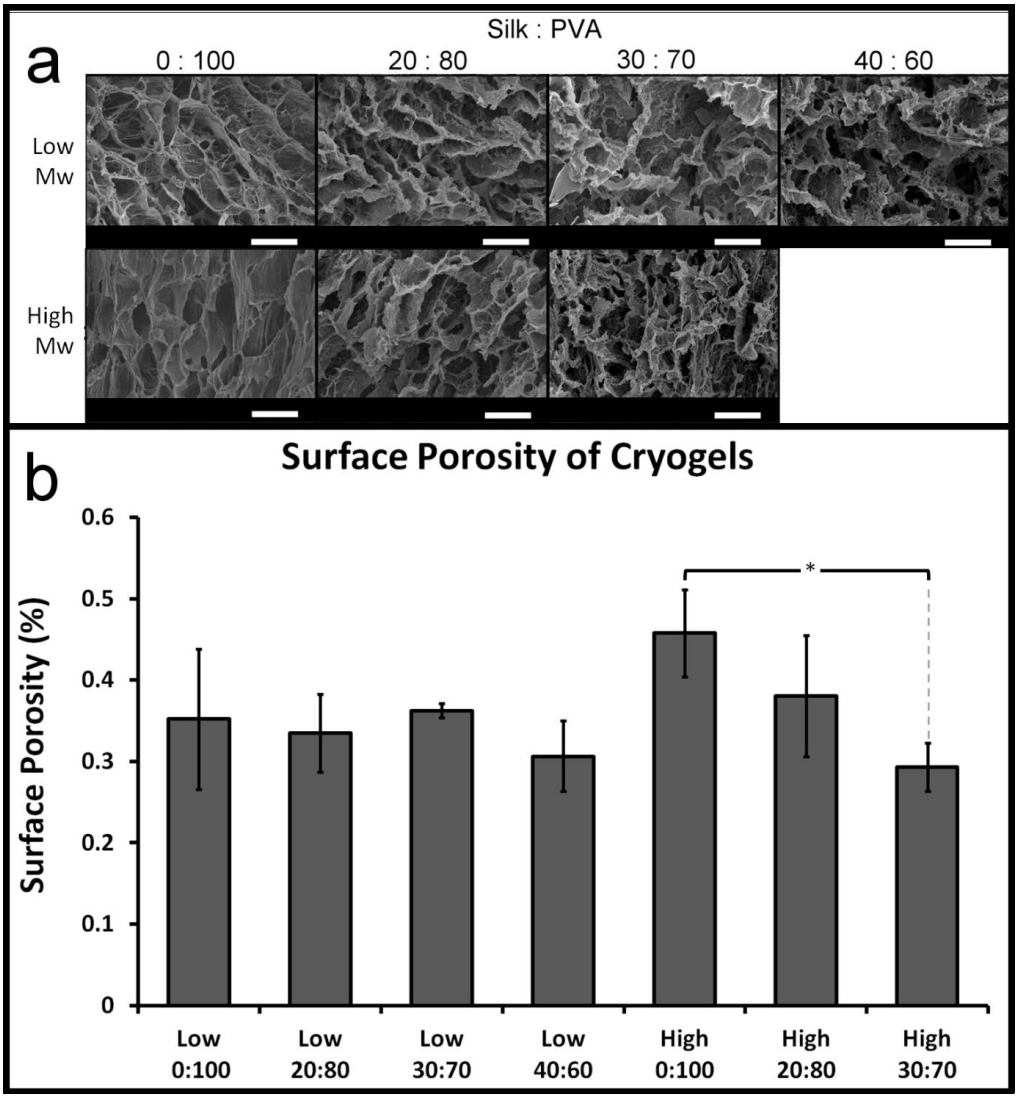

Figure 5-7. (a) SEM images of silk:PVA cryogels consisting of low Mw and high Mw PVA and (b) Estimated surface porosity calculated based on SEM images. *p<0.05. Scale bar: 50μm.

It was hypothesized that having a more hydrophobic surface would improve cellular attachment to the PVA based cryogels, while a more porous cross-sectional surface would imply better penetration of cells and better diffusion of nutrients. Hence a larger surface contact angle was desired which can be achieved by choosing a silk/PVA blend with higher silk content (**Figure 5-6**). However, as this would result

in a lower surface porosity (**Figure 5-7b**), a ranking system was developed (**Table 3**) to determine the optimal silk/PVA blend and best PVA Mw choice for stage three.

Table 3. Ranking Based on Hydrophobicity and Surface Porosity

	Low Molecular Weight			High Molecular Weight	
	Silk:PVA			Silk:PVA	
	20:80	30:70	40:60	20:80	30:70
Surface Porosity[a]	3	2	4	1	5
Contact Angle[b]	5	4	2	3	1
Total Score[c]	8	6	6	4	6

[a] A larger surface porosity is desired - the group with the highest porosity is ranked 1.
[b] Higher contact angles are desired - the group with the highest contact angle is ranked 1.
[c] The group with the lowest score is deemed to possess optimal balance of both characteristics.

5.3.3. Stage Three: Cellular Characterization and Mechanical Testing

From **Table 3**, the group with the lowest score (high Mw PVA with 20% silk) was considered the best candidate for stage three of the study.

a. DNA Quantification for rASCs Proliferation

Controls with no silk added (low Mw and high Mw) and the corresponding group (20% silk) with low Mw PVA were also seeded with cells for comparison purposes. From **Figure 5-8**, it can be seen that the selected group (high Mw PVA with 20% silk) displayed a significantly higher amount of DNA in the samples over 7 days of culture (Day 1: 5406 $\pm$ 778 ng. ; Day 3: 6616 $\pm$ 628 ng and Day 7: 4841 $\pm$ 651 ng) over the other three controls. This validated the hypothesis and indicated an improvement in the cell attachment and cell hosting abilities of the composite cryogel (high Mw 20% silk) over the controls.

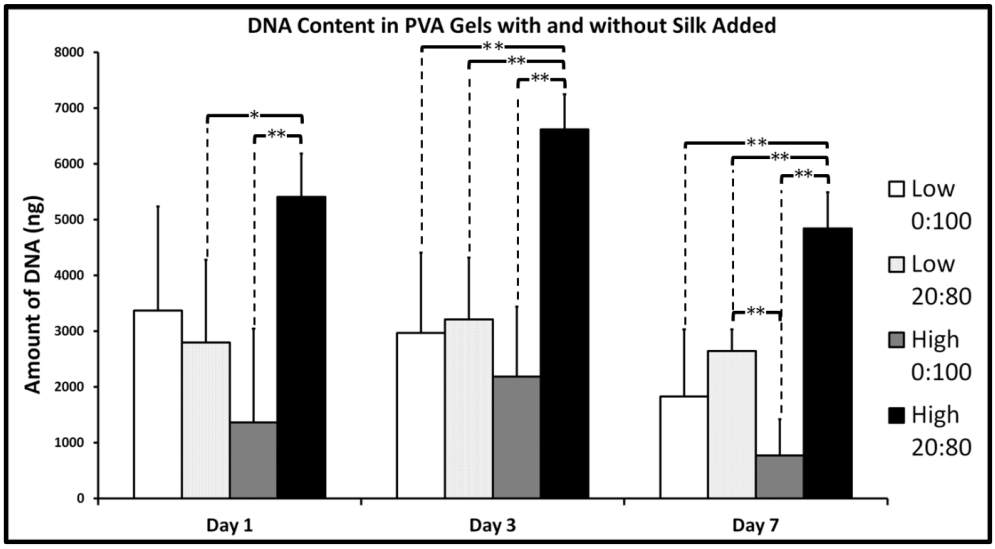

Figure 5-8. Amount of DNA content per cryogel sample quantified by PicoGreen assay. Ratios are indicated as silk:PVA. Groups consisting of low Mw PVA are indicated by "Low", while groups consisting of high Mw PVA are indicated by "High". **p<0.01; *p<0.05.

b. Mechanical Testing

The presence of cells significantly improved mechanical properties of the cryogels, as shown by the significant increment in compressive modulus and (swelling pressure) hoop stresses in the cell-seeded cryogels (high Mw, 20% silk) over their non-cell-seeded counterparts (**Figure 5-9** and **Figure 5-10** respectively). The compressive Young's modulus of the cell-seeded cryogels increased from 15% axial strain (0.229$\pm$ 0.067 MPa) to a maximum at 25% axial strain (0.348 $\pm$ 0.113 MPa), before decreasing thereafter with further increment in axial strain to 0.147 $\pm$ 0.029 MPa at 45% axial strain. Hoop stresses in the cell-seed cryogels (high Mw, 20% silk) increases with the amount of axial strain, attaining a maximum value of 0.0893 $\pm$ 0.029 MPa at 45% axial strain. Data from existing literature suggests that the deformation of the human IVD under loading or standing conditions corresponds approximately to strain values of 20% to 25% (86)**.** At 20% axial strain value, the compressive modulus and hoop stress is 0.335 $\pm$ 0.109 MPa and 0.025 $\pm$ 0.010 MPa respectively. At 25% axial strain, the compressive modulus and hoop stress is 0.348 $\pm$ 0.113 MPa and 0.040 $\pm$ 0.015 MPa respectively.

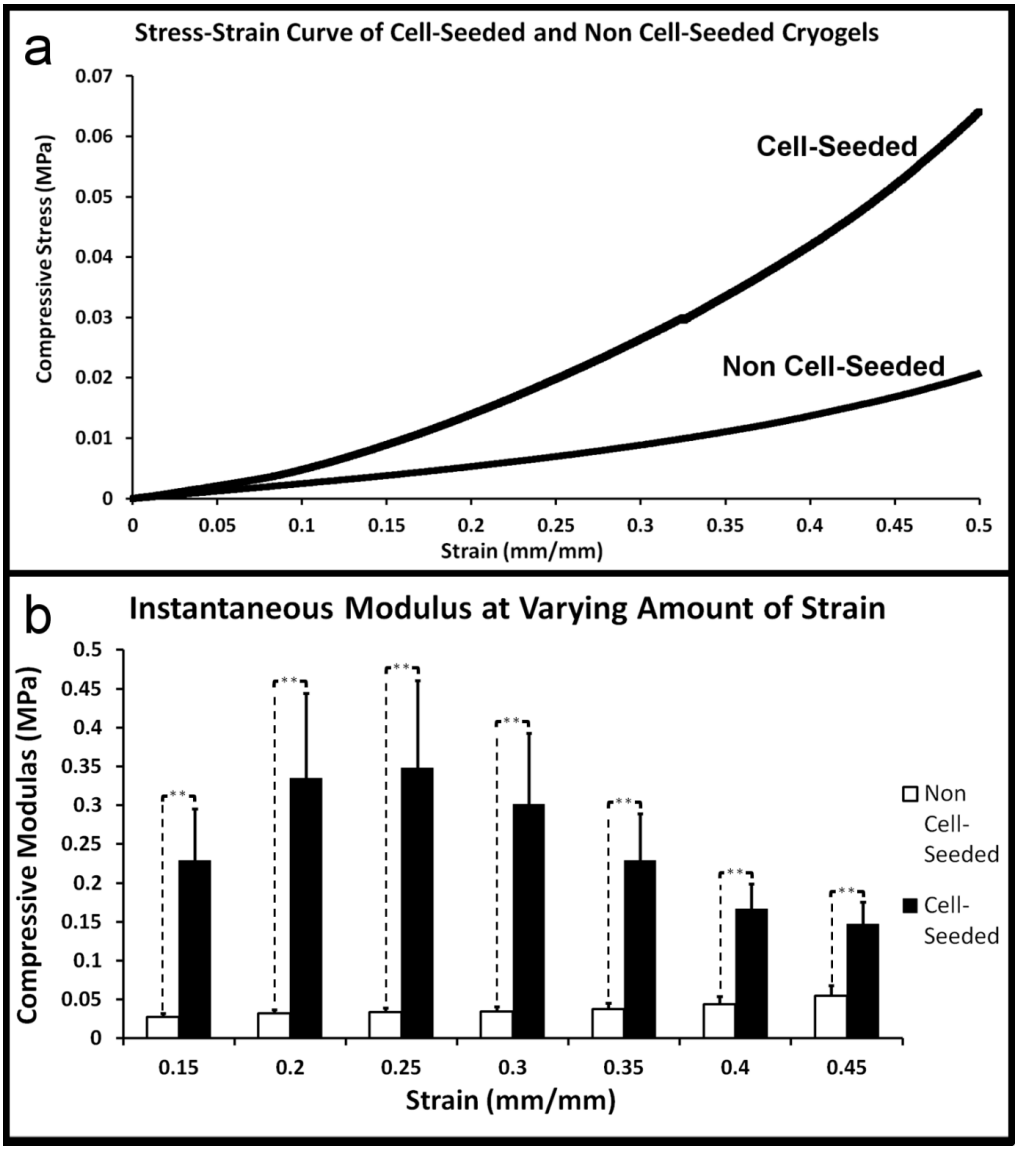

Figure 5-9. (a) Typical stress-strain curves of cell-seeded and non cell-seeded cryogels consisting of high Mw PVA with 20% silk content displaying hyperelastic responses. (b) Tangential compressive modulus of non cell-seeded and cell-seeded cryogels consisting of high Mw PVA with 20% silk content at different amounts of strain. **$p<0.01$; *$p<0.05$.

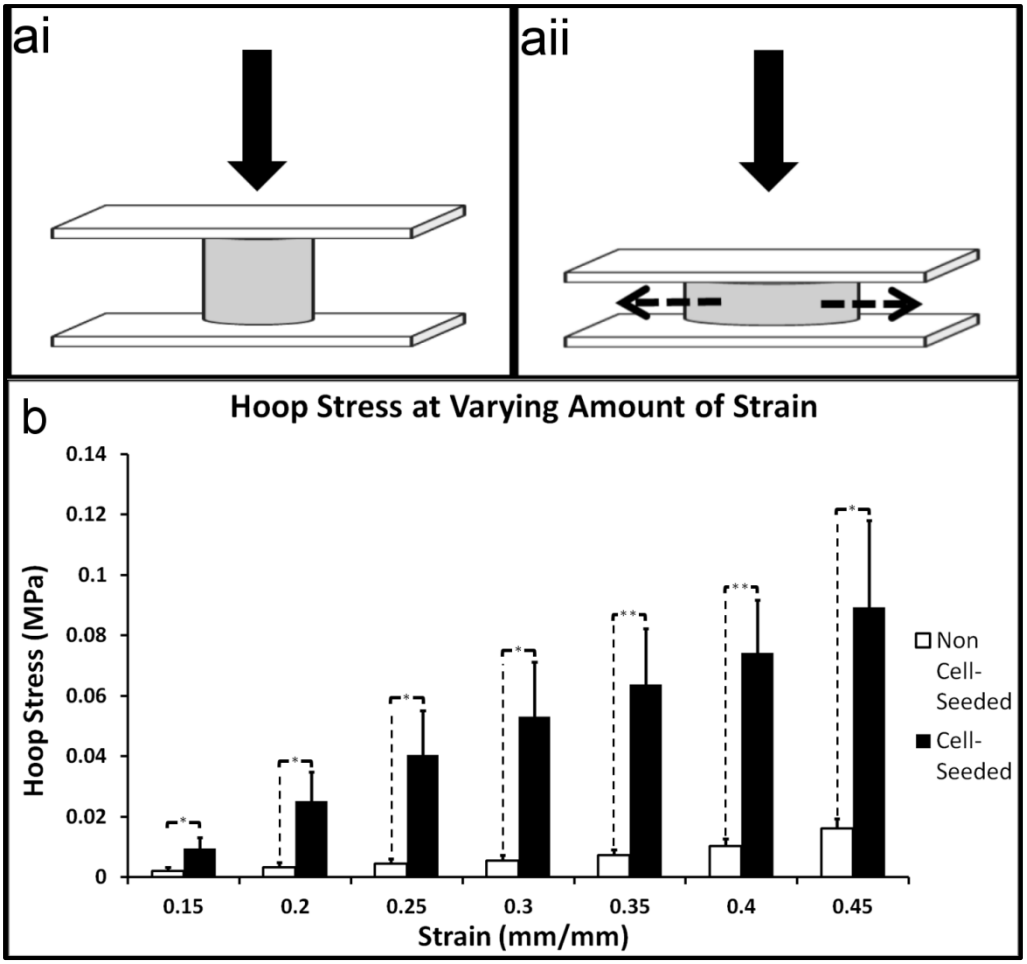

Figure 5-10. (a) Illustration of a cryogel sample at the start of compression testing (i) and while undergoing compression (ii). (b) Hoop stress values of non cell-seeded and cell-seeded cryogels consisting of high Mw PVA with 20% silk content at different amounts of strain. **p<0.01; *p<0.05.

5.4 Discussion

The use of repeated freezing-thawing to crosslink PVA had been reported in literature from as far back as the 1980s and early 1990s (226). Among the various reported methods used to cross-link PVA, physical crosslinking by repeated freeze-thawing has several advantages over the chemical approaches. In addition to the absence of toxic crosslinking reagents, freeze-thawed gels tend to be stronger that those which are chemically cross-linked (227,228). During the freezing and thawing process, physical cross-linking takes place by the formation of crystallites and the three-dimensional structure of these crystallites allow distribution of mechanical loads, hence giving rise to better mechanical strength and higher elasticity (226,228).

Although highly elastic and stronger, PVA by itself has low success rates in cellular adhesion - in part due to its hydrophilic nature. This is well documented in literature, and various strategies have been undertaken over the years to overcome this shortcoming by introducing a more hydrophobic component into the PVA gels, or by attaching proteins like fibronectin to promote cellular adhesion (215,216,218). Adhesion of cells precedes many processes (Eg. cellular migration) and determines the eventual proliferation of cells on or inside a scaffold/material. From Figure 5-**8**, it can be seen from the day 1 results that rASCs attached much better to the more hydrophobic composite silk/PVA gels (high Mw 20% silk) than the controls with either no silk added (low and high Mw 0% silk) or using low Mw PVA (low Mw 20% silk). The effect of an improved attachment in day 1 is carried over to the next two assessment time points at day 3 and day 7, whereby a significantly higher amount of DNA content was detected in the high Mw 20% silk group over the others. Interestingly, although a hydrophobic surface is more favorable for cellular attachment than a hydrophilic one, cell adhesion do not necessarily improve with increasing hydrophobicity - research has shown that cells adhere to polymeric surfaces of intermediate water wettability, and beyond a certain water contact angle, the percentage of adherent cells would actually decrease (229). From Figure 5-**6**, the water contact angles of the selected group for cell-seeding (high Mw 20% silk: 94.7± 5.6^{o}) and its corresponding control with no silk added (high Mw 0% silk: 56.3 ± 6.9^{o}) are in line with the consolidated data by Saltzman and Kyriakides (229) that estimated the highest percentage of adherent cells occur on polymeric surfaces with water-in-air contact angles of 70^{o} to 90^{o}.

Correlating the surface contact angle results with the mass loss profile results in Figure 5-**5**, a higher surface hydrophobicity most probably resulted in a more controlled mass loss profile that was observed in the low Mw silk:PVA cryogels

(20% to 40% silk) and high Mw silk:PVA cryogels (20% to 30% silk) over their respective controls with no silk added. Being significantly more water "repellent" than the pure PVA cryogels could potentially have prevented the interference of water molecules within the physical cross-linked network of the composite cryogels. Results in Figure 5-**5** also showed that within the groups of silk-doped composite cryogels, those made from low Mw PVA generally displayed a lower mass loss profile than their high Mw counterparts. The amount and extent of interaction of silk with the PVA chains is believed to be one of the factors responsible for such an observation. In line with literature, the amount of mass loss is also dependent on the amount of un-crosslinked PVA chains (230), hence the low Mw composite cryogels might be more stable because of better interaction of the silk with the lower Mw chains, thereby resulting in a better cross-linked network, and more controlled mass loss profile.

The low Mw cryogels generally had higher swelling ratios and water content than the high Mw cryogels. This is probably due to the shorter PVA chains in the low Mw groups rendering cryogels which are less stiff and able to swell to take in more water molecules. Such a definitive trend was however not clearly exhibited with the rehydration capability results in Figure 5-**4**. However, looking at the rehydration capability results in Figure 5-**4** and comparing it with the mass loss profiles observed in Figure 5-**5**, a converse relationship between both parameters can be generally observed. It is believed that a better rehydration capability would indicate a higher extent of cross-linking, which would therefore result in a more controlled (and lesser) mass loss. This is in line with work done by Liu and co-workers, using PVA and a range of natural macromolecules, where they correlated a higher reswelling ratio of the composite PVA gels with a larger extent of cross-linking between the PVA chains and the macromolecules (230).

In this study, silk fibroin solution was blended with PVA solution and freeze-thawed to form cryogels. Li and co-workers adopted the same fabrication approach in their studies (219,220). However, they did not report on the same physical and cellular assessments as those conducted in this study. There exist in literature today several other fabrication approaches which have incorporated silk with PVA. These include the one by Kundu and co-workers, which reported a photocrosslinked silk/PVA drug delivery hydrogel by functionalizing PVA with methacrylate groups (231). In the study, Kundu and co-workers reported an initial high rate of mass loss in all the hydrogels, similar to the trend observed in some of the groups in Figure 5-**5** of this study (low Mw: 0% and 60% silk; high Mw: 0%, 10% 50%, 60% and 70% silk). Such an observation was attributed to the release of the sol fraction, containing any PVA chains and silk fibroin which were not covalently bonded with the rest of the structural network (231). A slower rate of mass loss observed in the same study by Kundu et al was attributed to the slower diffusion speed of the heavy silk fibroin chains out of the gel network (231) - silk fibroin consists of a light chain of approximately 26kDa and a heavy chain of approximately 390kDa (131). From Figure 5-**5**, we also observed a slower rate of mass loss (from day 1 to day 14) after a high initial rate of mass loss at day 1. Although Kundu and co-workers reported a percentage mass loss increment in all the hydrogels with silk added (231), such a definitive trend was not observed in this study, as shown by results in Figure 5-**5**. The improvement in swelling ratios with the addition of silk that was reported by Kundu et al (231), was however corroborated by results observed in Figure 5-**3** of this study.

Other fabrication approaches which have incorporated silk with PVA also include the recent study by Zhang et al (232) which described the physical characterization of a composite PVA cryogel consisting of nano-hydroxyapatite and silk, fabricated using a repeated freeze-thaw approach. However, differing from this study, the silk

incorporated were micro-sized silk fibre threads. Similarly, Luo and co-workers mixed dried silk solution powder (consisting of nano-sized silk peptides) with PVA solutions (233) and fabricated films from the blends by water evaporation. Tsukada and co-workers also used a similar casting approach for their films after blending silk solution with PVA (234). The only study among these described that conducted a cell-on-material assessment reported better cellular adhesion with the silk-added groups - Luo et al reported an improvement in cellular adhesion and an increment in cell proliferation with increasing content of the nano silk pepetides in the blend films (233). This is similar to results from this study as shown in Figure 5-**8**, despite having different fabrication approaches. Luo et al however conducted tensile testing instead of compression testing, and hence mechanical testing data could not be compared. Unfortunately, as the photocrosslinked silk/PVA hydrogel reported by Kundu et al (231) was meant as a macromolecular drug delivery system, no mechanical assessments was conducted and cellular assessment was conducted as an hydrogel-extract cytotoxicity test on plated cells instead.

The pendant hydroxyl groups present in PVA makes it easy to blend various other materials with it. Apart from those already mentioned with silk, researchers have also blended other natural macromolecules with PVA. This include chitosan, gelatin, starch and agarose (230,235). In particular, researchers working with chitosan/PVA hydrogels reported an increment in cell attachment and cell growth of fibroblasts with increasing chitosan content (236). This mirrors the findings discussed in the preceding paragraph with silk and PVA.

NP cells are typically used in injectable NP hydrogel studies, however researchers have been studying the use of ASCs for IVD regeneration in recent years (189). Although the specific cues to differentiate ASCs into NP cells in vitro are not well developed at present, the idea of injecting ASCs into a degenerated NP for

regeneration purposes have been heavily explored (189). Researchers have been studying the effects of NP cells or the microenvironment of the NP on ASCs in the form of co-culture systems. Yang and co-workers demonstrated a significant increment in proteoglycan and collagen type II production by ASCs (transduced with the Sox-9 gene with a retroviral vector) after co-culturing them with mature NP cells (190). Similarly, Lu et al showed in a micromass co-culture system that soluble factors secreted by NP cells had a positive effect in directing ASCs towards a NP-like phenotype (191); while Choi et al demonstrated the importance of the quality of the NP cells in influencing ASCs micromass co-cultures towards a NP-like lineage (192).

Mechanical testing results from Figure 5-**9** and Figure 5-**10** showed that the cell-seeded cryogels had significantly higher compressive modulus and hoop stresses values over the non cell-seeded ones, despite having the exact constituents and being cultured in exactly the same environment. Such a phenomenon is in line with literature. Talukdar and co-workers demonstrated the importance of cell-seeding in the eventual mechanical characteristics of 3D silk sponges (237), and found that cell-seeded sponges with the highest density of cells had compressive stiffness and modulus 4 to 5 times that of non cell-seeded ones. A similar phenomenon was also mentioned by Chou et al between the cellular and acellular alginate hydrogels used in a NP replacement related study (73,74). Such a phenomenon can be attributed to a few possibilities: i) the presence of cells and the secreted ECM improving material properties, and ii) a better retaining of water molecules (and hence osmotic pressure) within the network, thereby improving overall turgidity of the hydrogels.

The high proteoglycan and water content of the native NP dictates its mechanical performance in load dissipation while conferring flexibility to the spine (238). Many studies in literature today have adopted a hydrogel approach to develop tissue engineered NPs, and have attempted to compare the compressive properties of the

tissue engineered constructs with native benchmarks (73,77). For example, Chou et al described a photocrosslinked alginate hydrogel with encapsulated NP cells that displayed equilibrium Young's modulus (under unconfined compression testing) of approximately 4.3kPa 8 weeks after implantation in a subcutaneous murine model (73); while Cloyd et al reported an equilibrium Young's modulus of 5.4 kPa for excised human NP tissue under unconfined compression testing and in the same study reported Young's modulus values of 7-22 kPa for a few hyaluronic acid based NP replacement hydrogels (77). Although the tissue engineered NPs showed compressive modulus values comparable to the native human NP tissue (5.4 kPa), it must be noted that the overall mechanical strength of the IVD is much higher, in part due to the strong restraining nature of the surrounding AF as the NP absorb and releases water in a diurnal fashion.

As pointed out by Nerurkar et al (90), in an in vivo situation, the lateral expansion and fluid flow of the NP (during compression) is restricted by the surrounding AF, and thus confined compression should be the key testing benchmark for tissue engineering strategies for the NP. A study by Johannessen and Elliot in 2005 showed that the swelling pressure in excised human NP tissues under confined compression was 0.138 MPa (239). Glover et al in the early 1990s showed using an osmometer that the swelling pressure of the NP of a porcine and canine model was approximately 0.05MPa and 0.23MPa respectively (240). A summarized literature review by Iatridis et al indicated that the swelling pressure of the NP can range from 0.05 MPa to 3MPa (241), while a recent study by Reitmaier and co-workers found that the intradiscal pressure in vivo was between 0.5 to 0.75MPa after inserting a piezoresistant pressure sensor into the intervertebral discs of sheeps (82). Promisingly, the hoop stresses values reported in this study (Figure 5-**9** and Figure 5-**10**) fall within the approximate ranges of these reported values.

5.5 Concluding Remarks

In phase three, results showed the addition of silk to PVA improves not only the cell-hosting abilities of the cryogels as hypothesized, but it also improves the cryogels' physical characteristics (Eg. water content, rehydration ratio, compressive modulus, hoop stress). Analogous to the highly negative proteoglycan content of the native NP, the similarly highly negative PVA allows for water to be imbibed into the silk/PVA croyogels to form a swollen network. The swelling of the NP is a lynchpin to the overarching strategy of this thesis, whereby the pressure from this swelling is translated to circumferential tension and radial compression forces on the surrounding TE AF from phase 2 in the final de novo disc assembly. A high Mw silk/PVA blend consisting of 20% silk was identified as the ideal candidate as a highly cellular compliant NP replacement. The next phase involves the assembling of both NP and AF components to form the eventual 3D IVD assembly and to assess the 3D assembly in a customized bioreactor developed.

Chapter 6. Phase Four: Assembly and Evaluation of Multimodal De Novo IVD Construct with Real-time Monitoring Compression Loading Bioreactor

As briefly mentioned in Chapter 4, epifluorescence imaging assessment of the hybrid laminates was interfered by the strong autofluorescence signals exhibited by the knitted silk mats. Work from Chapter 4 indicated that although the autofluorescence issue was mild using confocal imaging (with the use of lasers), and was within threshold-able limits, it was rather severe in epifluorescence-based assessments - immunostained proteins of interests (Eg. Col I) residing directly on the autofluorescing knitted silk threads could not be clearly distinguished. The de novo construct that will be assembled in this chapter will be made with multiple layers of the knitted silk mats. Hence, pivotal to the eventual successful imaging assessment of the de novo IVD construct is an effective modulation of the autofluorescence signals from silk using Sudan Black as an autofluorescence quencher. The entire experimental study conducted in this regard can be found in Appendix F. Work described in Appendix F showed that a SB treatment of 15mins is sufficient to effectively suppress the autofluorescence signals from silk-based materials (Eg. electrospun mats and silk threads) used in the assembly of the de novo IVD construct, thereby improving fluorescence imaging assessment.

6.1 Phase 4(a): Assembly and Evaluation of De Novo IVD Construct

6.1.1 Introduction

Whole disc TE strategies in literature typically utilize a biphasic approach in creating the TE disc. As mentioned in the earlier literature section (section 2.5.3), some of these biphasic approaches include the use of a PCL electrospun mat as the AF, and a agarose hydrogel as the NP (8,67,70), or the use of PGA/PLA as the AF and an alginate hydrogel as the NP (7,91). The approach undertaken in this dissertation utilizes a combination of electrospun-knitted hybrid laminates and knitted lamellar mats to recapitulate the inner and outer AF respectively, while a silk/PVA cryogel

forms the NP component. The lamellar form of the TE AF in this study is similar to that described by Nerurkar and colleagues (8,70), and enables a true reconstruction of the circumferentially oriented multi-ply lamellae architecture of the native AF. This is in contrast to some of the TE whole discs described in literature, including those by Park and colleagues (95), and Bhattacherjee and colleagues (97,98). Both groups had used silk to form oriented scaffolds, but were short of recreating the circumferential orientation of the native AF as mentioned earlier in the discussion section under chapter 4 (section 4.4). Development of the NP component is covered in the preceding chapter, and is a novel concept in the area of whole disc TE. As mentioned in various parts of the dissertation thus far, strategies such as gel injectables to replenish the NP volume would only be clinically successful with an intact AF. Applying this concept to the area of whole disc TE, similarly if typical hydrogels are utilized for the NP component of the TE whole disc, the TE AF will have to be robust enough to retain the NP gels filled within in order for such a TE disc to be clinically relevant. This is however, a huge challenge in TE, given that cells require time to produce ECM, and for the engineered tissue to mature to be mechanically robust. Hence, the idea of the silk/PVA NP component was derived from NP replacement strategies such as polymeric prostheses (Eg. PDN), which could be modified to be cellular compliant. This draws on the advantage of a mechanically robust starting scaffold material to hold up the TE disc, while having a modified material that is cell compliant to allow for infiltration of cells from the neighbouring vertebral bodies or from the surrounding AF.

To recap, at the end of phase 2 (Chapter 4), a hybrid laminate was developed that is capable of influencing ASCs to align along the oriented nano electrospun fibres. ASC CSs were however insensitive to the nano topographical cues, but nonetheless are important as an effective means to generate ECM (Col I). In phase 3 (Chapter 5), silk/PVA cryogels containing 20% silk were shown to be the most cellular compliant,

while being able to exhibit promising mechanical properties that are relevant to its role as the NP component of a TE de novo disc (Eg. compressive modulus, hoop stress). The objectives of section 6.1 are therefore, i) to assemble a de novo IVD construct using the TE AF and NP components from phase 2 and phase 3 respectively, ii) to study the effect of a 3D assembly on ASCs and ASC CSs responses, and iii) to evaluate the de novo construct's suitability as an IVD replacement.

6.1.2 Materials and Methods

a. Assembly of Experimental Groups

Hybrid laminates containing an aligned electrospun layer incorporated with a thin knitted silk mat were fabricated as described in section 4.2.2.c. Thin knitted silk mats with no electrospun layer were also prepared as results from chapter 4 demonstrated that ASC CS do not require the use of the electrospun layer. Silk/PVA cryogels containing 20% silk were prepared as described in section 5.2.1. All the hybrid laminates, knitted mats and silk/PVA cryogels were sterilized by an Anprolene Ethylene Oxide Gas Sterilizer System (Cole Parmer) according to the manufacturer's protocol prior to cell-seeding. ASCs were isolated from New Zealand white rabbits as described in section 3, and P3 to P4 ASCs were used in this phase. ASCs were seeded onto the hybrid laminates at a density of $3x10^5/cm^2$, while in line with work done in earlier chapters, one week old ASC CSs were used in this phase. ASC CSs were made as described in chapter 4.2.4. Briefly, ASCs were first seeded at a density of $3x10^5$ cells/cm^2 on commercially available thermosensitive culture plates (CellSeed Inc, Tokyo, Japan), and cultured in medium supplemented with 50 μg/ml ascorbic acid (Vit C, Wako) for one week before detachment to be incorporated with the knitted silk mats (no electrospun layer). Silk/PVA cryogels had no cells seeded into them.

Error! Reference source not found. shows the assembling steps for the 3D de novo disc. Silk/PVA cryogels were kept dry as the cell-seeded AF components were swiss-rolled around it. The de novo disc is then held together by a knitted silk cuff (Figure 6-**1d**), to prevent the AF lamellae from unraveling. Figure 6-**1e** shows the completed de novo disc with the silk cuff. Upon contact with culture medium, the silk/PVA cryogel (now partially wet, due to the culture medium retained on the AF scaffolds) would imbibe more culture medium and swell to create a tight fit between the swiss-rolled de novo disc and the silk cuff (Figure 6-**1f**).

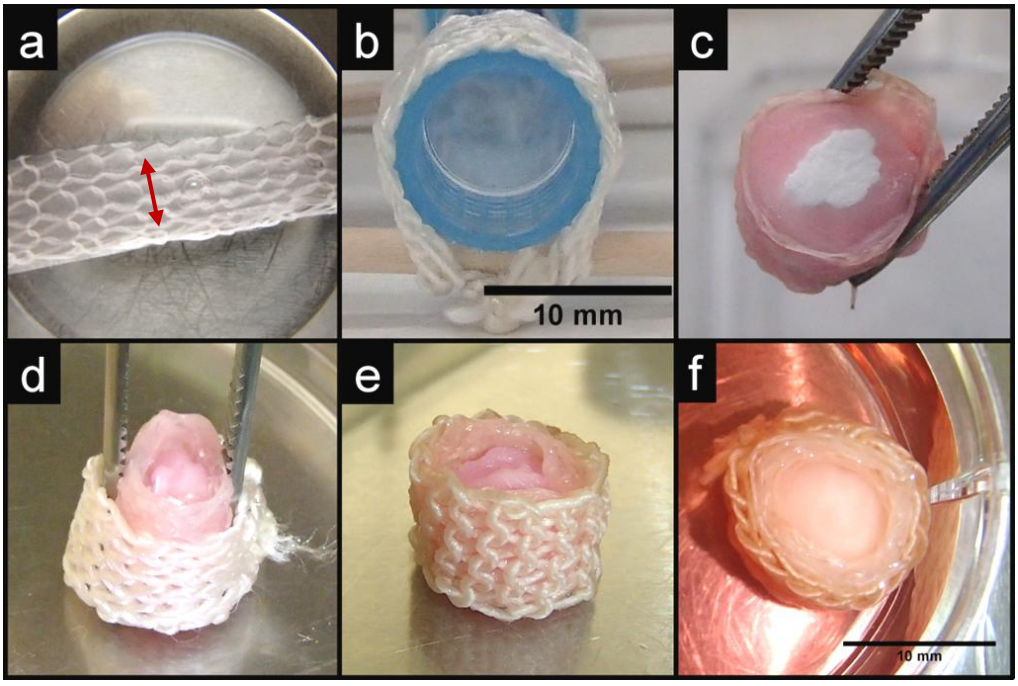

Figure 6-1. Assembling process of de novo disc showing (a) cell seeding on laminates (red arrow indicates electrospun fibre aligned direction), (b preparation of silk cuffs, (c) a completed swiss-rolled disc, (d) the subsequent fitting of disc into a cuff, to form (e) the completed de novo disc, and (f) allowing of silk/PVA cryogel in culture medium to create tight fit of disc in cuff.

The completed de novo disc consists of a cylindrical silk/PVA cryogel which was first rolled with two pieces of ASCs seeded hybrid laminates 3cm in length, followed by four pieces of CSs seeded knitted mats 3cm in length (hereafter termed "3D") (Figure 6-**2a**). This results in the completed disc having approximately 9 to 10 concentric layers of lamellae. In addition, results from phase 2 indicate that the

relationships between ASCs, CS and the scaffolds are complex. Hence, to study the effects of a 3D environment on the ASCs and CSs, two other types of assemblies were created (Figure 6-**2b**) using only 2 pieces of laminates, containing either only ASCs (hereafter termed "3D ASC") or CSs (hereafter termed "3D CS").

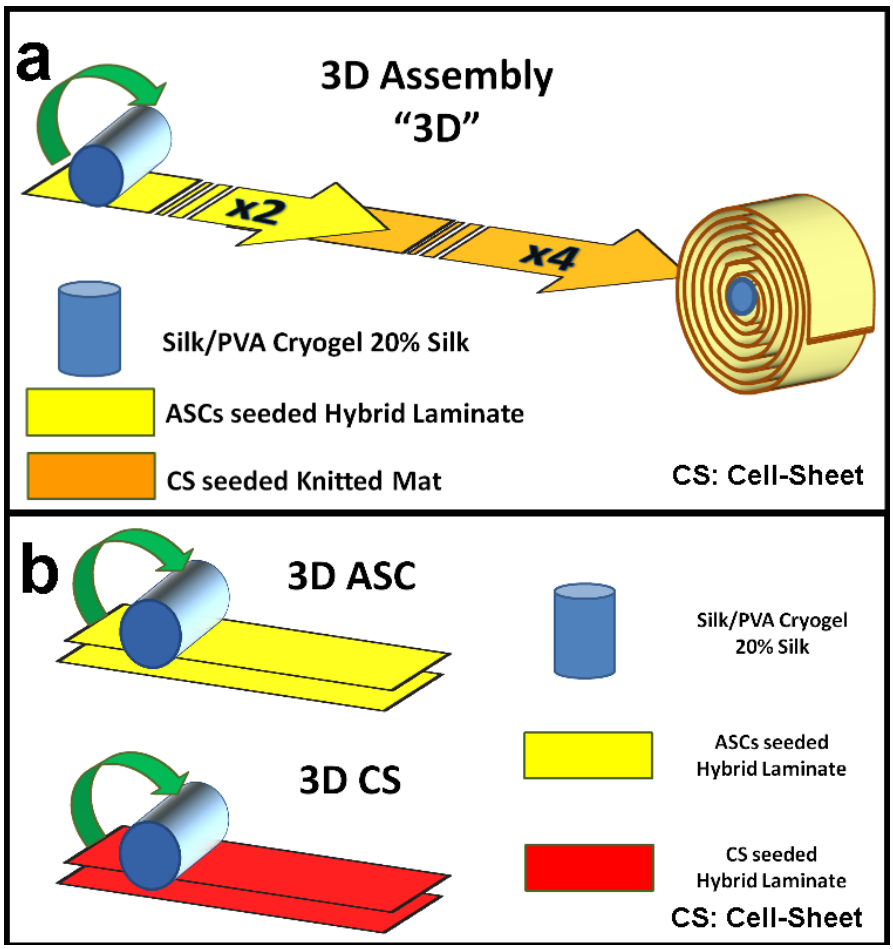

Figure 6-2. Experimental groups created for phase 4. (a) completed de novo disc and (b) additional groups set up to investigate effect of 3D assembling.

Gene expression results from chapter 4 indicated that without the presence of biochemical cues from the chondrogenic medium, there was almost an absence of gene expression of the target genes of interest (Eg. Col II, Agg etc). Hence, as a preliminary investigation on the assembled discs, chondrogenic medium was used for all samples. Chondrogenic medium contained 1% ITS+ (BD Biosciences), 100nM dexamethasone (Sigma), 50ug/ml Vit C (Wako), 10ng/ml TGF-ß3 (RayBiotech Inc) and 10ng/ml BMP-6 (R&D Systems). 3D samples were labeled as "3D Chon". 3D

ASC and 3D CS samples were labeled as “3D Chon ASC” and “3D Chon CS” accordingly.

b. Gene Expression Analysis of 3D Disc

To understand the effect of assembling on the overall gene expression of the ASCs and ASC CSs, 3D Chon samples were cultured for 2 weeks before being sacrificed for gene expression analysis by RT-PCR. RNA extraction and cDNA synthesis were conducted as described in section 3.2.2d, PCR analysis was carried out as described in section 3.2.2e. The genes of interests were those investigated in chapter 4 (section 4.2.8a), namely: Sox 9, Col I, Col II, Decorin, Biglycan, and Aggrecan. Expression levels of the target genes were normalized to the respective sample’s GAPDH gene and then tabulated with respect to a negative control group consisting of ASCs directly seeded onto TCPS culture plates ($3x10^4/cm^2$) and cultured in Vit C (50 μg/ml, Wako) for 2 weeks. Gene expressions calculations were conducted using the comparative CT ($2^{-\Delta\Delta CT}$) method (179,180) and details of the primer sequences for the target genes and GAPDH can be found in Appendix E.

c. SEM Analysis

3D Chon ASC and 3D Chon CS samples were first fixed in 4% methanol free formaldehyde (Thermo Fisher Scientific) for 1hr, before being washed with 1xPBS. The AF lamellae were then gently unrolled from the silk/PVA NP for further processing. The unrolled samples underwent progressive dehydration by saturating them in 70% ethanol for 1 day, followed by 100% ethanol overnight. Samples were then air-dried at room temperature for at least 2 days before being placed in a gold coat sputter (JEOL, Tokyo, Japan). Viewing was carried out using a scanning electron microscope from JEOL (JSM-5610 JEOL).

d. Fluorescence Imaging

Both F-actin and immunofluorescence staining for Col I was conducted on the 3D Chon ASC and 3D Chon CS samples. Protocols for both procedures are as previously described in Appendix F.2.c. For F-actin staining, samples were first fixed in 4% methanol free formaldehyde (Thermo Fisher Scientific) for 1hr, before being washed with 1xPBS. The AF lamellae were then gently unrolled from the silk/PVA NP for further processing for F-actin staining. For immunofluorescence staining for Col I, samples were also first fixed in 4% methanol free formaldehyde (Thermo Fisher Scientific) for 1hr, before being washed with 1xPBS. Thereafter samples were incubated with 40% sucrose overnight at 4°C before being embedded in tissue freezing medium (Shandon Cryomatrix, Thermo Fisher Scientific) for sectioning with a cryostat (Research Cryostat CM3050S, Leica Biosystems). Sections of 20μm thickness were then used for immunofluorescence staining. In addition, deriving from the results obtained in Appendix F.1, 15mins of SB treatment was introduced at the end of the staining procedures and prior to epifluorescence imaging.

All epifluorescence images were viewed with an inverted epifluorescence microscope (IX71, Olympus, Tokyo, Japan), and captured using a DP70 digital colour camera system (Olympus). Confocal images were viewed and captured using a FluorView FV1000 confocal imaging system.

e. Statistical Analysis

Pairwise comparisons were determined using a two-tailed unpaired Student's t-test and performed using Excel Analysis ToolPak (Microsoft Inc.). Statistical analysis involving multiple comparisons were conducted with a one-way analysis of variance (ANOVA) test and post-hoc Tukey correction using OriginPro9 (OriginLab). $p<0.05$ was taken as significant and all data are expressed as means ± standard deviation.

6.1.3 Results

RT-PCR results of the 3D Chon samples were plotted against the chondrogenically differentiated ASCs and ASC CSs results from **Figure 4-13** for ease of comparison (Figure 6-**3**). Except for Col II, the other 5 target genes displayed a drop in expression levels, even as when compared with the LmCh Co groups from section 4, which had displayed the lowest levels of gene expressions as compared to the LmCh ASC and LmCh CS groups. The Vit C condition was not explored in this chapter as the expression levels of the LmVi samples were already very low in the first place, and a meaningful comparison could not be made. However in the following chapter, the gene expression levels of the 3D construct itself will be studied in greater detail over both the Vit C and chondrogenic conditions.

Given the increment in the gene expression of the Col II gene in the 3D Chon samples (857.6 ± 170.9 fold) over the LmCh ASCs, LmCh CSs and LmCh Co samples, a further analysis was conducted by taking the ratios of Col II over that of Agg (Col II/Agg) and Col I (Col II/Col I) (Figure 6-**4**). The ratios of Col II/Agg and Col II/Col I have been reported in literature as possible indicators for differentiating the genotype of rabbits' articular chondrocytes (AC) from the NP cells and AF cells (242). Clouet and colleagues reported that among these three types of cells investigated, the ratios of Col II/Col I and Col II/Agg are both highest in ACs; however, the Col II/Col I ratio is higher in the NP cells than the AF cells, while the converse holds for the Col II/Agg ratio (242). (Col II/Agg: AC>AF>NP; Col II/Col I: AC>NP>AF). Results from Figure 6-**4** suggests that the ASCs and ASC CSs within the 3D construct are exhibiting a more chondrocyte-like genotype than those on the flat lamellae (LmCh ASCs, LmCh CSs and LmCh Co). This is further corroborated by the proximity of the ratio values to the pellet samples (PeCh ASC and PeCh CS).

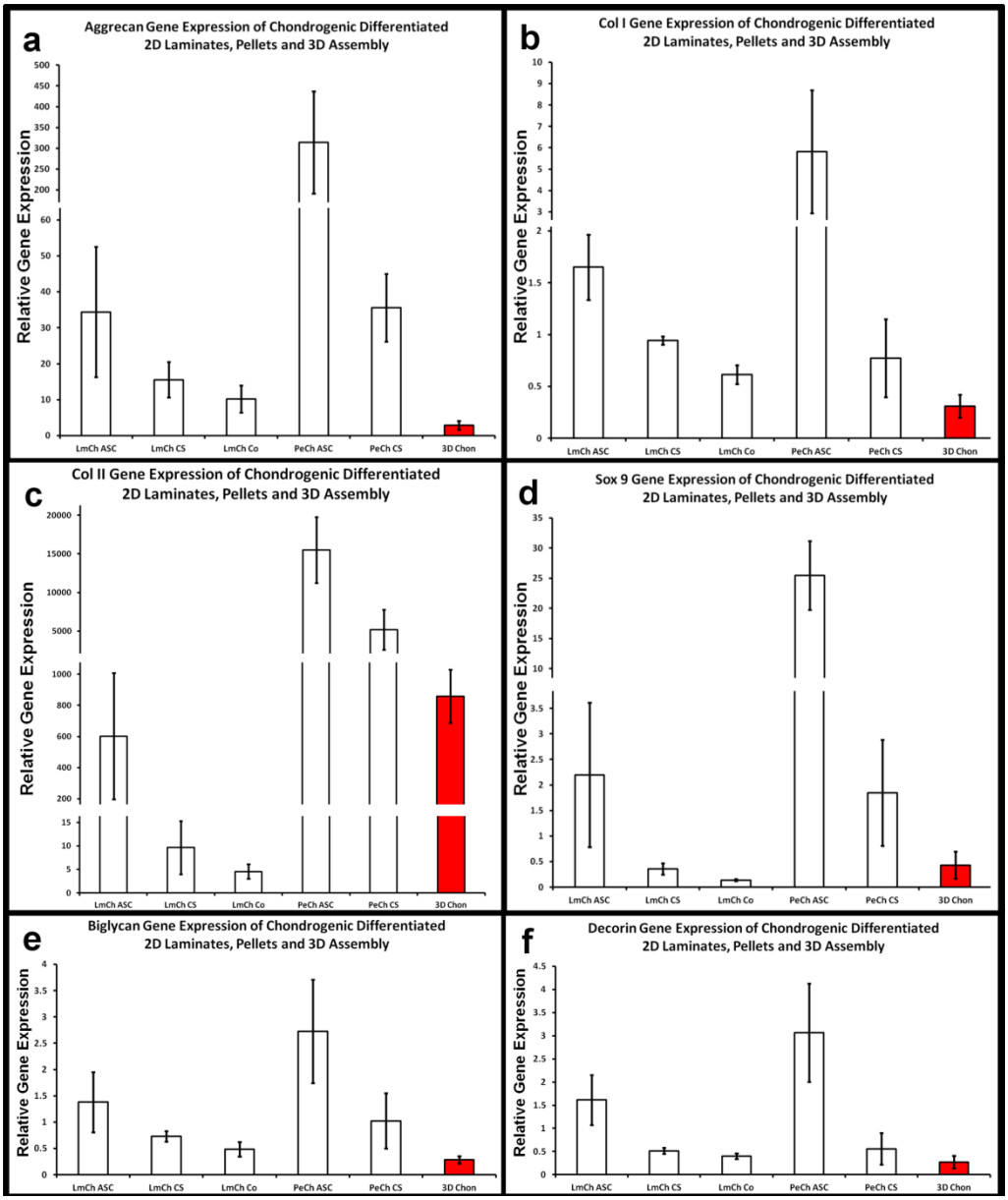

Figure 6-3. Gene expression analysis of 3D Chon samples (in shade) as compared to ASCs and CSs on hybrid laminates. The level of expression of each target gene was normalized to GAPDH and calculated using the 2–ΔΔCT formula with reference to the negative control group, which is set to 1.

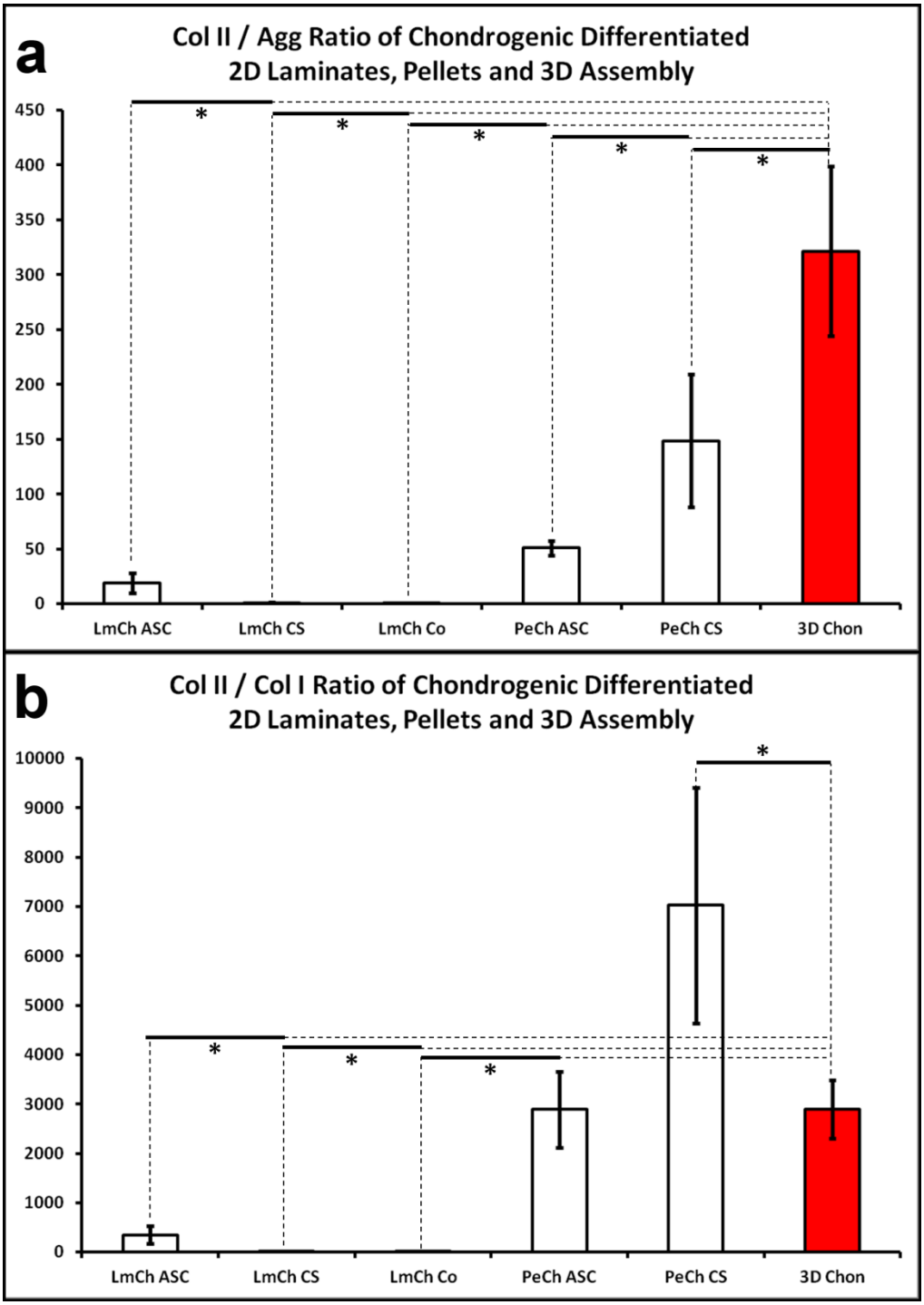

Figure 6-4. Col II/Agg and Col II/Col I gene expression ratios of 3D Chon (in shade) samples as compared to ASCs and CSs on hybrid laminates. *p<0.05

Results from chapter 4 showed the importance of ASC CSs in generating the required ECM on the AF lamellae. The next step was to investigate if such a finding still holds true in a 3D assembly by conducting a series of fluorescence imaging and SEM analysis. In order for the results to be comparable to those reported in Chapter 4,

hybrid laminates were used for both experimental groups, (despite knowing that CS samples would not require an electrospun layer). Results from Figure 6-**5** indicate the validity of chapter 4 findings even in a 3D assembly situation. The presence of F-actin (an intracellular structure) could be observed to be only sparsely present on the knitted mat silk threads in the 3D Chon ASCs samples, as compared to the robust distribution observed in the 3D Chon CS samples (Figure 6-**5a**). The increased presence of F-actin on the 3D Chon CS samples is further associated with an increased presence of Col I detected (Figure 6-**5b**) by immunofluorescence imaging.

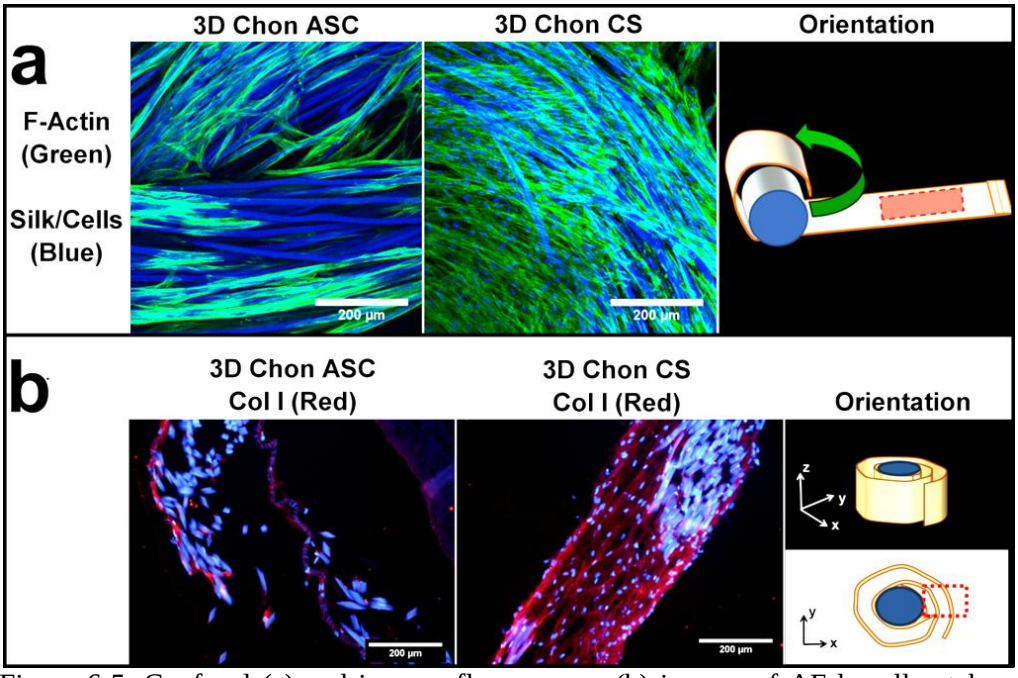

Figure 6-5. Confocal (a) and immunofluorescence (b) images of AF lamellae taken from 3D Chon ASC and 3D Chon CS samples after 14 days of chondrogenic culture. Samples were stained for Col I (red), F-actin (green), and counterstained with DAPI for nucleus (blue). Orientation by which samples were obtained from the 3D discs are as indicated by the red dotted boxes. Scale bar: 200□m.

The overall ECM deposition was further analysed by SEM under high magnification. From Figure 6-**6**, it can be observed that the ECM deposited (indicated by yellow arrows) by the CS samples were much more in amount. The ECM deposition of the 3D Chon CS samples were also more robust, covering the entire area of the hybrid laminates, as compared to the ASCs samples. High magnification (2000x) SEM

images also showed that the CSs integrated well with the laminates, given the tight wrap of ECM around the laminates' silk fibres. ASCs seeded were also able to deposit ECM between the silk fibres as shown by the yellow arrow in the high magnification image of the 3D Chon ASC sample.

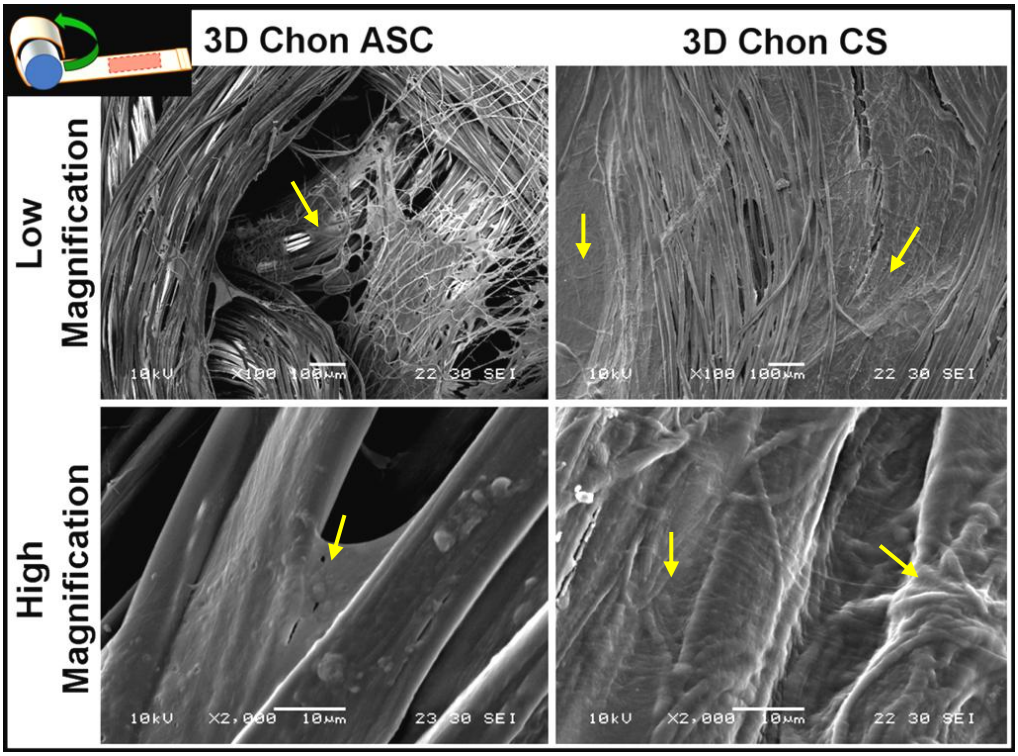

Figure 6-6. SEM images of AF lamellae taken from 3D Chon ASC and 3D Chon CS samples after 14 days of chondrogenic culture. Orientation by which samples were obtained from the 3D discs are as indicated by inset image. Yellow arrows indicate deposition of ECM.

6.1.4 Discussion

In this section, a de novo IVD construct using the TE AF and NP components from phase 2 and phase 3 respectively was assembled. This consists of a combination of electrospun-knitted hybrid laminates and knitted lamellar mats to recapitulate the inner and outer AF respectively, while a silk/PVA cryogel forms the NP component. The effect of the 3D assembling on ASCs and ASC CSs responses was investigated by RT-PCR and compared to the non-3D lamellar results from chapter 4. The individual inner and outer AF components of the de novo construct was also assessed

for suitability, and further supports the use of ASC CSs to recapitulate majority of the ECM needed in the de novo disc.

The more chondrocyte-like genotype that has been observed in the 3D samples as shown by the Col II/Agg and Col II/Col I ratios from Figure 6-**4** is believed to be due to the inter-lamellar compression effect the AF layers are experiencing as a 3D assembly within the de novo disc. The cell-seeded AF layers are swiss-rolled round the NP cryogel, which subsequently swelled and expanded in the presence of culture medium. This swelling effect pushes the AF layers against the rigid silk cuff to form a tight-fit, and simultaneously created a compression effect between the ASCs and ASC CSs seeded lamellae. Such an observation is supported by literature, which have demonstrated the effects of compression as a modulator in chondrogenesis in MSCs (243). For example, Huang and colleagues reported that not only does cyclic compressive loading promotes the chondrogenesis of rabbit BMSCs (suspended in agarose gels) through the TGF-β1 pathway, compressive loading alone is capable of inducing chondrogenesis as effectively as biochemical stimulation by TGF-β (243).

6.2 Phase 4(b): Assessment of De Novo IVD Assembly with Real-time Monitoring Compression Loading Bioreactor

6.2.1 Introduction

The application of stimulatory cues in TE is increasingly moving beyond the use of biochemical molecules (244). The role of mechanical signals as MSCs differentiation regulators are well documented in literature today, and extrinsic mechanical signals can be considered to be epigenetic factors in regulating the stem cell fate (245). The concept of mechanics in TE is multi faceted, including: i) understanding the biomechanical properties of native tissues, ii) development of biomaterials with

specific biomechanical properties, iii) studying the effects of mechanical signaling on native tissues, iv) capitalizing the use of mechanical signaling for tissue regeneration and enhancement of engineered tissues, and v) developing computational models encompassing one or more of the above mentioned areas (244). The use of bioreactors in this regard plays a pivotal role, as it provides a tightly controlled environment by which one or more of the above aspects can be carried out. The use of bioreactors in IVD TE has been covered in detail in section 2.8.2.

In the previous section of this chapter, we have successfully developed a 3D de novo disc consisting of both NP and AF components for whole disc replacement. Results further showed that the assembling and 3D form of the de novo disc exhibited influence on the ASCs and ASCs CSs responses. We believed that was due to the interlamellar forces experienced by the AF components due to the swelling pressure from the NP component. Looking at the aspect of mechanical forces further, in the native IVD, AF cells simultaneously undergo both a circumferential tensile stress and a radial compression stress due to the radial bulging of the NP. As mentioned, we have recapitulated a biphasic de novo disc in the first part of phase 4 that is capable of exhibiting such a behavior. To exert external physiological-like forces on the de novo disc in an in vitro environment would require the use of a suitable loading-based bioreactor. In this regard, See et al reported the use of a cyclic axial compression bioreactor to translate the radial bulge from a silicone NP-substitute to circumferential tensile stresses and radial compression stresses on a surrounding AF-like assembly (169). The bioreactor, however, was controlled by axial displacement with no load reading capabilities. The first part of Phase 4b covers the development of a real-time load monitoring axial compression bioreactor, before moving to the second half of Phase 4b covering the assessment of the 3D de novo IVD construct as a potential whole disc replacement.

The objectives of Phase 4b are hence i) to develop a bioreactor that can conduct real time load monitoring of the de novo IVD constructs while the constructs undergo dynamic compression culture mimicking physiological loading conditions and ii) to evaluate the de novo IVD constructs as potential whole disc replacements using the bioreactor to mimic in vivo mechanical conditioning, in comparison with constructs under the influence of chemical cues.

6.2.2 Materials and Methods

a. Development of Real-Time Load Monitoring Bioreactor System

The load monitoring bioreactor system consists of 4 bioreactor units, each possessing an individual rotating actuator (Mycom, Kyoto, Japan) and 50N load cell (ELFF, Measurement Specialties, VA, USA) (Figure 6-**7a**). The actuators are in turn controlled by a controller board (Mycom) that is connected to an user interface where the following parameters can be controlled by the end-user: i) amount of axial displacement, ii) duration of study and iii) frequency of cyclic compression.

The details of a single bioreactor unit are shown in Figure 6-**7b**. In particular, as the actuators are rotary in nature, a coupling (Figure 6-**7b**, inset) was designed to transform the rotation motion to uniaxial displacement motion. The motor attachment was designed to have a screw thread pitch of 1mm/turn, and in conjunction with the coupling, translate to a 1mm uniaxial displacement for every complete turn of the actuator motor. The sample chamber was designed with impermeable materials, and the compression platen used was impermeable as well. Detailed engineering drawings of the individual components of the bioreactor unit can be found in Appendix B.

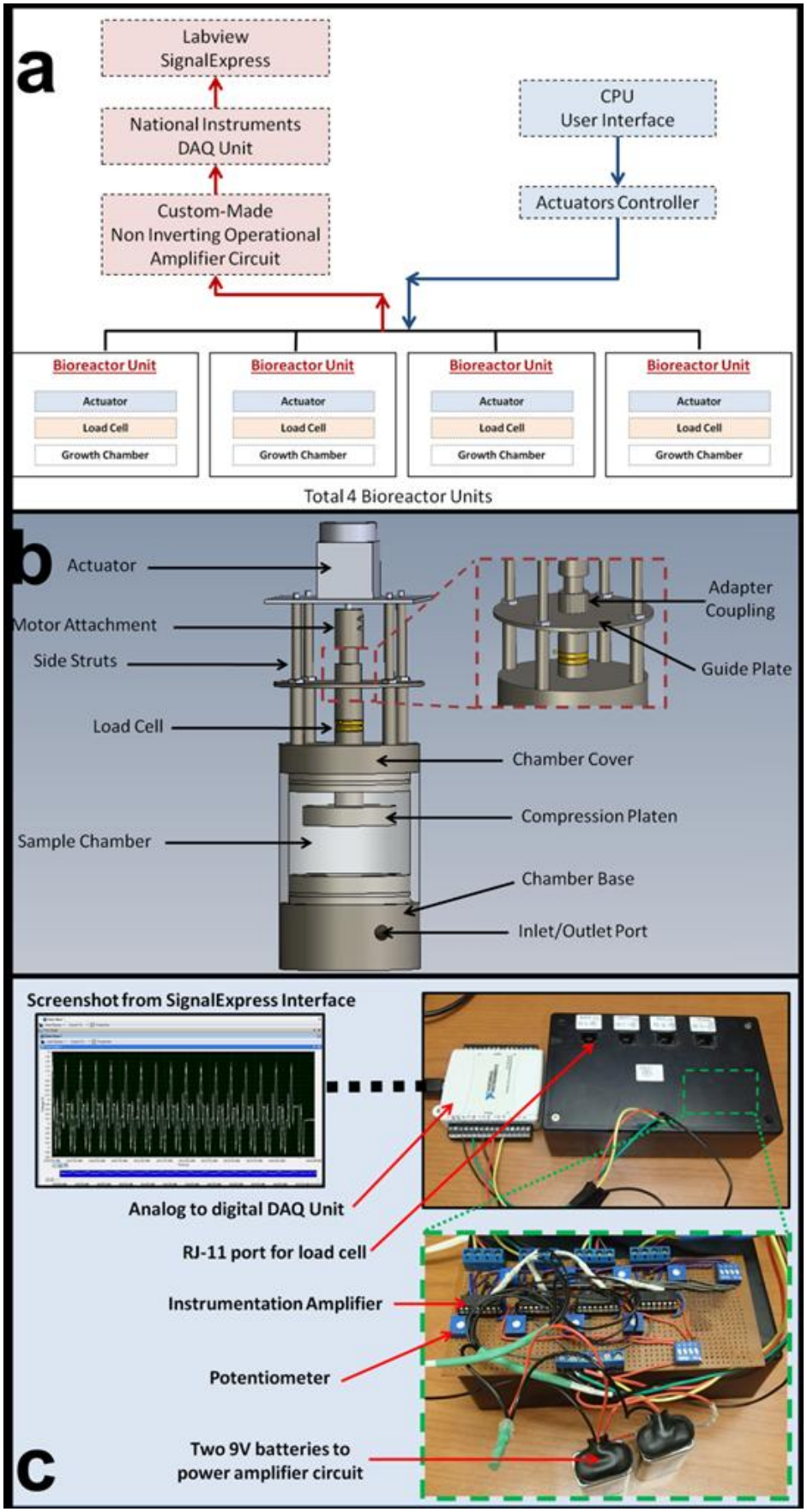

Figure 6-7. (a) Schematic overview of bioreactor system consisting of 4 bioreactor units. (b) Detailed view of a bioreactor unit. (c) Details of load cell reading component consisting of operational amplifier, DAQ unit, and SignalExpress.

Readings from the 4 individual load cells (which are piezoresistive strain gauges) were fed through a analog-to-digital data acquisition (DAQ) system (USB6008, National Instruments, Texas, USA), which is in turn connected by a USB port to a PC running LabVIEW SignalExpress (National Instruments) for data logging purposes (Figure 6-**7c**). The ELFF load cells (Measurement Specialities) used had a working load range of ±50N, an output signal resolution of 2mV/N, and requires an excitation voltage input of $5V_{dc}$. The DAQ unit had 8 analog inputs, and a working range of ±10V. The DAQ unit was however unable to provide the required excitation voltages to the load cells, and it also had a low analog-to-digital conversion resolution of 11 bits. Hence, a custom-made amplifier circuit was required. The circuit mainly consists of an instrumentation amplifier IC chip (INA125, Texas Instruments, USA), which had the capability to amplify output signals from the load cell by a gain of 4 to 10,000, and could also provide a precise excitation voltage of $5V_{dc}$ to the load cell. Details of the excitation and amplification circuitry can found in Figure 6-**7c**.

b. Calibration of Load Cells and Bioreactor System

The theoretical mV/N resolution of the load cells (together with the amplifier circuit) differs from the actual response due to wear and tear of the load cell connections, circuitry components and battery strength. Hence, a calibration of the load cells using standard weights is required before each bioreactor study can commence. This is carried out by subjecting the load cells to a series of dead weights (in both tension and compression modes) in conjunction with the amplifier circuit and DAQ unit (Figure 6-**8a**). Voltages are then recorded using LabView SignalExpress (National Instruments) and plotted into a voltage against load graph to determine the actual gradient response of the individual load cell, and determine the linearity of the load-voltage relationship. Hysteresis was also investigated due to prolonged use and re-use of the load cells. This was carried out by multiple loading and unloading of the load

cells using standard weights, and recording the corresponding voltages. Voltages were all zero-ed prior to addition of the standard weights.

A calibration of the friction between the moving parts of the bioreactor unit itself is also required. This is due to the location of the load cell being outside the sample chamber (Figure 6-**7b**), and hence in addition to the load of the sample, the load cell will also be reading the frictional loads between i) the moving platen and the chamber cover, and ii) between the moving adapter coupling and the guide plate. To measure the amount of frictional load, two calibrated load cells were used, of which one was placed in the sample chamber where a sample would normally be placed (Figure 6-**8b**). The difference in the amount of load measured between both load cells will account for the frictional forces in the bioreactor unit. To prevent overloading of the load cell in the sample chamber, it was fitted with two silicone discs which also acted as holders (Figure 6-**8b**). The bioreactor unit was then set to perform cyclic axial displacement. The readings from both load cells were recorded simultaneously using the amplifier and DAQ unit, and plotted into a force against time graph.

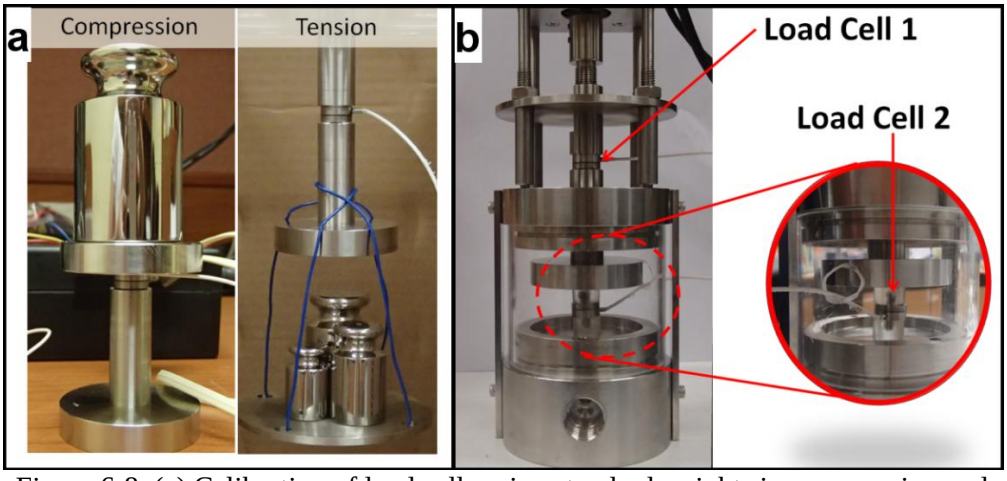

Figure 6-8. (a) Calibration of load cells using standard weights in compression and tension modes. (b) Calibration of friction in the bioreactor unit using two calibrated load cells.

c. Fabrication and Culture Conditions of 3D De Novo IVD Constructs

Two types of culture medium were used. One only supplemented with Vit C (50µg/ml, Wako), while the other is a chondrogenic medium containing 1% ITS+

(BD Biosciences), 100nM dexamethasone (Sigma), 50ug/ml Vit C (Wako), 10ng/ml TGF-ß3 (RayBiotech Inc) and 10ng/ml BMP-6 (R&D Systems). Samples cultured in both types of medium in culture plates as static samples were labeled as "3D Vit" and "3D Chon" accordingly. For the bioreactor system, only Vit C (50μg/ml, Wako) supplemented medium was used, and dynamic samples were subjected to a 1hr daily compression regime consisting of a 20% axial displacement and an axial loading rate of 1mm/min. Samples cultured in the bioreactor were labeled as "3D Bio", and readings from the four load cells were data-logged continuously during the 1hr compression regime.

Fabrication of the assembled de novo disc is as per described in section 6.1.2a and shown in Figure 6-**1** and Figure 6-**2a**. Briefly, silk/PVA cryogels containing 20% silk were swiss-rolled with two pieces of ASCs seeded hybrid laminates, and four pieces of CSs seeded knitted mats (all 3cm in length) to form approximately 9 to 10 concentric layers of AF lamellae. The completed swiss-rolled disc was then fitted ino a silk cuff to form the completed 3D de novo disc. Assembled discs were then left in culture plates overnight in normal expansion medium to allow for the cells to stabilize. The next day (termed "Day 0"), 3D Chon samples had their medium changed to a chondrogenic cocktail, while 3D Vit samples' medium was changed to a Vit C supplemented one. 3D Bio samples were meanwhile placed in the bioreactor units for the first round of compression.

All cultures were maintained for 2 weeks in a humidified 5% CO_2 incubator at 37^{o}C before being sacrificed for assessment. Culture medium for both the static cultures and bioreactors was changed every 3 to 4 days.

d. Mechanical Properties Assessments

After 2 weeks of culture, samples were removed from the bioreactor units (3D Bio) and imaged by a high resolution camera (Olympus). The top and bottom areas of the 3D disc were captured by the camera and measured using open source software FIJI (205). Taking into account the frictional load measured in section 6.2.2b, and using the calibrated voltage/load gradient response information of each load cell obtained from section 6.2.2b, and the logged data from the load cells from section 6.2.2c, the respective sample's stress-strain curves and compressive modulus values were tabulated for the entire 2 weeks of bioreactor study.

e. Gene Expression Assessment

RNA extraction and cDNA synthesis were conducted as described in section 3.2.2d, PCR analysis was carried out as described in section 3.2.2e. The genes of interests investigated were similar to those in the earlier chapters (Eg. section 4.2.8a), namely: Sox 9, Col I, Col II, Decorin, Biglycan, and Aggrecan. Expression levels of the target genes were normalized to the respective sample's GAPDH gene and then tabulated with respect to a negative control group. "3D Vit" samples were used as the negative controls. Gene expressions calculations were conducted using the comparative CT ($2^{-\Delta\Delta CT}$) method (179,180) and details of the primer sequences for the target genes and GAPDH can be found in Appendix E.

f. SEM Analysis

3D Bio, 3D Chon and 3D Vit samples were first fixed in 4% methanol free formaldehyde (Thermo Fisher Scientific) for 48hrs, before being washed with 1xPBS for 1hr. Samples were then transferred to tissue freezing medium (Shandon Cryomatrix, Thermo Fisher Scientific) for sectioning with a cryostat (Leica Biosystems). Each sample was then sectioned till the mid-point of the disc was reached. The remaining half of the sample on the cryostat stage holder was then

soaked in dH_2O on a shaker at room temperature to wash off the OCT. Samples then underwent progressive dehydration by saturating them in 70% ethanol for 1 day, followed by 100% ethanol overnight. Samples were then air-dried at room temperature for at least 2 days before being placed in a gold coat sputter (JEOL). Viewing was carried out using a scanning electron microscope from JEOL.

g. Histology and Fluorescence Based Imaging

3D Bio, 3D Chon and 3D Vit samples were first fixed in 4% methanol free formaldehyde (Thermo Fisher Scientific) for 48hrs, before being washed with 1xPBS for 1hr. Samples were then embedded in paraffin through serial dehydration in ethanol and xylene washes. Using a microtome (Leica), 5um thick sections were cut and collected on polylysine-coated glass slides for subsequent histology and immunofluorescence analysis. Hematoxylin and Eosin (H&E), Safranin-O and Alcian Blue staining were carried out for histology assessments. Immunofluorescence staining was conducted for detection of Col I and Col II.

Safranin-O staining was carried out as described in section 3.2.3.d. For H&E staining, after deparaffinization and rehydration of the slides, samples were first stained with Harris Hematoxylin for 10mins. Differentiation was carried out by a quick dip in 0.3% acid alcohol, following which ammonia water was added for 2min for blueing. Eosin was then added for 1min before the slides were rinsed in 70% ethanol, and dehydrated through a series of ethanol and xylene washes. Alcian blue staining was carried out after deparaffinization and rehydration of the slides by incubating the slides with alcian blue solution for 30mins. Slides were then washed before being counterstained with Nuclear fast red for 5mins, and dehydrated through serial ethanol and xylene washes. Slides were all mounted with Depex mounting medium (Sigma) for brightfield imaging.

For immunofluorescence staining, after deparaffinization and rehydration of the slides, samples were first digested in pepsin (Roche Diagnostics) at 37^{o}C for 30mins for antigen retrieval purposes, blocked with 1% BSA for 1 hr, before incubation with Col I (Sigma) and Col II primary antibodies (Merck Millipore) overnight at 4^{o}C. Secondary antibody conjugated with Alexa Fluor 594nm (Invitrogen) was then added with DAPI (Invitrogen) for 30mins at room temperature. Sudan black was added at the end of the staining procedures for 15mins and samples were mounted with FluorSave (Millipore) for epifluorescence viewing. All brightfield and epifluorescence images were viewed with an inverted microscope (IX71, Olympus, Tokyo, Japan), and captured using a DP70 digital colour camera system (Olympus).

h. Quantitative Assay Assessments

The metabolic activities of the 3D constructs were assessed by Alamar blue assay (Invitrogen) on day 0 (day of assembly) and at the end of 2 weeks of culture (Day 15). The procedure is as described earlier in section 3.2.2.a. 3D Bio samples were removed from the bioreactor units and placed in culture plates. All samples were incubated with 10% (v/v) alamar blue reagent for 1hr while placed in a 5% CO_2 incubator at 37^{o}. Alamar blue supplemented medium was also added to an assembled 3D construct with no ASCs nor CSs incorporated as blank. Metabolic activities were then tabulated as described in 3.2.2a.

Insoluble collagen in the samples was determined by Sircol Dye Reagent (Biocolor), while the total soluble sulfated GAGs present were determined by Blyscan Assay (Biocolor). Triplicate samples from all three groups (3D Bio, 3D Chon and 3D Vit) were first subjected to a pepsin digestion protocol as described earlier in section 3.2.2.c. Sircol Assay (Biocolor) was then carried out on the lysates as previously described in section 3.2.2.c. Blyscan Assay (Biocolor) was carried out using the lysates by following the manufacturer's protocol, with absorbance of the released 1,9

dimethyl methylene blue dye-complex measured at 656nm, and matched to a standard calibration curve to determine the sulphated GAGs content in the lysates. Collagen and sulphated GAGs contents were then normalized to its respective sample's DNA content, which was measured with a Quant-iT™ PicoGreen® dsDNA Kit (Molecular Probes, Invitrogen) using the protocol mentioned earlier in section 5.2.3.b.

i. Statistical Analysis

Pairwise comparisons were determined using a two-tailed unpaired Student's t-test and performed using Excel Analysis ToolPak (Microsoft Inc.). Statistical analysis involving multiple comparisons were conducted with a one-way analysis of variance (ANOVA) test and post-hoc Tukey correction using OriginPro9 (OriginLab). $p<0.05$ was taken as significant and all data are expressed as means ± standard deviation.

6.2.3 Results

a. Assessment by Quantitative Assays

Metabolic activities levels in the 3D constructs showed a significant increment between Day 14 and Day 0, indicating that the ASCs and ASCs CSs were healthy and viable within the construct assemblies (Figure 6-**9**). This is despite the size of the constructed de novo disc (approximately 7.5mm in height, 10mm in diameter), and the tightly packed multi-laminate nature of the surrounding TE AF. The 3D Bio samples displayed a significantly higher viability over the 3D Vit and 3D Chon samples. We believe this is due to an improvement in nutrients delivery and wastes exchange in the bioreactor samples, validated by the same culture medium being used for the 3D Vit and 3D Bio samples. The alamar blue results also showed that the extent and speed of compression chosen for this study did not cause any adverse effects on the ASCs and ASCs CSs.

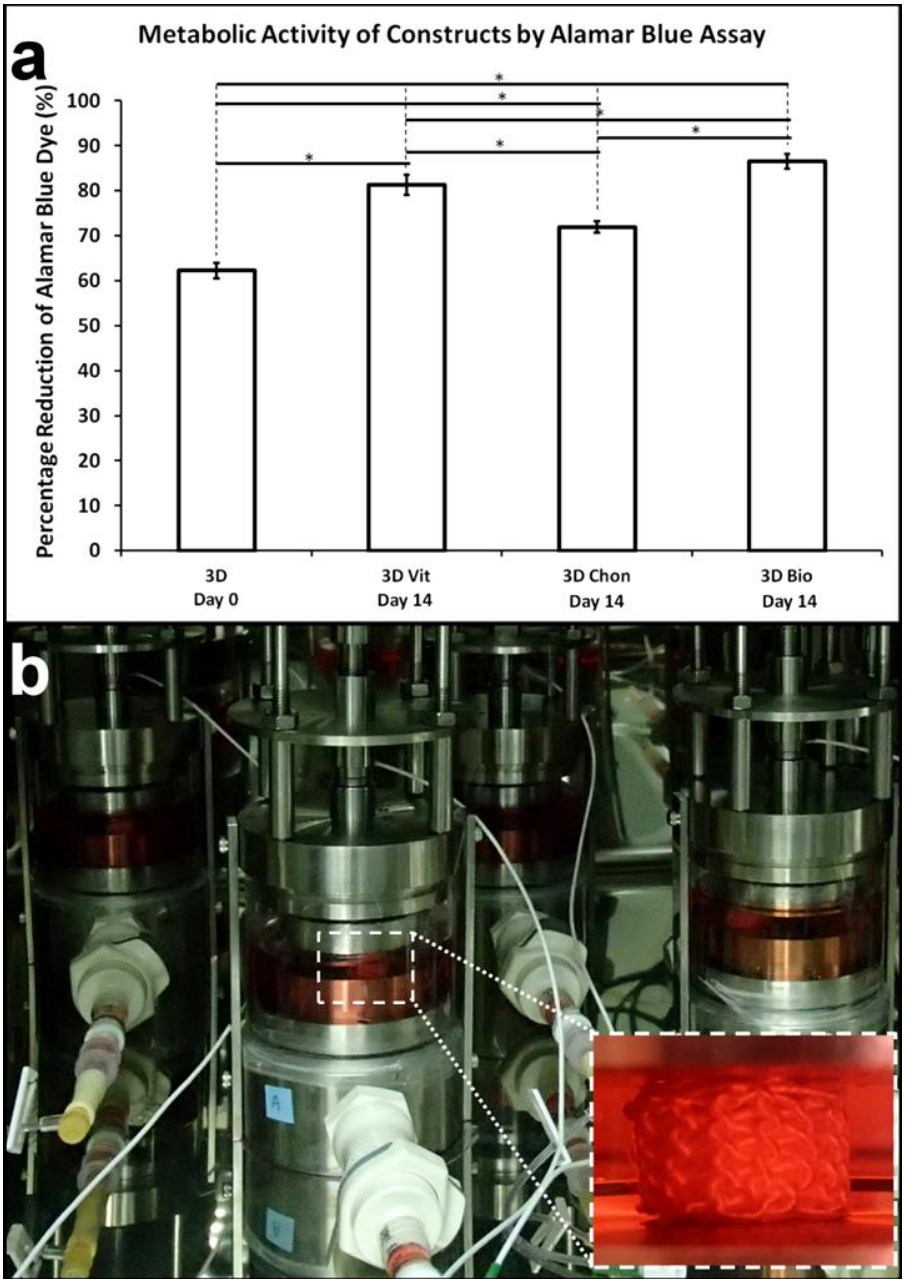

Figure 6-9. (a) Alamar blue assay results of 3D constructs at Day 0 and after 2 weeks of culture in static chondrogenic medium ("3D Chon"), bioreactor ("3D Bio"), and static Vit-C supplemented medium ("3D Vit"). (b) Photo of bioreactor system set up inside incubator. Inset: Close-up picture of 3D construct sandwiched below compression platen and inside sample chamber. *$p<0.05$

3D Chon samples displayed the highest amount of soluble collagen and sulpated GAGs contents after 2 weeks of culture (Figure 6-**10**). Conversely, 3D Bio samples displayed significantly the lowest amount of soluble collagen and sulphated GAGs. The significant difference in results between the 3D Vit and 3D Bio samples demonstrated that the physical conditions (Eg. free swelling versus constrained and

compressed) by which the 3D constructs were cultured affected the responses of the ASCs and ASCs CSs within the 3D assembly.

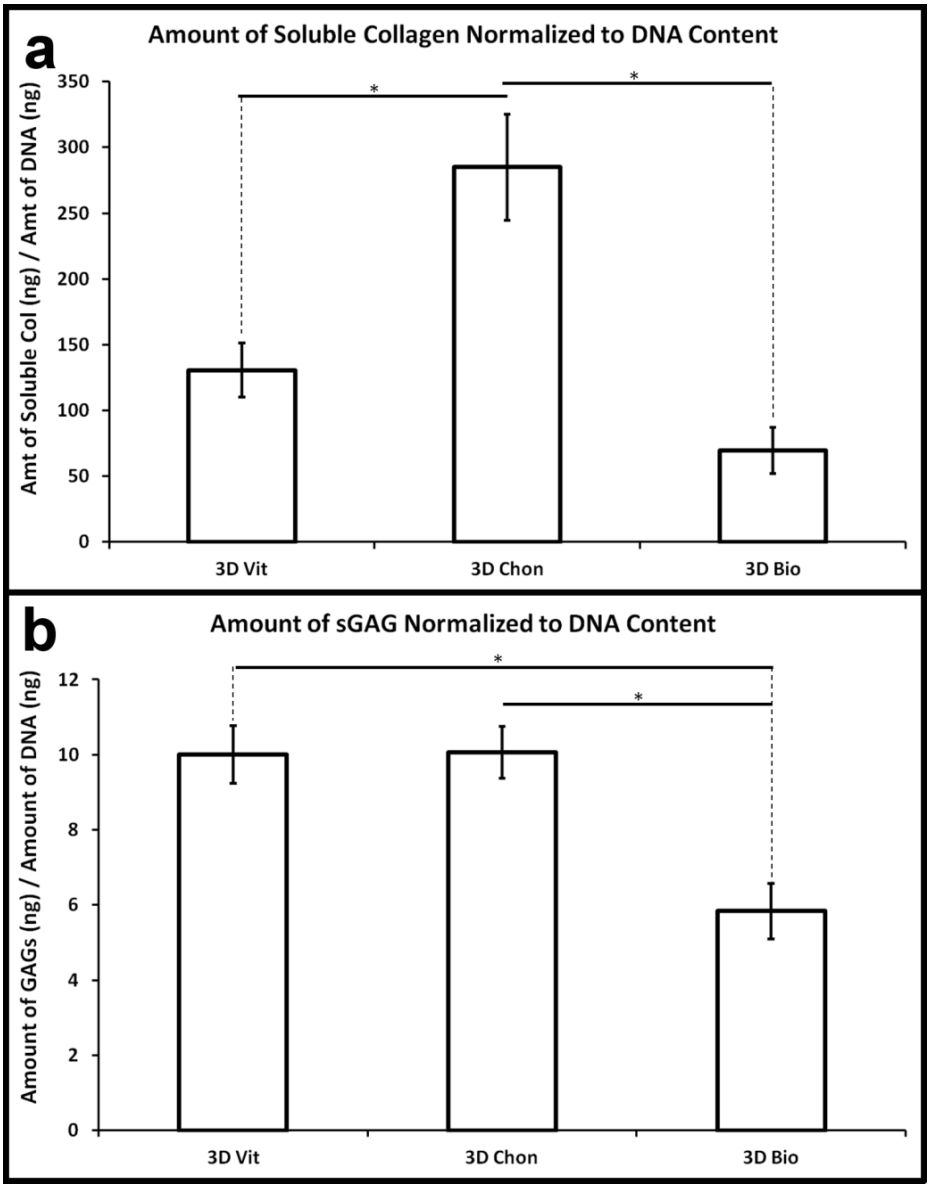

Figure 6-10. (a) Amount of soluble collagen in de novo discs after 2 weeks of culture in static chondrogenic medium ("3D Chon"), bioreactor ("3D Bio"), and static Vit-C supplemented medium ("3D Vit"), determined by Sircol assay and normalized to the respective DNA content. (b) Amount of sulpated GAGs after 2 weeks of culture, determined by Blyscan assay and normalized to the respective DNA content. *$p<0.05$

b. Gene Expression

RT-PCR results (Figure 6-**11**) showed that with respect to the control group (3D Vit), 3D Chon samples had a significant upregulation of gene expressions for Col II (3539.9 ± 997.9 fold increment) and Aggrecan (358.1 ± 162.5 fold increment). In particular, 3D Bio samples had a significant upregulation of the Aggrecan gene (14.2

± 4.3 fold increment) over the 3D Vit samples after 2 weeks of cyclic compression. Surprisingly, there were no significant upregulation or down regulation of Sox-9 among the three groups investigated. We believe as an early marker for chondrogenesis, a two-week assessment time point might be too late in capturing an upregulation of the Sox9 gene. This is corroborated by the 3D Chon samples, which despite having no upregulation of the Sox9 gene detected, had distinct upregulations of both Col II and Agg genes - both of which can be considered as later gene markers for chondrogenesis.

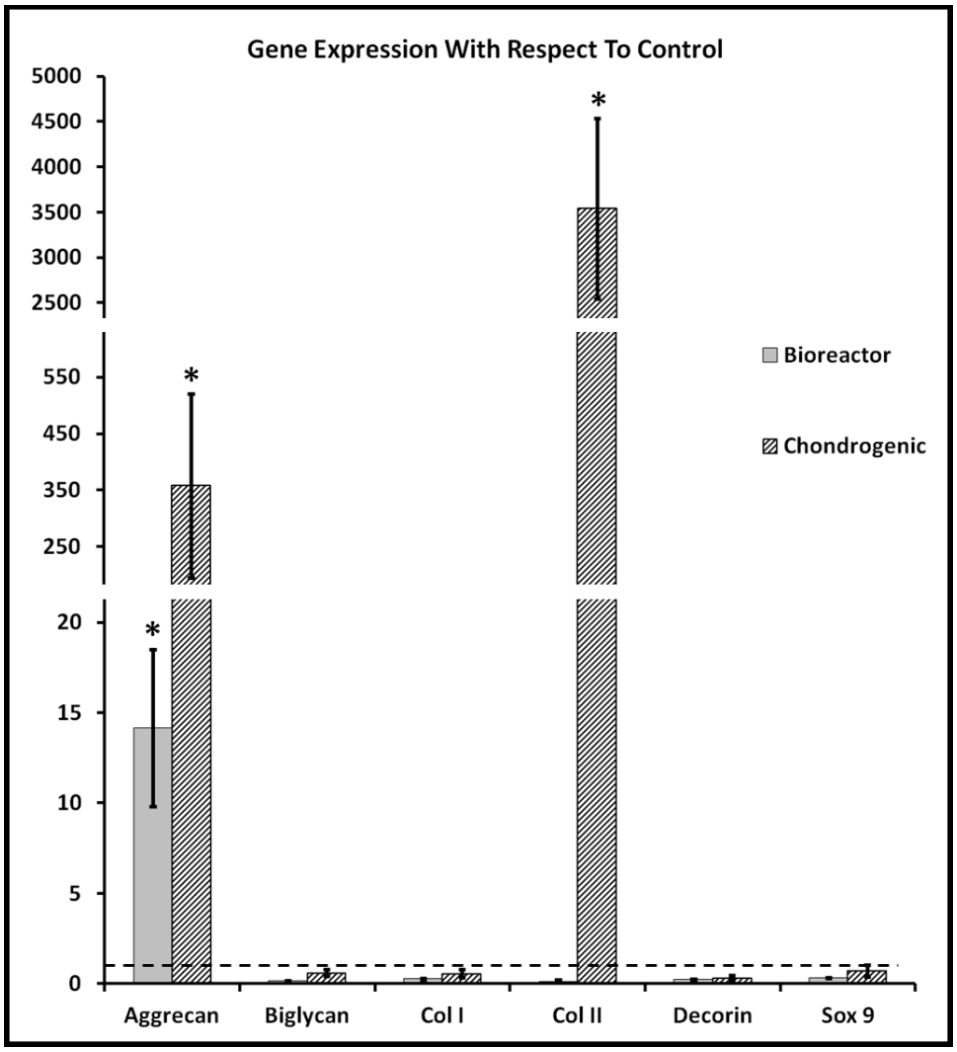

Figure 6-11. Gene expressions of de novo discs cultured in bioreactor and chondrogenic medium (static) determined by RT-PCR. The level of expression of each target gene was normalized to GAPDH and calculated using the $2^{-\Delta\Delta CT}$ formula with reference to the negative control group (static, Vit C supplemented medium), which is set to 1 (dotted line). *$p<0.05$*

c. SEM and Histology Assessments

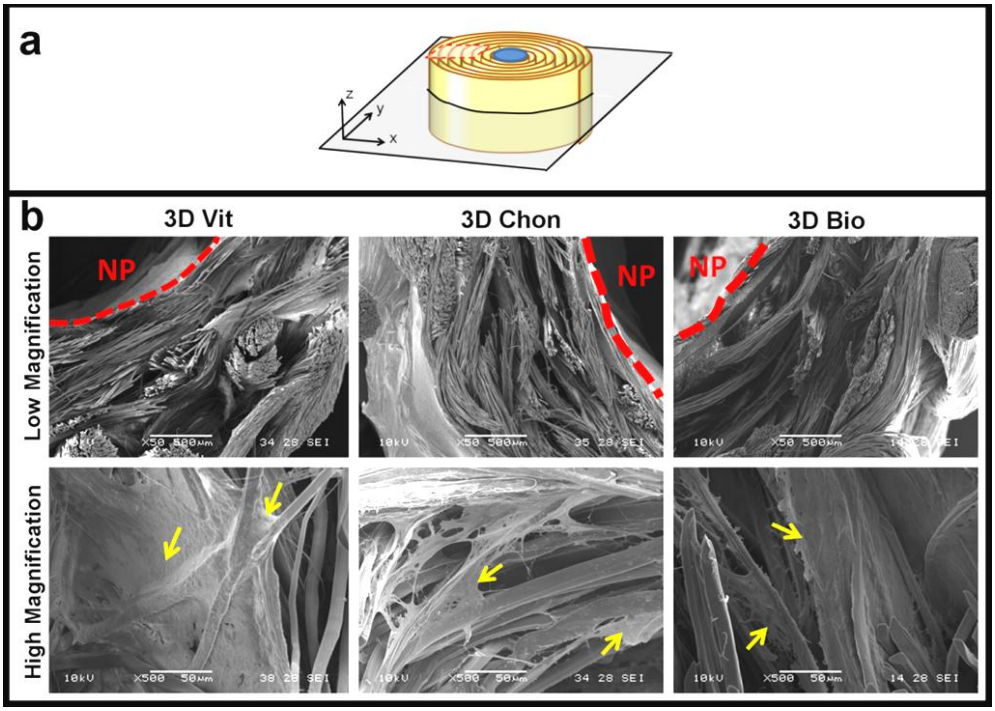

Figure 6-12. (a) Orientation of construct by which SEM images were obtained. (b) SEM images of de novo discs cultured in static chondrogenic medium ("3D Chon"), bioreactor ("3D Bio"), and static Vit-C supplemented medium ("3D Vit") taken on the x-y cross-section plane. Red dotted lines demarcate location of NP component, yellow arrows indicate ECM deposition.

SEM images (Figure 6-**12**) on the cross-sections of 3D Vit, 3D Chon and 3D Bio samples showed ample deposition of ECM on all three groups after 2 weeks of culture. The multi-lamellar structure of the AF can be observed to be maintained on all three sample groups, but is qualitatively the most distinct in the 3D Chon group. The 3D Chon group also displayed a more tightly packed laminate structure than the other two groups, and this can be correlated with the higher amount of ECM deposited as shown by the amount of collagen and sGAGs that were quantified by the colorimetric assays earlier (Figure 6-**10**). The NP components cannot be seen as the cryogels shrunk during the dehydration steps for sample preparation.

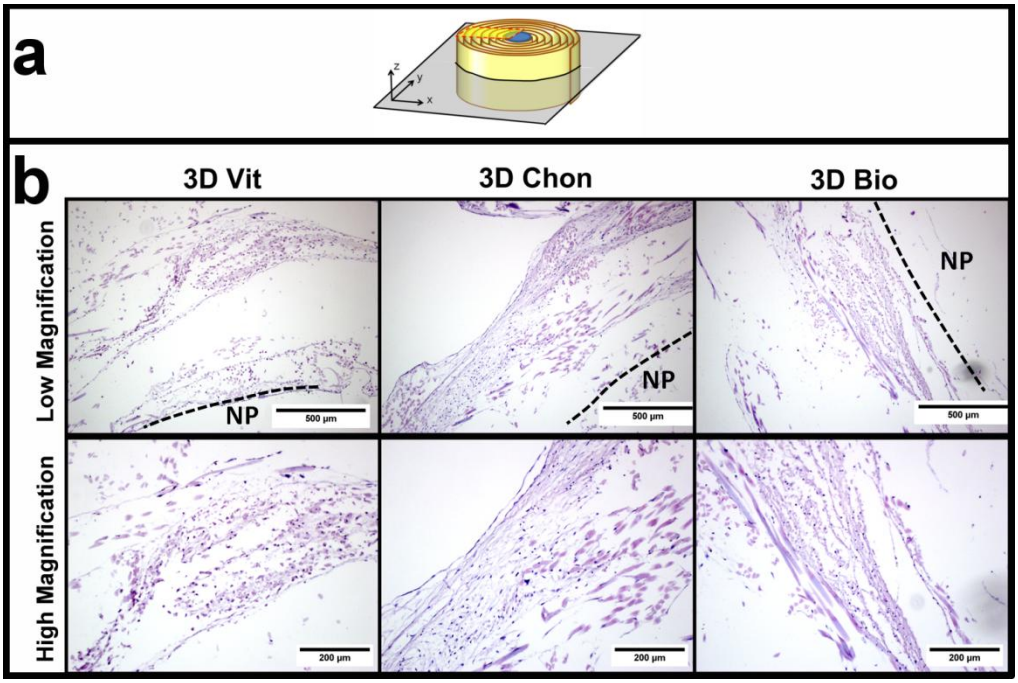

Figure 6-13. (a) Orientation by which constructs were sectioned to obtain slides for histology. (b) Hematoxylin and Eosin staining images of de novo discs cultured in static chondrogenic medium ("3D Chon"), bioreactor ("3D Bio"), and static Vit-C supplemented medium ("3D Vit") sections taken on the x-y cross-section plane. Black dotted lines demarcate location of NP component.

Correlating with SEM results (Figure 6-**12**), Hematoxylin and eosin staining (Figure 6-**13**) of 3D Vit, 3D Chon and 3D Bio samples indicate deposition of ECM in all three groups after 2 weeks of culture. This deposition can be observed in the lamellae from the inner AF to the outer AF, indicating the ability of the ASCs and ASCs CSs to deposit ECM though out the assembly construct, and thereby implying that the cells remain viable and proliferative despite the inner portions being near the core of the assembly. 3D Chon images were observed to display a higher density of ECM deposition, leading to a more robust and tightly packed structure. In this regard, the effect of cyclic compression was apparent in the 3D Bio sample. Compared to the 3D Vit sample, a better structured lamellar-like architecture can be observed in the 3D Bio samples ("3D Bio, High magnification"), which is also correlated with a qualitatively higher density of ECM deposition. The NP components cannot be seen as the cryogels shrunk during the dehydration steps for paraffin tissue embedding.

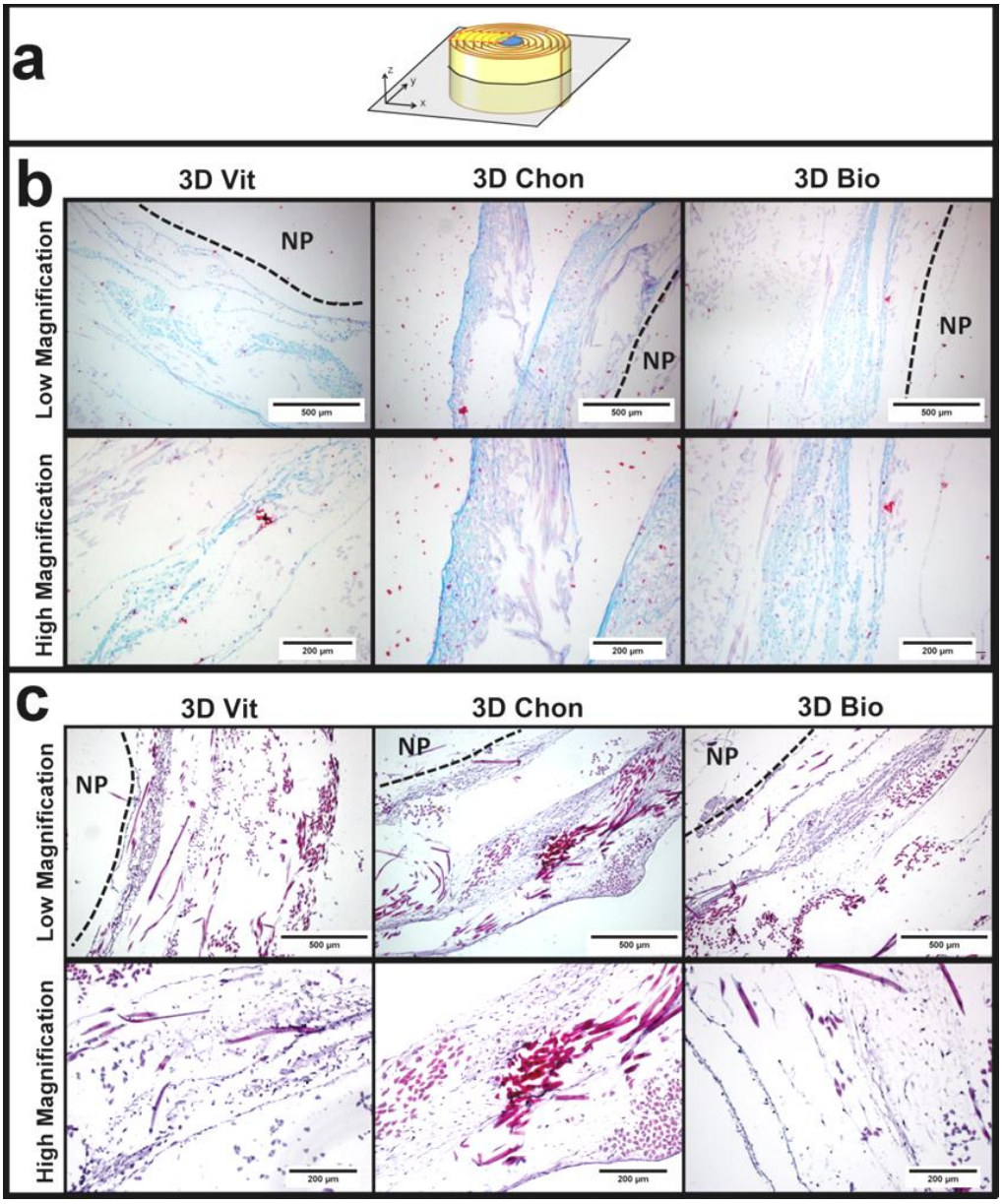

Figure 6-14. (a) Orientation by which constructs were sectioned to obtain slides for histology. (b) Alcian blue staining images of de novo discs cultured in static chondrogenic medium ("3D Chon"), bioreactor ("3D Bio"), and static Vit-C supplemented medium ("3D Vit") sections taken on the x-y cross-section plane. (c) Safranin-O staining images of 3D Vit, 3D Chon and 3D Bio sections taken on the x-y cross-section plane. Black dotted lines demarcate location of NP component.

Alcian blue stains for both sulphated and carboxylated GAGs, while the cationic based Safranin-O stains specifically for sulphated GAGs. Both Alcian blue (Figure 6-**14**) and Safranin-O (Figure 6-**14b**) results (after 2 weeks of culture) indicate that 3D Chon samples qualitatively contained the highest amount of GAGs over the 3D Vit and 3D Bio samples by the higher intensity of blue and red staining observed

respectively. This is in line with quantitative results shown in Figure 6-**10b**, where 3D Chon samples were found to have the significant highest amount of sulphated GAG contents over the other two groups, as determined by the 1,9 dimethyl methylene blue based Blyscan assay. Both 3D Vit and 3D Bio samples displayed a stronger blue staining under Alcian Blue than red staining under Safranin-O, indicating that perhaps the GAGs contents present in both groups were more carboxylated than sulphated. The NP components are not seen as the cryogels shrunk during the dehydration steps for paraffin tissue embedding.

Immunofluorescence staining for Col I (Figure 6-**15a**) showed that ample amounts of Col I was present in all three groups after 2 weeks of culture, and Col I was deposited in a lamellar-fashion as how the AF lamellae were assembled (in a swiss-roll fashion). This resulted in a circumferentially lamellar-oriented Col I deposition which is observed most distinctly in the 3D Bio images, but can also be seen in the 3D Vit and 3D Chon samples.

Immunolocalization for Col II (Figure 6-**15b**) showed no presence of Col II in the 3D Vit group, a slight deposition in the 3D Chon group, and some deposition in the 3D Bio group. This is an interesting finding given that no biochemical cues were given to the 3D Bio samples, but given the minute amount detected, and the relatively early assessment time point (2 weeks as compared to chondrogenic differentiation studies in literature which typically require a 4 to 6 weeks time point for confirmed Col II detection), longer time point studies will need to be conducted to confirm the presence of Col II.

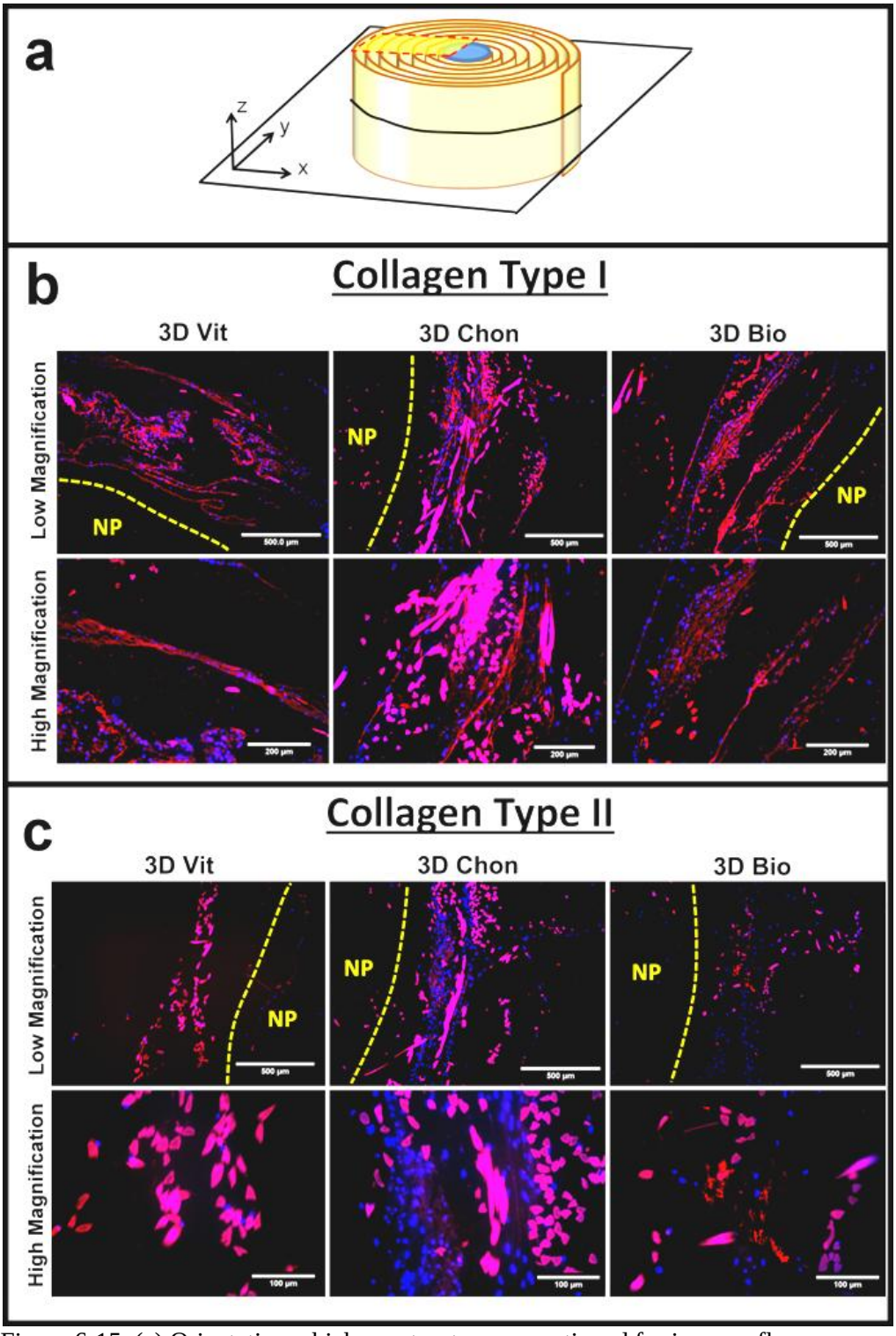

Figure 6-15. (a) Orientation which constructs were sectioned for immunofluorescence imaging. (b) Immunolocalization of Col Type I (red) on de novo discs cultured in static chondrogenic medium ("3D Chon"), bioreactor ("3D Bio"), and static Vit-C supplemented medium ("3D Vit") sections taken on the x-y cross-section plane. (c) Immunolocalization of Col Type II (red) on 3D Vit, 3D Chon, and 3D Bio sections taken on the x-y cross-section plane. Yellow dotted lines demarcate location of NP component. Samples were all counterstained with DAPI (blue) for cell nucleus localization. Silk fluoresces under both wavelengths, and appear pink.

d. Real-time Load Monitoring Results and Mechanical Properties

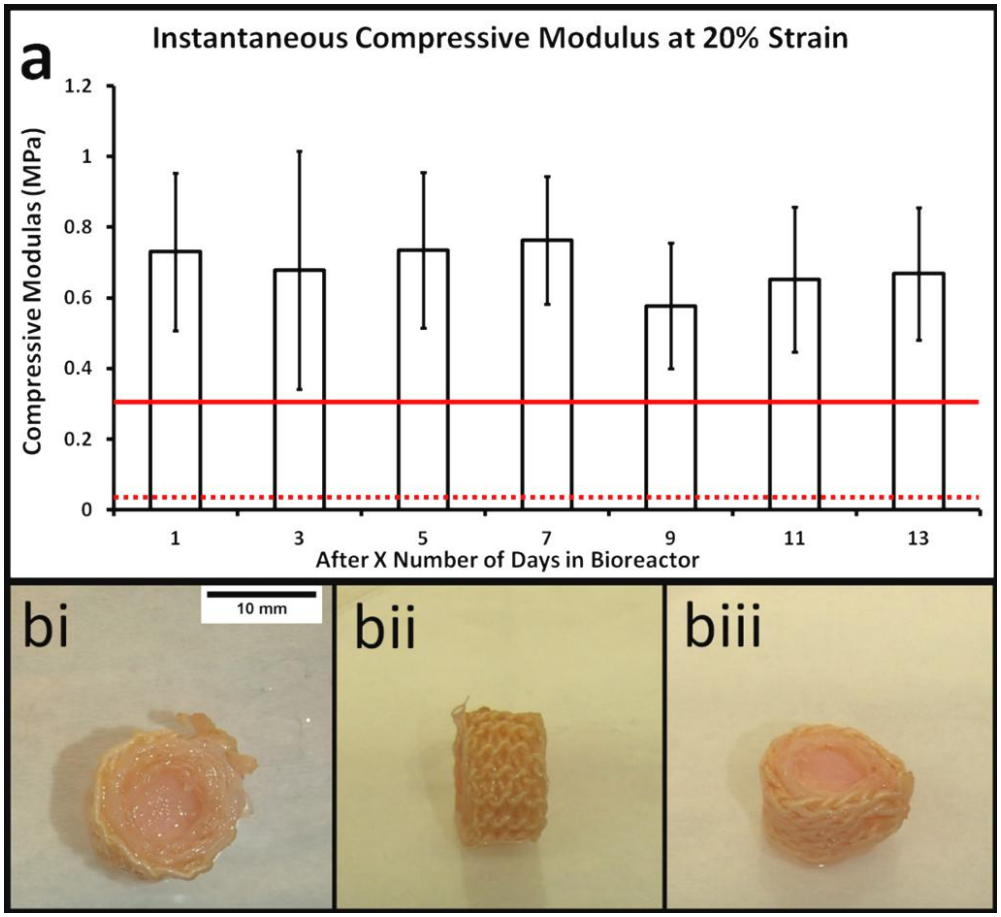

Figure 6-16. (a) Compressive modulus of de novo discs after being cultured for x days in the bioreactor. The compressive modulus values of cell-seeded and non cell-seeded silk/PVA cryogels with 20% silk at 20% strain obtained from Figure 5-9 are indicated by red bold and red dotted lines respectively. (b) Image of 3D constructs after 2 weeks of culture from the (i) top, (ii) side, and (iii) isometric views.

The details of the calibrated load/voltage responses of the load cells used can be found in Appendix C. The details on the calibrated frictional load of the bioreactor unit's moving parts can be found in Appendix D. A further discussion on the frictional load can be found in Appendix D as well. The compressive modulus and compressive stress properties in Figure 6-**16** have all been tabulated taking into account the calibrated results from Appendices C and D. Compressive modulus results from Figure 6-**16a** showed that the 3D Bio constructs maintained their mechanical properties integrity throughout the 2 weeks of culture. Interestingly, when comparing the compressive modulus values with those obtained on the silk/PVA cryogels with 20% silk and at 20% strain (**Figure 5-9**), distinct higher values were

observed in the 3D constructs (Figure 6-**16a**). This is despite the NP component not having any cells seeded in them in the 3D assembly. Images of the constructs after 2 weeks of culture (Figure 6-**16b**) showed that the constructs maintained their overall assembled structure and remain robust despite being compressed by the bioreactor daily for 14 days.

6.2.4 Discussion

In Phase 4b, we have successfully developed a bioreactor system that has several unique capabilities: i) independent control of loading and displacement parameters for each bioreactor unit, for a total of four units, ii) independent real-time load monitoring of sample in each of the unit's chamber, and iii) an uniaxial displacement compression system capable of mimicking the physiological loading conditions of the native IVD. This is an improvement to the system described by See at al (169), which did not have load reading capabilities. However, the uniaxial compression displacement to circumferential stretching concept described by See and colleagues (169) in their original design was retained for the development of this bioreactor. Hence the bioreactor system was modified (rather than redesigned) to incorporate load cells and a DAQ platform into the system to enable real time monitoring of the loading conditions experienced by the TE de novo disc.

A loading rate of 1mm/min was chosen to compress the samples in the bioreactor units. Although this loading rate is lower than the one used in section 5.2.3.c (2mm/min) to test for the compressive modulus and hoop stress of the silk/PVA cryogels, it is still in line with typical mechanical compression studies in literature that are related to the spine (224,225). A lower rate was chosen to allow time for culture medium to be re-imbibed into the NP gel as the compressive platen moves up at the end of each compression cycle. Under the loading conditions used for the 3D

Bio samples, creep was also not observed within the 1hr loading and monitoring regime daily for the 14 days of culture.

When 3D Bio samples are compressed, the compacted NP expels culture medium through the AF lamellae surrounding it into the chamber. When the bioreactor's platen moves up, the NP reabsorbs culture medium back into itself through the AF lamellae to swell back to its original dimensions. Such an exchange of culture medium brought about by the compression and decompression motions of the bioreactor mimics the physiological behavior of the NP and AF in the native IVD. As covered earlier in the literature section, the osmolarity of the NP and AF in the native IVD (conferred by its high proteoglycan contents) controls the swelling and contraction of the IVD, and in general controls the exchange of water and nutrients and expulsion of wastes. On a similar note, the increase in medium flow within the de novo disc consequently brought about an increase in metabolic activities and viability of the ASCs and CSs within the AF lamellae as shown by the significantly better alamar blue results in the 3D Bio samples (Figure 6-**9**).

Quantitative assays for soluble collagen and sulphated GAGs indicate that biochemical cues remain a more efficient means in inducing collagen and GAGs formation in the constructs than mechanical cues. This is shown by the significantly higher collagen and GAGs contents in the 3D Chon samples over the 3D Bio samples (Figure 6-**10**), and confirmed by qualitative imaging analysis using H&E, Safranin-O, Alcian blue and immunofluorescence staining. Nonetheless, repeated compression cycles brought about by the compression regime did not had any adverse effects on the mechanical strength of the 3D constructs over a 14 day period. Such results are promising as in an in vivo environment, both mechanical loading and biochemical signaling are present – the former resulting of the major concerns in whole disc TE is in the premature collapse of the TE disc.

The Young's modulus of the native human (whole disc) motion segment have been reported in literature to be in the range of 3 to 10MPa (90). Table 4 summarizes the modulus values reported in literature for the handful of whole-disc TE studies which have conducted compressive testing on the TE discs.

Table 4: Summary of Modulus Values for Tissue-Engineered Whole Discs

NP Component	AF Component	Mechanics Measured	Results	Study Design	Ref
Alginate	PGA/PLA	equilibrium compressive modulus	**50kPa**	16 weeks subcutaneous in vivo	Mizuno et al (91)
Agarose	PCL	equilibrium Young modulus	**45kPa**	6 weeks in vitro	Nerurkar et al (70)
Alginate	Collagen	equilibrium modulus	**235kPa**	6 months in vivo caudal implantation	Bowles et al (93)
Silk/PVA	Silk	compressive modulus	**~0.7MPa**	2 weeks in vitro with mechanical loading	This study

Mizuno and colleagues reported an equilibrium compressive modulus of up to 50kPa for the TE disc after 16 weeks of in vivo subcutaneous culture in athymic mice (91). Nerurkar and colleagues on the other hand reported an equilibrium Young modulus of 45kPa for the TE disc after 6 weeks of in vitro culture (70). Bowles et al implanted the TE disc into the caudal section of a rat model, and reported an equilibrium modulus of 235kPa for the intact motion segment after 6 months (93). The compressive modulus observed in this study (Figure 6-**16**) is interestingly much higher and closer to the native values with a range of approximately 0.6 to 0.8MPa observed over a much shorter 14 day assessment period.

Looking further into the mechanical properties of the de novo disc, apart from the reported compressive modulus reported in Figure 6-**16**, the aggregate modulas is another property of interest. However as it was not possible to capture a lateral image

of the 3D Bio samples as it underwent compression inside the culture chamber, the Poisson ratio (needed to determine the aggregate modulus) unfortunately could not be determined. An estimation could nonetheless be conducted based on the hoop stress and Poisson ratio data obtained in Chapter 5 on the non cell-seeded silk/PVA cryogel with 20% silk. At an axial strain of 20%, an average Poisson ratio of 0.316 could be determined from the working data for Figure 5-**9** and Figure 5-**10** . This is based on the assumption that majority of the mechanical strength of the de novo disc would be attributed to the cryogel in the middle, and that it's the cryogel's bulging that is pushing the AF lamellae outwards. Using the average compressive modulas over the 2 weeks culture (calculated to be 0.686MPa), the effective aggregate modulas (H_A^{eff}) at 20% strain equilibrium of the de novo disc can be estimated to be 0.970MPa. Such a value is on par with the reported native human NP's H_A^{eff} value of ~1MPa (239), indicating a significant advancement in the area of whole disc TE.

In a recent study by Chik et al (100), a TE whole disc (made entirely from collagen) consisting of the entire motion segment (NP, AF and osteochondro units) was subjected to compression and chondrogenic culture in a bioreactor system. Although Chik and colleagues only reported on the ultimate failure stress values of the motion segment's interface for mechanical assessment purposes, nonetheless some interesting observations could be made. At a 21 day time point, it was shown in the study that samples cultured in chondrogenic medium even without compression have an ultimate failure stress value of ~20MPa, as compared to samples cultured in normal medium but underwent compression (~5MPa) (100). When compression was introduced together with chondrogenic medium, samples displayed ultimate failure stresses of ~30MPa (100). Based on the findings by Chik and colleagues, it is reasonable to believe that the de novo disc in this study could be i) cultivated longer, and ii) using chondrogenic medium with compression to further improve on its mechanical properties to be even nearer of that of the native human IVD. This is

further validated by the studies summarized in **Table 4**, which have undertaken a much longer assessment period with the use of in vivo models.

In terms of culture duration, a two week assessment time point was chosen for this study as a proof of concept assessment of the developed de novo disc replacement under biochemical and mechanical cues. Chondrogenic medium was also not used in conjunction with the bioreactor to isolate the stimulatory effects of mechanical cues from chemical cues. The use of biochemical cues was shown to be more efficient in pushing the de novo disc down a chondrogenic-like lineage, however mechanical stimulation alone was efficient in improving nutrients transport into and out of the construct, in upregulating the Agg gene (Figure 6-**11**) and in producing a more tightly packed multi-ply ECM deposition (Figure 6-**15**). Through the means of the bioreactor developed specifically for the study's purpose, the mechanical strength of the de novo disc was also verified to be a suitable TE candidate as a whole disc replacement. Studies in literature in this area typically utilizes a 4 to 6 weeks assessment period for detection of chondrogenic genes and phenotypes (70,97,98,102,169). With just a two week assessment time point, it is promising that 3D Bio samples already produced an upregulation of the Agg gene, and started displaying slight presence of Col II (Figure 6-**15c**), despite the absence of biochemical cues.

6.3 Concluding Remarks

Results from the first part of phase 4 demonstrated the successful assembly of a de novo disc using the TE AF and NP components from Phase 2 and 3 respectively. The de novo disc was held together by a knitted silk cuff and a preliminary evaluation was conducted for its suitability as an IVD replacement. The effect of the inter-lamellar compression was further explored in the second part of phase 4 where the assembled 3D de novo disc as shown in Figure 6-**1f** and Figure 6-**2a** was subjected to

chondrogenic differentiation and mechanical stimulation by a custom built bioreactor for further assessment of its suitability as an IVD replacement.

In the second part of this last phase of the dissertation, a bioreactor that can conduct real-time load monitoring (while allowing for a simultaneous dynamic compression culture of the de novo disc assembly) was developed. Mimicking the behavior of a native disc, the NP cryogel bulges while undergoing compression, and exerts a circumferential tension and radial compression to the surrounding AF laminates. As hypothesized, results showed that culturing the de novo disc under compression (similar to those experienced in the native condition) influences the development of the de novo disc's ECM into a circumferential multi-ply like manner (similar to a native disc). Load monitoring results showed that the mechanical strength of the de novo disc developed is not only better than the other TE discs in literature, but is also comparable to reported values for human native discs. Therefore the overarching objective of this dissertation – to develop a de novo IVD for potential whole disc replacement application to address late stage DDD cases, has been achieved.

Chapter 7. Conclusion and Recommendations

7.1 Conclusion

Disc herniation and DDD are one of the most common reasons leading to LBP - a major socioeconomic burden on the healthcare system worldwide. However, current treatment options for DDD address its clinical symptoms as opposed to the pathophysiology of the problem. While early-stage DDD can be treated symptomatically with therapy and administration of medications, spinal fusion remains the more commonly used approach for late-stage DDD. These approaches however do not reverse nor repair the damages at the degenerated disc, and there remains a need for a better treatment solution that aims to either cure the disease or restore spinal function.

With a TE approach, the biology and structural architecture of the IVD can be mimicked to produce a TE disc for eventual replacement of the degenerated IVD. Success in IVD TE hinges on the advancement of strategies for both the NP and AF, given the intimate functional relationship both components share to confer the disc with abilities to carry out its daily functions. However, few TE studies have targeted the replacement of the entire disc, in part due to the challenges faced by such composite TE discs. Even for the handful of studies that do, majority of them lack the use of a dynamic culture to accurately reflect the physiological conditions native IVD tissue undergoes. Using a combination of TE strategies, the overarching objective of this dissertation was to develop a de novo IVD for potential whole disc replacement application. ASCs were used in conjunction with silk-based biomaterials to recapitulate the NP and AF of the IVD. Bio-mimetic culture was then conducted with a custom-designed bioreactor on the assembled de novo IVD.

Fundamental to the success of a whole disc replacement approach is the mechanical strength of the engineered disc. Even under non-loading conditions, studies have shown that residual stresses exist in the IVD. Hence, it is essential that an engineered disc has at least the ability to withstand such residual loads to ensure clinical success when implanted. Reported strategies for whole disc TE typically use of-the-shelf hydrogels (Eg. alginate, agarose) for the NP, while relying on the surrounding TE AF (the main focus) to retain the hydrogels. Contrary to such traditional approaches, a novel strategy was utilized in this dissertation, by placing more focus more on the NP. Drawing on the advantage of a mechanically robust core material to provide the mechanical strength, the idea was to modify a material commonly used in polymeric NP prostheses to be cellular compliant for the NP component, while leveraging on the versatility of silk to be processed into multiple forms to form the highly structured AF. A cellular compliant and mechanically robust NP core has two advantages: i) allowing infiltration of cells from the neighbouring vertebral bodies or from the surrounding AF for better integration, and ii) conferring overall strength to the de novo disc assembly.

Indeed load monitoring results in phase 4 showed that the mechanical strength of the de novo disc developed is not only mechanically superior than the other TE discs in literature, but is also comparable to reported values for human native discs. Analogous to the highly negative proteoglycan content of the native NP, the similarly highly negative PVA used for the NP allows for water to be imbibed into the silk/PVA cryogels to form a swollen network. The swelling of the NP forms the lynchpin to the overarching strategy of the de novo disc assembly - whereby the pressure from the swelling translates to a circumferential tension and radial compression on the surrounding TE AF. The thin morphology of the knitted mats and hybrid laminates making up the TE AF also enabled the true recapitulation of the circumferentially aligned multi-ply architecture of the native AF to be achieved in the

de novo disc assembly. Dynamic compression culture of the de novo disc assembly, made possible by the development of a custom-built bioreactor, also showed that culturing the de novo disc under physiologically mimetic forces influences the development of the disc's ECM into a circumferential multi-ply like manner (similar as a native disc).

Work in this dissertation was divided into four main phases, with the objectives and hypotheses under each phase accomplished and answered. Taken in whole, the overarching objective of this dissertation, which is to develop a de novo IVD for potential whole disc replacement application, has been achieved.

7.2 Recommendations

7.2.1 Pertaining to Phase One

Recommendations for future work pertaining to phase one would involve developing a better understanding (Eg. from a molecular biology perspective) on the reduced differentiability of the ASC CSs as compared to the ASCs. Results showed that despite the CSs retaining the benefits of an intact ECM as demonstrated by the early differentiation genes expression study in the first part of the study, to successfully translate that advantage further downstream, other limiting factors must concurrently be eliminated as well. It can be hypothesized that the formation of an ECM layer above the layer of confluent cells in the CSI groups might have posed as a hindrance to the diffusion of nutrients and gaseous exchanges. Further studies can be conducted in this regard to confirm this hypothesis.

The local cell density of the micromass pellets should also be taken into consideration, given that the densities between the cell-sheet pellets and the non cell-sheet pellets would be quite different, and might affect the efficiency of chondrogenic differentiation. Future studies can take into consideration the possibilities of

controlling the volume of the pellets in relation to cell numbers and ECM volume through a series of optimization studies on cell and ECM volumes.

In all, results from phase one can potentially induce future research interests to assess ASCs or ASC CSs for other orthopedic TE applications over the more commonly used BMSCs. ASCs have already started to be explored for orthopedic applications. However ASCs were mostly induced into chondrogenic or osteogenic lineages and seeded onto scaffolds, co-cultured with other types of cells under undifferentiated conditions or directly injected into an interest site undifferentiated. The knowledge of handling and manipulating ASC CSs gained from phase one will serve as a cornerstone for future ASC CSs related work that can be potentially done in the orthopedic area. This can include the use of it in tendon/ligament regeneration, autologous bone grafts substitutes or exploring further applications of tissue regeneration

7.2.2 Pertaining to Phase Two

Recommendations for future work pertaining to phase two would involve developing ASC CSs that have aligned ECM deposition to draw on the advantages of an ECM rich CS, and yet having the benefit of a biomimicking aligned ECM. To do so, the use of thermosensitive culture plates with nanotopographies could be explored. Results from phase two have shown that it is difficult to get the CSs to remodel their ECM orientation after formation of the thick ECM layer. Hence, it would be more feasible to achieve alignment of the ECM during CS formation. In this thesis, the laminates developed in phase two is primarily to serve as the AF component of a whole disc replacement strategy. However, these laminates could potentially be developed as AF patches as well for early DDD cases. To successfully implement the laminates as AF patches in a clinical setting, further work on tissue sealants or anchorage strategies would need to be conducted.

7.2.3 Pertaining to Phase Three

In this thesis, the surface porosity of the cryogels was determined by applying an image processing algorithm on the SEM images (of the cryogels' cross-sections). This serves as an estimate on the overall porosity of the samples. However, the pores of the samples are not uniformly sized and the action of freeze snapping the cryogels might slightly disrupt the pores at the sectioned interfaces. Given so, a less disruptive and more accurate measurement technique (Eg. mercury porosimetry or liquid displacement) can be used for future studies instead to determine porosity (246).

The silk/PVA cryogel developed in phase 3 was intended for use as the NP component for a whole disc replacement strategy. However, the cryogel developed can also be applicable for use as an NP replacement prosthesis. Further work can be done in this regard. For example, the ultimate form for such an application can have a "bag" like outer layer for eventual clinical application, similar to some of the replacement devices already described in literature (Eg. PDN) (88,89). In this study, the generalized Hooke's law was used as a simple methodology to quantify the hoop stresses (swelling pressure) experienced in the cryogels. To quantify the hoop strains and stresses in a "bag-like" composite structure, a more sophisticated mathematical model as described by Hudgins and Muzzy (247) would perhaps be needed. Silk/PVA cryogels can potentially have better implant integration at the vertebral end-plates interface with its better cellular compliance. To reduce incidences of NP replacement device migration, and ultimately bridging the gap between NP regeneration and NP replacement, further work into the osteoconductivity and osteoinductivity of the silk/PVA material can be done.

7.2.4 Pertaining to Phase Four

Recommendations for further work would include improvements to the bioreactor developed. In the current version, the vertical displacement of the compression platen

was determined by the number of turns made by the actuator. This is depended on the screw thread pitch of the motor adaptor, which might deviate over time through wear and tear. A linear variable differential transformer (LVDT) could be added to the bioreactor system to enable accurate measurement of linear displacement. Frictional forces were present between the moving parts of the bioreactor as shown in phase 4b. For this dissertation, frictional load was calibrated and zero-ed from the load monitoring results. However, redesigning the bioreactor to incorporate linear bearings between the moving parts would be a better long-term solution to minimize friction.

As a proof-of-concept, a two weeks assessment time point was chosen for phase 4b. Further work could be conducted using longer assessment time points (Eg. 4 to 6 weeks) and using chondrogenic medium with the bioreactor to study the combinatory effects of both biochemical and mechanical cues. The angle-ply structure of the native AF was also not entirely recapitulated in this thesis due to technical difficulties in getting angled and aligned electrospun mats efficiently in ample amounts to build the de novo disc. Hence, although the multi-lamellar structure and aligned nano-fibres components were replicated in the current de novo disc, "angle-ing" the aligned nano fibres by slanting the aligned mats and cutting it at an angle, as described by Nerurkar and co-workers (8) previously, can be considered for further improvements in future studies.

7.3 Other Recommendations

Further to a longer and chondrogenic culture in the bioreactor would be the translation of the de novo disc to an animal model. The next phases of the project would involve several things: i) an ex vivo assessment of the developed de novo disc using organ culture, in conjunction with the load monitoring bioreactor, and ii) an in vivo assessment of the de novo disc in a suitable animal model.

7.3.1 Ex Vivo Assessment

An ex vivo assessment of the de novo disc have several advantages over just in vitro dynamic culture in the bioreactor. In particular, this involves re-creating a similar physiological environment under controlled conditions by which the de novo disc can be studied. For example, the hypoxic environment of the native IVD space, and the mechanical boundary and chemical diffusion conditions can be recreated and controlled with the use of organ culture in conjunction with a bioreactor system. Organ culture work in IVD have been reported in literature for the past 30 years (248). Due to the differences in matrix contents and nutrients/wastes transport characteristics, large animal models (Eg. Bovine, Ovine) are often preferred over small animal models (Eg. Murine, Lapine) in organ culture models (248). Bovine coccygeal and ovine coccygeal discs are well characterized in literature as organ culture models (248), having a diameter of ~22mm and ~15mm in diameter respectively. Interestingly, there is a dearth in data regarding the use of porcine coccygeal discs for organ culture. The ease of accessibility and availability under the Institution's tissue sharing program makes porcine coccygeal discs an attractive option. Preliminary work has been conducted to characterize some of the morphometric parameters of porcine coccygeal discs for future work. These results can be found in Appendix G.

7.3.2 In Vivo Assessment

In terms of a load bearing model for in vivo assessment of TE discs, Bowles and colleagues are the pioneers in this regard, describing the implantation of a TE whole disc, made using collagen and alginate, in the caudal spine of athymic rats (93). A recent paper by Martin et al (249) described the translation of the AF portion of the TE disc earlier published by Nerurkar and colleagues (70) from the same research group into the caudal spines of Sprague Dawley rats. Early findings of graft displacements by Martin and colleagues motivated the use of an external fixation

system designed to stabilize the disc space in the same study (249)]. Future work deriving from the de novo disc assembly of this thesis could use these studies as references for experimental design, including the development and use of an external stabilizer, and incorporating sacrificial layers of the construct to promote cell migration (as was done by Martin and colleagues (249)).

List of Journal Publications

Neo PY, See EYS, Toh SL, Goh JCH. Temporal profiling of the growth and multi-lineage potentiality of adipose tissue-derived mesenchymal stem cells cell-sheets. J Tissue Eng Regen Med. 2013. *(Accepted, Epub ahead of print)*

Neo PY, Tan DJA, Shi P, Toh SL, Goh JCH. Enhancing Analysis of Cells and Proteins by Fluorescence Imaging on Silk-Based Biomaterials: Modulating the Autofluorescence of Silk. Tissue Eng Part C Methods. 2014. *(Accepted, Epub ahead of print)*

Neo PY, Shi P, Toh SL, Goh JCH. Characterization and Mechanical Performance Study of Silk/PVA Cryogels: Towards Nucleus Pulposus Tissue Engineering. Biomedical Materials. 2014; 9(6).

Neo PY, See EY, Goh JCH, Toh SL. Assembly and Evaluation of a Mechanically Robust De Novo Disc-Like Construct and Physiologically Mimetic Bioreactor: Towards Intervertebral Disc Replacement. *(In prep)*

List of Awards

*Only awards attained as presenting author are listed.

- **SYIS Poster Presentation Award**

Neo PY, Goh JC, Toh SL. The Use Of Adipose-Tissue Derived Stem Cells And Highly Hierarchical Silk Laminates With Nanotopography For Annulus Fibrosus Tissue Engineering. Tissue Engineering and Regenerative Medicine International Society (TERMIS) Asia Pacific Meeting. September 24-27, 2014. Daegu, South Korea.

- **Gold Medal Award: Graduate Category, Oral Presentation**

Neo PY, Shi P, Goh JC, Toh SL. Intervertebral Disc Tissue Engineering: Towards Complete Disc Replacement with Silk/PVA Hydrogels. **Biomedical Engineering Society (Singapore) 8th Scientific Meeting**. May 17, 2014. Singapore.

- **Silver Award: Graduate Category, Technical (Oral) Presentation**

Neo PY, Toh SL, Goh JC. The Effect of Hyperconfluent Culture Duration on Differentiation Capabilities of Adipose-Derived Mesenchymal Stem Cells. **Biomedical Engineering Society (Singapore) 6th Scientific Meeting**. May 19, 2012. Singapore.

- **Oral Presentation Award**

Neo PY, See EY, Toh SL, Goh JC. Multi-lineage Potential of Cell-Sheets: A Comparative Study using Adipose-Tissue Derived Stem Cells. **5th East Asian Pacific Student Workshop on Nano-Biomedical Engineering**. December 12-14, 2011. Singapore.

List of Conferences

*Only conferences attended/attending as presenting author are listed.

1. **Neo PY**, Goh JC, Toh SL. Tissue Engineering a Mechanically Robust De Novo Intervertebral Disc Using Silk-Based Biomaterials, Adipose-derived Stem Cells and Physiologically Mimetic Culture. Orthopaedic Research Society (ORS) 2015 Annual Meeting. March 28-31, 2015. Las Vegas, USA. (Accepted for oral)

2. **Neo PY**, Shi P, Goh JC, Toh SL. The Use of Silk/PVA Cryogels for Intervertebral Disc Replacements: Tissue Engineering From a Biomechanics Perspective. International Conference on Experimental Mechanics. November 15-17, 2014. Singapore . (Oral)

3. **Neo PY**, Shi P, Goh JC, Toh SL. The Use Of Silk/PVA Hydrogels For Nucleus Pulposus Tissue Engineering: Towards Whole Disc Replacement. Tissue Engineering and Regenerative Medicine International Society (TERMIS) Asia Pacific Meeting. September 24-27, 2014. Daegu, South Korea. (Poster)

4. **Neo PY**, Goh JC, Toh SL. The Use Of Adipose-Tissue Derived Stem Cells And Highly Hierarchical Silk Laminates With Nanotopography For Annulus Fibrosus Tissue Engineering. Tissue Engineering and Regenerative Medicine International Society (TERMIS) Asia Pacific Meeting. September 24-27, 2014. Daegu, South Korea. (Poster)

5. **Neo PY**, Shi P, Goh JC, Toh SL. Intervertebral Disc Tissue Engineering: Towards Complete Disc Replacement with Silk/PVA Hydrogels. Biomedical Engineering Society (Singapore) 8th Scientific Meeting. May 17, 2014. Singapore. (Oral)

6. **Neo PY**, Shi P, Goh JC, Toh SL. Tissue Engineering the Intervertebral Disc: A Whole Disc Approach Using Silk-Derived Scaffolds and Hydrogels with Adipose-Derived Stem Cells. 15th International Conference on Biomedical Engineering (ICBME 2013). December 4-7, 2013. Singapore. (Oral)

7. **Neo PY**, Shi P, Goh JC, Toh SL. Tissue Engineering the Intervertebral Disc with Adipose-Tissue Derived Stem Cells and Silk-Derived Biomaterials. Tissue

Engineering and Regenerative Medicine International Society (TERMIS) Asia Pacific Meeting. October 23-26, 2013. Shanghai and Wuzhen, China. (Oral)

8. **Neo PY**, Goh JC, Toh SL. Tissue Engineering the Intervertebral Disc – A De Novo Annulus Fibrosus with Adipose-Tissue Derived Stem Cells, Nano Silk Mats and Cell-Sheet Engineering. Biomedical Engineering Society (Singapore) 7th Scientific Meeting. May 18, 2013. Singapore. (Oral)

9. **Neo PY**, Goh JC, Toh SL. Tissue Engineering a De Novo Annulus Fibrosus - Combining Adipose-Tissue Derived Mesenchymal Stem Cells with Electrospun Silk Mats and Chondrogenic Induction Culture. Orthopaedic Research Society (ORS) 2013 Annual Meeting. January 26-29, 2013. San Antonio, USA. (Poster)

10. **Neo PY**, See EY, Toh SL, Goh JC. The Use of Adipose Derived Stem Cells and Cell-Sheets for Inner and Outer Annulus Fibrosus Regeneration. 3rd TERMIS World Congress. September 5-8, 2012. Vienna, Austria. (Poster)

11. **Neo PY**, See EY, Toh SL, Goh JC. Adipose-Tissue Derived Stem Cells Cell-Sheets for Regeneration of the Annulus Fibrosus. 9th World Biomaterials Congress (WBC). June 1-5, 2012. Chengdu, China. (Oral)

12. **Neo PY**, Toh SL, Goh JC. The Effect of Hyperconfluent Culture Duration on Differentiation Capabilities of Adipose-Derived Mesenchymal Stem Cells. Biomedical Engineering Society (Singapore) 6th Scientific Meeting. May 19, 2012. Singapore. (Oral)

13. **Neo PY**, See EY, Toh SL, Goh JC. Multi-lineage Potential of Cell-Sheets: A Comparative Study using Adipose-Tissue Derived Stem Cells. 5th East Asian Pacific Student Workshop on Nano-Biomedical Engineering. December 12-14, 2011. Singapore. (Oral)

14. **Neo PY**, See EY, Toh SL, Goh JC. Cell-sheet Tissue Engineering: A Characterization and Multilineage Potential Study of Adipose Tissue Derived Stem Cells Cell-Sheets. Tissue Engineering and Regenerative Medicine International Society (TERMIS) Asia Pacific Meeting. August 3-5, 2011. Singapore. (Poster)

References

1. Andersson GBJ. Epidemiological features of chronic low-back pain. The lancet. 1999;354(9178):581-5.

2. Walker BF. The prevalence of low back pain: a systematic review of the literature from 1966 to 1998. Journal of Spinal Disorders & Techniques. 2000;13(3):205-17.

3. Shapiro IM, Risbud MV. Introduction to the Structure, Function, and Comparative Anatomy of the Vertebrae and the Intervertebral Disc. 2014:3-15.

4. Takahashi K, Aoki Y, Ohtori S. Resolving discogenic pain. European Spine Journal. 2008;17(4):428-31.

5. Alini M, Li W, Markovic P, Aebi M, Spiro RC, Roughley PJ. The potential and limitations of a cell-seeded collagen/hyaluronan scaffold to engineer an intervertebral disc-like matrix. Spine. 2003;28(5):446-53.

6. Hukins DWL. Tissue engineering: A live disc. Nature materials. 2005;4(12):881-2.

7. Mizuno H, Roy AK, Vacanti CA, Kojima K, Ueda M, Bonassar LJ. Tissue-engineered composites of anulus fibrosus and nucleus pulposus for intervertebral disc replacement. Spine. 2004;29(12):1290-7.

8. Nerurkar NL, Baker BM, Sen S, Wible EE, Elliott DM, Mauck RL. Nanofibrous biologic laminates replicate the form and function of the annulus fibrosus. Nature materials. 2009;8(12):986-92.

9. Iatridis JC, Nicoll SB, Michalek AJ, Walter BA, Gupta MS. Role of biomechanics in intervertebral disc degeneration and regenerative therapies: what

needs repairing in the disc and what are promising biomaterials for its repair? The Spine Journal. 2013;13(3):243-62.

10. O'Halloran DM, Pandit AS. Tissue-engineering approach to regenerating the intervertebral disc. Tissue engineering. 2007;13(8):1927-54.

11. Roberts S, Menage J, Urban JPG. Biochemical and structural properties of the cartilage end-plate and its relation to the intervertebral disc. Spine. 1989;14(2):166-74.

12. Klein JA, Hickey DS, Hukins DWL. Radial bulging of the annulus fibrosus during compression of the intervertebral disc. Journal of biomechanics. 1983;16(3):211-7.

13. Hickey DS, Hukins DW. Collagen fibril diameters and elastic fibres in the annulus fibrosus of human fetal intervertebral disc. Journal of anatomy. 1981;133(Pt 3):351.

14. Hickey DS, Hukins DW. X-ray diffraction studies of the arrangement of collagenous fibres in human fetal intervertebral disc. Journal of anatomy. 1980;131(Pt 1):81.

15. Roberts S, Evans H, Trivedi J, Menage J. Histology and pathology of the human intervertebral disc. The Journal of Bone & Joint Surgery. 2006;88(suppl_2):10-4.

16. Urban J. Disc biochemistry in relation to function. The lumbar spine. 1996;1:271-81.

17. Holm SH. Nutritional and pathophysiologic aspects of the lumbar intervertebral disc. The lumbar spine WB Saunders, Philadelphia. 1996:285-310.

18. Eyre DR, Muir H. Types I and II collagens in intervertebral disc. Interchanging radial distributions in annulus fibrosus. Biochemical Journal. 1976;157(1):267.

19. Smith LJ, Fazzalari NL. The elastic fibre network of the human lumbar anulus fibrosus: architecture, mechanical function and potential role in the progression of intervertebral disc degeneration. European Spine Journal. 2009;18(4):439-48.

20. Cortes DH, Elliot Dawn M. The Intervertebral Disc: Overview of Disc Mechanics. In: Shapiro IM, Risbud MV, editors. The Intervertebral Disc. Wien2014. p. 17-31.

21. Nosikova YS, Santerre JP, Grynpas M, Gibson G, Kandel RA. Characterization of the annulus fibrosus–vertebral body interface: identification of new structural features. Journal of anatomy. 2012;221(6):577-89.

22. Olmarker K. Back Pain and Disc Degeneration: Are They Really Linked? In: Shapiro I, Risbud MV, editors. The Intervertebral Disc: Springer; 2014. p. 261-73.

23. Richardson SM, Freemont AJ, Hoyland JA. Pathogenesis of Intervertebral Disc Degeneration. In: Shapiro IM, Risbud MV, editors. The Intervertebral Disc. Wien: Springer; 2014. p. 177-200.

24. Lutz GK, Butzlaff M, Schultz-Venrath U. Looking back on back pain: trial and error of diagnoses in the 20th century. Spine. 2003;28(16):1899-905.

25. Chou D, Samartzis D, Bellabarba C, Patel A, Luk KDK, Kisser JMS, et al. Degenerative magnetic resonance imaging changes in patients with chronic low back pain: a systematic review. Spine. 2011;36:S43-S53.

26. Cheung KMC, Karppinen J, Chan D, Ho DWH, Song Y-Q, Sham P, et al. Prevalence and pattern of lumbar magnetic resonance imaging changes in a population study of one thousand forty-three individuals. Spine. 2009;34(9):934-40.

27. Whatley BR, Wen X. Intervertebral disc (IVD): Structure, degeneration, repair and regeneration. Materials Science and Engineering: C. 2012;32(2):61-77.

28. Sztrolovics R, Alini M, Roughley P, Mort J. Aggrecan degradation in human intervertebral disc and articular cartilage. Biochem J. 1997;326:235-41.

29. Sztrolovics R, Grover J, Cs-Szabo G, Shi SL, Zhang Y, Mort JS, et al. The characterization of versican and its message in human articular cartilage and intervertebral disc. Journal of orthopaedic research. 2002;20(2):257-66.

30. Peng B, Hao J, Hou S, Wu W, Jiang D, Fu X, et al. Possible pathogenesis of painful intervertebral disc degeneration. Spine. 2006;31(5):560-6.

31. Freemont AJ, Watkins A, Le Maitre C, Baird P, Jeziorska M, Knight MTN, et al. Nerve growth factor expression and innervation of the painful intervertebral disc. The Journal of pathology. 2002;197(3):286-92.

32. Frino J, McCarthy RE, Sparks CY, McCullough FL. Trends in adolescent lumbar disk herniation. Journal of Pediatric Orthopaedics. 2006;26(5):579-81.

33. Gabr MA, Jing L, Helbling AR, Sinclair SM, Allen KD, Shamji MF, et al. Interleukin-17 synergizes with IFNγ or TNFα to promote inflammatory mediator release and intercellular adhesion molecule-1 (ICAM-1) expression in human intervertebral disc cells. Journal of Orthopaedic Research. 2011;29(1):1-7.

34. Studer RK, Vo N, Sowa G, Ondeck C, Kang J. Human nucleus pulposus cells react to IL-6: independent actions and amplification of response to IL-1 and TNF-α. Spine. 2011;36(8):593-9.

35. Le Maitre CL, Freemont AJ, Hoyland JA. The role of interleukin-1 in the pathogenesis of human intervertebral disc degeneration. Arthritis Res Ther. 2005;7(4):R732-R45.

36. Deyo RA, Weinstein JN. Low back pain affects men and women equally, with onset most often between the ages of 30 and 50 years. It is the most common cause of work-related disability in people under 45 years of age and the most expensive. N Engl J Med. 2001;344(5).

37. McGirt MJ, Eustacchio S, Varga P, Vilendecic M, Trummer M, Gorensek M, et al. A prospective cohort study of close interval computed tomography and magnetic resonance imaging after primary lumbar discectomy: factors associated with recurrent disc herniation and disc height loss. Spine. 2009;34(19):2044-51.

38. Lebow RL, Adogwa O, Parker SL, Sharma A, Cheng J, McGirt MJ. Asymptomatic same-site recurrent disc herniation after lumbar discectomy: results of a prospective longitudinal study with 2-year serial imaging. Spine. 2011;36(25):2147-51.

39. Inc R, Richmond VA, DePalma MJ, Director ISC, Biotech S. Is the history of a surgical discectomy related to the source of chronic low back pain? Pain physician. 2012;15:E53-E8.

40. Guterl CC, See EY, Blanquer SBG, Pandit A, Ferguson SJ, Benneker LM, et al. Challenges and strategies in the repair of ruptured annulus fibrosus. European cells & materials. 2013;25:1.

41. Ahlgren BD, Lui W, Herkowitz HN, Panjabi MM, Guiboux J-P. Effect of anular repair on the healing strength of the intervertebral disc: a sheep model. Spine. 2000;25(17):2165-70.

42. Carragee EJ, Han MY, Suen PW, Kim D. Clinical outcomes after lumbar discectomy for sciatica: the effects of fragment type and anular competence. The Journal of Bone & Joint Surgery. 2003;85(1):102-8.

43. Deyo RA, Gray DT, Kreuter W, Mirza S, Martin BI. United States trends in lumbar fusion surgery for degenerative conditions. Spine. 2005;30(12):1441-5.

44. Levin DA, Hale JJ, Bendo JA. Adjacent segment degeneration following spinal fusion for degenerative disc disease. BULLETIN-HOSPITAL FOR JOINT DISEASES NEW YORK. 2007;65(1):29.

45. Harrop JS, Youssef JA, Maltenfort M, Vorwald P, Jabbour P, Bono CM, et al. Lumbar adjacent segment degeneration and disease after arthrodesis and total disc arthroplasty. Spine. 2008;33(15):1701-7.

46. Freeman BJC, Davenport J. Total disc replacement in the lumbar spine: a systematic review of the literature. European Spine Journal. 2006;15(3):439-47.

47. Costi JJ, Freeman BJC, Elliott DM. Intervertebral disc properties: challenges for biodevices. Expert Rev Med Devices. 2011;8(3):357-76.

48. Ross ERS. Revision in artificial disc replacement. The Spine Journal. 2009;9(9):773-5.

49. Cunningham BW, Hu N, Beatson HJ, Serhan H, Sefter JC, McAfee PC. Revision strategies for single-and two-level total disc arthroplasty procedures: a biomechanical perspective. The Spine Journal. 2009;9(9):735-43.

50. Kurtz SM, van Ooij A, Ross R, de Waal Malefijt J, Peloza J, Ciccarelli L, et al. Polyethylene wear and rim fracture in total disc arthroplasty. The Spine Journal. 2007;7(1):12-21.

51. Resnick DK, Watters WC. Lumbar disc arthroplasty: a critical review. Clinical neurosurgery. 2006;54:83-7.

52. Bae WC, Masuda K. Enhancing Disc Repair by Growth Factors and Other Modalities. In: Shapiro IM, Risbud MV, editors. The Intervertebral Disc. Wien: Springer; 2014. p. 401-16.

53. Thompson JP, Oegema TR, Bradford D. Stimulation of mature canine intervertebral disc by growth factors. Spine. 1991;16(3):253-60.

54. Gruber HE, Fisher Jr EC, Desai B, Stasky AA, Hoelscher G, Hanley Jr EN. Human intervertebral disc cells from the annulus: three-dimensional culture in agarose or alginate and responsiveness to TGF-β1. Experimental cell research. 1997;235(1):13-21.

55. Genevay S, Finckh A, Mezin F, Tessitore E, Guerne P-A. Influence of cytokine inhibitors on concentration and activity of MMP-1 and MMP-3 in disc herniation. Arthritis Research and Therapy. 2009;11(6):R169.

56. Kim D-J, Moon S-H, Kim H, Kwon U-H, Park M-S, Han K-J, et al. Bone morphogenetic protein-2 facilitates expression of chondrogenic, not osteogenic, phenotype of human intervertebral disc cells. Spine. 2003;28(24):2679-84.

57. Mwale F, Pichika R, Epure L, Yoshikawa T, Hemmad A, Bokar M, et al. The efficacy of Link N as a mediator of repair in a rabbit model of intervertebral disc degeneration. Spine Journal. 2010;10(9):6.

58. Langer R, Vacanti JP. Tissue engineering. Science (New York, NY). 1993;260(5110):920-6.

59. Williams DF. On the nature of biomaterials. Biomaterials. 2009;30(30):5897-909.

60. Michalek AJ, Gardner-Morse MG, Iatridis JC. Large residual strains are present in the intervertebral disc annulus fibrosus in the unloaded state. Journal of biomechanics. 2012;45(7):1227-31.

61. Jin L, Shimmer AL, Li X. The challenge and advancement of annulus fibrosus tissue engineering. European Spine Journal. 2013;22(5):1090-100.

62. Sato M, Asazuma T, Ishihara M, Kikuchi T, Masuoka K, Ichimura S, et al. An atelocollagen honeycomb-shaped scaffold with a membrane seal (ACHMS-scaffold) for the culture of annulus fibrosus cells from an intervertebral disc. Journal of Biomedical Materials Research Part A. 2003;64(2):248-56.

63. Chang G, Kim HJ, Vunjak-Novakovic G, Kaplan DL, Kandel R. Enhancing annulus fibrosus tissue formation in porous silk scaffolds. Journal of Biomedical Materials Research Part A. 2010;92(1):43-51.

64. Chang G, Kim HJ, Kaplan D, Vunjak-Novakovic G, Kandel RA. Porous silk scaffolds can be used for tissue engineering annulus fibrosus. European Spine Journal. 2007;16(11):1848-57.

65. Vadalà G, Mozetic P, Rainer A, Centola M, Loppini M, Trombetta M, et al. Bioactive electrospun scaffold for annulus fibrosus repair and regeneration. European Spine Journal. 2012;21(1):20-6.

66. Koepsell L, Zhang L, Neufeld D, Fong H, Deng Y. Electrospun nanofibrous polycaprolactone scaffolds for tissue engineering of annulus fibrosus. Macromolecular bioscience. 2011;11(3):391-9.

67. Nerurkar NL, Elliott DM, Mauck RL. Mechanics of oriented electrospun nanofibrous scaffolds for annulus fibrosus tissue engineering. Journal of orthopaedic research. 2007;25(8):1018-28.

68. Shao X, Hunter CJ. Developing an alginate/chitosan hybrid fiber scaffold for annulus fibrosus cells. Journal of Biomedical Materials Research Part A. 2007;82(3):701-10.

69. Bowles RD, Williams RM, Zipfel WR, Bonassar LJ. Self-assembly of aligned tissue-engineered annulus fibrosus and intervertebral disc composite via collagen gel contraction. Tissue Engineering Part A. 2010;16(4):1339-48.

70. Nerurkar NL, Sen S, Huang AH, Elliott DM, Mauck RL. Engineered disc-like angle-ply structures for intervertebral disc replacement. Spine. 2010;35(8):867.

71. Pereira DR, Silva-Correia J, Oliveira JM, Reis RL. Hydrogels in acellular and cellular strategies for intervertebral disc regeneration. Journal of tissue engineering and regenerative medicine. 2013;7(2):85-98.

72. Sasson A, Patchornik S, Eliasy R, Robinson D, Haj-Ali R. Hyperelastic mechanical behavior of chitosan hydrogels for nucleus pulposus replacement—Experimental testing and constitutive modeling. Journal of the mechanical behavior of biomedical materials. 2012;8:143-53.

73. Chou AI, Akintoye SO, Nicoll SB. Photo-crosslinked alginate hydrogels support enhanced matrix accumulation by nucleus pulposus cells in vivo. Osteoarthritis and Cartilage. 2009;17(10):1377-84.

74. Chou AI, Nicoll SB. Characterization of photocrosslinked alginate hydrogels for nucleus pulposus cell encapsulation. Journal of Biomedical Materials Research Part A. 2009;91(1):187-94.

75. Wilke H-J, Heuer F, Neidlinger-Wilke C, Claes L. Is a collagen scaffold for a tissue engineered nucleus replacement capable of restoring disc height and stability in an animal model? European Spine Journal. 2006;15(3):433-8.

76. Bron JL, Koenderink GH, Everts V, Smit TH. Rheological characterization of the nucleus pulposus and dense collagen scaffolds intended for functional replacement. Journal of Orthopaedic Research. 2009;27(5):620-6.

77. Cloyd JM, Malhotra NR, Weng L, Chen W, Mauck RL, Elliott DM. Material properties in unconfined compression of human nucleus pulposus, injectable hyaluronic acid-based hydrogels and tissue engineering scaffolds. European Spine Journal. 2007;16(11):1892-8.

78. Park S-H, Cho H, Gil ES, Mandal BB, Min B-H, Kaplan DL. Silk-fibrin/hyaluronic acid composite gels for nucleus pulposus tissue regeneration. Tissue Engineering Part A. 2011;17(23-24):2999-3009.

79. Silva-Correia J, Oliveira JM, Caridade SG, Oliveira JT, Sousa RA, Mano JF, et al. Gellan gum-based hydrogels for intervertebral disc tissue-engineering applications. Journal of tissue engineering and regenerative medicine. 2011;5(6):e97-e107.

80. Bron JL, van der Veen AJ, Helder MN, van Royen BJ, Smit TH. Biomechanical and in vivo evaluation of experimental closure devices of the annulus fibrosus designed for a goat nucleus replacement model. European Spine Journal. 2010;19(8):1347-55.

81. Schek RM, Michalek AJ, Iatridis JC. Genipin-crosslinked fibrin hydrogels as a potential adhesive to augment intervertebral disc annulus repair. European cells & materials. 2011;21:373.

82. Reitmaier S, Wolfram U, Ignatius A, Wilke H-J, Gloria A, Martín-Martínez JM, et al. Hydrogels for nucleus replacement—Facing the biomechanical challenge. journal of the mechanical behavior of biomedical materials. 2012;14:67-77.

83. Wiltsey C, Kubinski P, Christiani T, Toomer K, Sheehan J, Branda A, et al. Characterization of injectable hydrogels based on poly (N-isopropylacrylamide)-g-chondroitin sulfate with adhesive properties for nucleus pulposus tissue engineering. Journal of Materials Science: Materials in Medicine. 2013;24(4):837-47.

84. Bertagnoli R, Sabatino CT, Edwards JT, Gontarz GA, Prewett A, Parsons JR. Mechanical testing of a novel hydrogel nucleus replacement implant. The Spine Journal. 2005;5(6):672-81.

85. Carl A, Ledet E, Yuan H, Sharan A. New developments in nucleus pulposus replacement technology. The Spine Journal. 2004;4(6):S325-S9.

86. Wang BH, Campbell G. Formulations of polyvinyl alcohol cryogel that mimic the biomechanical properties of soft tissues in the natural lumbar intervertebral disc. Spine. 2009;34(25):2745-53.

87. Joshi A, Fussell G, Thomas J, Hsuan A, Lowman A, Karduna A, et al. Functional compressive mechanics of a PVA/PVP nucleus pulposus replacement. Biomaterials. 2006;27(2):176-84.

88. Ray CD. The PDN® prosthetic disc-nucleus device. European Spine Journal. 2002;11(2):S137-S42.

89. Klara PM, Ray CD. Artificial nucleus replacement: clinical experience. Spine. 2002;27(12):1374-7.

90. Nerurkar NL, Elliott DM, Mauck RL. Mechanical design criteria for intervertebral disc tissue engineering. Journal of biomechanics. 2010;43(6):1017-30.

91. Mizuno H, Roy AK, Zaporojan V, Vacanti CA, Ueda M, Bonassar LJ. Biomechanical and biochemical characterization of composite tissue-engineered intervertebral discs. Biomaterials. 2006;27(3):362-70.

92. Nerurkar NL, Sen S, Baker BM, Elliott DM, Mauck RL. Dynamic culture enhances stem cell infiltration and modulates extracellular matrix production on aligned electrospun nanofibrous scaffolds. Acta biomaterialia. 2011;7(2):485-91.

93. Bowles RD, Gebhard HH, Härtl R, Bonassar LJ. Tissue-engineered intervertebral discs produce new matrix, maintain disc height, and restore biomechanical function to the rodent spine. Proceedings of the National Academy of Sciences. 2011;108(32):13106-11.

94. Nesti LJ, Li W-J, Shanti RM, Jiang YJ, Jackson W, Freedman BA, et al. Intervertebral disc tissue engineering using a novel hyaluronic acid–nanofibrous scaffold (HANFS) amalgam. Tissue Engineering Part A. 2008;14(9):1527-37.

95. Park SH, Gil ES, Mandal BB, Cho H, Kluge JA, Min BH, et al. Annulus fibrosus tissue engineering using lamellar silk scaffolds. Journal of tissue engineering and regenerative medicine. 2012;6(S3):s24-s33.

96. Park S-H, Gil ES, Cho H, Mandal BB, Tien LW, Min B-H, et al. Intervertebral disk tissue engineering using biphasic silk composite scaffolds. Tissue Engineering Part A. 2011;18(5-6):447-58.

97. Bhattacharjee M, Chameettachal S, Pahwa S, Ray AR, Ghosh S. Strategies for replicating anatomical cartilaginous tissue gradient in engineered Intervertebral disc. ACS applied materials & interfaces. 2013;6(1):183-93.

98. Bhattacharjee M, Miot S, Gorecka A, Singha K, Loparic M, Dickinson S, et al. Oriented lamellar silk fibrous scaffolds to drive cartilage matrix orientation: towards annulus fibrosus tissue engineering. Acta biomaterialia. 2012;8(9):3313-25.

99. Lazebnik M, Singh M, Glatt P, Friis LA, Berkland CJ, Detamore MS. Biomimetic method for combining the nucleus pulposus and annulus fibrosus for

intervertebral disc tissue engineering. Journal of tissue engineering and regenerative medicine. 2011;5(8):e179-e87.

100. Chik TK, Chooi WH, Li YY, Ho FC, Cheng HW, Choy TH, et al. Bioengineering a Multicomponent Spinal Motion Segment Construct—A 3D Model for Complex Tissue Engineering. Advanced healthcare materials. 2014.

101. Tsai T-L, Nelson BC, Anderson PA, Zdeblick TA, Li W-J. Intervertebral Disc and Stem Cells Co-cultured in Biomimetic Extracellular Matrix Stimulated by Cyclic Compression in Perfusion Bioreactor. The Spine Journal. 2014.

102. See EY-S, Toh SL, Goh JCH. Simulated intervertebral disc-like assembly using bone marrow-derived mesenchymal stem cell sheets and silk scaffolds for annulus fibrosus regeneration. Journal of tissue engineering and regenerative medicine. 2011.

103. Arthur A, Zannettino A, Gronthos S. The therapeutic applications of multipotential mesenchymal/stromal stem cells in skeletal tissue repair. Journal of cellular physiology. 2009;218(2):237-45.

104. Asanuma H, Meldrum DR, Meldrum KK. Therapeutic applications of mesenchymal stem cells to repair kidney injury. The Journal of urology. 2010;184(1):26-33.

105. Kagami H, Agata H, Tojo A. Bone marrow stromal cells (bone marrow-derived multipotent mesenchymal stromal cells) for bone tissue engineering: basic science to clinical translation. The international journal of biochemistry & cell biology. 2011;43(3):286-9.

106. Hanson SE, Gutowski KA, Hematti P. Clinical applications of mesenchymal stem cells in soft tissue augmentation. Aesthetic surgery journal / the American Society for Aesthetic Plastic surgery. 2010;30(6):838-42.

107. Soejitno A, Wihandani DM, Kuswardhani RAT. Clinical applications of stem cell therapy for regenerating the heart. Acta medica Indonesiana. 2010;42(4):243-57.

108. Joe AW, Gregory-Evans K. Mesenchymal stem cells and potential applications in treating ocular disease. Current eye research. 2010;35(11):941-52.

109. Estes BT, Diekman BO, Gimble JM, Guilak F. Isolation of adipose-derived stem cells and their induction to a chondrogenic phenotype. Nature protocols. 2010;5(7):1294-311.

110. Bunnell BA, Flaat M, Gagliardi C, Patel B, Ripoll C. Adipose-derived stem cells: isolation, expansion and differentiation. Methods (San Diego, Calif). 2008;45(2):115-20.

111. Augello A, Kurth TB, De Bari C. Mesenchymal stem cells: a perspective from in vitro cultures to in vivo migration and niches. European cells & materials. 2010;20:121-33.

112. Chamberlain G, Fox J, Ashton B, Middleton J. Concise review: mesenchymal stem cells: their phenotype, differentiation capacity, immunological features, and potential for homing. Stem cells (Dayton, Ohio). 2007;25(11):2739-49.

113. Fraser JK, Wulur I, Alfonso Z, Hedrick MH. Fat tissue: an underappreciated source of stem cells for biotechnology. Trends in biotechnology. 2006;24(4):150-4.

114. Fraser JK, Zhu M, Wulur I, Alfonso Z. Adipose-derived stem cells. Methods in molecular biology (Clifton, NJ). 2008;449:59-67.

115. Mosna F, Sensebé L, Krampera M. Human bone marrow and adipose tissue mesenchymal stem cells: a user's guide. Stem cells and development. 2010;19(10):1449-70.

116. Ying C, Hu W, Cheng B, Zheng X, Li S. Neural differentiation of rat adipose-derived stem cells in vitro. Cellular and molecular neurobiology. 2012;32(8):1255-63.

117. Masuda S, Shimizu T, Yamato M, Okano T. Cell sheet engineering for heart tissue repair. Advanced drug delivery reviews. 2008;60(2):277-85.

118. Ito A, Hayashida M, Honda H, Hata K-I, Kagami H, Ueda M, et al. Construction and harvest of multilayered keratinocyte sheets using magnetite nanoparticles and magnetic force. Tissue engineering. 2004;10(5-6):873-80.

119. Akiyama H, Ito A, Kawabe Y, Kamihira M. Genetically engineered angiogenic cell sheets using magnetic force-based gene delivery and tissue fabrication techniques. Biomaterials. 2010;31(6):1251-9.

120. Guillaume-Gentil O, Gabi M, Zenobi-Wong M, Vörös J. Electrochemically switchable platform for the micro-patterning and release of heterotypic cell sheets. Biomedical microdevices. 2011;13(1):221-30.

121. Zahn R, Thomasson E, Guillaume-Gentil O, Vörös J, Zambelli T. Ion-induced cell sheet detachment from standard cell culture surfaces coated with polyelectrolytes. Biomaterials. 2012;33(12):3421-7.

122. Nagai N, Yunoki S, Satoh Y, Tajima K, Munekata M. A method of cell-sheet preparation using collagenase digestion of salmon atelocollagen fibrillar gel. Journal of bioscience and bioengineering. 2004;98(6):493-6.

123. Shimizu T, Yamato M, Kikuchi A, Okano T. Cell sheet engineering for myocardial tissue reconstruction. Biomaterials. 2003;24(13):2309-16.

124. L'Heureux N, Pâquet S, Labbé R, Germain L, Auger FA. A completely biological tissue-engineered human blood vessel. FASEB journal : official publication of the Federation of American Societies for Experimental Biology. 1998;12(1):47-56.

125. Kushida A, Yamato M, Konno C, Kikuchi A, Sakurai Y, Okano T. Temperature-responsive culture dishes allow nonenzymatic harvest of differentiated Madin-Darby canine kidney (MDCK) cell sheets. Journal of biomedical materials research. 2000;51(2):216-23.

126. Thibault RA, Scott Baggett L, Mikos AG, Kasper FK. Osteogenic differentiation of mesenchymal stem cells on pregenerated extracellular matrix scaffolds in the absence of osteogenic cell culture supplements. Tissue engineering Part A. 2010;16(2):431-40.

127. Nicholas DE, Eileen G, Xinyong C, Clive JR, Julia MP, Molly MS. Extracellular matrix-mediated osteogenic differentiation of murine embryonic stem cells. Biomaterials. 2010;31(12):3244-52.

128. Chen C, Loe F, Blocki A, Peng Y, Raghunath M. Applying macromolecular crowding to enhance extracellular matrix deposition and its remodeling in vitro for tissue engineering and cell-based therapies. Advanced drug delivery reviews. 2011;63(4-5):277-90.

129. See EY-S, Toh SL, Goh JCH. Multilineage potential of bone-marrow-derived mesenchymal stem cell cell sheets: implications for tissue engineering. Tissue engineering Part A. 2010;16(4):1421-31.

130. Altman GH, Diaz F, Jakuba C, Calabro T, Horan RL, Chen J, et al. Silk-based biomaterials. Biomaterials. 2003;24(3):401-16.

131. Vepari C, Kaplan DL. Silk as a biomaterial. Progress in polymer science. 2007;32(8):991-1007.

132. Yang Y, Shao Z, Chen X, Zhou P. Optical spectroscopy to investigate the structure of regenerated Bombyx mori silk fibroin in solution. Biomacromolecules. 2004;5(3):773-9.

133. Rockwood DN, Preda RC, Yücel T, Wang X, Lovett ML, Kaplan DL. Materials fabrication from Bombyx mori silk fibroin. Nature protocols. 2011;6(10):1612-31.

134. Wenk E, Wandrey AJ, Merkle HP, Meinel L. Silk fibroin spheres as a platform for controlled drug delivery. Journal of Controlled Release. 2008;132(1):26-34.

135. Wenk E, Merkle HP, Meinel L. Silk fibroin as a vehicle for drug delivery applications. Journal of Controlled Release. 2011;150(2):128-41.

136. Teh TKH, Toh S-L, Goh JCH. Aligned hybrid silk scaffold for enhanced differentiation of mesenchymal stem cells into ligament fibroblasts. Tissue Engineering Part C: Methods. 2011;17(6):687-703.

137. Kim D-H, Viventi J, Amsden JJ, Xiao J, Vigeland L, Kim Y-S, et al. Dissolvable films of silk fibroin for ultrathin conformal bio-integrated electronics. Nature materials. 2010;9(6):511-7.

138. Lakowicz JR. Principles of Fluorescence Spectroscopy: Springer; 2007. 980 p.

139. Georgakoudi I, Tsai I, Greiner C, Wong C, DeFelice J, Kaplan D. Intrinsic fluorescence changes associated with the conformational state of silk fibroin in biomaterial matrices. Optics express. 2007;15(3):1043-53.

140. Coleman R. The impact of histochemistry–a historical perspective. Acta histochemica. 2000;102(1):5-14.

141. Reneker DH, Chun I. Nanometre diameter fibres of polymer, produced by electrospinning. Nanotechnology. 1996;7(3):216.

142. Shin YM, Hohman MM, Brenner MP, Rutledge GC. Experimental characterization of electrospinning: the electrically forced jet and instabilities. Polymer. 2001;42(25):09955-67.

143. Teo WE, Ramakrishna S. A review on electrospinning design and nanofibre assemblies. Nanotechnology. 2006;17(14):R89.

144. Lannutti J, Reneker D, Ma T, Tomasko D, Farson D. Electrospinning for tissue engineering scaffolds. Materials Science and Engineering: C. 2007;27(3):504-9.

145. Kumbar SG, James R, Nukavarapu SP, Laurencin CT. Electrospun nanofiber scaffolds: engineering soft tissues. Biomedical Materials. 2008;3(3):034002.

146. Ma Z, Kotaki M, Inai R, Ramakrishna S. Potential of nanofiber matrix as tissue-engineering scaffolds. Tissue engineering. 2005;11(1-2):101-9.

147. Nair LS, Bhattacharyya S, Laurencin CT. Nanotechnology and tissue engineering: the scaffold based approach. Nanotechnologies for the Life Sciences. 2006.

148. Lee CH, Shin HJ, Cho IH, Kang Y-M, Kim I, Park K-D, et al. Nanofiber alignment and direction of mechanical strain affect the ECM production of human ACL fibroblast. Biomaterials. 2005;26(11):1261-70.

149. Vaquette C, Kahn C, Frochot C, Nouvel C, Six JL, De Isla N, et al. Aligned poly (L-lactic-co-e-caprolactone) electrospun microfibers and knitted structure: A novel composite scaffold for ligament tissue engineering. Journal of Biomedical Materials Research Part A. 2010;94(4):1270-82.

150. Spadaccio C, Rainer A, Trombetta M, Vadalá G, Chello M, Covino E, et al. Poly-L-lactic acid/hydroxyapatite electrospun nanocomposites induce chondrogenic differentiation of human MSC. Annals of biomedical engineering. 2009;37(7):1376-89.

151. Yim EKF, Leong KW. Significance of synthetic nanostructures in dictating cellular response. Nanomedicine: Nanotechnology, Biology and Medicine. 2005;1(1):10-21.

152. Agarwal S, Wendorff JH, Greiner A. Use of electrospinning technique for biomedical applications. Polymer. 2008;49(26):5603-21.

153. Martin I, Wendt D, Heberer M. The role of bioreactors in tissue engineering. TRENDS in Biotechnology. 2004;22(2):80-6.

154. Plunkett N, O'Brien FJ. Bioreactors in tissue engineering. Technology and Health Care. 2011;19(1):55-69.

155. Altman G, Horan R, Martin I, Farhadi J, Stark P, Volloch V, et al. Cell differentiation by mechanical stress. Faseb Journal. 2002;16(2):270-2.

156. Chan SCW, Ferguson SJ, Gantenbein-Ritter B. The effects of dynamic loading on the intervertebral disc. European spine journal. 2011;20(11):1796-812.

157. Walsh AJL, Lotz JC. Biological response of the intervertebral disc to dynamic loading. Journal of biomechanics. 2004;37(3):329-37.

158. Wuertz K, Godburn K, MacLean JJ, Barbir A, Stinnett Donnelly J, Roughley PJ, et al. In vivo remodeling of intervertebral discs in response to short-and long-term dynamic compression. Journal of Orthopaedic Research. 2009;27(9):1235-42.

159. Stokes IAF, Iatridis JC. Mechanical conditions that accelerate intervertebral disc degeneration: overload versus immobilization. Spine. 2004;29(23):2724-32.

160. Setton LA, Chen J. Cell mechanics and mechanobiology in the intervertebral disc. Spine. 2004;29(23):2710-23.

161. Handa T, Ishihara H, Ohshima H, Osada R, Tsuji H, Obata Ki. Effects of hydrostatic pressure on matrix synthesis and matrix metalloproteinase production in the human lumbar intervertebral disc. Spine. 1997;22(10):1085-91.

162. Hutton WC, Elmer WA, Boden SD, Hyon S, Toribatake Y, Tomita K, et al. The effect of hydrostatic pressure on intervertebral disc metabolism. Spine. 1999;24(15):1507.

163. Reza AT, Nicoll SB. Hydrostatic pressure differentially regulates outer and inner annulus fibrosus cell matrix production in 3D scaffolds. Annals of biomedical engineering. 2008;36(2):204-13.

164. Ching CTS, Chow DHK, Yao FYD, Holmes AD. Changes in nuclear composition following cyclic compression of the intervertebral disc in an in vivo rat-tail model. Medical engineering & physics. 2004;26(7):587-94.

165. MacLean JJ, Lee CR, Alini M, Iatridis JC. Anabolic and catabolic mRNA levels of the intervertebral disc vary with the magnitude and frequency of in vivo dynamic compression. Journal of orthopaedic research. 2004;22(6):1193-200.

166. Rannou F, Richette P, Benallaoua M, François M, Genries V, Korwin-Zmijowska C, et al. Cyclic tensile stretch modulates proteoglycan production by intervertebral disc annulus fibrosus cells through production of nitrite oxide. Journal of cellular biochemistry. 2003;90(1):148-57.

167. Walter BA, Illien-Jünger S, Nasser PR, Hecht AC, Iatridis JC. Development and validation of a bioreactor system for dynamic loading and mechanical characterization of whole human intervertebral discs in organ culture. Journal of biomechanics. 2014.

168. Peroglio M, Grad S, Mortisen D, Sprecher CM, Illien-Jünger S, Alini M, et al. Injectable thermoreversible hyaluronan-based hydrogels for nucleus pulposus cell encapsulation. European Spine Journal. 2012;21(6):839-49.

169. See EY-S, Toh SL, Goh JC-H. Effects of radial compression on a novel simulated intervertebral disc-like assembly using bone marrow-derived mesenchymal stem cell cell-sheets for annulus fibrosus regeneration. Spine. 2011;36(21):1744-51.

170. Miyahara Y, Nagaya N, Kataoka M, Yanagawa B, Tanaka K, Hao H, et al. Monolayered mesenchymal stem cells repair scarred myocardium after myocardial infarction. Nature medicine. 2006;12(4):459-65.

171. Lu Y, Qiu F, Chen Y, Zhao X. [Cell sheet fabrication of hepatocyte-like cells differentiated from adipose tissue mesenchymal stem cells]. Sheng wu gong cheng xue bao = Chinese journal of biotechnology. 2009;25(4):599-604.

172. Labbé B, Marceau-Fortier G, Fradette J. Cell sheet technology for tissue engineering: the self-assembly approach using adipose-derived stromal cells. Methods in molecular biology (Clifton, NJ). 2011;702:429-41.

173. Torres FC, Rodrigues CJ, Stocchero IN, Ferreira MC. Stem cells from the fat tissue of rabbits: an easy-to-find experimental source. Aesthetic plastic surgery. 2007;31(5):574-8.

174. Peptan IA, Hong L, Mao JJ. Comparison of osteogenic potentials of visceral and subcutaneous adipose-derived cells of rabbits. Plastic and reconstructive surgery. 2006;117(5):1462-70.

175. Arrigoni E, Lopa S, de Girolamo L, Stanco D, Brini AT. Isolation, characterization and osteogenic differentiation of adipose-derived stem cells: from small to large animal models. Cell and tissue research. 2009;338(3):401-11.

176. Hata RI, Senoo H. L-ascorbic acid 2-phosphate stimulates collagen accumulation, cell proliferation, and formation of a three-dimensional tissuelike substance by skin fibroblasts. Journal of cellular physiology. 1989;138(1):8-16.

177. See EY-S, Toh SL, Goh JCH. Technique to accurately quantify collagen content in hyperconfluent cell culture. Journal of molecular histology. 2008;39(6):643-7.

178. Gallagher SR. Quantification of DNA and RNA with absorption and fluorescence spectroscopy. Current protocols in cell biology / editorial board, Juan S Bonifacino [et al]. 2001;Appendix 3:Appendix 3D.

179. Livak KJ, Schmittgen TD. Analysis of relative gene expression data using real-time quantitative PCR and the 2(-Delta Delta C(T)) Method. Methods (San Diego, Calif). 2001;25(4):402-8.

180. Schmittgen TD, Livak KJ. Analyzing real-time PCR data by the comparative C(T) method. Nature protocols. 2008;3(6):1101-8.

181. Fan H, Liu H, Toh SL, Goh JCH. Enhanced differentiation of mesenchymal stem cells co-cultured with ligament fibroblasts on gelatin/silk fibroin hybrid scaffold. Biomaterials. 2008;29(8):1017-27.

182. Yu G, Floyd ZE, Wu X, Hebert T, Halvorsen Y-DC, Buehrer BM, et al. Adipogenic differentiation of adipose-derived stem cells. Methods in molecular biology (Clifton, NJ). 2011;702:193-200.

183. Kroeze RJ, Knippenberg M, Helder MN. Osteogenic differentiation strategies for adipose-derived mesenchymal stem cells. Methods in molecular biology (Clifton, NJ). 2011;702:233-48.

184. Camplejohn KL, Allard SA. Limitations of safranin 'O' staining in proteoglycan-depleted cartilage demonstrated with monoclonal antibodies. Histochemistry. 1988;89(2):185-8.

185. Kiviranta I, Jurvelin J, Tammi M, Säämänen AM, Helminen HJ. Microspectrophotometric quantitation of glycosaminoglycans in articular cartilage sections stained with Safranin O. Histochemistry. 1985;82(3):249-55.

186. Schwarz C, Leicht U, Rothe C, Drosse I, Luibl V, Röcken M, et al. Effects of different media on proliferation and differentiation capacity of canine, equine and porcine adipose derived stem cells. Research in veterinary science. 2012;93(1):457-62.

187. Ren Y, Wu H, Zhou X, Wen J, Jin M, Cang M, et al. Isolation, expansion, and differentiation of goat adipose-derived stem cells. Research in veterinary science. 2012;93(1):404-11.

188. Taha MF, Hedayati V. Isolation, identification and multipotential differentiation of mouse adipose tissue-derived stem cells. Tissue & cell. 2010;42(4):211-6.

189. Hoogendoorn RJW, Lu ZF, Kroeze RJ, Bank RA, Wuisman PI, Helder MN. Adipose stem cells for intervertebral disc regeneration: current status and concepts for the future. Journal of cellular and molecular medicine. 2008;12(6a):2205-16.

190. Yang Z, Huang CY, Candiotti KA, Zeng X, Yuan T, Li J, et al. Sox-9 facilitates differentiation of adipose tissue-derived stem cells into a chondrocyte-like phenotype in vitro. Journal of Orthopaedic Research. 2011;29(8):1291-7.

191. Lu ZF, Zandieh Doulabi B, Wuisman PI, Bank RA, Helder MN. Differentiation of adipose stem cells by nucleus pulposus cells: configuration effect. Biochemical and biophysical research communications. 2007;359(4):991-6.

192. Choi E-H, Park H, Park K-S, Park KS, Kim B-S, Han I-B, et al. Effect of nucleus pulposus cells having different phenotypes on chondrogenic differentiation of adipose-derived stromal cells in a coculture system using porous membranes. Tissue Engineering Part A. 2011;17(19-20):2445-51.

193. Gebraad A, Miettinen S, Grijpma D, Haimi S, editors. Human Adipose Stem Cells in Chondrogenic Differentiation Medium without Growth Factors Differentiate Towards Annulus Fibrosus Phenotype In Vitro. Macromolecular Symposia; 2013: Wiley Online Library.

194. Gruber HE, Deepe R, Hoelscher GL, Ingram JA, Norton HJ, Scannell B, et al. Human adipose-derived mesenchymal stem cells: direction to a phenotype sharing similarities with the disc, gene expression profiling, and coculture with human annulus cells. Tissue Engineering Part A. 2010;16(9):2843-60.

195. Yu J, Tu Y-K, Tang Y-B, Cheng N-C. Stemness and transdifferentiation of adipose-derived stem cells using l-ascorbic acid 2-phosphate-induced cell sheet formation. Biomaterials. 2014;35(11):3516-26.

196. Mohsen-Kanson T, Hafner A-L, Wdziekonski B, Villageois P, Chignon-Sicard B, Dani C. Expression of cell surface markers during self-renewal and differentiation of human adipose-derived stem cells. Biochemical and biophysical research communications. 2013;430(3):871-5.

197. Bell DM, Leung KK, Wheatley SC, Ng LJ, Zhou S, Ling KW, et al. SOX9 directly regulates the type-II collagen gene. Nature genetics. 1997;16(2):174-8.

198. Furumatsu T, Ozaki T. Epigenetic regulation in chondrogenesis. Acta medica Okayama. 2010;64(3):155-61.

199. Strioga M, Viswanathan S, Darinskas A, Slaby O, Michalek J. Same or Not the Same? Comparison of Adipose Tissue-Derived Versus Bone Marrow-Derived Mesenchymal Stem and Stromal Cells. Stem cells and development. 2012;21(14):2724-52.

200. De Ugarte DA, Morizono K, Elbarbary A, Alfonso Z, Zuk PA, Zhu M, et al. Comparison of multi-lineage cells from human adipose tissue and bone marrow. Cells, tissues, organs. 2003;174(3):101-9.

201. Zhang X, Baughman CB, Kaplan DL. In vitro evaluation of electrospun silk fibroin scaffolds for vascular cell growth. Biomaterials. 2008;29(14):2217-27.

202. Meinel AJ, Kubow KE, Klotzsch E, Garcia-Fuentes M, Smith ML, Vogel V, et al. Optimization strategies for electrospun silk fibroin tissue engineering scaffolds. Biomaterials. 2009;30(17):3058-67.

203. Jin H-J, Chen J, Karageorgiou V, Altman GH, Kaplan DL. Human bone marrow stromal cell responses on electrospun silk fibroin mats. Biomaterials. 2004;25(6):1039-47.

204. Min B-M, Lee G, Kim SH, Nam YS, Lee TS, Park WH. Electrospinning of silk fibroin nanofibers and its effect on the adhesion and spreading of normal human keratinocytes and fibroblasts in vitro. Biomaterials. 2004;25(7):1289-97.

205. Schindelin J, Arganda-Carreras I, Frise E, Kaynig V, Longair M, Pietzsch T, et al. Fiji: an open-source platform for biological-image analysis. Nature methods. 2012;9(7):676-82.

206. Ayres C, Bowlin GL, Henderson SC, Taylor L, Shultz J, Alexander J, et al. Modulation of anisotropy in electrospun tissue-engineering scaffolds: analysis of fiber alignment by the fast Fourier transform. Biomaterials. 2006;27(32):5524-34.

207. Wu H, Fan J, Chu C-C, Wu J. Electrospinning of small diameter 3-D nanofibrous tubular scaffolds with controllable nanofiber orientations for vascular grafts. Journal of Materials Science: Materials in Medicine. 2010;21(12):3207-15.

208. Chen F, Su Y, Mo X, He C, Wang H, Ikada Y. Biocompatibility, Alignment Degree and Mechanical Properties of an Electrospun Chitosan–P (LLA-CL) Fibrous Scaffold. Journal of Biomaterials Science, Polymer Edition. 2009;20(14):2117-28.

209. Wulf E, Deboben A, Bautz FA, Faulstich H, Wieland T. Fluorescent phallotoxin, a tool for the visualization of cellular actin. Proceedings of the National Academy of Sciences. 1979;76(9):4498-502.

210. Fan H, Liu H, Toh SL, Goh JCH. Anterior cruciate ligament regeneration using mesenchymal stem cells and silk scaffold in large animal model. Biomaterials. 2009;30(28):4967-77.

211. Liu H, Fan H, Wang Y, Toh SL, Goh JCH. The interaction between a combined knitted silk scaffold and microporous silk sponge with human mesenchymal stem cells for ligament tissue engineering. Biomaterials. 2008;29(6):662-74.

212. Bron JL, Helder MN, Meisel H-J, Van Royen BJ, Smit TH. Repair, regenerative and supportive therapies of the annulus fibrosus: achievements and challenges. European spine journal. 2009;18(3):301-13.

213. Allen MJ, Schoonmaker JE, Bauer TW, Williams PF, Higham PA, Yuan HA. Preclinical evaluation of a poly (vinyl alcohol) hydrogel implant as a replacement for the nucleus pulposus. Spine. 2004;29(5):515-23.

214. Alves MH, Jensen BEB, Smith AAA, Zelikin AN. Poly (vinyl alcohol) physical hydrogels: new vista on a long serving biomaterial. Macromolecular bioscience. 2011;11(10):1293-313.

215. Nuttelman CR, Mortisen DJ, Henry SM, Anseth KS. Attachment of fibronectin to poly (vinyl alcohol) hydrogels promotes NIH3T3 cell adhesion, proliferation, and migration. Journal of biomedical materials research. 2001;57(2):217-23.

216. Schmedlen RH, Masters KS, West JL. Photocrosslinkable polyvinyl alcohol hydrogels that can be modified with cell adhesion peptides for use in tissue engineering. Biomaterials. 2002;23(22):4325-32.

217. Nuttelman CR, Henry SM, Anseth KS. Synthesis and characterization of photocrosslinkable, degradable poly (vinyl alcohol)-based tissue engineering scaffolds. Biomaterials. 2002;23(17):3617-26.

218. Bonakdar S, Emami SH, Shokrgozar MA, Farhadi A, Ahmadi SAH, Amanzadeh A. Preparation and characterization of polyvinyl alcohol hydrogels crosslinked by biodegradable polyurethane for tissue engineering of cartilage. Materials Science and Engineering: C. 2010;30(4):636-43.

219. Li M, Lu S, Wu Z, Tan K, Minoura N, Kuga S. Structure and properties of silk fibroin–poly (vinyl alcohol) gel. International journal of biological macromolecules. 2002;30(2):89-94.

220. Li M, Minoura N, Dai L, Zhang L. Preparation of Porous Poly (vinyl alcohol)-Silk Fibroin (PVA/SF) Blend Membranes. Macromolecular Materials and Engineering. 2001;286(9):529-33.

221. Braddon LG, Ku DN, Wootton DM, inventorsPoly (vinyl alcohol) cryogel patent US5981826. 1999.

222. Ku D, inventorMethods of making medical implants of poly (vinyl alcohol) hydrogel patent US20070299540 A1. 2007.

223. Abdullah M, Khairurrijal K. A simple method for determining surface porosity based on SEM images using OriginPro software. Indonesian Journal of Physics. 2009;20(2):37-40.

224. Van Dijk M, Smit TH, Arnoe MF, Burger EH, Wuisman PI. The use of poly-L-lactic acid in lumbar interbody cages: design and biomechanical evaluation in vitro. European Spine Journal. 2003;12(1):34-40.

225. Heini PF, Berlemann U, Kaufmann M, Lippuner K, Fankhauser C, van Landuyt P. Augmentation of mechanical properties in osteoporotic vertebral bones–a biomechanical investigation of vertebroplasty efficacy with different bone cements. European Spine Journal. 2001;10(2):164-71.

226. Stauffer SR, Peppast NA. Poly (vinyl alcohol) hydrogels prepared by freezing-thawing cyclic processing. Polymer. 1992;33(18):3932-6.

227. Hassan CM, Peppas NA. Structure and Morphology of Freeze/Thawed PVA Hydrogels. Macromolecules. 2000;33(7):2472-9.

228. Hassan CM, Peppas NA, Chang JY. Structure and applications of poly (vinyl alcohol) hydrogels produced by conventional crosslinking or by freezing/thawing methods. Biopolymers/PVA Hydrogels/Anionic Polymerisation/ Nanocomposites. 153: Springer; 2000. p. 221.

229. Saltzman WM, Kyriakides TR, Lanza R, Langer R, Vacanti JP. Cell interactions with polymers. Principles of Tissue Engineering. 3: Academic Press; 2013. p. 1936.

230. Liu Y, Vrana NE, Cahill PA, McGuinness GB. Physically crosslinked composite hydrogels of PVA with natural macromolecules: structure, mechanical properties, and endothelial cell compatibility. Journal of Biomedical Materials Research Part B: Applied Biomaterials. 2009;90(2):492-502.

231. Kundu J, Poole-Warren LA, Martens P, Kundu SC. Silk fibroin/poly (vinyl alcohol) photocrosslinked hydrogels for delivery of macromolecular drugs. Acta biomaterialia. 2012;8(5):1720-9.

232. Zhang D, Chen K, Wu L, Wang D, Ge S. Synthesis and characterization of PVA-HA-silk composite hydrogel by orthogonal experiment. Journal of Bionic Engineering. 2012;9(2):234-42.

233. Luo Q, Chen Z, Hao X, Zhu Q, Zhou Y. Preparation and properties of nanometer silk fibroin peptide/polyvinyl alcohol blend films for cell growth. International journal of biological macromolecules. 2013;61:135-41.

234. Tsukada M, Freddi G, Crighton JS. Structure and compatibility of poly (vinyl alcohol)-silk fibroin (PVA/SA) blend films. Journal of Polymer Science Part B: Polymer Physics. 1994;32(2):243-8.

235. Lyons JG, Geever LM, Nugent MJD, Kennedy JE, Higginbotham CL. Development and characterisation of an agar–polyvinyl alcohol blend hydrogel. Journal of the mechanical behavior of biomedical materials. 2009;2(5):485-93.

236. Minoura N, Koyano T, Koshizaki N, Umehara H, Nagura M, Kobayashi K-i. Preparation, properties, and cell attachment/growth behavior of PVA/chitosan-blended hydrogels. Materials Science and Engineering: C. 1998;6(4):275-80.

237. Talukdar S, Nguyen QT, Chen AC, Sah RL, Kundu SC. Effect of initial cell seeding density on 3D-engineered silk fibroin scaffolds for articular cartilage tissue engineering. Biomaterials. 2011;32(34):8927-37.

238. Shapiro IM, Risbud MV. The Intervertebral Disc Molecular and Structural Studies of the Disc in Health and Disease: Springer Vienna; 2014. 446 p.

239. Johannessen W, Elliott DM. Effects of degeneration on the biphasic material properties of human nucleus pulposus in confined compression. Spine. 2005;30(24):E724-E9.

240. Glover MG, Hargens AR, Mahmood MM, Gott S, Brown MD, Garfin SR. A new technique for the in vitro measurement of nucleus pulposus swelling pressure. Journal of orthopaedic research. 1991;9(1):61-7.

241. Iatridis JC, Weidenbaum M, Setton LA, Mow VC. Is the nucleus pulposus a solid or a fluid? Mechanical behaviors of the nucleus pulposus of the human intervertebral disc. Spine. 1996;21(10):1174-84.

242. Clouet J, Grimandi G, Pot-Vaucel M, Masson M, Fellah HB, Guigand L, et al. Identification of phenotypic discriminating markers for intervertebral disc cells and articular chondrocytes. Rheumatology. 2009;48(11):1447-50.

243. Huang C, Charles Y, Hagar KL, Frost LE, Sun Y, Cheung HS. Effects of Cyclic Compressive Loading on Chondrogenesis of Rabbit Bone-Marrow Derived Mesenchymal Stem Cells. Stem cells. 2004;22(3):313-23.

244. Guilak F, Butler DL, Goldstein SA, Baaijens F. Biomechanics and mechanobiology in functional tissue engineering. Journal of biomechanics. 2014.

245. Kelly DJ, Jacobs CR. The role of mechanical signals in regulating chondrogenesis and osteogenesis of mesenchymal stem cells. Birth Defects Research Part C: Embryo Today: Reviews. 2010;90(1):75-85.

246. Mabrouk M, Mostafa A, Oudadesse H, Mahmoud A, Gaafar A. Fabrication, Characterization and Drug Release of Ciprofloxacin Loaded Porous Polyvinyl Alcohol/Bioactive Glass Scaffold for Controlled Drug Delivery. Bioceram Dev Appl S. 2013;1:2.

247. Hudgins RG, Muzzy JD. Analytical stress model for a composite prosthetic intervertebral disc. Polymer composites. 1998;19(6):837-45.

248. Illien-Junger S, Walter Benjamim A, Mayer Jillian E, Hecht Andrew C, Iatridis James C. Intervertebral Disc Culture Models and Their Applications to Study Pathogenesis and Repair. In: Shapiro IM, Risbud MV, editors. The Intervertebral Disc. Wien: Springer; 2014. p. 353-70.

249. Martin JT, Milby AH, Chiaro JA, Kim DH, Hebela NM, Smith LJ, et al. Translation of an engineered nanofibrous disc-like angle-ply structure for

intervertebral disc replacement in a small animal model. Acta biomaterialia. 2014;10(6):2473-81.

250. Baer PC, Geiger H. Adipose-derived mesenchymal stromal/stem cells: tissue localization, characterization, and heterogeneity. Stem cells international. 2012;2012:812693.

251. Gimble JM, Bunnell BA, Chiu ES, Guilak F. Concise Review: Adipose-Derived Stromal Vascular Fraction Cells and Stem Cells: Let's Not Get Lost in Translation. Stem cells (Dayton, Ohio). 2011;29(5):749-54.

252. Poole AR, Kojima T, Yasuda T, Mwale F, Kobayashi M, Laverty S. Composition and structure of articular cartilage: a template for tissue repair. Clinical orthopaedics and related research. 2001(391 Suppl):S26-33.

253. Wong M, Carter DR. Articular cartilage functional histomorphology and mechanobiology: a research perspective. Bone. 2003;33(1):1-13.

254. Allon AA, Schneider RA, Lotz JC. Co-culture of Adult Mesenchymal Stem Cells and Nucleus Pulposus Cells in Bilaminar Pellets for Intervertebral Disc Regeneration. SAS Journal. 2009;3(2):41-9.

255. Hwang CS, Loftus TM, Mandrup S, Lane MD. Adipocyte differentiation and leptin expression. Annual review of cell and developmental biology. 1997;13:231-59.

256. Wezeman FH, Gong Z. Adipogenic effect of alcohol on human bone marrow-derived mesenchymal stem cells. Alcoholism, clinical and experimental research. 2004;28(7):1091-101.

257. Um S, Choi JR, Lee JH, Zhang Q, Seo B. Effect of leptin on differentiation of human dental stem cells. Oral diseases. 2011;17(7):662-9.

258. Liang G, Gao W, Liang A, Ye W, Peng Y, Zhang L, et al. Normal leptin expression, lower adipogenic ability, decreased leptin receptor and hyposensitivity to Leptin in Adolescent Idiopathic Scoliosis. PloS one. 2012;7(5):e36648.

259. Thomas T, Gori F, Khosla S, Jensen MD, Burguera B, Riggs BL. Leptin acts on human marrow stromal cells to enhance differentiation to osteoblasts and to inhibit differentiation to adipocytes. Endocrinology. 1999;140(4):1630-8.

260. Hamrick MW, Della-Fera MA, Choi Y-H, Pennington C, Hartzell D, Baile CA. Leptin treatment induces loss of bone marrow adipocytes and increases bone formation in leptin-deficient ob/ob mice. Journal of bone and mineral research : the official journal of the American Society for Bone and Mineral Research. 2005;20(6):994-1001.

261. Qi H, Aguiar DJ, Williams SM, La Pean A, Pan W, Verfaillie CM. Identification of genes responsible for osteoblast differentiation from human mesodermal progenitor cells. Proceedings of the National Academy of Sciences of the United States of America. 2003;100(6):3305-10.

262. Termine JD, Kleinman HK, Whitson SW, Conn KM, McGarvey ML, Martin GR. Osteonectin, a bone-specific protein linking mineral to collagen. Cell. 1981;26(1 Pt 1):99-105.

263. McKee MD, Nanci A. Osteopontin at mineralized tissue interfaces in bone, teeth, and osseointegrated implants: ultrastructural distribution and implications for mineralized tissue formation, turnover, and repair. Microscopy research and technique. 1996;33(2):141-64.

264. Siiteri JE, Ensrud KM, Moore A, Hamilton DW. Identification of osteopontin (OPN) mRNA and protein in the rat testis and epididymis, and on sperm. Molecular reproduction and development. 1995;40(1):16-28.

265. Joyce MM, González JF, Lewis S, Woldesenbet S, Burghardt RC, Newton GR, et al. Caprine uterine and placental osteopontin expression is distinct among epitheliochorial implanting species. Placenta. 2005;26(2-3):160-70.

266. Jaafar IH, LeBlon CE, Wei M-T, Ou-Yang D, Coulter JP, Jedlicka SS. Improving fluorescence imaging of biological cells on biomedical polymers. Acta biomaterialia. 2011;7(4):1588-98.

267. Viegas MS, Martins TC, Seco F, Do Carmo A. An improved and cost-effective methodology for the reduction of autofluorescence in direct immunofluorescence studies on formalin-fixed paraffin-embedded tissues. European Journal of Histochemistry. 2007;51(1):59-66.

268. Neumann M, Gabel D. Simple method for reduction of autofluorescence in fluorescence microscopy. Journal of Histochemistry & Cytochemistry. 2002;50(3):437-9.

269. Baschong W, Suetterlin R, Laeng RH. Control of autofluorescence of archival formaldehyde-fixed, paraffin-embedded tissue in confocal laser scanning microscopy (CLSM). Journal of Histochemistry & Cytochemistry. 2001;49(12):1565-71.

270. Cowen T, Haven AJ, Burnstock G. Pontamine sky blue: a counterstain for background autofluorescence in fluorescence and immunofluorescence histochemistry. Histochemistry. 1985;82(3):205-8.

271. Mosiman VL, Patterson BK, Canterero L, Goolsby CL. Reducing cellular autofluorescence in flow cytometry: an in situ method. Cytometry. 1997;30(3):151-6.

272. Schnell SA, Staines WA, Wessendorf MW. Reduction of lipofuscin-like autofluorescence in fluorescently labeled tissue. Journal of Histochemistry & Cytochemistry. 1999;47(6):719-30.

273. Oliveira VC, Carrara RCV, Simoes DLC, Saggioro FP, Carlotti Jr CG, Covas DT, et al. Sudan Black B treatment reduces autofluorescence and improves resolution of in situ hybridization specific fluorescent signals of brain sections. Histology and histopathology. 2010;25(7):1017.

274. Bayliss H. The histochemical versatility of Sudan Black B. Acta histochemicaSupplementband. 1981;24:247-55.

275. Frederiks WM. Some aspects of the value of Sudan Black B in lipid histochemistry. Histochemistry. 1977;54(1):27-37.

276. Miyamoto S, Kathz BZ, Lafrenie RM, Yamada KM. Fibronectin and integrins in cell adhesion, signaling, and morphogenesis. Annals of the New York Academy of Sciences. 1998;857(1):119-29.

277. Ruoslahti E. Fibronectin in cell adhesion and invasion. Cancer and Metastasis Reviews. 1984;3(1):43-51.

278. Ganta SR, Piesco NP, Long P, Gassner R, Motta LF, Papworth GD, et al. Vascularization and tissue infiltration of a biodegradable polyurethane matrix. Journal of Biomedical Materials Research Part A. 2003;64(2):242-8.

279. Lu B, Zheng S, Quach BQ, Tai Y-C. A study of the autofluorescence of parylene materials for μTAS applications. Lab on a Chip. 2010;10(14):1826-34.

280. Chiu Y-C, Brey EM, Pérez-Luna VH. A Study of the Intrinsic Autofluorescence of Poly (ethylene glycol)-co-(L-Lactic acid) Diacrylate. Journal of fluorescence. 2012;22(3):907-13.

281. Shadpour H, Musyimi H, Chen J, Soper SA. Physiochemical properties of various polymer substrates and their effects on microchip electrophoresis performance. Journal of Chromatography A. 2006;1111(2):238-51.

282. Clarke RJ, Oprysa A. Fluorescence and light scattering. Journal of chemical education. 2004;81(5):705.

283. Panilaitis B, Altman GH, Chen J, Jin HJ, Karageorgiou V, Kaplan DL. Macrophage responses to silk. Biomaterials. 2003;24(18):3079-85.

284. Teuschl AH, van G, Redl H. Sericin Removal from Raw Bombyx mori Silk Scaffolds of High Hierarchical Order. Tissue engineeringPart C, Methods. 2014.

285. Zaoming W, Codina R, Fernandez-Caldas E, Lockey RF. Partial characterization of the silk allergens in mulberry silk extract. Journal of investigational allergology & clinical immunology. 1995;6(4):237-41.

286. Aramwit P, Sangcakul A. The effects of sericin cream on wound healing in rats. Bioscience Biotechnology And Biochemistry. 2007;71(10):2473.

287. Nagai N, Murao T, Ito Y, Okamoto N, Sasaki M. Enhancing effects of sericin on corneal wound healing in rat debrided corneal epithelium. Biological & pharmaceutical bulletin. 2009;32(5):933-6.

288. Acharya C, Ghosh SK, Kundu SC. Silk fibroin protein from mulberry and non-mulberry silkworms: cytotoxicity, biocompatibility and kinetics of L929 murine fibroblast adhesion. Journal of Materials Science: Materials in Medicine. 2008;19(8):2827-36.

289. Acharya C, Ghosh SK, Kundu SC. Silk fibroin film from non-mulberry tropical tasar silkworms: A novel substrate for in vitro fibroblast culture. Acta Biomaterialia. 2009;5(1):429-37.

290. Kundu SC, Kundu B, Talukdar S, Bano S, Nayak S, Kundu J, et al. Nonmulberry silk biopolymers. Biopolymers. 2012;97(6):455-67.

Appendices

A. In-depth Discussion on Experimental Design and Gene Expression Results for Chapter 3 (Phase 1)

Further Discussion On Experimental Design

The experiment doe Phase 1 was designed to address concerns on the heterogeneous nature of isolated ASCs that may cause any biasness in the results comparison between experimental groups. There is general consensus in literature today that ASCs harvested from the stromal vascular fraction of adipose tissues is not a homogeneous population, but rather contain a mixture of cell types, including progenitor cells which can be more or less committed than others (250,251). For this thesis, after isolation, ASCs were cryopreserved in liquid nitrogen for subsequent experiments. For the differentiation study, vials of ASCs were thawed and expanded in expansion flasks, and subsequently trypsinized and divided into samples for the CI, CSI and CSNI experimental groups. In other words, while acknowledging the heterogeneous nature of the ASCs populations, the proportion of progenitor cells in the CI, CSI and CSNI groups should however be similar.

Three experimental groups were set up for the second half of the study (CSI, CSNI and CI). It should be noted that long term culture (up to 5 weeks for osteogenic differentiation) of the CI groups would also result in the accumulation of ECM and hence formation of cell-sheets under the described adipogenic and osteogenic differentiation protocols. Looking from such a perspective, two types of ASCs cell-sheets are being investigated in this study for the two above mentioned differentiation lineages. One involves the differentiation of hyperconfluent ASCs within a pre-formed ECM layer (CSI groups) and the other being the differentiation of non-confluent ASCs, while allowing the ECM to be formed simultaneously (CI groups).

Hence, not only the effect of a hyperconfluent environment on the differentiability of ASCs was investigated (as in the CSI groups), the potentiality of ASCs cell-sheets per se (referring to both the CSI and CI groups) down the osteogenic and adipogenic lineages for tissue engineering purposes was also assessed.

The temporal nature of this study, by having weekly assessment time points for the differentiation studies, allowed for an interesting stage-wise observation to be made for the chondrogenic differentiation of ASCs and ASCs within the cell-sheets. Regardless of the presence of a pre-formed ECM, a three-stage process was universally observed for chondrogenesis of the ASCs (in both the CI and CSI groups). In the first stage of chondrogenesis, there was formation of a fibrocartilage-like band on the periphery of the pellet after 2 weeks of induction. In the CI group, the fibrocartilage-like band was approximately one-fifth of the pellet's radius (**Figure 3-12a**) and was much thicker than the fibrocartilage-like band on the periphery of the CSI pellet (**Figure 3-12b**). Such a phenomenon hints at the inherent ability of ASCs to structurally organize itself in a spontaneous fashion. In the 2nd stage of chondrogenesis, the differentiated ASCs started to deposit glycosaminoglycans and proteoglycans within the fibrocartilage-like band. This do not take place uniformly throughout the entire band, but rather take place in a colony-like fashion to give rise to circular regions of positive Safranin-O staining developing from the fibrocartilage-like band. The 3rd and last stage of chondrogenesis involves the invagination of the fibrocartilage-like band around circular regions that are positively stained with high intensity of Safranin-O to form satellite pellets that started to bud off the main pellet. A close observation of the satellite pellets at high magnification reveals an articular-cartilage-like kind of zonal architecture (252,253) developing within. On the periphery of the satellite pellets, the presence of flattened cells (like in the periphery zone of articular cartilage) was observed, while the inner regions of the satellite pellets displayed cells surrounded by numerous lacunae, like in the transitional zone

of articular cartilage (**Figure 3-12m** and **Figure 3-12n**). To our best of knowledge, such a budding and pellet formation phenomena, resembling a reverse phagocytosis mechanism, has never been described in literature before for chondrogenesis of ASCs. Apart from a paper by Allon et al (254) describing a similar budding phenomenon using micromass co-culture of nucleus pulposus cells and MSCs (but with no chondrogenic induction medium), there is a dearth in published information in the occurrence and mechanism of this phenomenon.

Further Discussion on Adipogenic and Osteogenic Gene Expressions

Adipogenesis was assessed by Oil Red O staining for lipid droplets and gene expressions of PPARγ2, leptin and aP2. PPARγ2 belongs to a family of nuclear hormone receptors, and is a master transcription factor in adipogenic differentiation (255,256). Gene expression for PPARγ2 was consistently upregulated in the CSI samples relative to the CSNI samples. However, interestingly the CI samples in turn displayed a higher gene expression of PPARγ2 than the CSI samples over both assessment time points. A similar trend was observed for the aP2 gene. aP2 is regulated upstream by PPARγ2 and is a very late stage marker for adipogenic differentiation (256). Leptin gene expressions between CSI and CSNI and between CSI and CI were however almost converse to those of PPARγ2 and aP2. Leptin is a hormone secreted by adipose tissues and plays a key role in energy regulation and bone metabolism (257,258). Leptin is also known to be a regulator in cell differentiation, with studies reporting it to influence bone-marrow cells to an osteogenic lineage over the adipogenic lineage (259,260).

Four genes were tested for differentiation down the osteogenic lineage: Runx2, Osteonectin, Osteopontin and Col I. By playing a central role in facilitating the convergence of several osteogenic pathways down the osteogenic lineage, Runx2 is a critical transcription factor for differentiation down the osteogenic phenotype (261).

An early gene marker, Runx2 expression was consistently higher in the CSI groups from as early as week 2 and for up to 5 weeks of induction culture (**Figure 3-11**). Bone matrix proteins, Col I, osteonectin and osteopontin, are later gene markers and started to display a consistent incremental trend in the CSI groups only after 3 to 4 weeks of induction (**Figure 3-11**). Although not bone specific, Col I is a major and important component of bone ECM. Osteonectin on the other hand is a bone specific protein that binds selectively to both hydroxyapatite and collagen, linking mineral to collagen (262). Osteopontin is a multifunctional glycophosphoprotein that is not only abundantly found in bone and teeth tissues (263), but is also present in other tissues like the testes (264) and placenta (265). Thus, osteopontin is not bone specific, but nonetheless performs important bone related functions, especially in the area pertaining to interfacial properties (263). Comparing the gene expression results of the osteogenic genes to the eventual phenotypic assessment of calcium deposition using Alizarin Red staining, it is interesting to note the inconsistency between the genotypic and phenotypic results obtained between the CI and CSI samples. Such discrepancies can be attributed to several reasons including: i) the result of gene expression kinetics, ii) the involvement of epigenetics factors, and iii) a possible feedback system present regulating gene expression.

B. Mechanical Drawings of Bioreactor Assembly and Parts

Motor Attachment

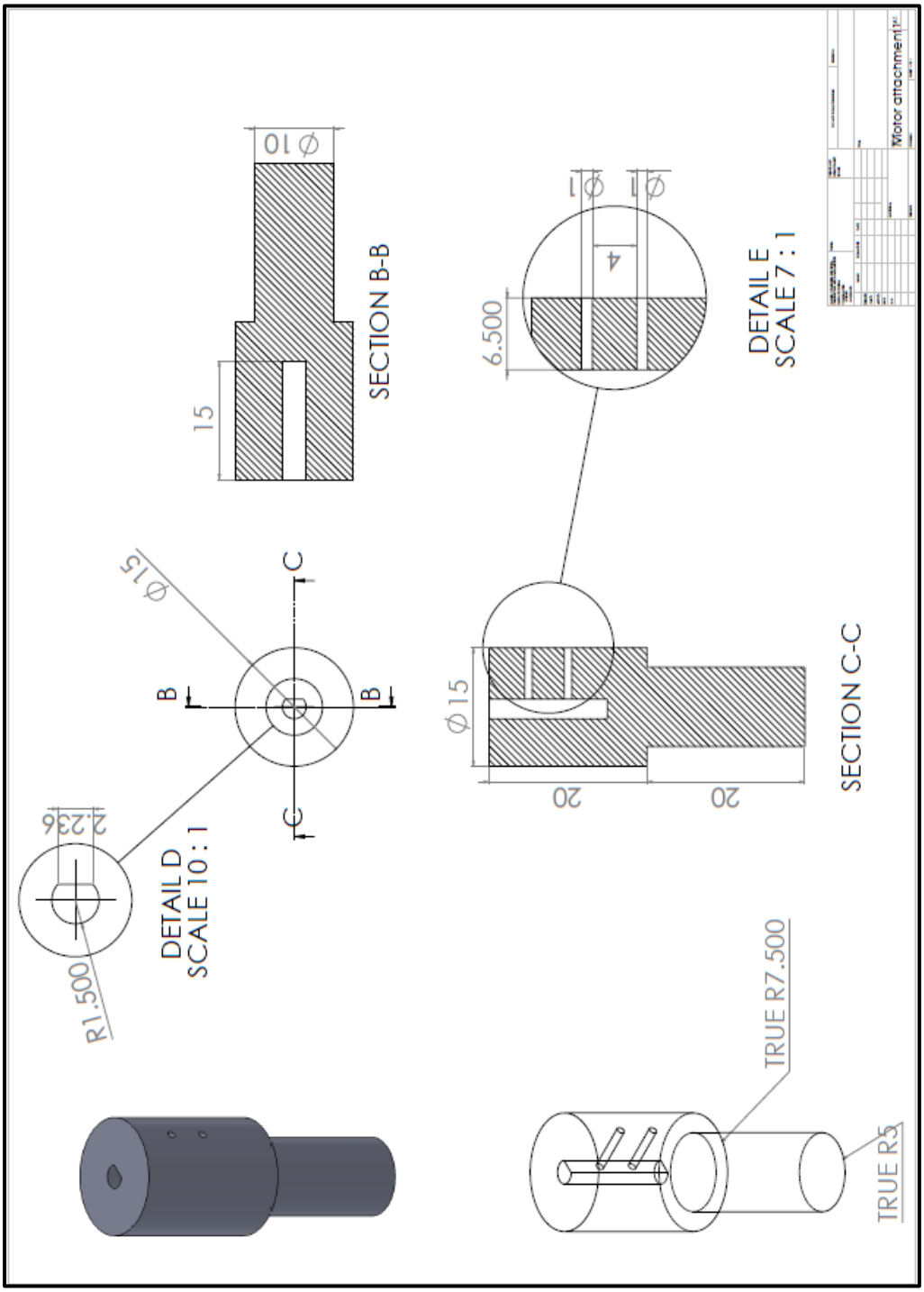

Side Struts

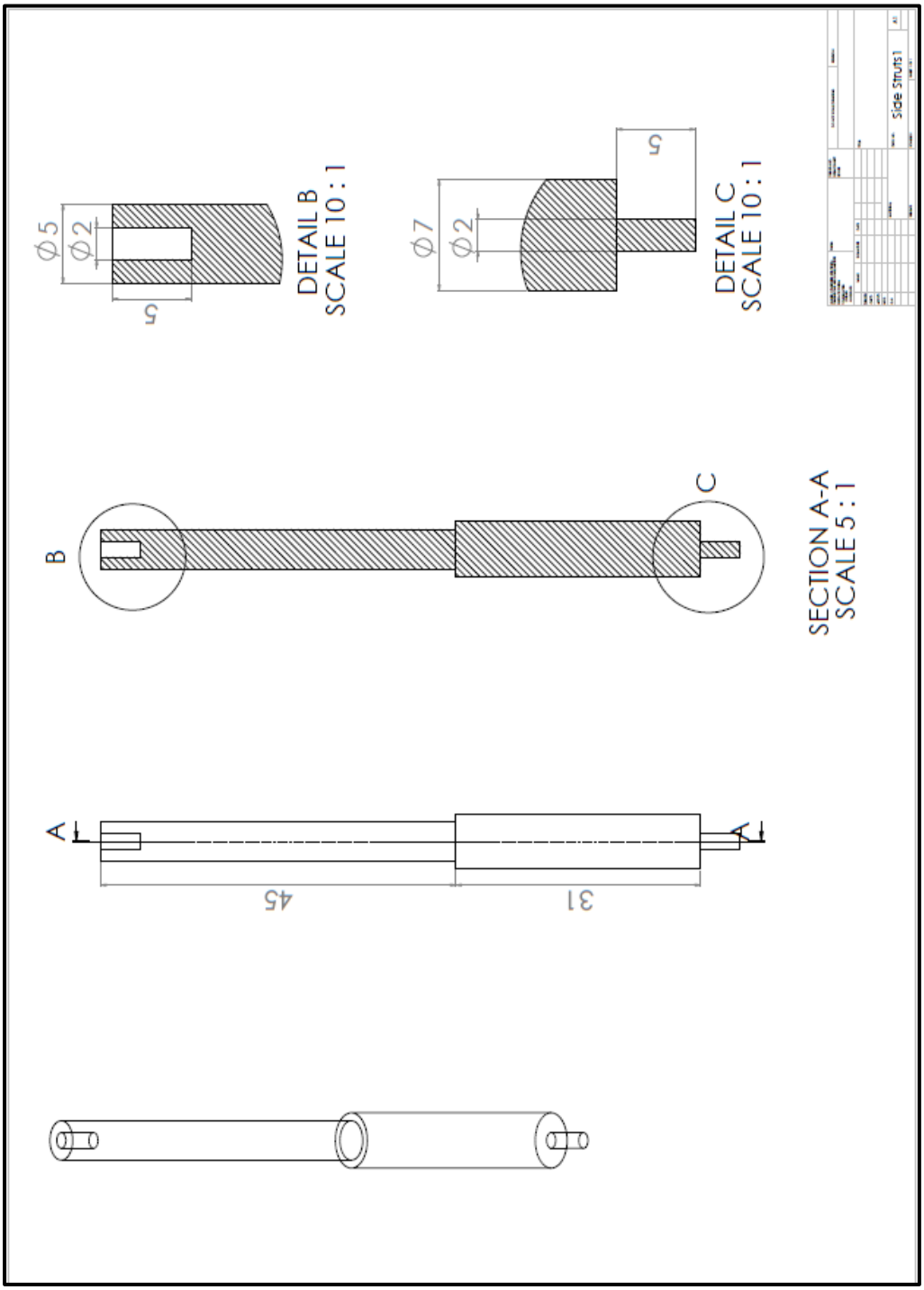
DETAIL B
SCALE 10 : 1
DETAIL C
SCALE 10 : 1
SECTION A-A
SCALE 5 : 1
B
C
A
A
45
31
Side Struts 1

Guide plate for coupling

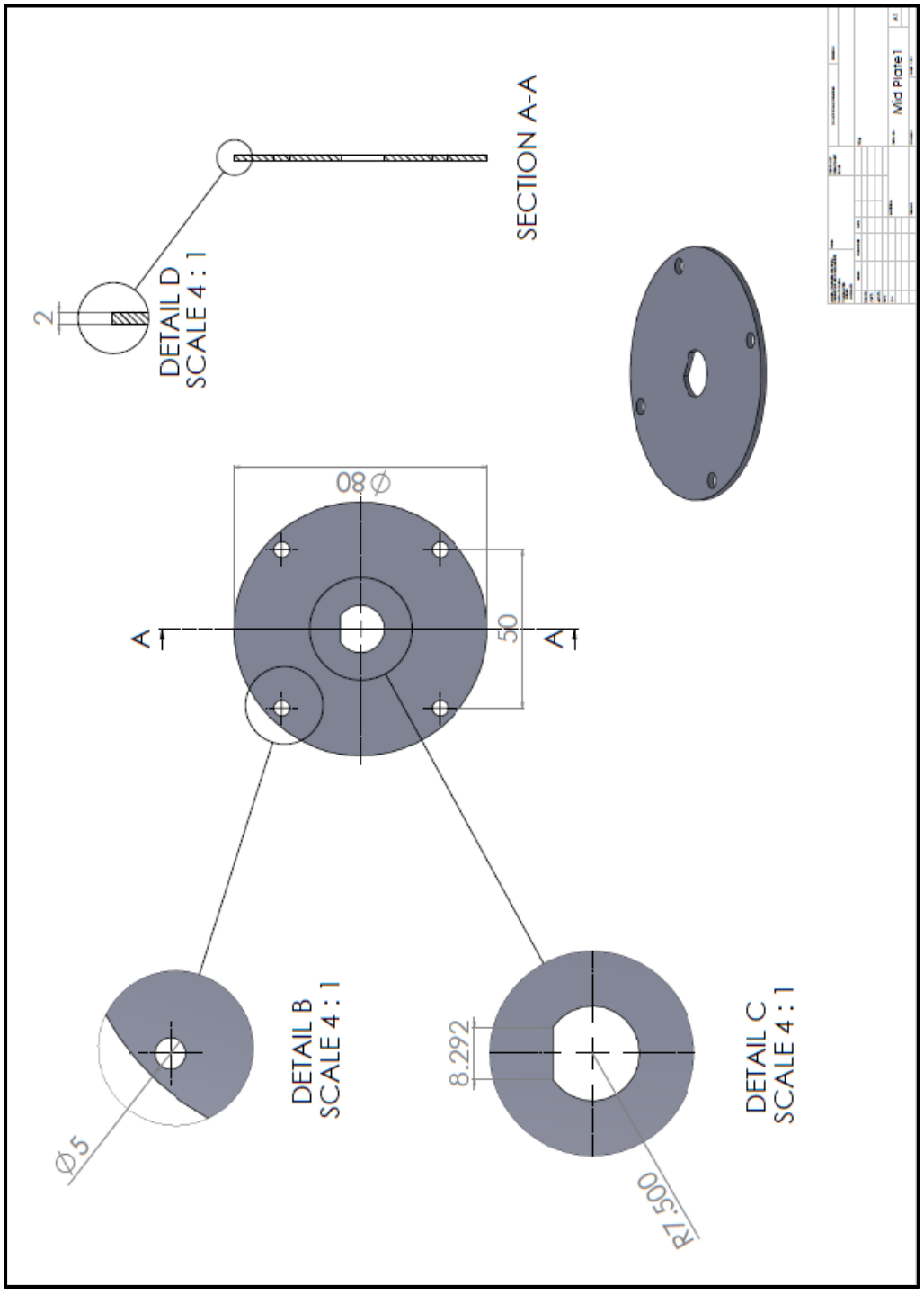

Adapter for coupling

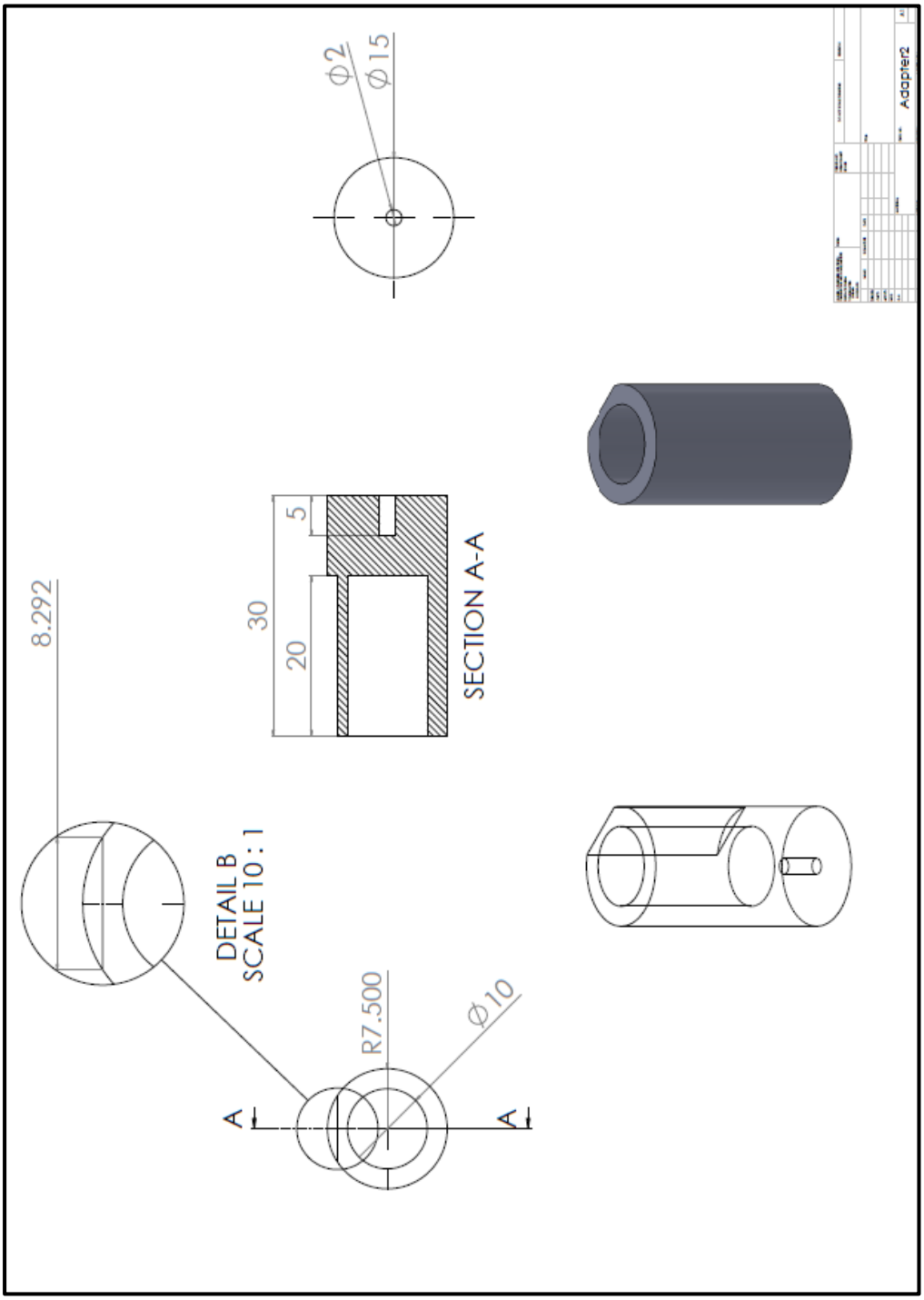

Compression platen

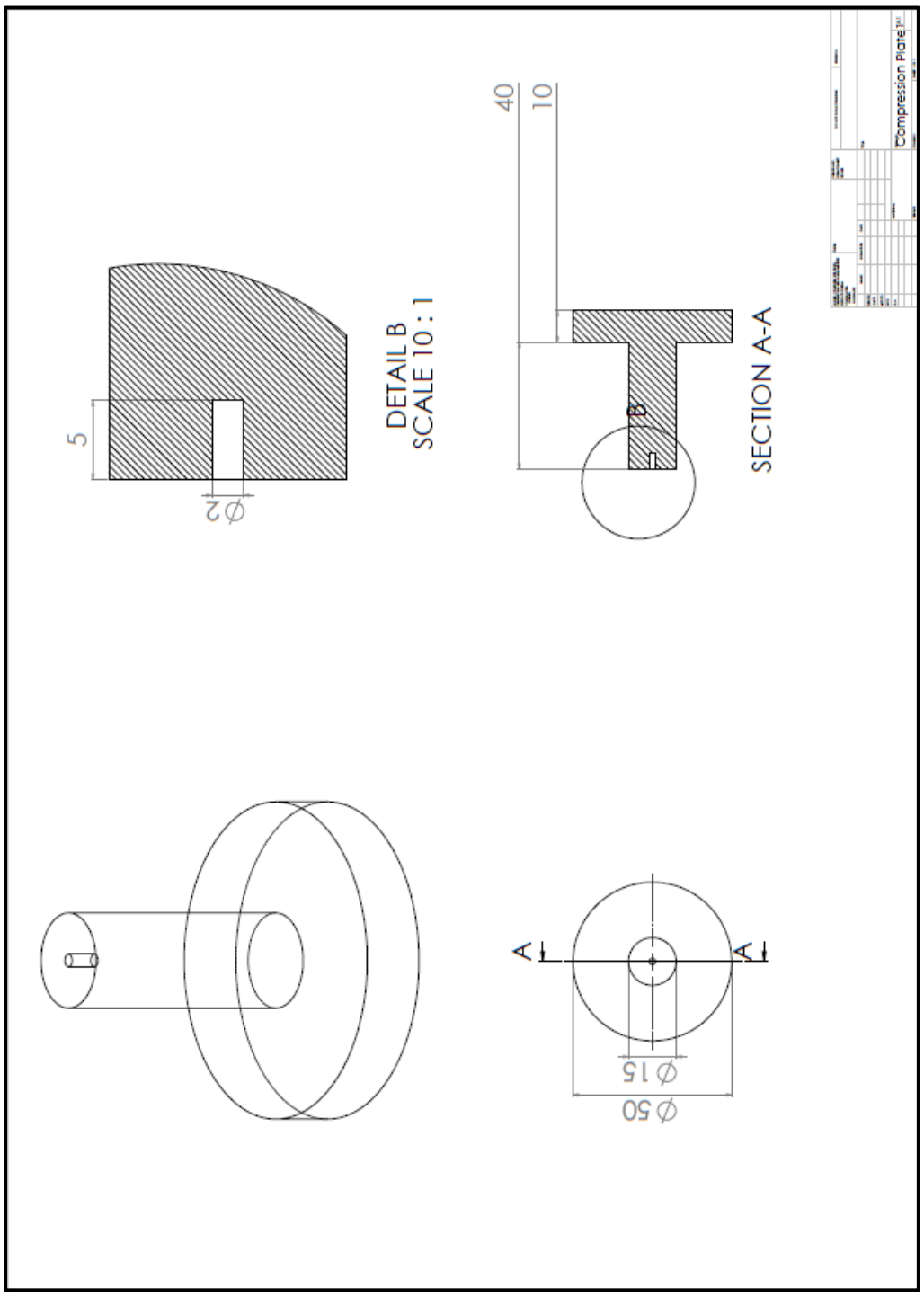

Chamber cover

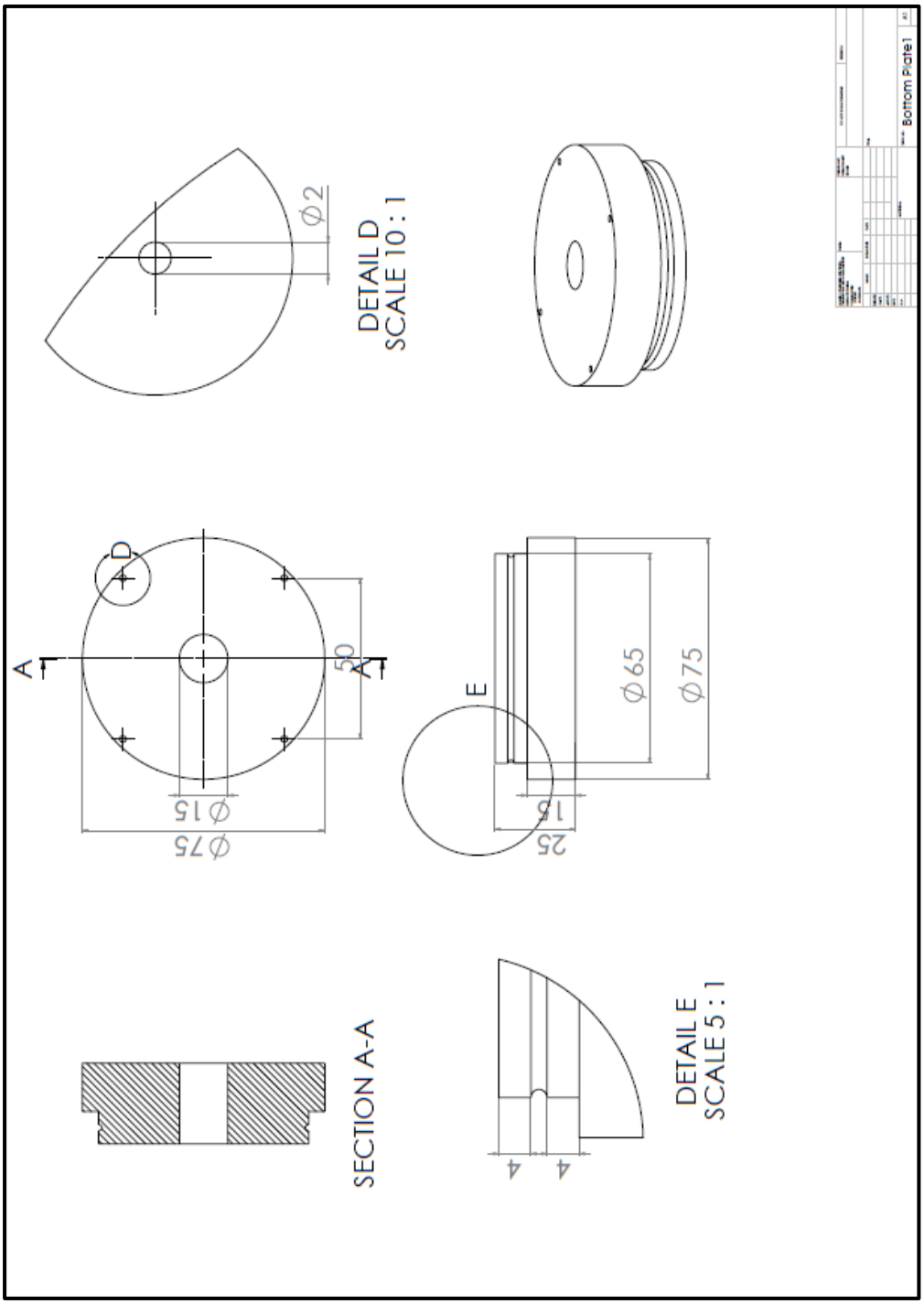

Chamber base

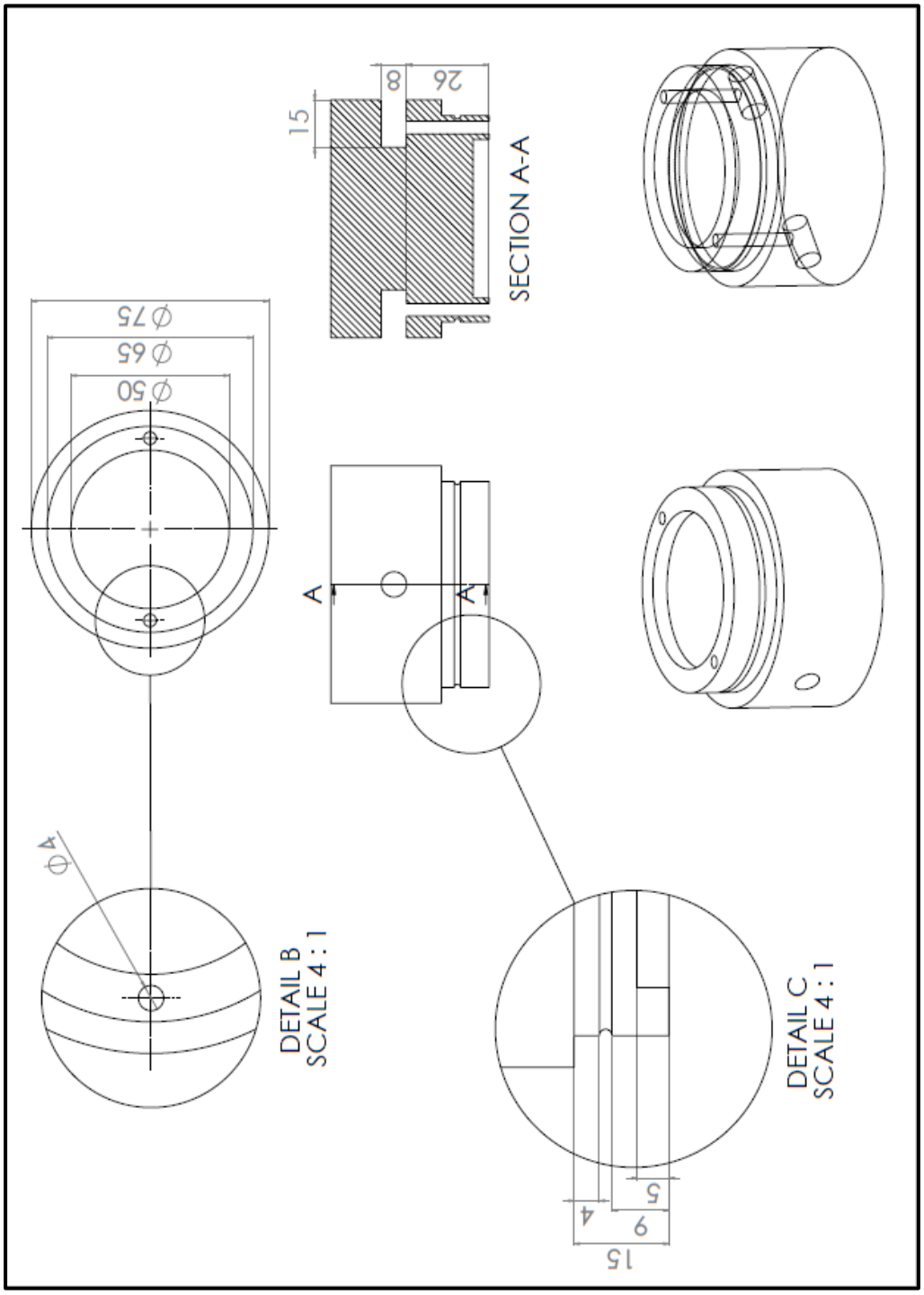

C. Calibration of Load Cells and Data Acquisition System

Calibration results showed that the load cells did not exhibit significant hysteresis, although the load cells should be preferably pre-loaded for one loading cycle for conditioning. Hence readings were taken from the average of the second and third loading/unloading rounds to generate the final Voltage/Load response gradient. The load cells' voltage/load response gradients were also a little different between under tension and under compression modes. Given that the load cells will be primary reading compression loads in the bioreactor, only the compression readings were taken into consideration for finalizing the response equations to be used for the next phases of the study. Table 5 summarizes the final equations used. The working graphs from the multiple calibration sessions are as shown in this Appendix section. The differences in responses between the first loading rounds as compared to the second and third rounds can also be observed from the graphs.

Table 5. Consolidation of Calibrated Voltage/Load Response Gradients Used

Load Cell (DAQ Port)	Fitted Response (mV/g)	R^2 value
Load Cell 1 (AI 4)	y = 1.43x + 32.33	0.996
Load Cell 2 (AI 1)	y = 1.64x + 6.75	0.999
Load Cell 3 (AI 6)	y = 0.94x + 1.14	0.999
Load Cell 4 (AI 3)	y = 0.36x – 3.36	0.999

Calibration Session 1

Loading once only.

Voltage/Load response fitted across compression and tension.

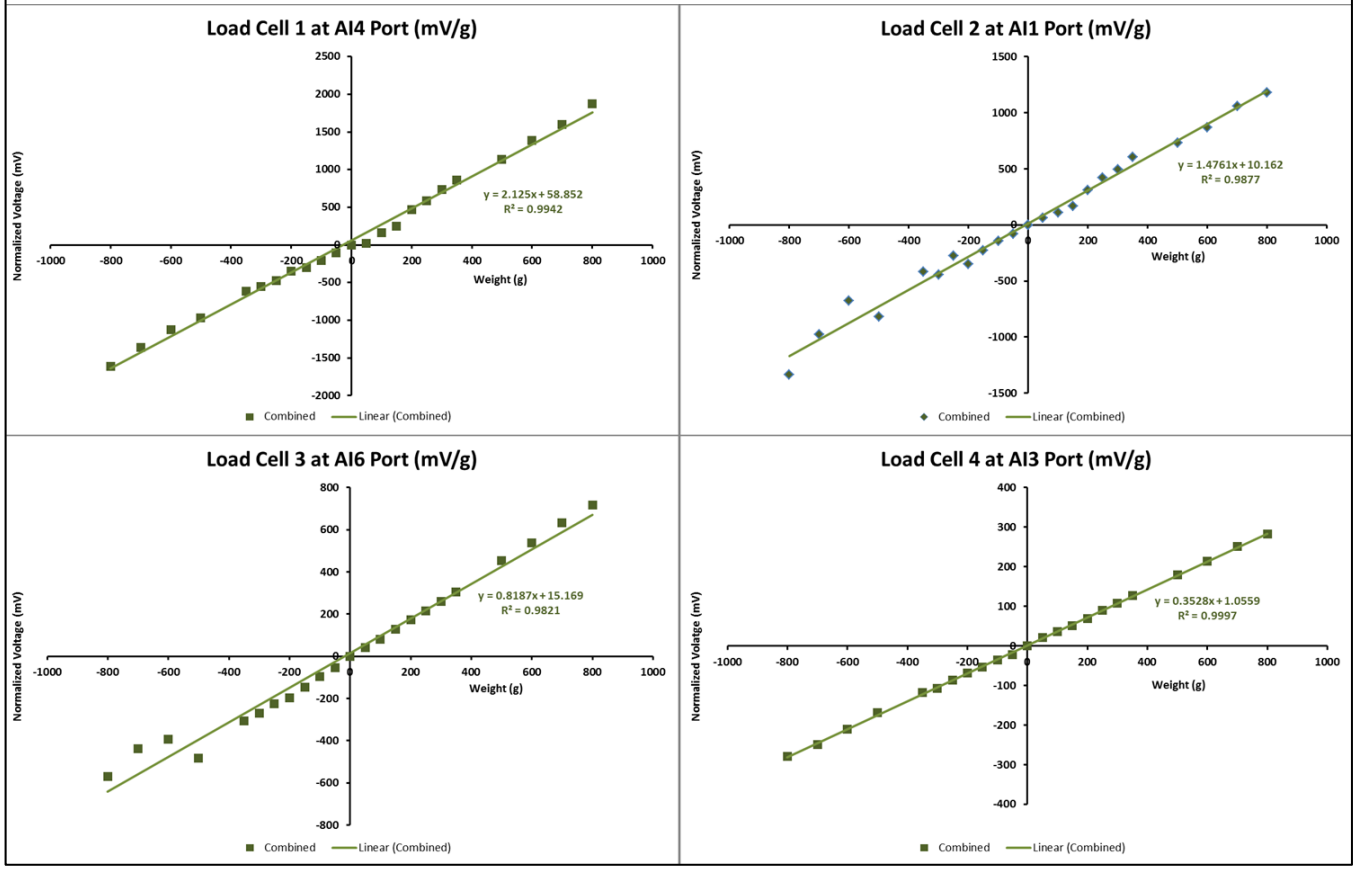

Calibration Session 1

Loading once only.

Voltage/Load response fitted specifically for compression and tension.

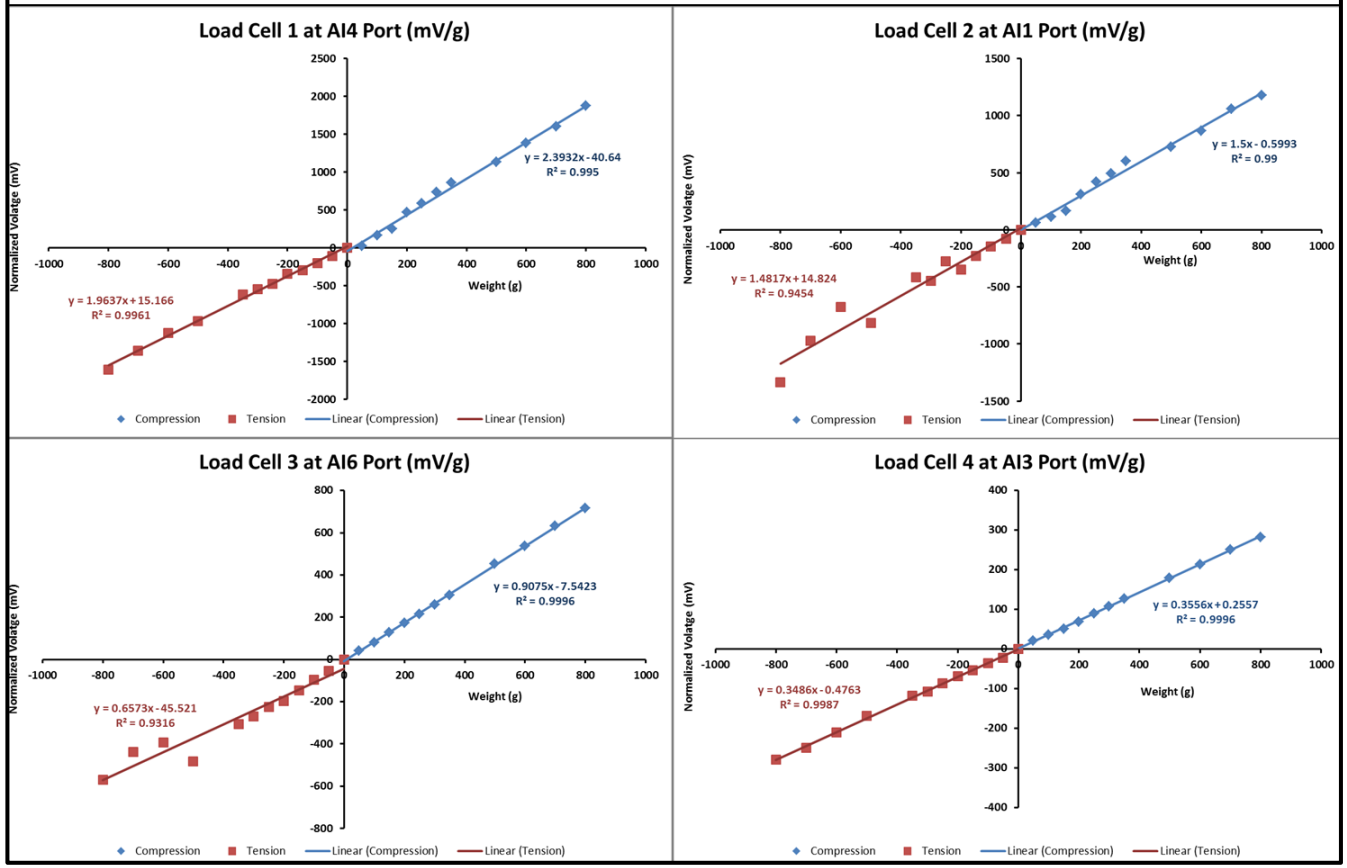

Calibration Session 2

Loading -> Unloading -> Loading

Voltage/Load response fitted specifically for compression and tension.

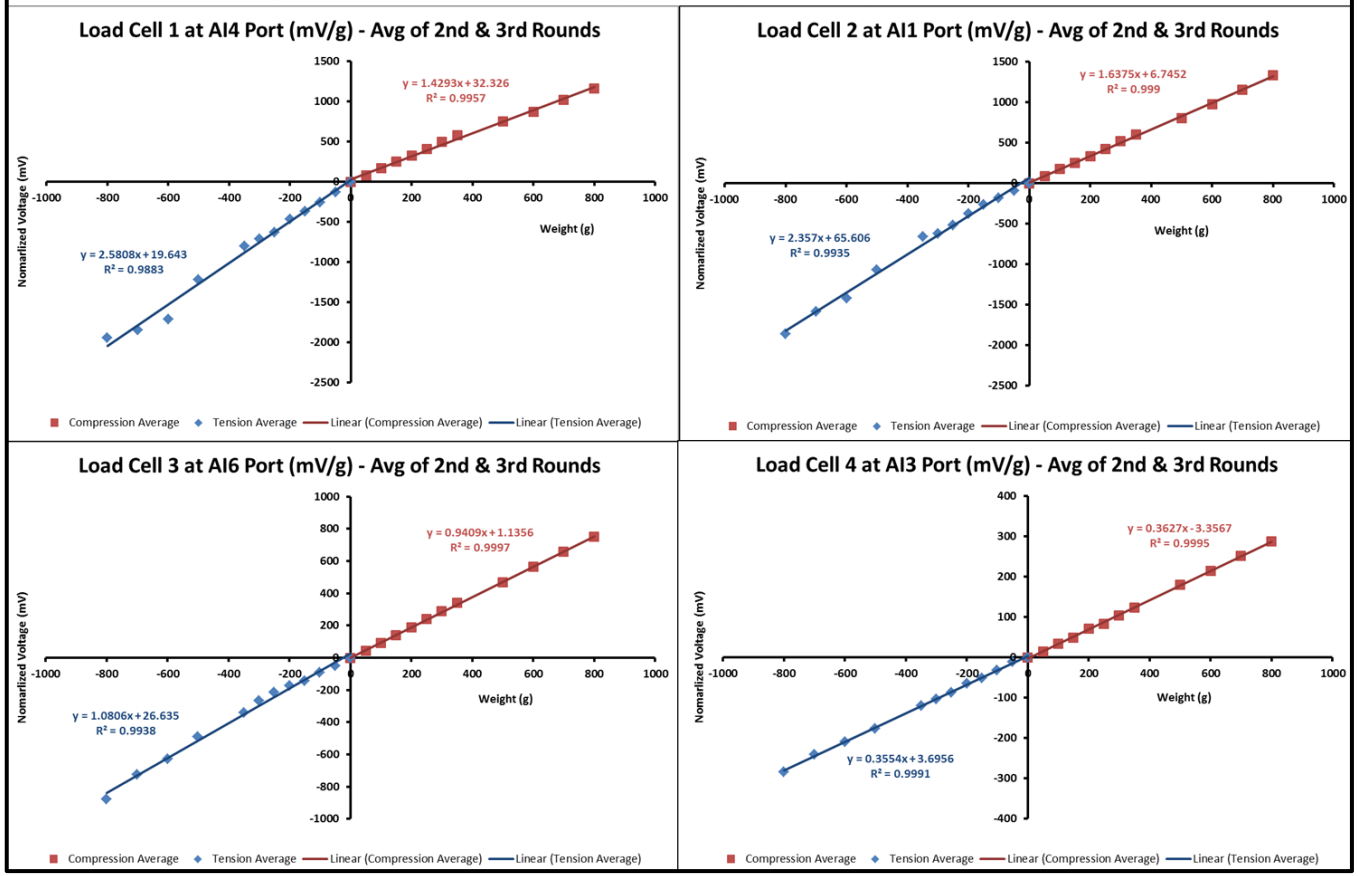

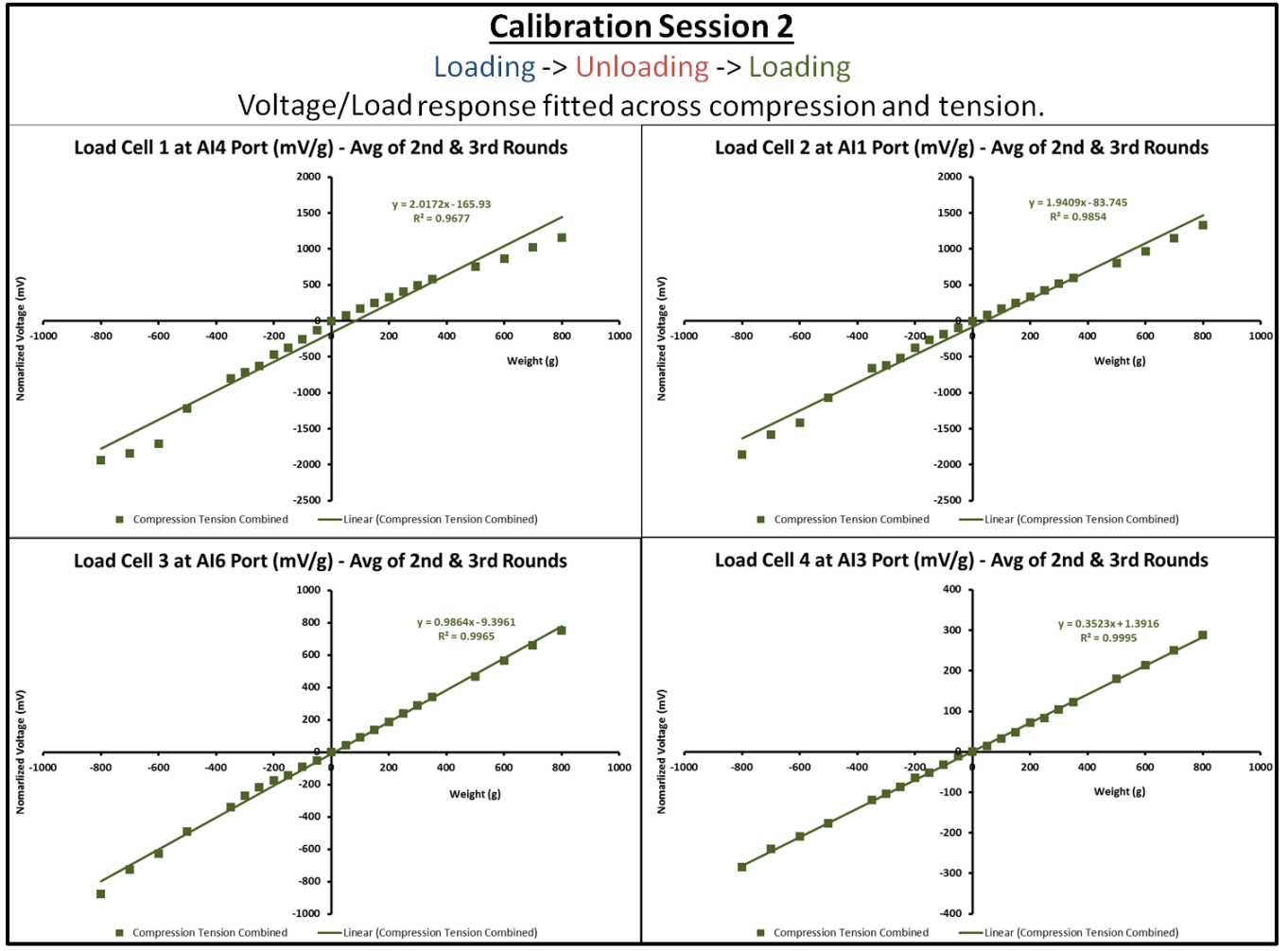
Calibration Session 2
Loading -> Unloading -> Loading
Voltage/Load response fitted across compression and tension.
Load Cell 1 at AI4 Port (mV/g) - Avg of 2nd & 3rd Rounds
y = 2.0172x - 165.93
R² = 0.9677
Nomarlized Voltage (mV)
Weight (g)
Compression Tension Combined
Linear (Compression Tension Combined)
Load Cell 2 at AI1 Port (mV/g) - Avg of 2nd & 3rd Rounds
y = 1.9409x - 83.745
R² = 0.9854
Nomarlized Voltage (mV)
Weight (g)
Compression Tension Combined
Linear (Compression Tension Combined)
Load Cell 3 at AI6 Port (mV/g) - Avg of 2nd & 3rd Rounds
y = 0.9864x - 9.3961
R² = 0.9965
Nomarlized Voltage (mV)
Weight (g)
Compression Tension Combined
Linear (Compression Tension Combined)
Load Cell 4 at AI3 Port (mV/g) - Avg of 2nd & 3rd Rounds
y = 0.3523x + 1.3916
R² = 0.9995
Nomarlized Voltage (mV)
Weight (g)
Compression Tension Combined
Linear (Compression Tension Combined)

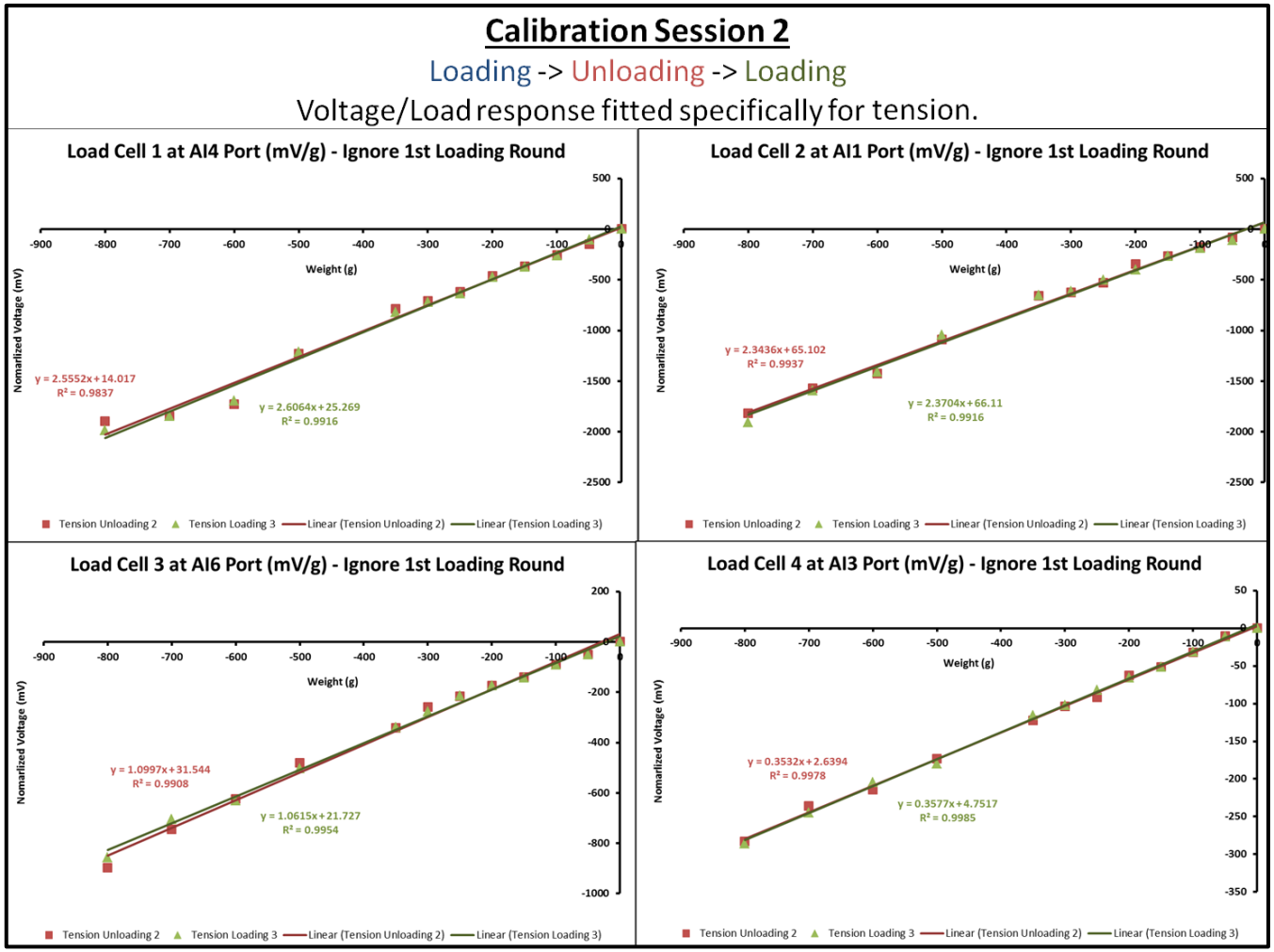
Calibration Session 2
Loading -> Unloading -> Loading
Voltage/Load response fitted specifically for tension.
Load Cell 1 at AI4 Port (mV/g) - Ignore 1st Loading Round
Nomarlized Voltage (mV)
Weight (g)
y = 2.5552x+14.017
R² = 0.9837
y = 2.6064x+25.269
R² = 0.9916
Tension Unloading 2
Tension Loading 3
Linear (Tension Unloading 2)
Linear (Tension Loading 3)
Load Cell 2 at AI1 Port (mV/g) - Ignore 1st Loading Round
Nomarlized Voltage (mV)
Weight (g)
y = 2.3436x+65.102
R² = 0.9937
y = 2.3704x+66.11
R² = 0.9916
Tension Unloading 2
Tension Loading 3
Linear (Tension Unloading 2)
Linear (Tension Loading 3)
Load Cell 3 at AI6 Port (mV/g) - Ignore 1st Loading Round
Nomarlized Voltage (mV)
Weight (g)
y = 1.0997x+31.544
R² = 0.9908
y = 1.0615x+21.727
R² = 0.9954
Tension Unloading 2
Tension Loading 3
Linear (Tension Unloading 2)
Linear (Tension Loading 3)
Load Cell 4 at AI3 Port (mV/g) - Ignore 1st Loading Round
Nomarlized Voltage (mV)
Weight (g)
y = 0.3532x+2.6394
R² = 0.9978
y = 0.3577x+4.7517
R² = 0.9985
Tension Unloading 2
Tension Loading 3
Linear (Tension Unloading 2)
Linear (Tension Loading 3)

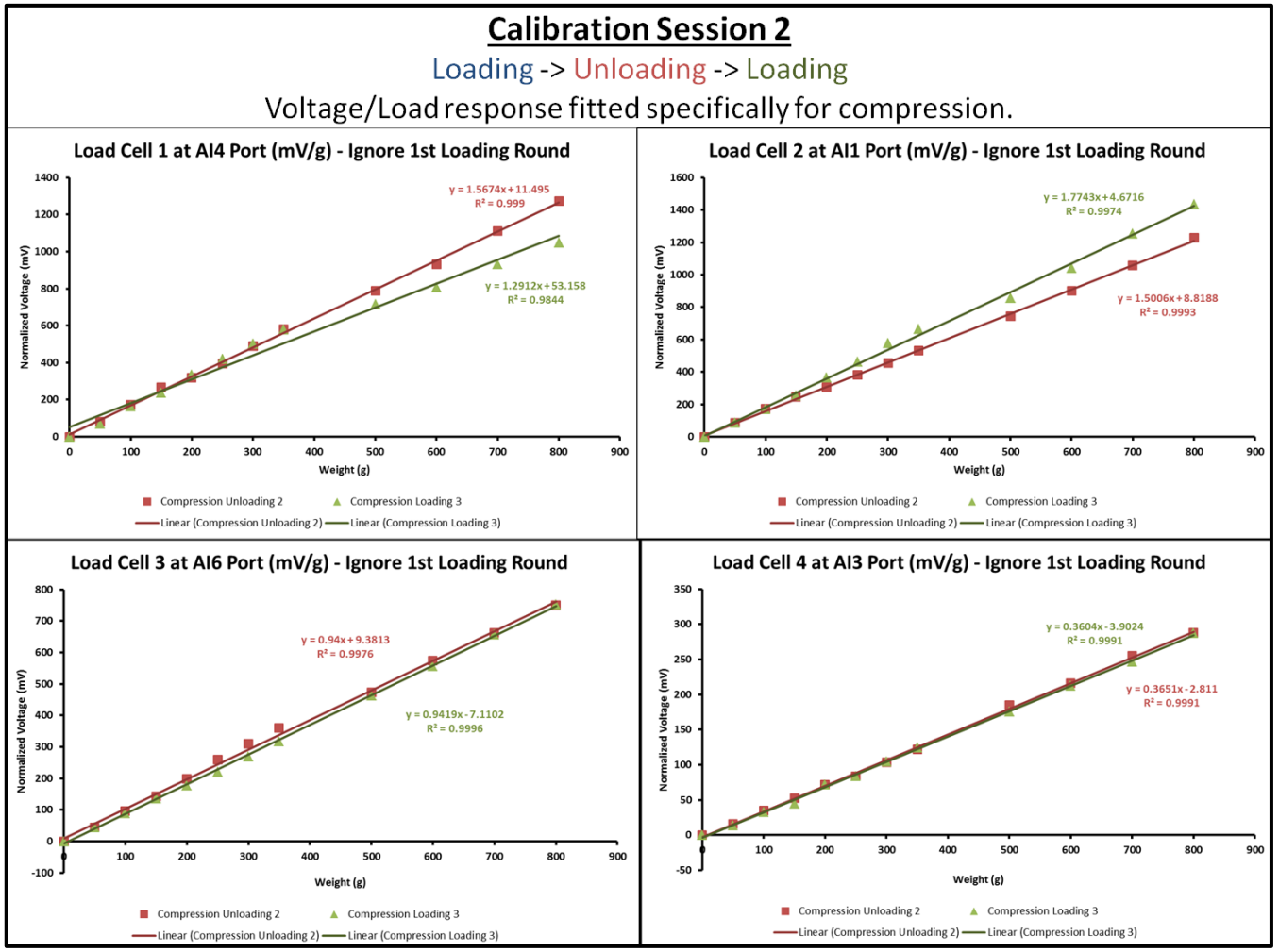
Calibration Session 2
Loading -> Unloading -> Loading
Voltage/Load response fitted specifically for compression.
Load Cell 1 at AI4 Port (mV/g) - Ignore 1st Loading Round
y = 1.5674x+11.495
R² = 0.999
y = 1.2912x+53.158
R² = 0.9844
Normalized Voltage (mV)
Weight (g)
Compression Unloading 2
Compression Loading 3
Linear (Compression Unloading 2)
Linear (Compression Loading 3)
Load Cell 2 at AI1 Port (mV/g) - Ignore 1st Loading Round
y = 1.7743x+4.6716
R² = 0.9974
y = 1.5006x+8.8188
R² = 0.9993
Normalized Voltage (mV)
Weight (g)
Compression Unloading 2
Compression Loading 3
Linear (Compression Unloading 2)
Linear (Compression Loading 3)
Load Cell 3 at AI6 Port (mV/g) - Ignore 1st Loading Round
y = 0.94x+9.3813
R² = 0.9976
y = 0.9419x-7.1102
R² = 0.9996
Normalized Voltage (mV)
Weight (g)
Compression Unloading 2
Compression Loading 3
Linear (Compression Unloading 2)
Linear (Compression Loading 3)
Load Cell 4 at AI3 Port (mV/g) - Ignore 1st Loading Round
y = 0.3604x-3.9024
R² = 0.9991
y = 0.3651x-2.811
R² = 0.9991
Normalized Voltage (mV)
Weight (g)
Compression Unloading 2
Compression Loading 3
Linear (Compression Unloading 2)
Linear (Compression Loading 3)

D. Dynamic Calibration of Friction of Moving Platen

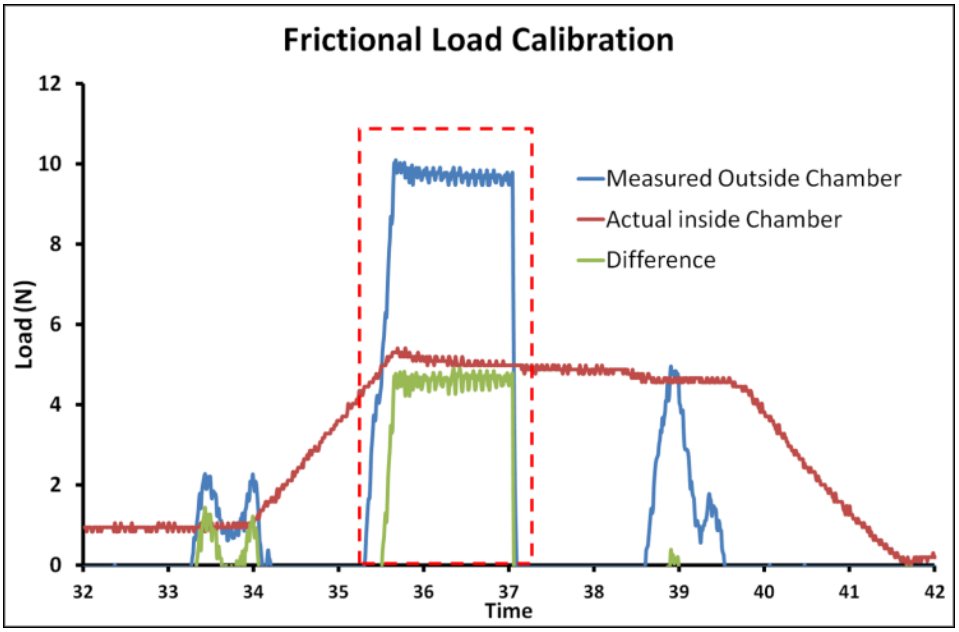

The average difference in load measured by the load cell fixed to the bioreactor unit (but outside the sample chamber) and of the load measured by the load cell inside the sample chamber at maximum displacement is on average 4.64N. There were slight peaks throughout the compression cycle due to the moving parts, but the primary interest is in the frictional load measured at maximum displacement as that would be the value of interest when the actual samples are loaded (maximum stress obtained, and Young's Modulus at maximum strain).

Further Discussion on Differences Observed Between Load Cells Inside and Outside of Bioreactor Chamber

The observed discrepancies in the forces measured between the load cell within the bioreactor chamber and that measured from the load cell external of the chamber can actually be attributed to two possible reasons:

1) frictional forces acting against the direction of motion of the platen and adapter, and

2) the force required to accelerate and decelerate the moving platen and adapter as the actuator undergoes periodic motion.

However, we have eliminated the second possibility in this thesis because of the low displacement rate and small amplitude of strain used. Hence, the force required to accelerate and decelerate the platen and adapter is almost negligible, making the observed discrepancy in load readings most likely caused by frictional loads.

E. List of Primers Used for RT-PCR

aP2	F: 5’ TTG ATG AAG TCA CCG CAG AT 3’ R: 5’ CAT TCC ACC ACC AGT TTA TCA C 3’
Aggrecan	F: 5’ GTG AAA GGT GTT GTG TTC CAC T 3’ R: 5’ TGG GGT ACC TGA CAG TCT GAT 3’
Biglycan	F: 5’ ATG GCC TGA AGC TCA ACT ACC T 3’ R: 5’ ATC ATC CGG ATC TGG TTG TG 3’
Collagen I (α2)	F: GCA TGT CTG GTT AGG AGA AAC C R: ATG TAT GCA ATG CTG TTC TTG C
Collagen II	F: 5’ AAG AGC GGT GAC TAC TGG ATA G 3’ R: 5’ TGC TGT CTC CAT AGC TGA AGT 3’
Decorin	F: 5’ CCT TCT CTT ACG GAA CTA CAT C 3’ R: 5’ TGA AAC TCA GAC CCA ACT TAG 3’
GADPH	F: GAC ATC AAG AAG GTG GTG AAG C R: CTT CAC AAA GTG GTC ATT GAG G
Leptin	F: 5’ CAC CAG GAT CAG TGA CAT CTC 3’ R: 5’ GTT GGC TAT TTG GAT CAC ATT T 3’
Osteonectin	F: 5’ GAA GTT GAG GAA ACC GAA GA 3’ R: 5’ GGC AGG AGG AGT CGA AG 3’
Osteopontin	F: 5’ GCT CAG CAC CTG AAT GTA CC 3’ R: 5’ CTT CGG CTC GAT GGC TAG C 3’
PPARγ2	F: 5’ CCT GGC AAA GCA CTT GTA TGA 3’ R: 5’ AAC GGT GAT TTG TCT GTC GTC T 3’
Runx2	F: 5’ CCT TCC ACT CTC AGT AAG AAG A 3’ R: 5’ TAA GTA AAG GTG GCT GGA TAG T 3’
Sox9	F: 5’ CTT CAT GAA GAT GAC CGA CGA G 3’ R: 5’ CTC TTC GCT CTC CTT CTT GAG G 3’

F. Modulation of Autofluorescence in Silk

F.1 Introduction

It is interesting to note that the issue with autofluorescence in microscopy is not distinctive to silk. Artificial polymeric biomaterials such as poly(urethane) and poly(lactic acid-co-glycolic acid) have been reported in literature to exhibit autofluorescence behaviours which interfere with detection analysis of fluorescently tagged targets (266). Methods described in literature that addresses this autofluorescence issue includes the use of photobleaching (267,268), borohydride addition (269), and treatment with quencher dyes such as Pontamine Sky Blue (270), Trypan Blue (271) and Sudan Black B (SB). Of these, one of the most successful and effective methods is the use of low concentrations SB (267,272,273). SB is a lysochrome dye originally used in histology to stain for lipids (274,275). In a recent study by Jaafar and co-workers, SB was used to successfully quench the undesirable auto fluorescence signals from artificial biomedical polymers and thereby improved fluorescence imaging analysis (266). It is hypothesized that SB will have a similar quenching phenomenon on silk, and can hence improve fluorescence based imaging analysis involving silk-based biomaterials.

The success of SB as a useful autofluorescence quencher for imaging purposes, hinges on the condition that it doesn't adversely affect the signals from commercially available fluorescent dyes used in staining protocols. Hence, the first part of this study was dedicated to i) investigate the duration of SB treatment on several immunofluorescent labels and ii) conduct an in-depth study on the effect of SB treatment duration and juncture of treatment introduction on fluorescence staining of actin by fluorescently conjugated phalloidin toxin.

The aims for the second part of the study were: i) to study the suppressing effects of SB on the intrinsic fluorescent signals of the silk biomaterials, and ii) to investigate any improvement to fluorescence analysis brought about by SB treatment.

F.2 Materials and Methods

a. Preparation of Silk-Based Biomaterials

Silk-based biomaterials were fabricated using SF solution prepared as described earlier in section 4.2. Silk films were fabricated using a modified protocol in literature (133) by evaporating a thin layer of 5% (w/v) silk fibroin solution on 24-well culture plates overnight, before adding absolute methanol (Fisher Chemical) for β-sheet formation to render the film insoluble in an aqueous environment. Electrospun mats were fabricated and treated as described in section 4.2 and collected on glass cover slips placed on the collecting platform. Composite sponge-fibre scaffolds consisting of silk sponge embedded with fibres were fabricated by fixing fine silk yarns to the bottom of a standard 90mm petri dish, on which 10 ml of 5% (w/v) silk fibroin solution was added with gentle swirling to ensure uniform coverage. The petri dishes with the silk fibroin solution and fibres were then freeze-dried in a freeze dryer (Epsilon 1-4; Martin Christ GmbH) for 16 hours to remove water content in order to obtain the composite sponge-fibre scaffold consisting of silk fibres encased within a silk sponge. Absolute methanol was then added to allow for β-sheet formation for the sponge component.

b. Cell Culture and Experimental Design

rASCs of passages 5 to 6 were used for all the cellular experiments in this section. Unless otherwise stated, cell cultures were conducted in medium consisting of LG-DMEM (Invitrogen) supplemented with 10% FBS (Hyclone, Thermo Fisher

Scientific) and 1% P/S (PAN-Biotech GmbH, Aidenbach, Germany). All cultures were maintained in a humidified 5% CO_2 incubator at 37^{o}C.

Five groups of fluorescence staining experiments were conducted to address the objectives of this study. They were as follows: Group I - Effect of SB on fluorescent probes conjugated to secondary antibodies; Group II - Effect of SB on fluorescent probes conjugated to phalloidin toxin; Group III - Effect of SB treatment on F-actin staining with silk films and electrospun mats; Group IV - Enhancing co-localization imaging of F-actin and fibronectin on silk electrospun mats; and Group V - Improving resolution of proteins and cells on composite silk sponge-fibre scaffolds.

For groups I and II, ASCs were seeded at a density of ~5x10^3 cells/cm^2 on 24-well TCPS culture plates. This addresses the first part of the study involving the effect of SB treatment and duration on fluorescent probes. These samples did not contain any silk biomaterials to avoid any fluorescence disturbances in assessment. Plates were sacrificed for assessment after (i) 3 days for staining protocols involving collagen Type I detection (Group I), and (ii) 1 day for staining protocols involving just F – actin detection (Group II). Culture medium for group I was further supplemented with 50 μg/ml Vit C (Wako), to improve ECM deposition, and aid in collagen Type I (Col I) detection (176).

For groups III, IV and V, composite sponge-fibres scaffolds, electrospun mats and silk films were sterilized by 70% ethanol treatment, followed by UV irradiation before cell-seeding. ASCs were seeded at a density of 6x10^3 cells/cm^2 on the silk films, ~1.5x10^4 cells/cm^2 on the electrospun mats, and ~1x10^5 cells/cm^2 on the composite sponge-fibre scaffolds. The seeding densities for the latter two were higher to account for the 3D nature of the mat (~30 to 40μm thick) and composite scaffold

(~ 700 to 900μm thick). Films and electrospun samples were sacrificed for assessment after 1 day for staining protocols involving only F–actin detection (Group III), and also for staining protocols involving detection of extracellular matrix (ECM) proteins (Eg. Fibronectin, Group IV). Cell-seeded composite sponge-fibre scaffolds were maintained in ascorbic acid supplemented medium for 28 days before being sacrificed for assessment (Group V).

c. Immunofluorescence Staining

ASCs from group I were first fixed with -20^{o}C methanol for 10mins, before being washed with 1x PBS. The samples were then blocked with 1% BSA (Sigma Aldrich) for 1 hr, before overnight incubation with a primary Col I antibody (Sigma Aldrich) in a humidified chamber at 4^{o}C. Secondary antibodies (conjugated with Alexa Fluor 488nm (Invitrogen) and Alexa Fluor 594nm (Invitrogen) probes) targeting the primary antibody were then added with DAPI (0.5μg/ml; Invitrogen) for counterstaining of the nucleus for 30mins at room temperature.

ASCs from groups II and III were first fixed in 4% methanol free formaldehyde (Thermo Fisher Scientific) for 10mins, before being washed with 1xPBS. Intracellular F-actin staining required cell membrane permeabilization by 0.1% (v/v) Triton-X (Bio-Rad Laboratories). Phalloidin conjugated with Alexa Fluor 488nm fluorescent probes (Invitrogen) and DAPI (0.5μg/ml; Invitrogen) which was used as a counterstain, were added for 30mins at room temperature.

ASCs from group IV were fixed and permeabilized the similar way as described for groups II and III. The samples were then blocked with 1% BSA for 1 hr, before overnight incubation with a primary fibronectin antibody (Sigma) in a humidified chamber at 4^{o}C. Secondary antibodies (conjugated with Alexa Fluor 594nm

(Invitrogen) probes) targeting the primary antibody were then added with DAPI (0.5μg/ml; Invitrogen) for 30mins at room temperature.

.

As the composite sponge-fibre scaffolds from group V were too thick for direct fluorescence imaging as those conducted for groups I to IV, cryosectioning was undertaken to carry out analysis. Group V samples were first fixed in 10% neutral buffered formalin at room temperature overnight before being washed with 1xPBS. Samples were then incubated with 40% sucrose overnight at 4°C before being embedded in tissue freezing medium (Shandon Cryomatrix, Thermo Fisher Scientific) for sectioning with a cryostat (Research Cryostat CM3050S, Leica Biosystems, Wetzlar, Germany). Sections of 20μm thickness were then used for immunofluorescence staining. As antigen retrieval was necessary for collagen Type I detection following formaldehyde fixation, this was carried out by pepsin (Roche Diagnostics) digestion at 37^{o}C for 15mins. Blocking was then carried out with 1% BSA for 1hr, before overnight incubation with the primary fibronectin and Col I antibodies (both Sigma) in a humidified chamber at 4^{o}C. Secondary antibodies (conjugated with Alexa Fluor 488nm (Invitrogen) Alexa Fluor 594nm (Invitrogen) probes) targeting the primary antibodies were then added with DAPI (0.5μg/ml; Invitrogen) for 30mins at room temperature.

All images were viewed with an inverted epifluorescence microscope (IX71, Olympus), equipped with filters (Olympus) conventionally used in fluorescence microscopy. These filters are: i) WU filter set (excitation filter 330-385nm, emission filter 420nm) for DAPI (blue) viewing, WIBA filter set (excitation filter 460-495nm, emission filter 510-550nm) for Alexa Fluor 488nm (green) viewing and WIY filter set (excitation filter 545-580nm, emission filter 610nm) for Alexa Fluor 594nm (red)

viewing. Microscopy images were all captured using a DP70 digital colour camera system (Olympus) at ISO200.

d. Sudan Black B (SB) Quenching

SB powder form (Sigma Aldrich) was dissolved in 70% ethanol to form 0.3% (w/v) working solutions, in line with published protocols which had used SB as a quencher dye (266,272). Samples were incubated with SB for 15 to 120mins, at room temperature, before rinsing in 1x PBS to remove excess SB. All SB quenching were conducted at the last step of fluorescence-based staining protocols except for groups II and III, whereby in addition to introducing SB post fluorescence staining, SB treatment was also introduced before the permeabilization and fluorescence staining steps to investigate the possibility of introducing SB treatment earlier in the staining process.

e. Scanning Electron Microscopy (SEM)

SEM was conducted on cross-sections of cell-seeded samples from group V and on acellular electrospun mats used for groups II, III and IV to correlate the structures seen on the fluorescence images with SEM imaging. Prior to SEM, group V samples were first fixed in 4% methanol free formaldehyde (Thermo Fisher Scientific) for 1hr, before being washed with 1xPBS. The samples then underwent progressive dehydration by saturating them in 70% ethanol for 1 day, followed by 100% ethanol overnight. Samples were then placed in a critical point dryer (Autosamdri®-815 Series A, Tousimis, Rockville, MD, USA) for preservation of the surface structure. All samples (including the electrospun mats) were placed in a gold coat sputter (JEOL) before being viewed using scanning electron microscopes from JEOL (JSM-5610/JSM6510; JEOL).

f. Fluorescence Spectroscopy and Statistical Analysis

Fluorescence intensities of untreated and SB treated silk films and electrospun mats were read using a microplate reader (PHERAstar Plus) with the following three filter sets: blue filter set (excitation: 340nm / emission: 460nm), green filter set (excitation: 485nm / emission: 520nm) and red filter set (excitation: 545nm / emission: 610nm). Fluorescence spectral measurements between controls (no SB treatment) and SB treated groups (5mins, 15mins, 30mins, 60mins and 120mins SB treatment) were all conducted either in one plate or back-to back and normalized to the highest fluorescence to account for day to day variations and random background spectral noises from the instrument. Statistical analysis of the spectral data were conducted using a one-way analysis of variance (ANOVA) test with post-hoc Tukey correction using OriginPro9 (OriginLab). $p<0.05$ was taken as significant.

F.3 Results

a. SB treatment does not detrimentally affect signals from fluorescent probes

The duration of SB treatment on the signal strength of commercial AlexaFluor fluorescent probes was investigated. For comparison purposes, SB treated samples' images were taken at the same exposure time and ISO as the respective controls with no SB treatment. Each set (comprising the experimental groups and the control group) of images were also taken within a single imaging session to avoid variances in lamp strength and fluorophore bleaching. No silk was used in this part of study as any effect on the signal strength of the fluorescent probes is to be accounted for solely by SB treatment. It can be seen in Figure F-**1ai to** Figure F-**1av** that SB treatment of up to 2 hours did not detrimentally affect the signals of the fluorescent probes of DAPI and the immuno-tagged Alexa Fluor 594nm. The same can be observed for the immuno-tagged Alexa Fluor 488nm probes as seen in Figure F-**1b**.

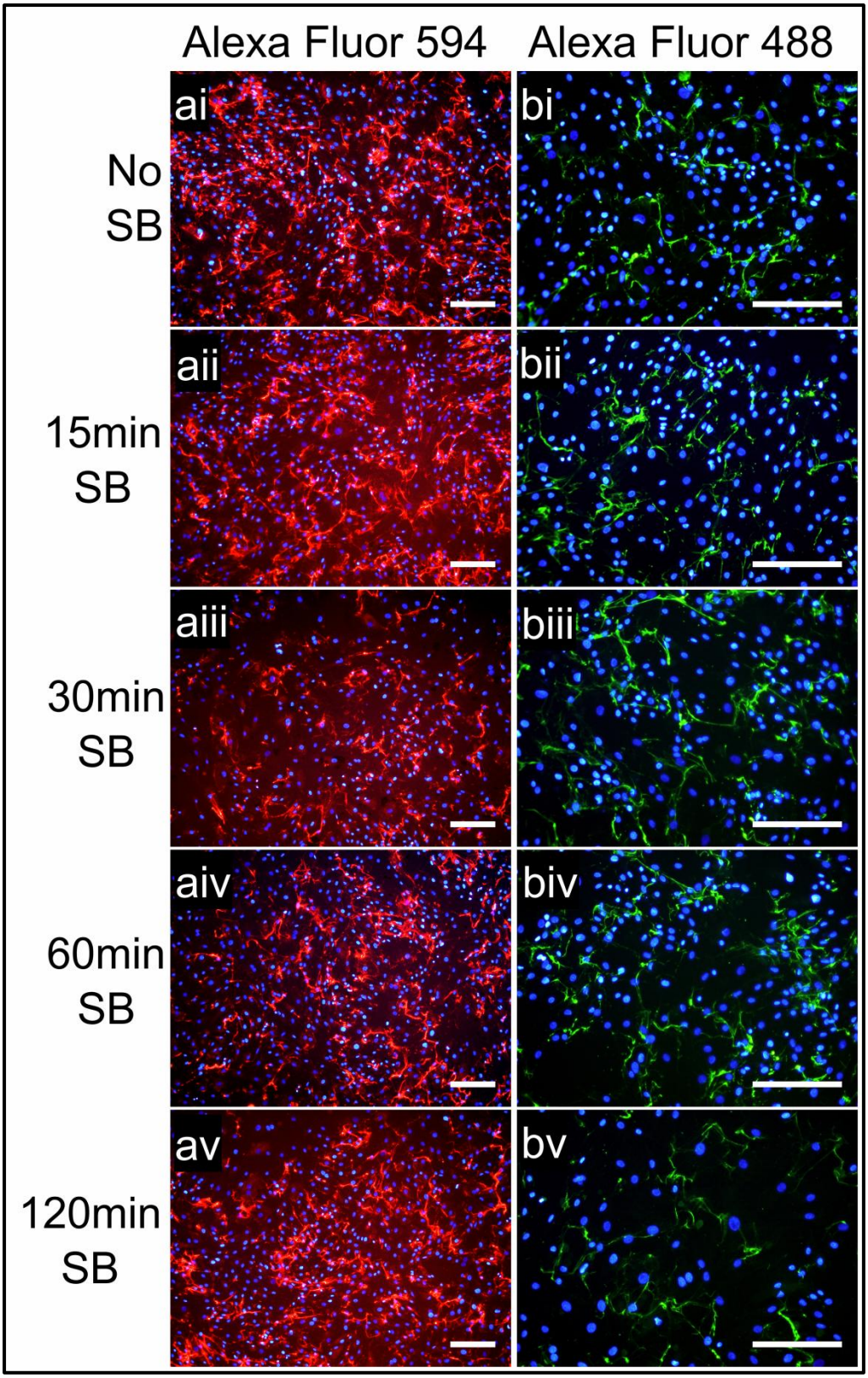

Figure F-1. Effect of SB treatment duration on fluorescence intensity of secondary antibodies conjugated with (a) Alexa Fluor 594nm (red) and (b) Alexa Fluor 488nm (green) probes. Cells were counterstained with DAPI (blue). Scale bars: 200μm.

Further to introducing SB at the end of staining protocols as commonly published, the introduction of SB before fluorescence staining was investigated in Figure F-**2**. SB treatment was chosen to be added before the cell membrane permeabilization step in order to avoid any possible destruction of the intra-cellular actin due to the ethanol-based SB staining solution. When compared to the control (No SB treatment, Figure 6-**2c),** it can be seen that SB treatment affected the signal strength of the Alexa Fluor 488nm fluorescent probe attached to the phalloidin toxin (Figure F-**2a** and Figure F-**2b**). Introducing SB treatment before permeabilization and fluorescence staining Figure F-**2a**) resulted in stronger signals from the probes as compared to after permeabilization and fluorescence staining (Figure F-**2b**). A duration of up to 30mins SB treatment did not further decrease the fluorescent signals significantly as what was already suppressed with a 15mins SB treatment duration in the before permeabilization and fluorescence staining groups (Figure F-**2a**), while the contrary was observed in the after permeabilization and fluorescence staining groups (Figure F-**2b**, 30min treatment versus 15min treatment).

Images in Figure F-**2ai**, aiii, bi, biii and c were taken at the same exposure time and ISO parameters (DAPI: ISO200, 1/50sec; 488nm: ISO200, 1/2sec) for comparison purposes. It must be noted that the green signals seen in the SB treated samples (albeit weak) could be made stronger by increasing either the ISO or the exposure time of the microscope digital camera to clearly show the structure of the actin filaments if needed. This is demonstrated by Figure F-**2aii**, 2aiv, 2bii and 2biv (DAPI: ISO200, 1/50sec; 488nm: ISO200, 1sec), which show signals of considerable equal strength as that of the control (Figure F-**2c**) taken at a shorter exposure time.

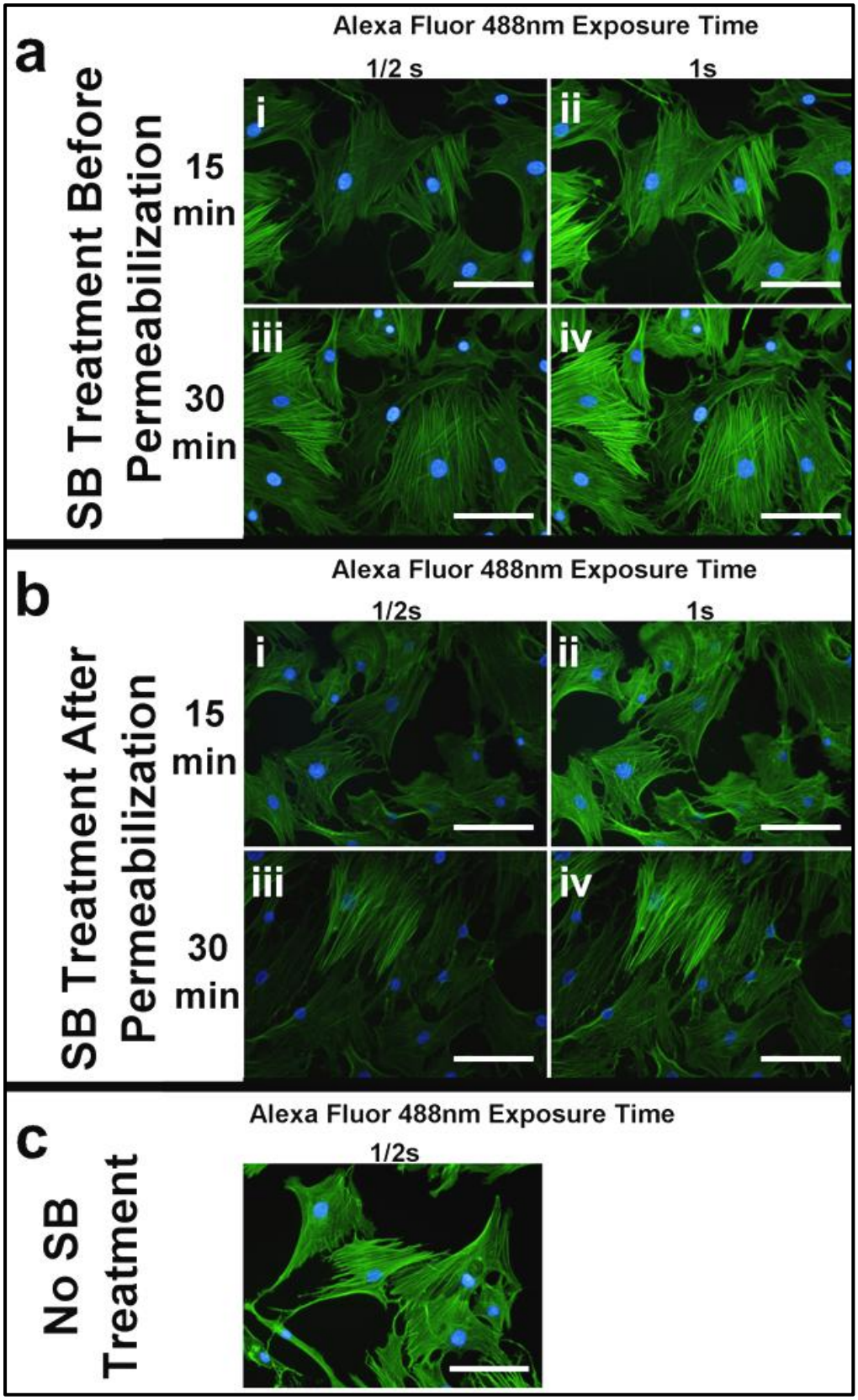

Figure F-2. Effect of SB treatment duration on phalloidin toxin conjugated Alexa Fluor 488nm (green) probes, when introduced before permeabilization with Triton-X (a) and after permeabilization with Triton-X (b), as compared to control (c) with no SB treatment. Cells were counterstained with DAPI (blue). All images were taken at ISO 200, exposure time of 1/50s for DAPI. Exposure time for Alexa Fluor as indicated in figure. Scale bars: 100μm.

b. SB treatment effectively suppresses endogenous fluorescence signals from silk biomaterials

The suppressing effects of SB treatment on the intrinsic fluorescence signals of silk films and silk electrospun mats were first quantitated by fluorescence spectroscopy. From Figure F-**3**, results indicated that for typical fluorescence based assessments of silk films and electrospun mats, a red emission wavelength fluorescent dye (Eg. Texas Red, TRITC) would be more preferable given that the silk materials displayed much lower intrinsic fluorescence values in the red wavelength as compared to the green and blue wavelengths. It is however still important to improve imaging in the latter two wavelengths given the need for nucleus counterstaining and co-localization studies. 5mins of SB treatment significantly brought down the intrinsic fluorescence values of silk films (Figure F-**3a**) and silk mats (Figure F-**3b**). Longer SB treatment durations did not brought about further suppression of endogenous fluorescence signals from the silk films (Figure F-**3a**), but did so with the electrospun mats (Figure F-**3b**). There were three other significant drops in endogenous fluorescence intensities in the electrospun mats group (Figure F-**3b**) with respect to no SB treatment - after 30mins, 60mins and 120mins of SB treatment.

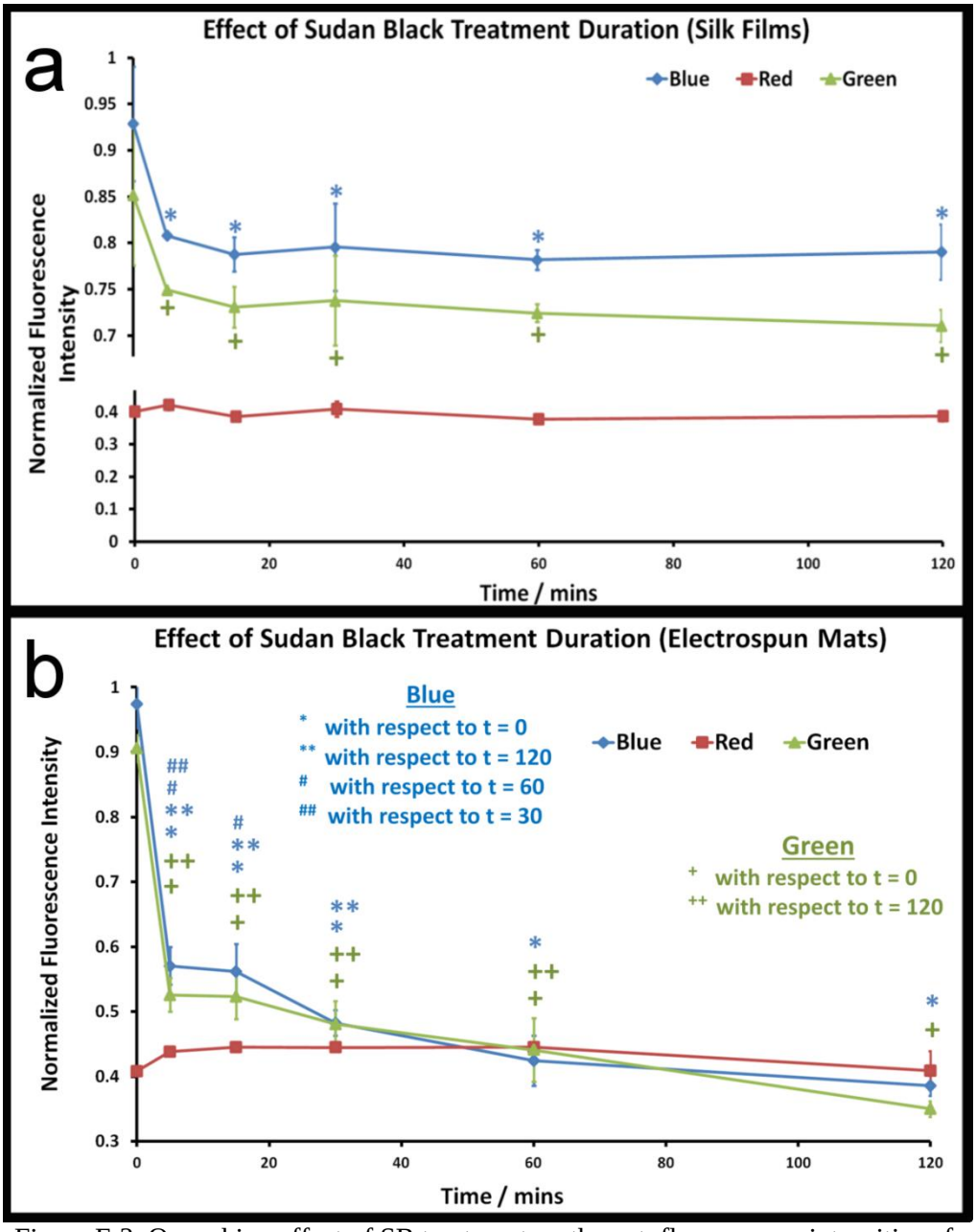

Figure F-3. Quenching effect of SB treatment on the autofluorescence intensities of (a) silk films, and (b) silk electrospun mats over the blue, green and red wavelengths. $p<0.05$.

c. SB treatment improves imaging resolution of cells and proteins on silk biomaterials

Cells were then seeded on the silk-based biomaterials and stained fluorescently with and without SB treatment to investigate the use of SB in improving fluorescence microscopy imaging. From Figure F-**4a** and Figure F-**4b**, it can be observed that SB treatment played a more important role in improving imaging in the electrospun mats

rather than the silk films. This is due to the relatively weaker endogenous fluorescence signals exhibited by the silk films compared to the signals from the DAPI and Alexa Fluor 488nm probes - enabling effective thresholding to be conducted even without SB treatment (Figure F-**4a**). However, in cases where the endogenous fluorescence signals are relatively strong in relation to the DAPI and Alexa Fluor probes (Figure F-**4b**, control group), SB treatment effectively improved imaging by suppressing the intrinsic signals coming from the silk material itself and thus enabling effective thresholding to be conducted to eliminate the background signals (Figure F-**4b**, SB treated groups). For actin staining by phalloidin toxin on electrospun mats (Figure F-**4b**), introducing SB treatment before permeabilization and fluorescence staining (rather than after) resulted in stronger Alexa Fluor 488nm and DAPI probes specific signals, as can be seen in differences shown in the before and after groups of images in Figure F-**4b**. Prolonged SB treatment durations did not necessarily translated to better images, as shown in the 30min treatment images as compared to the 15min treatment images (Figure F-**4b**). This is due to the slight decrement in signal strength of the DAPI and Alexa Fluor 488nm probes due to the SB treatment. These are in line with results reported in Figure 3, which reported no significant decrement in endogenous intensities between 15min and 30min of SB treatment duration.

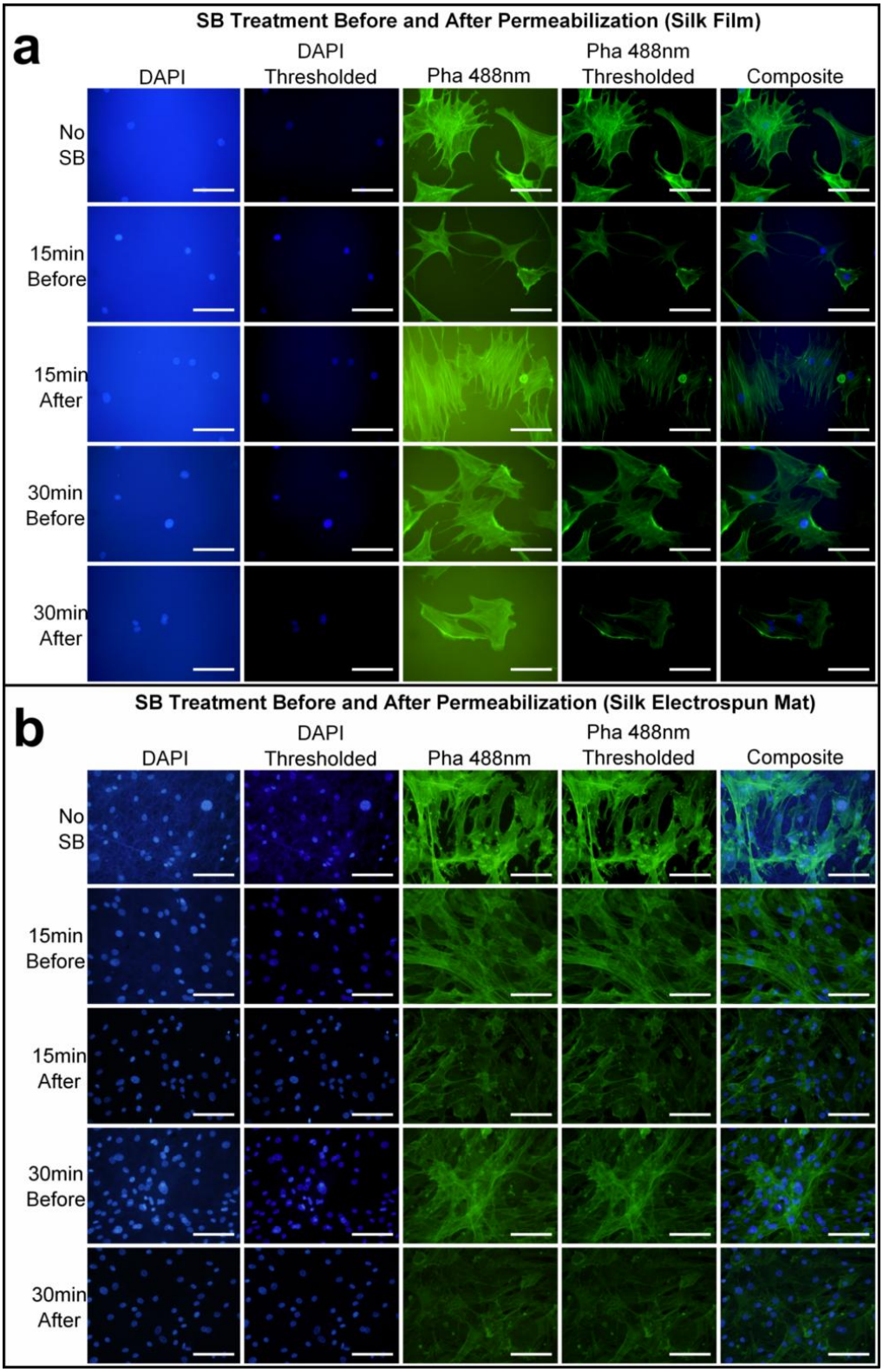

Figure F-4. Effect of SB treatment duration and juncture of introduction on microscopy images of ASCs seeded on silk films (a) and silk electrospun mats (b), and stained for F-actin using phalloidin conjugated with Alexa Fluor 488nm and counterstained with DAPI for nucleus. All images for (a) were taken at ISO 200, 1/5s for Alexa Fluor 488nm, 1/100s for DAPI. All images for (b) were taken at ISO 200, 1/10s for Alexa Fluor 488nm, 1/200s for DAPI. Scale bars: 100μm.

Apart from improving imaging of intracellular actin labelled with a fluorescent labelled phalloidin toxin, SB is also suitable for use in improving imaging analysis of immuno-stained proteins and DAPI labelled cells in conjunction with phalloidin (Figure F-**5**). Fibronectin, an important cell adhesion and migration mediator (276) (277), was chosen as the protein of interest to be studied in co-localization with F-actin and the nucleus of cells seeded on the silk electrospun mats. SB treatment enabled a much clearer view of the locations of fibronectin (stained with a primary fibronectin antibody, and conjugated with a Alexa Fluor 594nm secondary antibody), F-actin (stained with a Alexa Fluor 488nm conjugated phalloidin toxin), and the cell nucleus (stained with DAPI) as compared to the control group with no SB treatment (Figure F-**5**) – where the non-specific background signals (especially in the DAPI wavelength) masked the signals from the F-actin and fibronectin. The blue lines observed in the No SB group in Figure F-**5** (inset) corresponds to the electrospun fibres of the electrospun mat as depicted in an SEM format shown in Figure F-**6a**. SB treatment suppressed the blue wavelength signals, and the resultant composite image of the electrospun fibres of the SB treated electrospun mat appeared a purplish colour (Figure F-**5**, 15mins SB inset) instead, aiding in the discretion of protein, actin, nucleus and mat within a single image. Due to reported literature on the detrimental effect of SB treatment on immunocytochemistry based staining [239], SB treatment was done after permeabilization and fluorescence staining.

Figure F-**6b** depicts the ECM deposited by ASCs after 28 days of culture on the sponge-fibres composite scaffolds. It can be observed from the SEM images the close proximity of the ECM deposited with the silk sponge and silk fibres. With this information, sponge-fibres composite scaffolds after 28 days of culture were sectioned and stained for common extracellular proteins like collagen Type I and fibronectin to investigate whether SB treatment can help in identification of ECM proteins residing in close proximity with autofluorescing silk scaffolds.

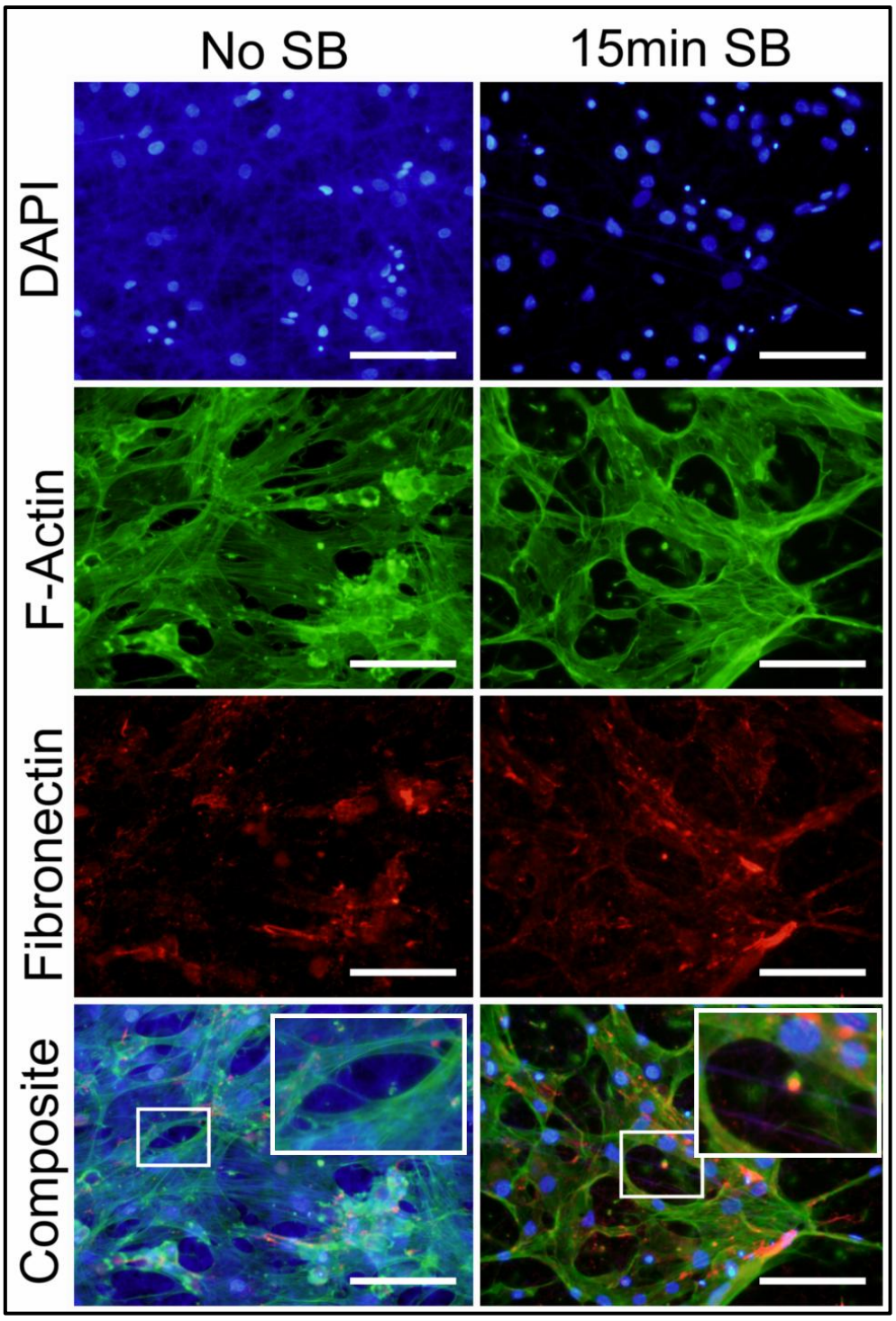

Figure F-5. Triple staining fluorescence images of ASCs seeded onto silk electrospun mats with and without SB treatment. F-actin was stained with phalloidin conjugated with Alexa Fluor 488nm (green), fibronectin was immuno-tagged with Alexa Fluor 594nm (red). Cells were counterstained with DAPI. Blue lines in No SB composite image (inset) and purple lines in 15min SB composite image (inset) correspond to electrospun silk fibres. Scale bars represent: 100μm.

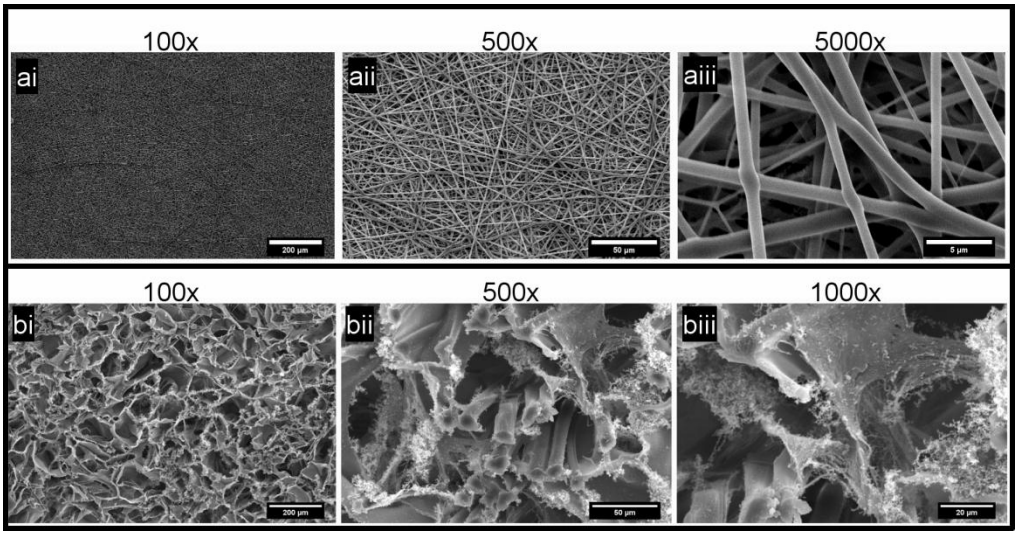

Figure F-6. SEM images of electrospun silk mats (a), and cell-seeded sponge-fibre composite scaffolds after 28 days of culture (b). Morphologies observed under SEM for (a) corroborate with those observed under fluorescence imaging. Extracellular matrix observed to be deposited on the silk scaffold in (b) were only clearly visible in SB treated samples in Figure 6-7 and Figure 6-8.

Figure F-**7** and Figure F-**8** demonstrated that SB treatment indeed helped in suppressing the endogenous signals from silk that are capable of masking the signals from fluorescently tagged proteins which would have gone unidentified (no SB groups in Figure F-**7** and Figure F-**8**) due to its close proximity with the silk scaffolds. This is even true with proteins tagged with a red wavelength fluorescent probe (Figure F-**7b** and Figure F-**8b**), due to the strong signals from the blue wavelength in general, which masked the presence of cells and the proteins located on the silk sponges (inset images of Figure F-**7b** and Figure F-**8b**). For these cases, SB treatment played an important role by suppressing non-specific signals in the blue wavelength, thereby creating a purplish hue indicative of the silk scaffolds, and therefore highlighting the fluorescently red proteins. Interestingly, in the green wavelength (Figure F-**7a** and Figure F-**8a**), SB treatment suppressed the green endogenous signals from the silk scaffolds to an extent by which silk appears in a golden hue relative to the green signals from the immuno-fluorescently tagged proteins, thereby helping to distinguish clearly the locations of the proteins (inset images of Figure F-**7a** and Figure F-**8a**) .

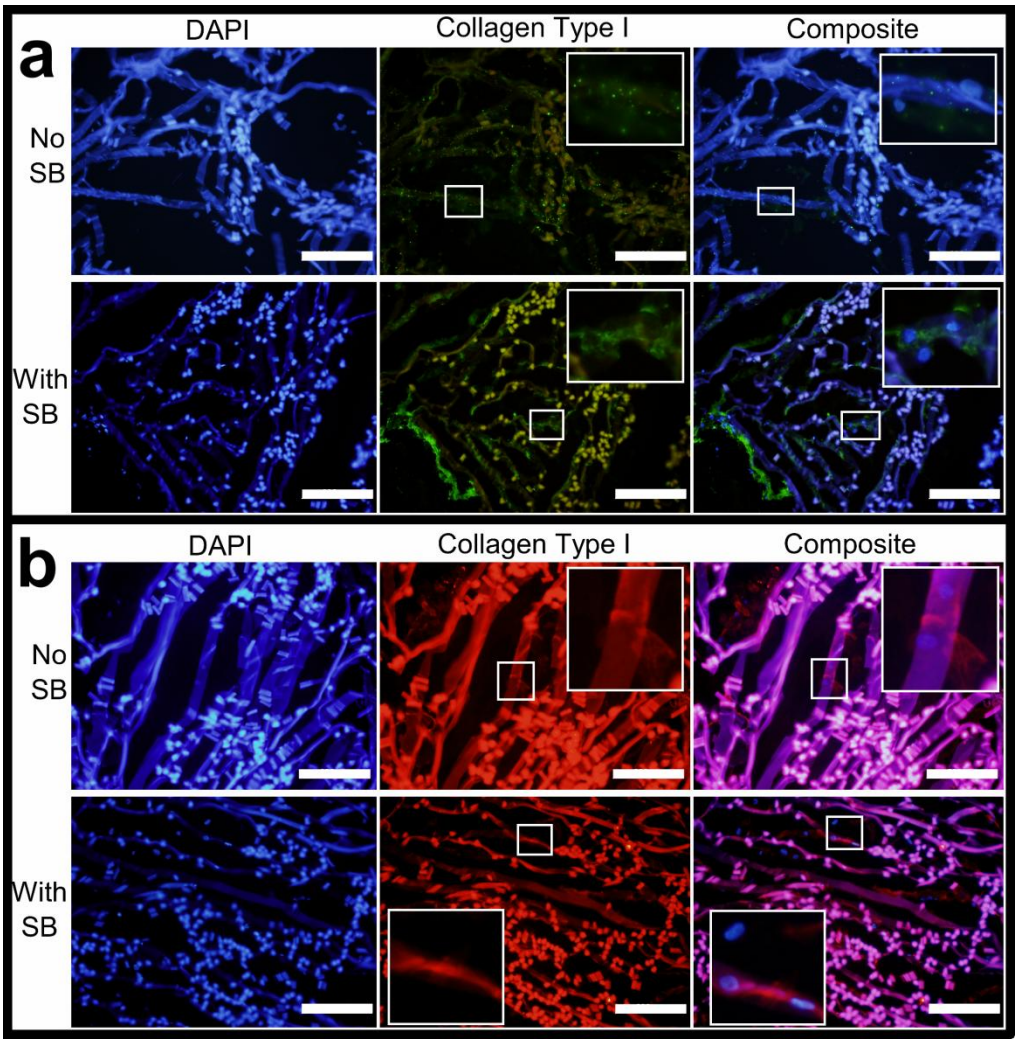

Figure F-7. Immunostained fluorescence images of cell-seeded sponge-fibre composite scaffolds cryosectioned at 20μm per section and tagged for collagen Type I and secondarily conjugated to Alexa Fluor 488nm (a) and Alexa Fluor 594nm (b). DAPI was used as a counterstain, with SB treatment set at 15minutes. Scale bars: 200μm

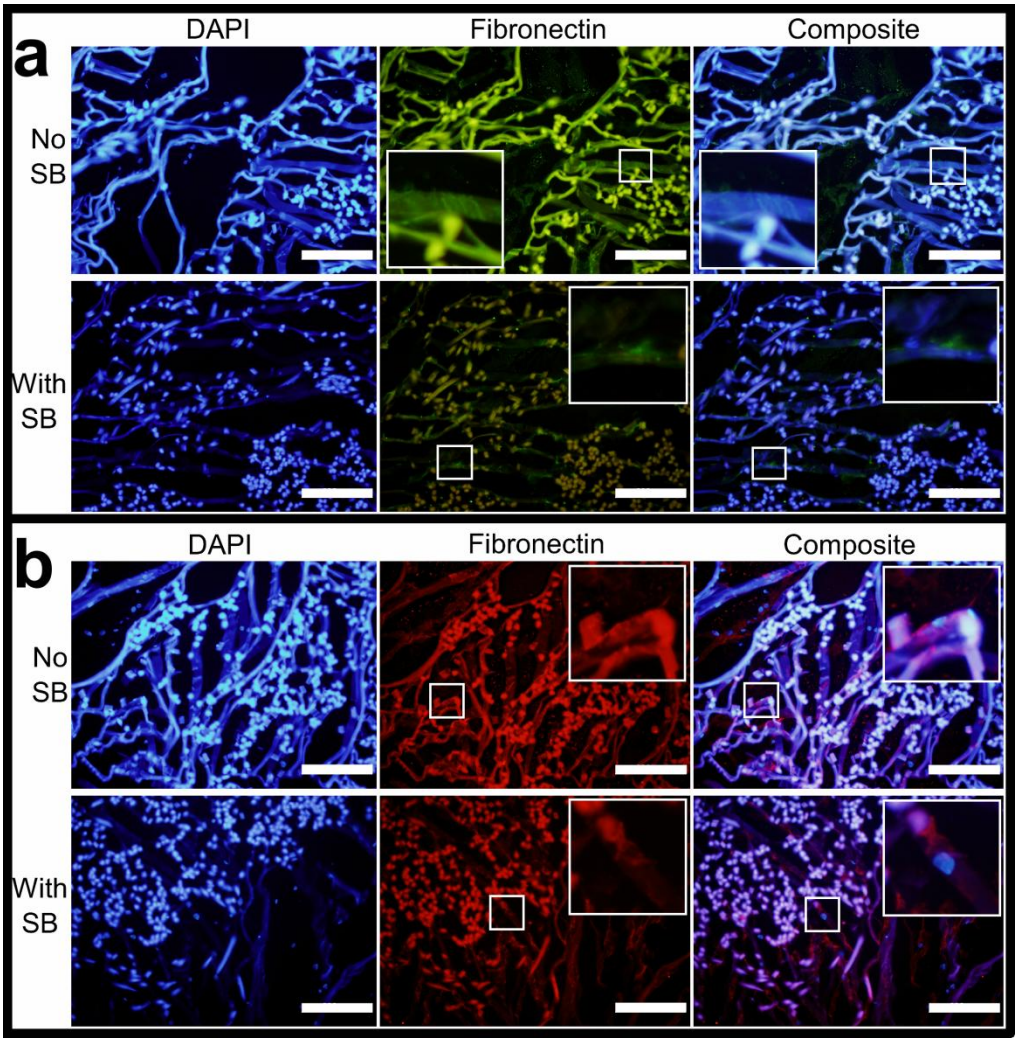

Figure F-8. Immunostained fluorescence images of cell-seeded sponge-fibre composite scaffolds cryosectioned at 20μm per section and tagged for fibronectin and secondarily conjugated to Alexa Fluor 488nm (a) and Alexa Fluor 594nm (b). DAPI was used as a counterstain, with SB treatment set at 15minutes. Scale bars: 200μm.

F.4 Discussion

Silk is a highly hierarchical protein consisting of several forms of secondary structures. They include i) random coil structure, ii) α-helical structure, iii) Silk I structure (a pre-crystallization glandular state) and iv) Silk II (β-sheet) structure (131,139). The β-sheet structure is highly insoluble and happens in the crystalline region, whereas the first three kinds of mentioned structures occur in the solution state and correspond to the non-crystalline region of the silk protein (139). As silk fibroin (from the solution state) undergoes conformational changes to become gels (semi-solid state) and sponges (solid state), the proportion of the secondary structures

changes such that there is a general increment in the β-sheet proportion (139). The β-sheets can further cross-link, thereby creating a highly ordered structure which is insoluble, and also changing the spatial locations of the Tyr and Trp residues (139). For example, using a combination of fluorescence spectroscopy and circular dichroism spectroscopy, Yang and co-workers found that Trp residues, in the unfolded random coil form of the silk fibroin, are mostly located in a heterogeneous manner on the surface of the protein. The Trp residues then change their relative locations to a more homogeneous manner as the silk fibroin undergoes conformational changes from a random coil structure to a β-sheet structure (132). The work by Georgakoudi and workers attributed the fluorescence spectral properties of silk to three components, namely Try and Trp residues and the degree of crosslinking.

In one of the first papers that described the use of SB to quench autofluorescence signals from tissues sections, Schnell and co-workers carried out a dose dependent study of SB concentration on the detrimental effect SB might have on immunofluorescent labelling (272). Although Jaafar and co-workers (266) mentioned the need for adjustment of treatment duration depending on the staining specimen thickness, no study has conducted a time dependent investigation on the resultant effects of SB treatment on the signals from fluorescent probes. Hence, part one of this study was dedicated to investigate the duration of SB treatment on the effects of the signal strengths from fluorescent probes. Samples (Figure F-**1 and** Figure F-**2**) were prepared to not contain any autofluorescing materials present to avoid confounding effects. This is a further improvement to the dose-dependent study carried out by Schnell and co-workers in 1999, where samples used to carry out the dose-dependent effects on immunofluorescent labels were spinal cord sections which would contain to some degree some amount of autofluorescence signals (272).

Despite the presence of several literature on the quenching phenomena of SB for immunohistochemistry, the use of SB treatment to improve actin visualization has only been described in one other study by Jaafar and co-workers (266) using a similar phalloidin approach. In that study (266), SB treatment was introduced at the last step of staining protocol as per the methodology described in other published literature on the use of SB as an autofluorescence quencher. In this study, we have attempted to introduce SB prior to the fluorescence staining for actin staining and had compared it with results obtained by introducing SB after the fluorescence staining steps (Figure F-**2** and Figure F-**4**). As one of the pioneers using SB as a quencher dye, Schnell and co-workers anecdotally mentioned in their paper (272) that SB added before immunofluorescence staining resulted in an unacceptably reduction of immunocytochemical labelling of monkey tissues. This might account for the reason why SB treatment was always introduced (in subsequent studies published in literature) as the last step after fluorescence staining is completed. However, results from Figure F-**2** and Figure F-**4** showed that for a direct fluorescence staining protocol (Eg. Phalloidin toxin) where immunocytochemical labelling is not needed, SB treatment can be introduced before the fluorescence staining step to avoid suppressing the signals from the desired fluorescent probes instead, thereby giving slightly better images as can be seen in Figure F-**2a** (versus Figure F-**2b**) and Figure F-**4b** ("before" versus "after" groups).

The studies by Yang et al (132) and Georgakuodi et al (139) demonstrated that the intrinsic spectral profiles of different forms of silk are not the same and provided sufficient evidence for this study to hypothesize a difference in SB effect between different forms of silk biomaterials. Hence, to account for any possible differences in SB quenching, a range of commonly reported forms of silk biomaterials were used in this study for investigation – from highly hierarchical fibres to sponges, films and

electrospun nano mats reconstituted from extracted silk fibroin solutions using different methodology approaches. This hypothesis was validated by the quantitative differences in SB effect response showed between the film (Figure F-**3a**) and electrospun mat (Figure F-**3b**) groups, and the resultant qualitative differences observed between Figure F-**4a** and Figure F-**4b**.

Autofluorescence is a ubiquitous phenomenon in histochemistry. Fixation induced autofluorescence and naturally occurring autofluorescence in mammalian tissue sections from the kidneys, brain and livers are routinely described in literature (267-269,272,273). The latter was the reason which led to the discovery of SB to be an effective fluorescence quencher. Such autofluorescence in tissue sections (mostly from the kidneys, brain and livers) have been mainly attributed to the presence of endogenous fluorophores such as flavins and lipofuscins (267,272). Similarly, synthetic polymers have also been mentioned in literature to exhibit autofluorescence (266,278-281). For some of these polymers with no aromatic rings in their chemical structures, it has been postulated that light scattering from the polymers might be the cause for the reflected light exhibited during fluorescence microscopy, which results in similar inhibitory effects as autofluorescence signals (266,282). In the case of Jaafar and co-workers (266), it was suggested that the quenching effect of SB on some of the synthetic polymers tested in their study might be attributed to SB being able to absorb large amounts of light (thereby absorbing photons scattered and emitted from the polymers itself), and reducing the amount of light scattering by having SB binding to and smoothing the polymers' surfaces to change their refraction indexes. It can be postulated that a combination of several reasons, including those described by Jaafar et al (266), and a possible chemical interaction between SB and the aromatic Trp and Tyr residues from the silk fibroin sequences could be possible explanations for the modulatory effects of SB on silk-based biomaterials. Although not within the scope of this thesis, and results shown are not entirely corroborative,

the differences in the effects of SB between silk materials of different forms (Eg. films versus electrospun mats as shown in Figure F-**3** and Figure F-**4**; stronger autofluorescence in yarns versus sponges as observed in Figure F-**7** and Figure F-**8**) suggest that the structure of the silk protein plays a pivotal influence on the resultant quenching effects of SB.

As compared to the immunologically inert silk fibroin core, sericin has been largely associated with eliciting immune responses in vivo (283-285). Hence sericin is routinely removed from the silk fibroin before further processing to make biomaterials. In line with common practice and for relevance of applicability, silk biomaterials used in this study were all degummed to remove sericin. However, it must be noted that sericin, in recent years, have been found to be a good biomaterial, especially in the area of wound healing (286,287). Further work can be done with regards to SB treatment on sericin based biomaterials. Silk used as biomaterials can be broadly divided into two types – mulberry and non-mulberry. Domesticated B Mori silk used in this study is of the mulberry type, and is more extensively established as a biomaterial. However, the use of non-mulberry silk as a biomaterial has been increasingly reported in literature (288,289). Given the differences in protein sequences and structures between both types (290), further studies can be carried out to explore the effects of SB treatment on non-mulberry silk based biomaterials as well.

G. Morphometric Characterization of Porcine Caudal IVDs for Future Organ Culture Work

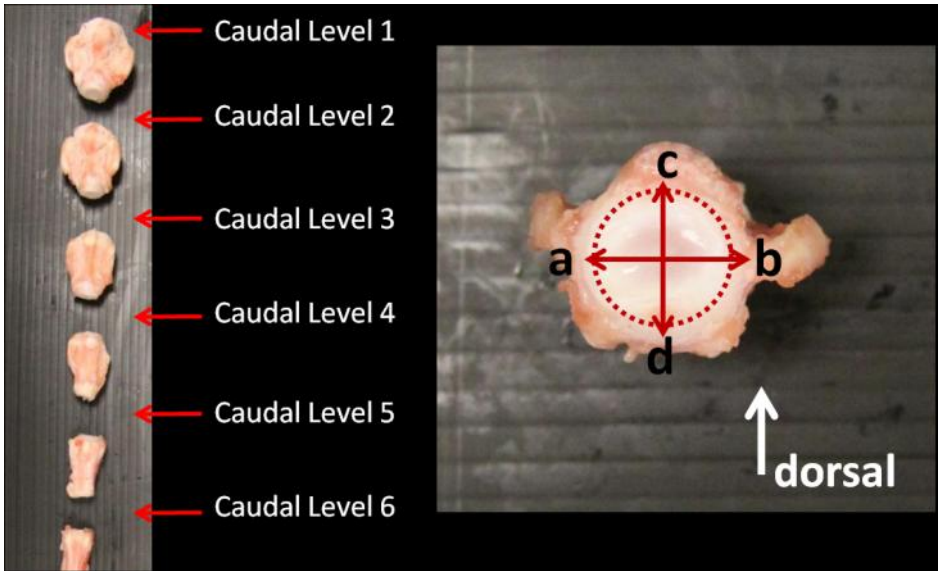

Figure G1. Overview of porcine caudal discs and orientation of morphometric measurements.

Table G1. Summary of Morphometric Measurements

Caudal Level	Distance (mm) a-b	Distance (mm) c-d	Best fit circle (mm^2)
1	14.88	13.17	140.70
2	12.98	11.92	123.19
3	10.60	9.60	79.65
4	7.80	9.00	51.52
5	8.27	9.04	60.69
6	7.17	6.42	38.68